Compact Circularly Polarized Tri-, Dual- and Single-Band Dielectric Resonator Antennas

by

CHAUDHARY PANKAJ PRABHUBHAI
201521001

A Thesis Submitted in Partial Fulfilment of the Requirements for the Degree of

DOCTOR OF PHILOSOPHY

to

Dhirubhai Ambani Institute of Information and Communication Technology

December, 2021

Declaration

I hereby declare that

i) the thesis comprises of my original work towards the degree of Doctor of Philosophy at Dhirubhai Ambani Institute of Information and Communication Technology and has not been submitted elsewhere for a degree,

ii) due acknowledgment has been made in the text to all the reference material used.

Chaudhary Pankaj Prabhubhai

Certificate

This is to certify that the thesis work entitled COMPACT CIRCULARLY POLARIZED TRI-, DUAL- AND SINGLE-BAND DIELECTRIC RESONATOR ANTENNAS has been carried out by CHAUDHARY PANKAJ PRABHUBHAI for the degree of Doctor of Philosophy at *Dhirubhai Ambani Institute of Information and Communication Technology* under our supervision.

Prof. Deepak K. Ghodgaonkar
Thesis Supervisor

Prof. Sanjeev Gupta
Thesis Co-Supervisor

Acknowledgments

First of all, i would like to thank Almighty and my respected Gurus for providing me this wonderful opportunity to pursue higher study. This work is possible due to grace of Ambaji Maa, Arbuda Maa, Hanumanji Maharaj, Sahajanand Swami Maharaj, and my Gurus Joshi Deviprasad Maharaj and Mahant Swami Maharaj.

I would express my sincere gratitude to my supervisor Prof. Deepak Kumar Ghodgaonkar and my co-supervisor Prof. Sanjeev Gupta for their support and contribution throughout this PhD journey. Their philosophy of balanced life is an inspiration for me. They always motivated me whenever i feel down. They always encourage me to experiment new things. I would like to thank them for providing their precious time for discussions and problem solving.

I am very thankful to Prof. Yash Vasavada, Prof. Bhaskar Chaudhury and Prof. Ranjendra Mitharwal for their constructive criticisms and suggestions during research progress seminars. I would also like to thank Prof. Hemant Patil and Prof. Yash Vasavada for their valuable suggestions during the PhD synopsis.

I am very thankful to Distinguished Scientist Shri Rajeev Jyoti, Deputy Director, Space Applications Centre (SAC), Indian Space Research Organization (ISRO), Ahmedabad, and Dr. Milind Mahajan, Group Director, Antenna Systems Group, SAC, ISRO for providing all necessary facilities required for this work. I am also very thankful to Scientists Mr. Abhishek Shukla and Mr. Alok Kumar Singhal and Antennas Measurement Group, SAC, ISRO.

I am very thankful to DA-IICT staff members Mr. Krunal Patel, Rameshbhai, Rajendrabhai, Bhargavbhai, Sanjaybhai, Nareshbhai, Mr. Abhishek and help desk staff for their support. I am very thankful to all other staff members of DA-IICT who have directly or indirectly supported me during this journey.

I would like to thank my PhD colleagues Rahul Vashishth, Rishikant Rajdeepak, Jignesh Patel and Miral Shah for their support. I would also like to thank PhD graduates Dr. Hardik Patel, Dr. Gautam Makwana, Dr. Sanket Patel and Dr. Ashish Sarvaiya.

Last but not the least, i would like to thank my parents Shri Prabhubhai and Shrimati Navalben for their support and patience during this PhD journey. I am also very thankful to my brother Ashokbhai and my wife Mrs. Sejal for encouraging me throughout the study.

Contents

Abstract

The Dielectric Resonator Antennas (DRAs) have received wide attention due to low loss, high radiation efficiency, small size, wider bandwidth and simple feed network as compared to the microstrip antennas. Microstrip antennas have many challenges such as low radiation efficiency, high conductor loss, poor polarization purity, multiple frequency bands and multiple polarizations with a large footprint area of the antenna, low gain and narrow bandwidth.

The existing design techniques for tri-, dual- and single-band DRAs reported in the literature have various limitations such as ground plane area of DRA, volume of Dielectric Resonator (DR) and DRA not sufficient for small physical area applications, realization of Circular Polarization (CP) over large ground plane area and unavailability of single DR geometry with multi-mode for multi-band applications.

In this thesis, compact CP tri-band (L5, L1 and S-bands) staired Rectangular Dielectric Resonator Antennas (RDRAs) (two port, single port) using tri-, dual- and single-sections Wilkinson Power Dividers (WPDs) with wide-band 90° phase shifters are designed, analyzed, fabricated and tested. These tri-band RDRAs are used in Indian Regional Navigation Satellite System (IRNSS) and GPS-Aided GEO Augmented Navigation (GAGAN) applications. The ground plane footprint areas of tri-band RDRAs and volumes of staired Rectangular Dielectric Resonators (RDRs) are significantly reduced by using high dielectric constant of DR materials and high dielectric constant of dielectric substrates. The broadside radiation patterns of tri-band RDRAs are produced by TE^y_{111}, TE^y_{113} and TE^y_{112} modes for L5, L1 and S-bands, respectively. Various parameters of tri-band RDRAs like return loss, Right Hand Circularly Polarized (RHCP) - Left Hand Circularly Polarized (LHCP) radia-

tion patterns, RHCP gains and axial ratios are analyzed and measured.

Compact CP dual-(L5 and L1) and single-band RDRAs are designed, analyzed, fabricated and tested using feed networks of dual- and single-sections WPDs with wide-band 90° phase shifters. The miniaturized volumes of RDRs and ground plane areas of dual- and single-bands RDRAs are achieved using high dielectric constant of DR materials and high dielectric constant of dielectric substrates. The broadside radiation patterns of dual-band RDRA are produced by TE^y_{111} and TE^y_{113} modes for L5 and L1-bands, respectively. The TE^y_{111} modes are produced in three single-band RDRAs for L5, L1 and S-bands. The simulated and measured parameters of dual- and single-band RDRAs are return loss, RHCP-LHCP far field radiation patterns, RHCP gain and axial ratio.

The design and analysis of finite ground plane single-band CP RDRAs using WPD with wide-band 90° phase shifter for L1 and L5-bands are carried out by using high dielectric constant of DRs and dielectric substrates. Also, the effect of different radii of finite circular ground planes of single- and dual-band RDRAs are investigated by using the Method of Moments (MoM). The effect of different radii of circular ground plane on single- and dual-band RDRAs are analyzed for return loss and gains.

List of Tables

List of Figures

Chapter 1

Introduction

1.1 General Introduction

In modern wireless communication technologies, small size, low profile, high radiation efficiency, wider bandwidth, Circular Polarization (CP), multi-band and multiple polarization antennas have received more attention in systems such as satellite, mobile and other communication systems. The microstrip and Dielectric Resonator Antennas (DRAs) are used [1, 2]. Microstrip antennas have many challenges such as the low radiation efficiency, high conductor loss, multi-band and multiple polarizations with large footprint area, low gain and narrow bandwidth [1, 2].

The DRAs are preferred due to low loss, high radiation efficiency, small size, wider bandwidth and simple feed network compared to microstrip antennas [2]. At lower microwave frequency band (L- and S-bands), physical size of dielectric resonator antenna is very large because of larger wavelength achieved at lower microwave frequency. Compact DRAs are very useful in lower microwave frequency band [2].

1.1.1 Applications

The ground terminals of Global Navigation Satellite System (GNSS) are occupied by two bands such as lower L-band from 1.164 to 1.300 GHz and the upper L-band from 1.559 to 1.612 GHz [3]. The ground terminals of Indian Regional Navigation Satellite System (IRNSS) operate in L5 (1.164-1.188 GHz) and S (2.48-2.50 GHz) bands [3]. Also, user segment of GPS-Aided GEO Augmented Navigation (GAGAN) operates in L5 and L1 (1.565-1.585 GHz)-bands [4]. Tri-band (L5, L1 and S-bands) antennas can be used for IRNSS and GAGAN applications.

The GNSS, IRNSS and GAGAN receivers capable of tracking all-in-view GNSS, IRNSS and GAGAN signals require multi-band or wide-band and broadbeam CP antennas [5]. CP antennas are used to reduce the effect of multipath interferences and improve the system performance for navigation satellite application [6, 7]. All the received GNSS, IRNSS and GAGAN signals are RHCP [5]. The dual-band antenna is preferred to mitigate the effect of ionosphere on the IRNSS signal.

The minaturized DRAs are achieved using high dielectric constant materials of Dielectric Resonator (DR) and optimized aspect ratios of DR [6, 7]. Several research groups have studied different aspects of the DRAs such as compactness, low-profile design, wider bandwidth operation, circular polarized radiations, high gain and modified shape etc separately [2, 6, 7]. The reported DRAs are operated at L, S, C, X, Ku, K, and Ka-bands [2]. L and S-bands are lower frequency ranges compared to other band such as C, X, Ku and Ka-bands [2]. Size of L and S-bands DRAs are very large compared to other band such as C, X, Ku and Ka-bands [2]. Compact designs of DRAs have been implemented in the frequency range of 3 to 10 GHz [2]. IRNSS at L5 and S-bands (seven satellites in geostationary orbit) is implemented by Indian Space Research Organisation (ISRO) [4].

1.1.2 Design Challenges and Motivation

The ground terminals of GNSS, IRNSS and GAGAN are operated in lower microwave frequency due to which physical size of the antennas become very large. The ground terminals of IRNSS and GAGAN applications required multi-band operation in single-compact antenna. Compact antenna size over multi-band (lower microwave frequency), Right Hand Circular Polarization (RHCP) generation and broadside radiation patterns generation become very **challenging design issues** [3].

The 3-D geometry of DRAs allows them to generate various modes in single antenna volume which reduces overall cost and system size [8]. The stable radiation patterns over required bands can be obtained by using higher-order modes of DRAs. The use of linearly polarized antennas at the receiver-end results in 3 dB loss due to polarization mismatch. For optimal performance, the receiver antennas are required to be RHCP. The key advantages of the circular polarization as compared to linear polarization are : 1) insensitivity to the relative orientation between the satellite based transmit and receive antennas, 2) decreased sensitivity to the earth's ionospheric effects on signal polarization and 3) inherent discrimination between the direct and single bounce reflected signals [5].

1.2 Dielectric Resonator Antennas

1.2.1 History of Dielectric Resonator Antennas

Okaya and Barash first analyzed modes in DRAs in the early 1960s. The study of DRs as antenna elements began in the early 1980s with examination of characteristics of cylindrical, rectangular and hemispherical shaped DRAs by Long, McAllister and Shen [2]. Analysis of excitation, resonant modes and radiation patterns made it apparent that these DRs can be used as antennas and offered a new attractive alternative to traditional conductor based radiators [2].

In 1990s, various feeding techniques to excite the DRAs were realized and numerical techniques were applied for determining input impedance and Q-factor of DRAs. In 1994, Mongia and Bhartia [2] proposed resonant modes and set of simple equations for predicting the resonant frequency and Q-factor for various DRA shapes.

1.2.2 Important Characteristics of Dielectric Resonator Antenna

The main characteristics of DRA are:

- The physical size of DRA is proportional to ($\frac{\lambda_0}{\sqrt{\epsilon_r}}$) where, λ_0 is free-space wavelength at resonant frequency and ϵ_r is dielectric constant of dielectric resonator material.
- Low conductor loss due to dielectric material.
- High radiation efficiency.
- Resonant frequency of DRA is a function of shape, size and dielectric constant of Dielectric Resonator (DR) material.
- Dielectric constant of DR material is in the range of 8 to over 100 which allows designer to have control over physical size and bandwidth of DRAs.
- Resonant frequency and Q-factor will be affected by the aspect ratio of DRA for a fixed dielectric constant of DR material.
- High power handling capability.
- Mostly suitable for microwaves and millimeter waves.

1.2.3 Working Principle of Dielectric Resonator Antenna

The Electromagnetic (EM) waves produced from rapid oscillations of electrons in atoms causes acceleration or deaccelerations which become electromagnetic wave radiation [9]. The radio waves from RF transmitter circuits are fed into ceramics forming resonator as shown in Figure 1.1 (a). The RLC equivalent circuit is shown in Figure 1.1 (b) for DRA based on electric properties of ceramic dielectric resonator. These RF waves bounce back and forth between resonator walls, thus forming standing waves, hence stores electrical energy [9].

The oscillating current introduces oscillating electric fields (E-fields) and oscillating magnetic fields (H- fields) [9]. Due to the accelerrating currents, time-varying fields are radiated away from DRA into free space [9]. The walls of ceramic are formed partially transparent magnetic walls. Because of fringing effect, the magnetic energy leaks through these transparent walls. Thus, the radio power is radiated into free

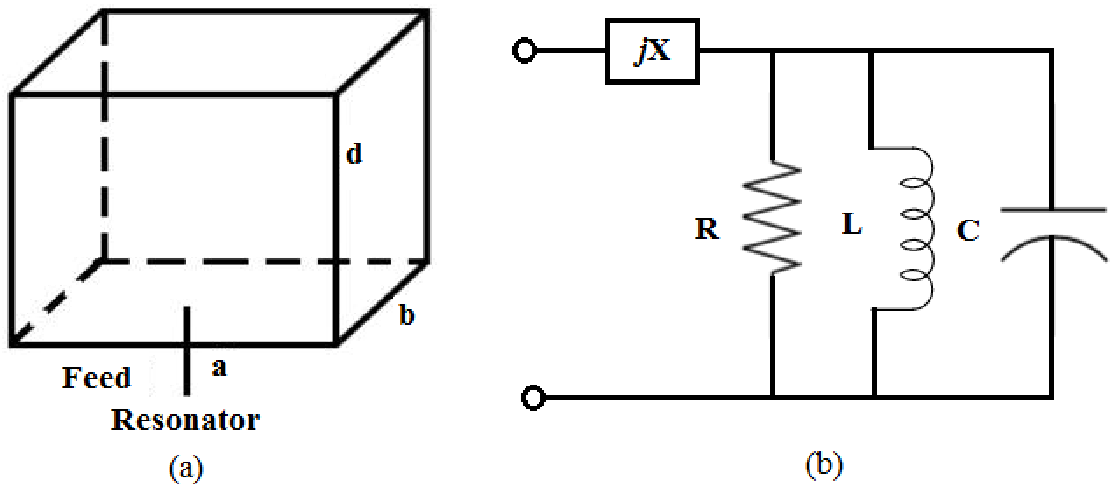

Figure 1.1: (a) Ceramic dielectric resonator antenna with dimensions of a, b and d (b) DRA equivalent RLC circuit [9]

space [9]. As per the principle of conservation of energy, probe currents are equated with DRA radiating currents. In other words, time-average electric energies are equated with time-average magnetic energies inside the DRA as given in equation (1.1) [9].

$$\int_V |E|^2 dV = \int_V |H|^2 dV \tag{1.1}$$

1.3 Objective and Design Specifications

Compact CP tri-, dual-, single-band DRAs will be designed, analyzed, fabricated and tested for lower frequency bands such as L5 (1.164-1.188 GHz), L1 (1.565-1.585 GHz) and S (2.48-2.5 GHz)-bands. The design specifications of tri-, dual- and single-band DRAs are given in Table 1.

Table 1.1: Design specifications of tri-band DRA at L5, L1 and S-bands, dual-band DRA at L5 and L1-bands, single-band DRA at each of L5, L1 and S-bands

Tri-band	**L5-band**	**L1-band**	**S-band**
Dual-band	**L5-band**	**L1-band**	**-**
Single-bands	**L5-band**	**L1-band**	**S-band**
Design Parameters	**L5-band**	**L1-band**	**S-band**
Frequency Band	1176±12MHz	1575±10MHz	2490±10MHz
Return Loss (RL)	$>$ 10 dB	$>$ 10 dB	$>$ 10 dB
Polarization	RHCP	RHCP	RHCP
Radiation Pattern	Broadside	Broadside	Broadside
RHCP Gain at $\theta = 0°$	2.0 dB	2.0 dB	2.0 dB
RHCP Gain at $\theta = \pm 60°$	-4.0 dB	-4.0 dB	-4.0 dB
RHCP Gain at $\theta = \pm 70°$	-5.5 dB	-5.5 dB	-5.5 dB
RHCP Gain at $\theta = \pm 80°$	-7.0 dB	-7.0 dB	-7.0 dB
Axial Ratio (AR) at $\theta = 0°$ to $\pm 60°$	$<$ 3.0 dB	$<$ 3.0 dB	$<$ 3.0 dB

1.4 Novel Contributions of the Proposed Research Work

- **Compact CP tri-band staired RDRA** (two-port) for IRNSS and GAGAN applications is designed, analyzed, fabricated and tested at L5, L1-and S-bands. RHCP of tri-band RDRA for L5, L1-bands is obtained using novel design feed network of dual-section Wilkinson Power Divider (WPD) with wide-band 90° phase shifter. Single geometry staired RDRA produces multi-modes such as TE^y_{111} mode at 1.176 GHz, TE^y_{113} mode at 1.575 GHz and TE^y_{112} mode at 2.49 GHz with broadside radiation patterns which reduces overall cost and system size. Tri-band RDRA was significantly miniaturized ground plane area to 0.16 λ_0 × 0.16 λ_0 (40 mm × 40 mm) and volume of staired RDR to 27 mm × 27 mm × 35.3 mm using high dielectric constant of dielectric resonator and dielectric substrate. Simulated and measured parameters are return loss, isolation, RHCP-LHCP radiation patterns, RHCP gain and axial ratio. Also, miniaturized CP tri-band staired RDRA (single port) is investigated using novel design feed network of tri-section WPD with wide-band 90° phase shifter.

RHCP of tri-band DRA is produced using tri-section WPD with wide-band 90° phase shifter. Ground area and volume of tri-band DRA are remarkably reduced to 0.16 λ_0 × 0.16 λ_0 (40 mm × 40 mm) and 23.2 mm × 23.2 mm × 28.25 mm, respectively.

- **Miniaturized CP dual-band RDRA** for L5 and L1-band is developed using novel design feed network of dual-section WPD with wide-band 90° phase shifter. Dual-band RDRA significantly reduces ground plane area to 40 mm × 40 mm and volume of RDR to 24.2 mm × 24.2 mm × 26.2 mm using high dielectric constant of dielectric resonator and dielectric substrate. Rectangular Dielectric Resonator (RDR) generated dual mode such as TE^y_{111} mode at 1.176 GHz and TE^y_{113} mode at 1.575 GHz with broadside radiation patterns. Simulated and measured parameters of dual-band RDRA are observed.

- **Compact single-band (L5, L1 and S-bands) RDRAs** are designed, analyzed, fabricated and tested. CP of single band RDRAs are generated using WPD with wide-band 90° phase shifter. RDRs for single-band (L5, L1 and S-band) generated single TE^y_{111} mode. Single-band (L5, L1 and S-bands) RDRAs have significantly miniaturized ground planes area and volume of RDRs using high dielectric constant of dielectric resonator and dielectric substrate.

- **Design and analysis of finite ground plane CP single-band RDRAs** (L5 and L1-bands) are presented using feed network of WPD with wide-band 90° phase shifter. In this work, high dielectric constant of RDR and dielectric substrate are used. Design and analysis of effect of different radii finite ground plane in two ports CP single- and dual-band DRAs are investigated using Method of Moments (MoM).

- **Simultaneously achieved design specifications of DRAs** such as return loss, polarization, radiation patterns, RHCP gain at different zenith angle and axial ratio over tri-, dual- and single-bands with compact ground plane area and volume of DRAs.

1.5 Organization of Thesis

In chapter 2, theoretical aspect of Hemispherical DRA (HDRA), Cylindrical DRA (CDRA), Rectangular DRA (RDRA), modes in DRA, Dielectric Waveguide Model (DWM), curve-fitting method, circular polarization and MoM are provided. It includes the literature review of tri-/multi-, dual-, single-/wide-band DRAs and analysis DRAs using MoM. The research gap and design challenges of tri-, dual- and single-band DRAs are also discussed.

Chapter 3 presents compact CP tri-band staired RDRA (two-port) and miniaturized CP tri-band staired RDRA (single port). Tri-band RDRAs are designed, analyzed, fabricated and tested at L5, L1 and S-bands for IRNSS and GAGAN applications. The design steps, structures, mathematical formulation, feed networks, electric field distributions, fabrications, testings, simulated results and measured results are described for tri-band RDRAs.

Chapter 4 investigates compact CP dual-band RDRA. This RDRA is designed, analyzed, fabricated and tested at L5 and L1-bands. The geometry, excitation, electric field distribution, fabrication, testing, simulated results and measured results of dual-band RDRA are described.

Chapter 5 presents compact CP single-bands RDRAs. These single-band RDRAs at L5, L1 and S-bands are designed, analyzed, fabricated and tested. The structures, feed networks, modes, fabrications, testing, simulated results and measured results of single-band RDRAs are also described.

In chapter 6, the design and analysis of effect of finite ground plane in CP single- and dual-bands RDRAs are carried out. The finite ground plane CP single-bands RDRAs are designed and analyzed at L5 and L1-bands. Also, the finite ground plane CP single- and dual-bands RDRAs are designed and analyzed using MoM.

Finally chapter 7 contains a summary and discussion of the finding and results from the work contains within this thesis. The potential revenues of future work and other applications are also suggested.

In Appendix A, automated measurement system, measurement of radiation patterns, gain transfer method and rotating source method are discussed. In Appendix B, MoM formulation of two-port single- and dual-band CP RDRAs and energy conservation are presented. In Appendix C, Matlab codes of tri-, dual- and single-band RDRAs are provided.

References

[1] C. A. Balanis, "Antenna Theory: Analysis and Design," *John Wiley & Sons*, New York,USA, 1989.

[2] A. Petosa, "Dielectric Resonator Antenna Handbook," *Artech House*, Norwood, MA, USA, 2007.

[3] S. Jović, M. Clénet and Y. M. M. Antar, "A compact wideband 4-port circularly polarized dielectric resonator antenna," *2017 11th European Conference on Antennas and Propagation (EUCAP)*, Paris, 2017, pp. 1957-1959.

[4] C. J. Hegarty and E. Chatre, "Evolution of the Global Navigation SatelliteSystem (GNSS)," *Proceedings of the IEEE*, vol. 96, no. 12, pp. 1902-1917, Dec. 2008.

[5] S. Jovic, M. Clenet and Y. M. M. Antar, " Novel wideband antenna for GNSS and satellite communication," *2020 14th European Conference on Antennas and Propagation (EuCAP)* , Copenhagen, Denmark, 2020, pp. 1-5.

[6] G. Massie, M. Caillet, M. Clenet and Y. M. M. Antar, "A new wideband circularly polarized hybrid dielectric resonator antenna," *IEEE Antennas and Wireless Propagation Letters*, vol. 9, pp. 347-350, 2010.

[7] R. Han, S. Zhong and J. Liu, "Design of circularly-polarized dielectric resonator antenna with wideband feed network," *Proceedings of 2014 3rd Asia-Pacific Conference on Antennas and Propagation*, Harbin, 2014, pp. 48-50.

[8] L.Zou, "Dielectric Resonator Antennas: From Multifunction Microwave Devices to Optical Nano-antennas," PhD Thesis, School of Electrical and Electronics Engineering, The University of Adelaide, Australia, March 2013.

[9] R. S. Yaduvanshi and H. Parthasarathy, " Rectangular Dielectric Resonator Antennas Theory and Design," *Springer*, India, 2016.

[10] R. Kumar Mongia and A. Ittipiboon, "Theoretical and experimental investigations on rectangular dielectric resonator antennas," in *IEEE Transactions on Antennas and Propagation*, vol. 45, no. 9, pp. 1348-1356, Sept. 1997.

[11] K. M. Luk and K. W. Leung, "Dielectric Resonator Antennas," *Research Studies Press LTD*, Baldock, England, 2003.

[12] S.Keyrouz and D. Caratelli, "Dielectric resonator antennas: Basic concepts, design guidelines, recent developments at millimeter-wave frequencies," *International Journal of Antennas and Propagation*, vol. 2016, article id. 9, pp. 1-20, Sept. 2016.

[13] Ansys High Frequency Structure Simulator (HFSS) is a 3-D Electromagnetic (EM) simulation software for designing and simulating high-frequency electronic products such as antennas, antenna arrays, Radio Frequency (RF) or microwave components, high-speed interconnects, filters, connectors, Integrated Circuit (IC) packages and printed circuit boards. https://www.ansys.com/en-in/products/electronics/ansys-hfss

Chapter 2

Dielectric Resonator Antennas

2.1 Theory

The characteristics of Dielectric Resonator Antennas (DRAs) are low loss, high radiation efficiency, small size, wider bandwidth and simple feed network [1]. Figure 2.1 shows different Dielectric Resonator (DR) shapes of DRAs. There are three basic shapes in DRAs [2].

1. Hemispherical DRA (HDRA)
2. Cylindrical DRA (CDRA)
3. Rectangular DRA (RDRA).

2.1.1 Hemispherical Dielectric Resonator Antenna

HDRA is characterized by radius (a) and dielectric constant (ϵ_r) of DR material with no degree of freedom in design [2, 3]. Figure 2.2 shows geometry of HDRA [1]. The Transverse Electric (TE) and Transverse Magnetic (TM) modes are generated in HDRA [2, 3]. TE and TM modes have zero value for radial component of electric field (E_r=0) and zero value for radial component of magnetic field (H_r=0), respectively. The mode index is mnl, where m is the field variation in radial (r) direction, n is the field variation in azimuth (ϕ) direction and l is the field variation in elevation (θ) direction [2, 3]. TE_{111} and TM_{111} are two fundamental modes in HDRA. TE_{111} and TM_{111} modes have radiation patterns similar to short horizontal magnetic dipole and short electric monopole, respectively [2, 3].

2.1.2 Cylindrical Dielectric Resonator Antenna

CDRA is characterized by radius (a), height (h) and dielectric constant (ϵ_r) of DR material as shown in Figure 2.3 with one degree of freedom in design compared to HDRA [1, 2, 3]. TE, TM and Hybrid Electromagnetic (HEM) modes are generated in CDRA [2, 3]. The mode index is mnl, where m is the field variation in azimuth (ϕ), n is the field variation in radial (r) direction and l is the filed variation in z-direction.

$TM_{01\delta}$, $TE_{01\delta}$ and $HE_{11\delta}$ modes are produced in CDRA, where δ is fraction of half cycle field variation. $TM_{01\delta}$, $TE_{01\delta}$ and $HE_{11\delta}$ modes have radiation patterns similar to short electrical monopole, short magnetic monopole, short horizontal magnetic dipole, respectively [2, 3]. TE and TM modes are not dependent on ϕ-direction but hybrid modes are dependent on ϕ-direction.

2.1.3 Rectangular Dielectric Resonator Antenna

RDRA is characterized by length (d), width (a), height (b) and dielectric constant (ϵ_r) of DR material as shown in Figure 2.4 with two degrees of freedom in form of aspect ratios $\frac{a}{d}$ and $\frac{b}{d}$ [1, 2]. RDRA is most versatile basic shape because of two more degrees of freedom as compared to one degree of freedom of CDRA and no degree of freedom of HDRA [2].

TE and TM modes were produced in isolated rectangular dielectric waveguide. RDRA mounted on ground plane generates only TE mode [2]. TE^x, TE^y and TE^z modes are radiated like short magnetic dipoles in x-, y- and z-directions, respectively. $TE^x_{\delta 11}$, $TE^y_{1\delta 1}$ and $TE^z_{11\delta}$ modes are fundamental lower order modes where subscripts indicate field variations in x-, y- and z-directions, respectively.

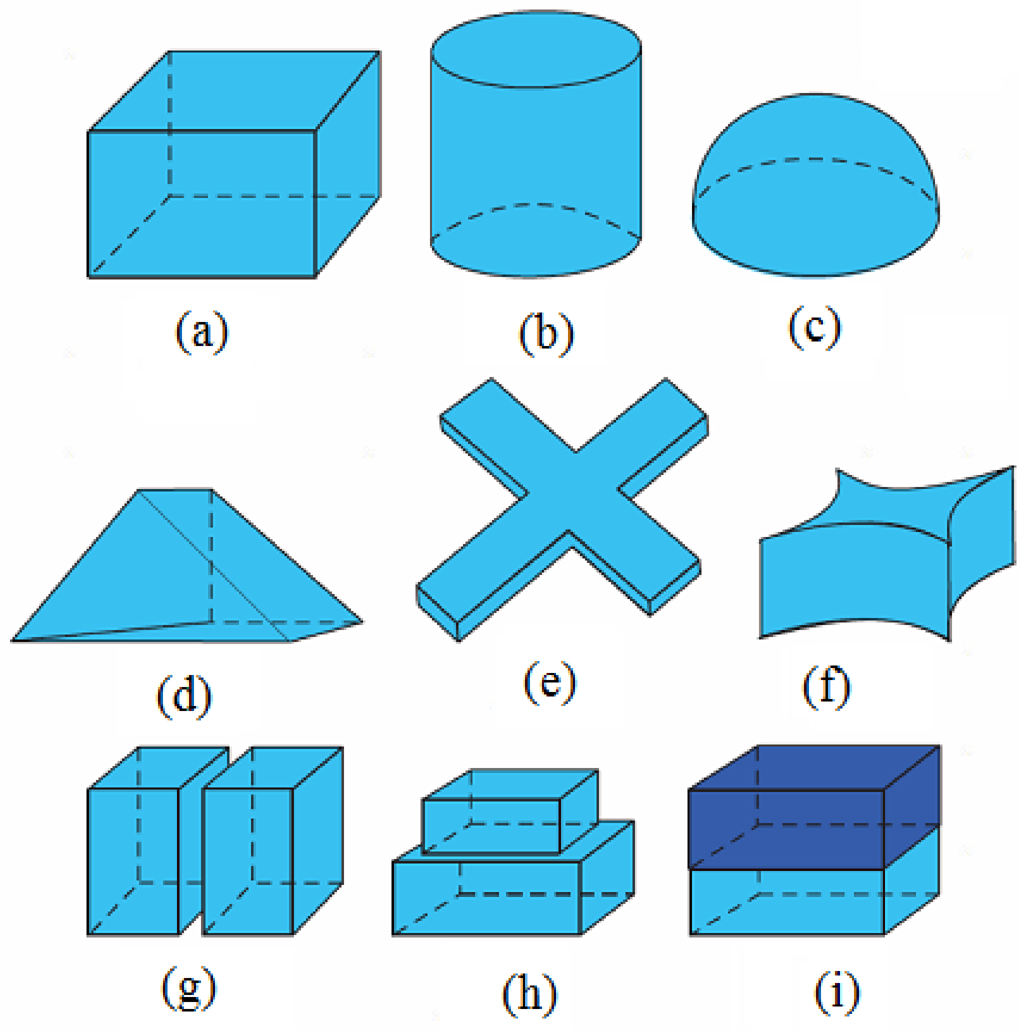

Figure 2.1: Different radiating geometries of DRAs [1]

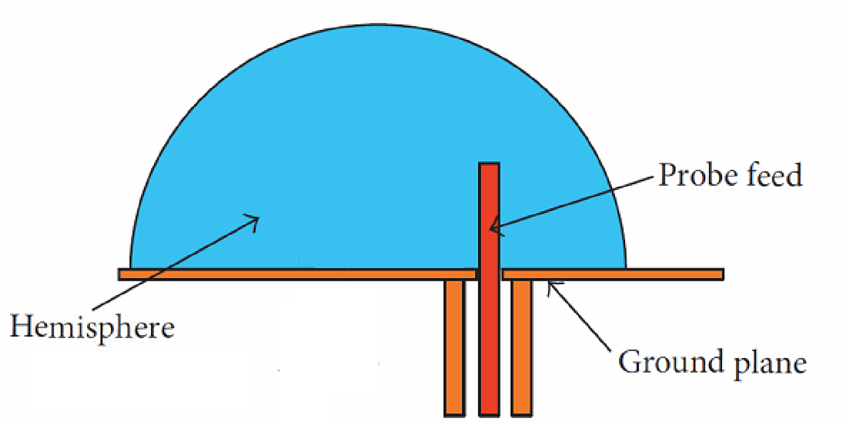

Figure 2.2: HDRA with probe-fed [1]

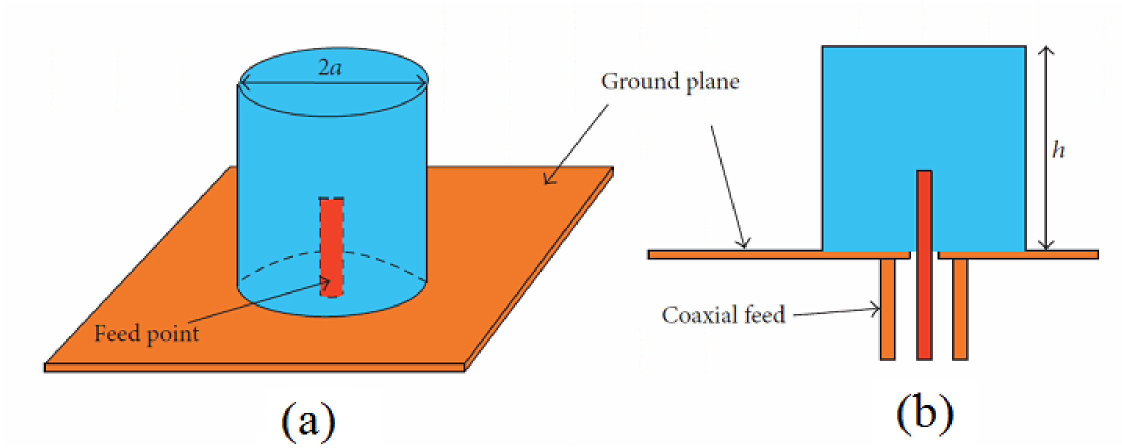

Figure 2.3: (a) 3-D cross-sectional view of CDRA (b) probe-fed CDRA [1]

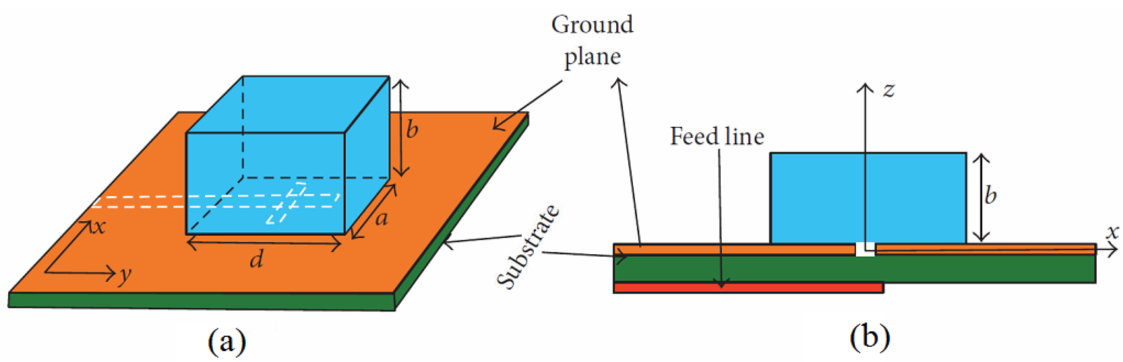

Figure 2.4: (a) 3-D cross-sectional view of RDRA (b) aperture-fed RDRA [1]

2.1.4 Modes in Dielectric Resonator Antenna

The electric field distributions of TE^{y}_{111}, TE^{y}_{112} and TE^{y}_{113} modes of DRA are shown in Figures 2.5 (a), 2.5 (b) and 2.5 (c), respectively. The fields of TE^{y}_{11m} modes with odd m can be expressed as [4]:

$$E_{0x} = -k_z A cos(k_x x) cos(k_y y) sin(k_z z) \tag{2.1}$$

$$E_{0y} = 0 \tag{2.2}$$

$$E_{0z} = k_x A sin(k_x x) cos(k_y y) cos(k_z z) \tag{2.3}$$

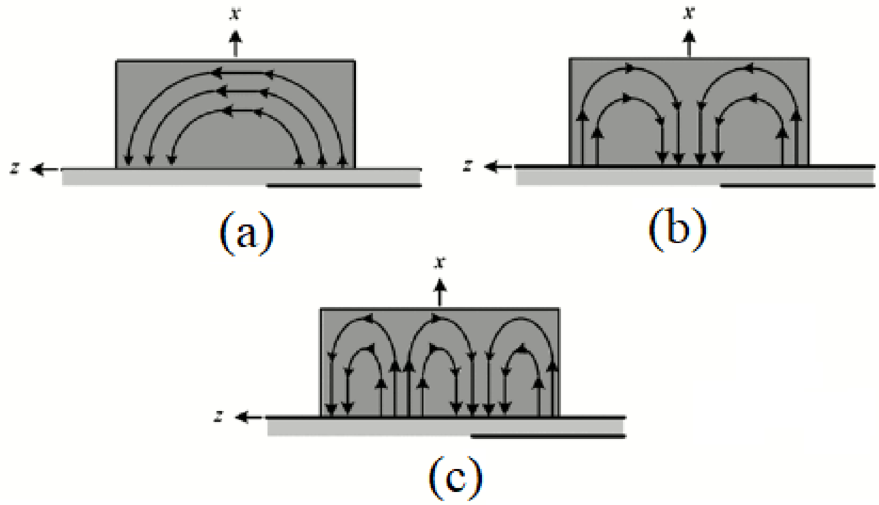

Figure 2.5: Electric field distribution of (a) TE^y_{111} mode (b) TE^y_{112} mode (c) TE^y_{113} mode of DRA [4]

$$H_{0x} = \frac{k_x k_y}{j\omega\mu} A sin(k_x x) sin(k_y y) cos(k_z z) \tag{2.4}$$

$$H_{0y} = \frac{k_x^2 + k_z^2}{j\omega\mu} A cos(k_x x) cos(k_y y) cos(k_z z) \tag{2.5}$$

$$H_{0z} = \frac{k_z k_y}{j\omega\mu} A cos(k_x x) sin(k_y y) sin(k_z z) \tag{2.6}$$

where A is arbitrary constant.

The fields of TE^y_{11m} modes with even m can be expressed as [4]:

$$E_{0x} = -k_z B cos(k_x x) cos(k_y y) cos(k_z z) \tag{2.7}$$

$$E_{0y} = 0 \tag{2.8}$$

$$E_{0z} = k_x B sin(k_x x) cos(k_y y) sin(k_z z) \tag{2.9}$$

$$H_{0x} = \frac{k_x k_y}{j\omega\mu} B sin(k_x x) sin(k_y y) sin(k_z z) \quad (2.10)$$

$$H_{0y} = \frac{k_x^2 + k_z^2}{j\omega\mu} B cos(k_x x) cos(k_y y) sin(k_z z) \quad (2.11)$$

$$H_{0z} = -\frac{k_z k_y}{j\omega\mu} B cos(k_x x) sin(k_y y) cos(k_z z) \quad (2.12)$$

where B is arbitrary constant. k_x, k_y and k_z are wave-numbers in x-, y- and z-directions, respectively.

2.1.5 Dielectric Waveguide Model

The rectangular dielectric resonator with dimensions $a \times b \times d$ on ground plane is shown in Figure 2.6 (a), which is equivalent to an isolated dielectric resonator with dimensions $a \times b \times 2d$ in free-space as shown in Figure 2.6 (b). For rectangular dielectric resonator, the resonant frequencies of TE mode can be estimated with reasonable accuracy using Dielectric Waveguide Model (DWM) [2, 5, 6]. The fields of this model are assumed to be totally reflected by two opposite sides of the DR, while the other four sides behave like Perfect Magnetic Conductor (PMC) walls [6].

For TE^y_{11m} modes, wave-number k_y is obtained by solving the following transcendental equation [2, 5]:

$$k_y \tan(k_y b/2) = \sqrt{(\epsilon_r - 1)k_0^2 - k_y^2} \quad (2.13)$$

where k_0 is free-space wave-number given by equation:

$$k_0 = \frac{2\pi f_r}{c} \quad (2.14)$$

and c is the velocity of light in free-space. The wave-numbers k_x, k_y and k_z satisfy following separation equation [2, 5]:

$$k_x^2 + k_y^2 + k_z^2 = \epsilon_r k_0^2 \quad (2.15)$$

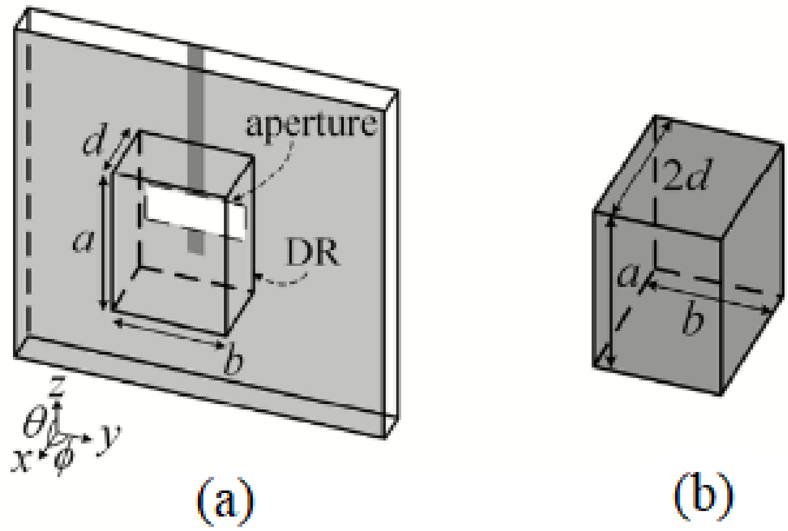

Figure 2.6: (a) Dielectric resonator on ground plane (b) equivalent dielectric resonator in free-space [6]

For TE^{y}_{11m} modes, the resonant frequency f_r of DRA can be obtained from equations (2.14) and (2.15) [4, 6]:

$$f_r = \frac{c\sqrt{k_x^2 + k_y^2 + k_z^2}}{2\pi\sqrt{\epsilon_r}} \tag{2.16}$$

where,

$$k_x = \frac{\pi}{2d} \tag{2.17}$$

$$k_z = \frac{m\pi}{a} \tag{2.18}$$

$$k_y = \frac{2\tan^{-1}(\frac{\sqrt{(\epsilon_r-1)k_0^2 - k_y^2}}{k_y})}{b} \tag{2.19}$$

2.1.6 Curve-Fitting Method

The geometry of the strip-fed rectangular DRA is shown in Figure 2.2. Initially, DRA is considered as excitation free [7]. The length, width and height of Rectangular Dielectric Resonator (RDR) are a, b and d with a>b, respectively [7]. In the analysis, it was determined that it requires only three curve-fitting variables ($\frac{b}{a}$,$\frac{d}{a}$, ϵ_r) and only four design parameters (a, b, d, ϵ_r) [7]. The curve-fitting data generated using DWM model [7]. The frequency changes exponentially with p=$\frac{b}{a}$. The resonant frequency f_r of DRA can be expressed as [7]:

$$f_r = \frac{c}{2\pi a\sqrt{\epsilon_r}}\left(\frac{s_1}{s_2 e^{(s_3 p)}} + s_4\right) \tag{2.20}$$

where,

$$s_1 = -5.29q^4 + 15.97q^3 - 17.74q^2 + 8.812q - 3.198 \tag{2.21}$$

$$s_2 = 0.2706q^4 - 0.7232q^3 + 0.7857q^2 - 0.4558q - 1.023 \tag{2.22}$$

$$s_3 = -8.03q^4 + 23.06q^3 - 24.53q^2 + 11.75q - 3.588 \tag{2.23}$$

$$s_4 = 43.18q^4 - 124.7q^3 + 134.5q^2 - 65.85q + 15.37 \tag{2.24}$$

with q=$\frac{d}{a}$. The f_r as function of ϵ_r for different ratios of d/a are shown in Figure 2.8. The results of curve-fitting method are compared with DWM, the errors are less than 3% over 0.4 $\leq$ p $\leq$1, 0.2 $\leq$ q $\leq$1 and 6 $\leq \epsilon_r \leq$ 100 [7]. The DWM results are matched with the curve-fitting method [7].

Conversely, if the design resonance frequency f_r is specified, length a of RDRA can be calculated from equation (2.20) as follows when the parameters of ϵ_r, p and q are given [7]:

$$a = \frac{c}{2\pi f_r\sqrt{\epsilon_r}}\left(\frac{s_1}{s_2 e^{(s_3 p)}} + s_4\right) \tag{2.25}$$

After a is obtained, the other two dimensions b and d can be determined from two aspect ratios p and q, respectively [7]. If the ratios p and q are not specified, then they can be arbitrarily chosen with the valid ranges of 0.4 $\leq$ p $\leq$1 and 0.2 $\leq$ q $\leq$1 [7].

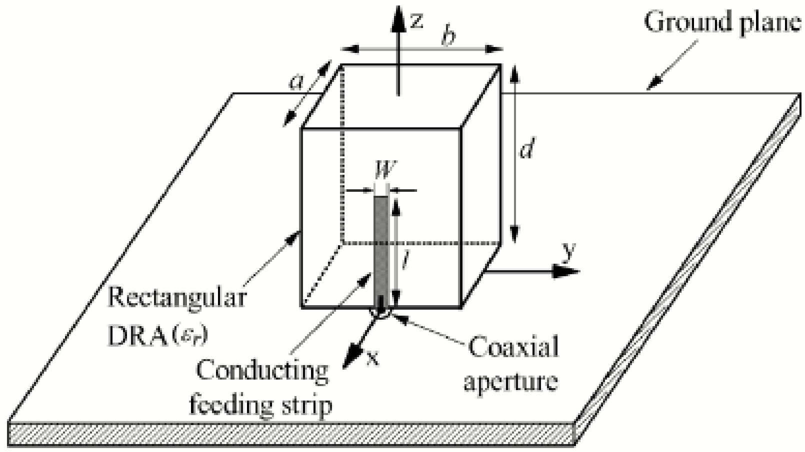

Figure 2.7: Geometry of the strip-fed RDRA [7]

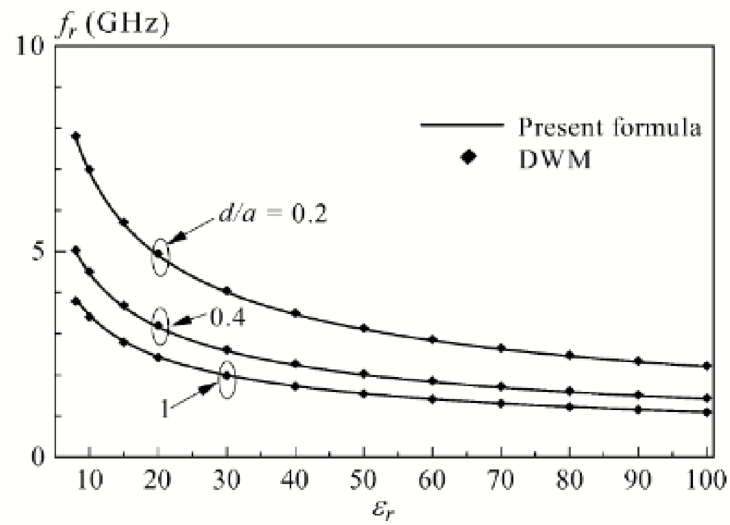

Figure 2.8: The resonance frequency of RDRA as function of ϵ_r for d/a=0.2, 0.4 and 1: a=20 mm and b=12 mm [7]

2.1.7 Circular Polarization in Dielectric Resonator Antennas

Circular polarized signals are used in many communications, radars and navigation satellite applications to improve system performance [2]. Satellite communications use circular polarization to overcome polarization rotation effects due to the atmosphere [2]. Two methods are available for generating circular polarization [2, 8]:

- Two point feeding systems.
- Orthogonal degenerate mode.

2.1.7.1 Polarization

The polarization of an electromagnetic wave refers to the rotation of the electric field vector at a fixed location as function of time [2]. Assume uniform plane wave travelling in the z-direction, electric fields (**E**) have component in both x and y-directions. At z = 0, the time-harmonic electric field can be written as [2]:

$$\mathbf{E} = E_x cos(\omega t + \phi_x)\hat{x} + E_y cos(\omega t + \phi_y)\hat{y} \tag{2.26}$$

If phase of two electrical components are equal (ϕ_x=ϕ_y=ϕ_0), then the amplitude of Electric field (E-field) [2],

$$|E| = \sqrt{E_x^2 + E_y^2} cos(\omega t + \phi_0) \tag{2.27}$$

and angular orientation ψ at y-axis [2]:

$$\psi = arctan\left(\frac{E_y}{E_x}\right) \tag{2.28}$$

The angular orientation is independent of the time. The orientation of the wave is linearly polarized, since the electric field vector traces out a straight line over time [2]. For the case where, E_x=E_y=E_0 and (ϕ_x-ϕ_y=$\pm\pi/2$), the electric field amplitude will be [2]:

$$|E| = \sqrt{((E_0 cos(\omega t + \phi_y \pm \pi/2))^2 + (E_0 cos(\omega t + \phi_y))^2)} = \sqrt{2}E_0 \tag{2.29}$$

and the angle is [2]

$$\psi = arctan\left(\frac{E_0 cos(\omega t + \phi_y \pm \pi/2)}{E_0 cos(\omega t + \phi_y)}\right) = arctan\left(\frac{\pm sin(\omega t + \phi_y)}{cos(\omega t + \phi_y)}\right) = \phi_y \pm \omega t \tag{2.30}$$

Above equations describe a vector with constant amplitude, which rotates in either a clockwise or counterclockwise direction, tracing out a circle with time is known as circular polarization [2].

The wave will be elliptically polarized, where both the magnitude and orientation of the E-field will vary with time, tracing out an ellipse [2]. The axial ratio (AR) is a measure of the elliptically polarized electromagnetic wave and is the ratio of the major axis to the minor axis of the ellipse. It can be expressed as [2]:

$$AR[dB] = 20\log(E_{max}/E_{min}) \tag{2.31}$$

where, E_{max} and E_{min} are the magnitudes of the maximum and minimum E-fields, respectively [2]. The axial ratio equals 0 dB for a circularly polarized wave and is infinite for a linearly polarized wave [2]. An axial ratio of less than or equal to 3 dB is still considered an acceptable value when a circularly-polarized wave is required [2].

The circularly polarized wave consists of two orthogonal linearly polarized waves that are in phase quadrature (two waves are $\pm\pi/2$ phase offset between them) [2]. The circular polarization is realized in antennas by generating two linearly polarized waves which are spatially orthogonal and in phase quadrature using two points fed [2].

The purity of the circular polarization will depend on the relationship between the magnitude and phase of the two linearly polarized components [2]. The axial ratio can be expressed as [2]:

$$AR[dB] = 20\log\left(\frac{E_x^2 + E_y^2 + \sqrt{E_x^4 + E_y^4 + \sqrt{E_x^4 + E_y^4 + 2E_x^2E_x^2cos(\psi)}}}{E_x^2 + E_y^2 - \sqrt{E_x^4 + E_y^4 + \sqrt{E_x^4 + E_y^4 + 2E_x^2E_x^2cos(\psi)}}}\right) \tag{2.32}$$

where, ψ=2(ϕ_y-ϕ_x).

In the DRAs, circular polarization can be generated by using either a two-point feed or a single-point feed technique [2, 8].

2.1.7.2 Dual-Point Feed

Two linearly polarized waves are orthogonal and have equal amplitude, the DRA must be capable of supporting degenerate modes. This will occur for DRAs that exhibit symmetry along the x- and y-axes [2, 8]. Three examples of two-point feed DRAs are shown in Figure 2.9.

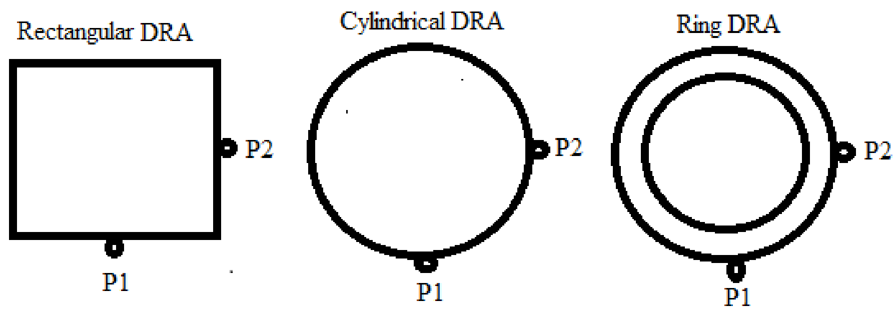

Figure 2.9: Dual-point CP DRAs [8]

2.1.7.3 Single-Point Feed

Most research has been focused on the developing DRAs of circularly polarized radiation from a single feed point [2, 8]. A single point fed DRA does not achieve the same axial ratio bandwidth as compared with dual-point feed case, but it does not require complex feed network and is better suited for an array design [2, 8].

2.1.8 Method of Moments

Method of Moments (MoM) is a numerical technique which converts electric field integral equations in to linear system of equations [9, 10]. Figure 2.10 shows block diagram of MoM technique converting integral equations to matrix form. Consider general problem [9, 10]:

$$L(f) = g \tag{2.33}$$

where L is a linear operator, g is a known function and f is unknown. In electromagnetic problems, L is typically an integral-differential operator, f is the unknown function (current) and g is a known excitation source (voltage). In MoM, the basic approach is to expand the unknown quantity in integral equations using set of known basis functions with unknown coefficients. The resulting equation is then converted into a linear system of equations by applying boundary conditions [9, 10]. The unknown coefficients are evaluated numerically [9, 10].

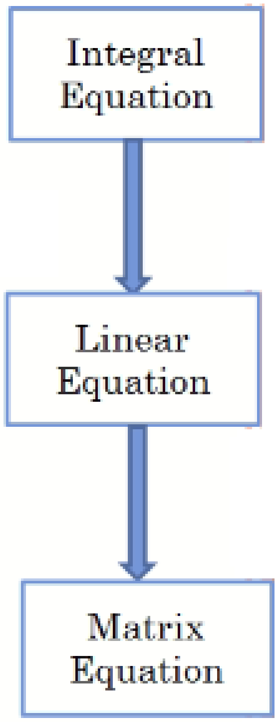

Figure 2.10: Block diagram of MoM technique converting integral equation to matrix equation form

The steps of MoM are as follows [9, 10]:

- Step-1: Expand unknown function f into a sum of N weighted set of basis functions:

$$L(f) = L\left(\sum_{n=1}^{N} a_n f_n\right) = \sum_{n=1}^{N} a_n L\left(f_n\right) = g \tag{2.34}$$

Define an inner product or moment between a basis function $f_n(r^{'})$ and testing or weighting function f_m(r) as

$$\langle f_m, f_n\rangle = \int\limits_{f_m} f_m(r) \cdot \int\limits_{f_n} f_n(r^{'}) \cdot dr^{'} dr \tag{2.35}$$

In Galerkin method, basis functions themselves are used as the testing or weighting functions.

- Step-2: Take inner product between a basis function and testing or weighting function:

$$\sum_{n=1}^{N} a_n \langle f_m, L(f_n) \rangle = \langle f_m, g \rangle \tag{2.36}$$

$$\left\langle f_m, L\left(\sum_{n=1}^{N} a_n f_n\right) \right\rangle = \langle f_m, g \rangle \tag{2.37}$$

- Step-3: Convert above linear equations in to matrix equations form:

$$\begin{bmatrix} \langle f_1, L(f_1) \rangle & \langle f_1, L(f_2) \rangle & . & . & . & . \\ \langle f_2, L(f_1) \rangle & \langle f_2, L(f_2) \rangle & . & . & . & . \\ . & . & . & . & . & . \\ . & . & . & . & . & . \\ . & . & . & . & . & . \\ . & . & . & . & . & \langle f_M, L(f_N) \rangle \end{bmatrix} \begin{bmatrix} a_1 \\ a_2 \\ . \\ . \\ . \\ a_M \end{bmatrix} = \begin{bmatrix} g_1 \\ g_2 \\ . \\ . \\ . \\ g_M \end{bmatrix} \tag{2.38}$$

2.2 Literature Review

Literature survey of tri-/multi-, dual-, single- and wide-band DRAs are given in sections 2.2.1, 2.2.2 and 2.2.3, respectively. In section 2.2.4, literature survey of analysis of DRAs using MoM is given.

2.2.1 Tri- and Multi-Band Dielectric Resonator Antennas

The tri-band dual-sense CP hybrid DRA was developed using feed of vertical-tapered-strip connected to a 50 Ω microstrip line for three operating frequency bands of 1.705-2.03 GHz, 2.23-2.96 GHz and 3.65-3.76 GHz with ground plane footprint area of 80 mm × 70mm [11]. TM_{11} mode at lower-band, TE_{111} mode at central-band and combination of the quasi-TM_{21} mode & quasi-TE_{111} mode at upper-band were generated through Square Microstrip Ring (SMR), modified hexagonal DR and combination of SMR & DR, respectively. Top and side views of tri-band hybrid DRA are shown in Figures 2.11 (a) and 2.11 (b), respectively. The mathematical formulation of tri-band hybrid DRA is given in reference [11].

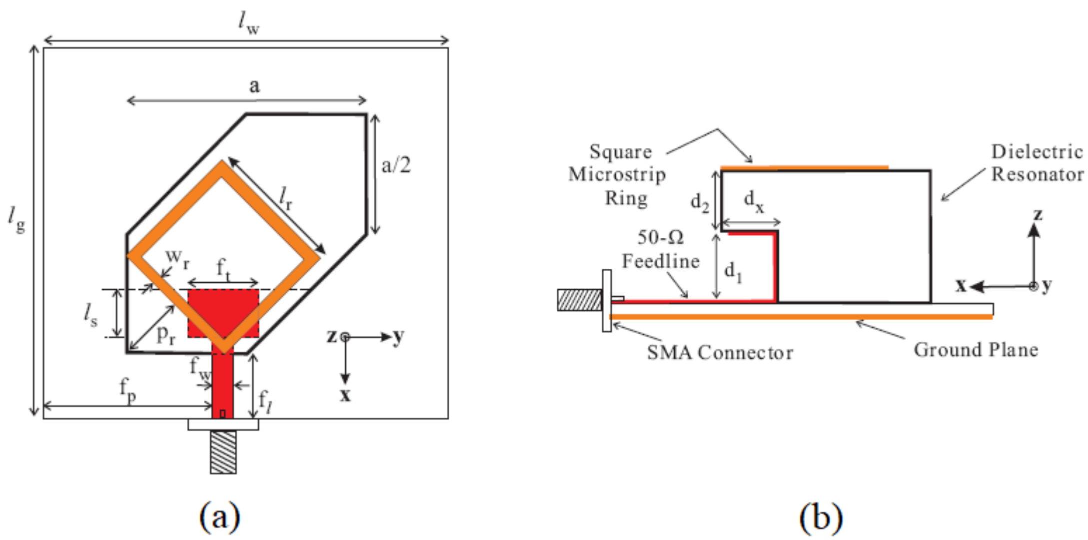

Figure 2.11: Structure of of tri-band hybrid DRA (a) top view (b) side view [11]

All Global Positioning System (GPS) bands (L1, L2, L3, L4 and L5) CP DRA for GPS application has been proposed using hybrid ring feed network with ground plane footprint area of 75 mm × 75 mm [12]. Figure 2.12 shows 3-D structure of all GPS bands CP DRA. Tri-band omnidirectional CP DRA with top-loaded alford loop using axial probe feed was investigated in operating frequency range of 1.92-1.955 GHz, 2.315-2.5 GHz and 3.415–3.55 GHz for Global System for Mobile communications (GSM), Wireless Local Area Network (WLAN) and Worldwide Interoperability for Microwave Access (WiMAX) applications with ground plane diameter of 50 mm, respectively [13]. The top and side views of tri-band CP DRA are shown in Figures 2.13 (a) and 2.13 (b), respectively.

In [14], quad-band quad-sense CP CDRA using modified circular-shaped aperture feed was presented by Sharma *et al* with ground plane area of 120 mm × 120 mm for L1/L2 GPS band (1.2/1.5 GHz), Compass Navigation Satellite System (CNSS) and WLAN (2.4 GHz) & WiMAX (2.5 GHz) applications. $HEM_{11\delta}$, $HEM_{11\delta+1}$, $HEM_{12\delta-like}$, $HEM_{12\delta}$, $HEM_{13\delta}$ and $HEM_{14\delta}$ modes have been produced in quad-band quad-sense CP CDRA. The cylindrical shape quad-band quad-sense CP DRA (dielectric constant ϵ_r=9.8 of dielectric resonator material) was designed, analyzed, fabricated and tested. The top and isometric views of quad-band CP CDRA are represented in Figures 2.14 (a) and 2.14 (b), respectively.

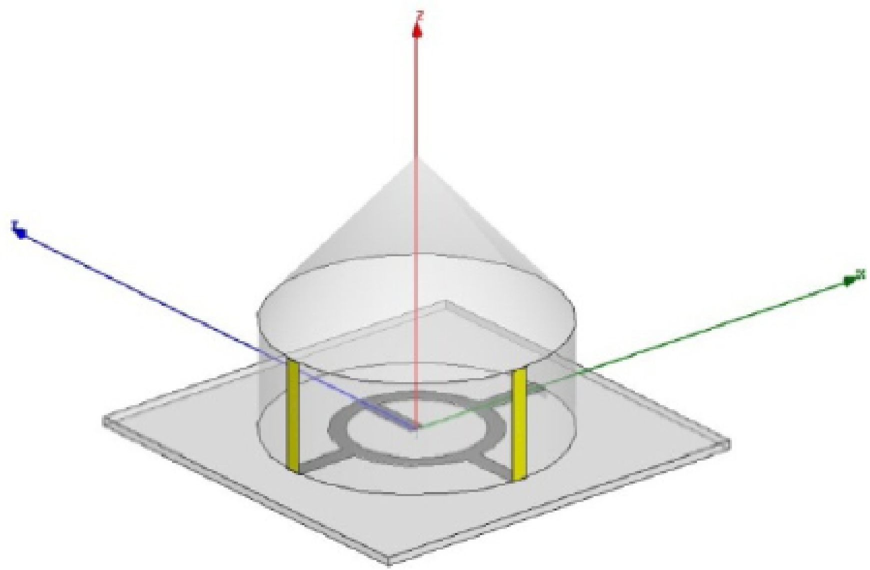

Figure 2.12: 3-D geometry of all GPS bands CP DRA with hybrid ring excitation [12]

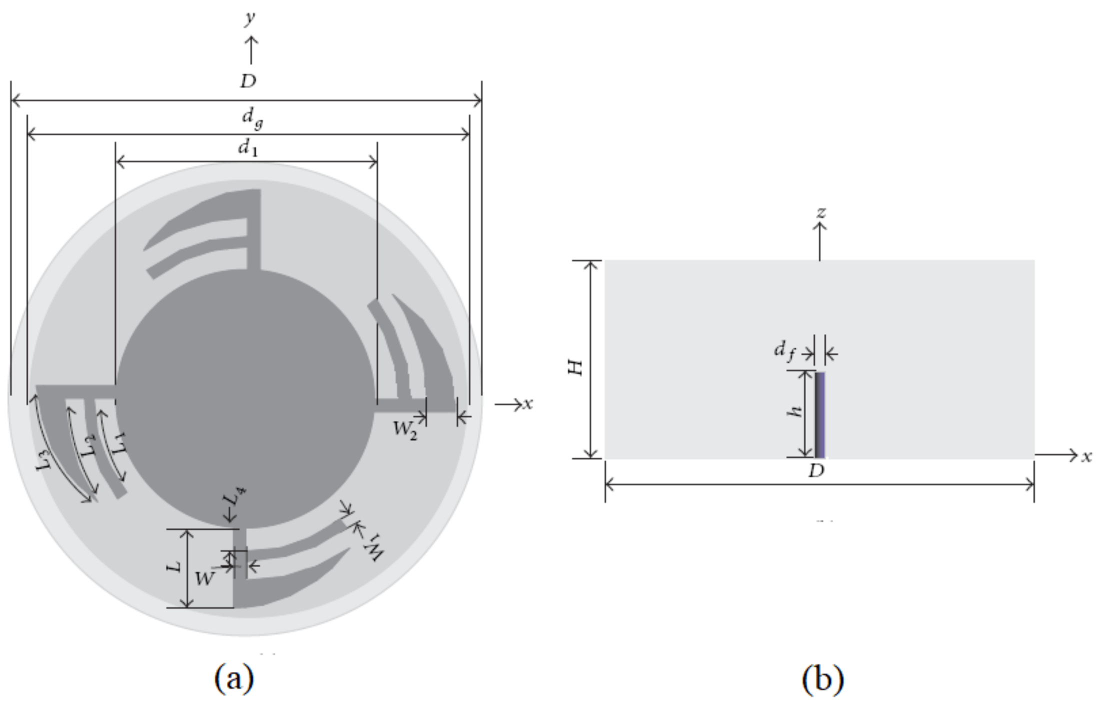

Figure 2.13: Geometry of tri-band CP DRA with top-loaded alford loop (a) top view (b) side view [13]

The compact tri-band CDRA using feed of annular-shaped microstrip line for wireless applications is reported in operating frequency ranges of 2.35–2.55 GHz, 3.35–3.65 GHz and 5.1–5.4 GHz [15]. In the past, DRAs for wideband applications

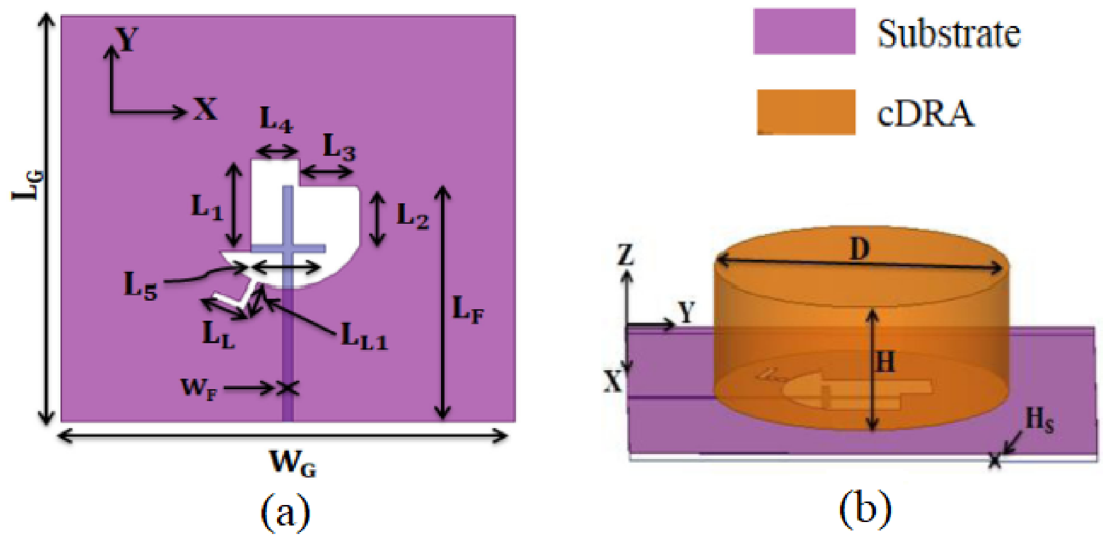

Figure 2.14: Geometry of quad-band quad-sense CP CDRA (a) top view without cylindrical DR (b) isometric view [14]

were developed with different shapes such as flipped staired pyramid [16] and three-stepped rectangular shapes [17]. RDRA was most versatile over CDRA and HDRA due to two reason. First, RDRA has more degrees of freedom than CDRA or HDRA [2, 18]. Second, RDRA has low cross-polarization than CDRA which is used for finding better CP [18].

A novel tri-band CDRA with coaxial probe feed using varying permittivity in ϕ-direction was analyzed at center frequencies of 4.93 GHz, 6.46 GHz and 7.41 GHz [19]. The permittivities ϵ_{r1}, ϵ_{r2} and ϵ_{r3} of tri-band CDRA are 4, 14 and 6, respectively. Top and front views of tri-band CDRA are shown in Figures 2.15 (a) and 2.15 (b), respectively.

Tri-band CDRA using coaxial probe feed with ground plane area of 60 mm $\times$ 60 mm was simulated using embedded CDR within another CDR with a different permittivity at operating frequency ranges of 3.306 – 3.403 GHz, 3.698 – 4.006 GHz and 4.541 – 5.450 GHz [20]. A novel small tri-band RDRA for WLAN and WiMAX applications has been presented with omnidirectional radiation patterns at resonance frequencies of 2.4 GHz, 3.5 GHz and 5.8 GHz [21]. Low cost and low profile tri-band RDRA for multiple applications has been investigated using plexiglass dielectric

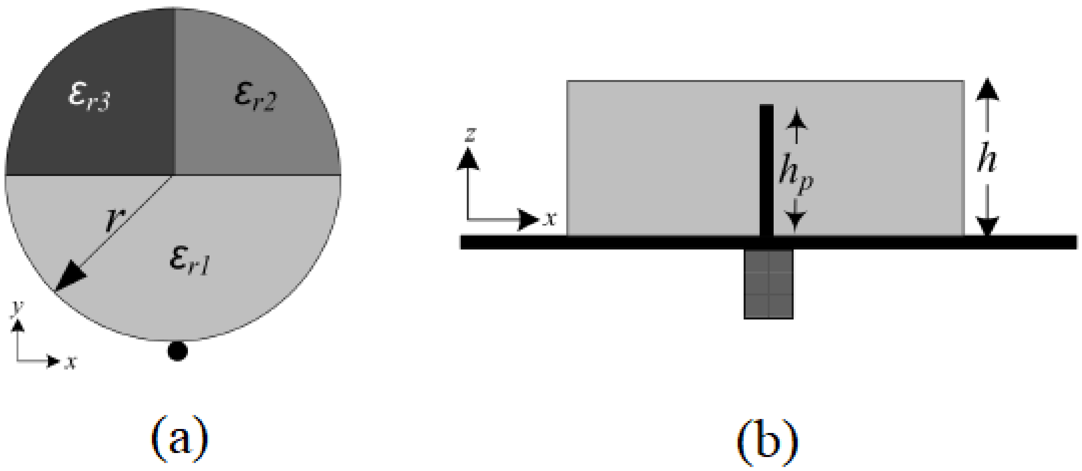

Figure 2.15: Structure of tri-band CDRA using varying permittivity in ϕ-direction (a) top view (b) front view [19]

resonators on FR4 substrate. The top view, side view and metalized plates of tri-band RDRA are shown in Figures 2.16 (a), 2.16 (b) and 2.16 (c), respectively.

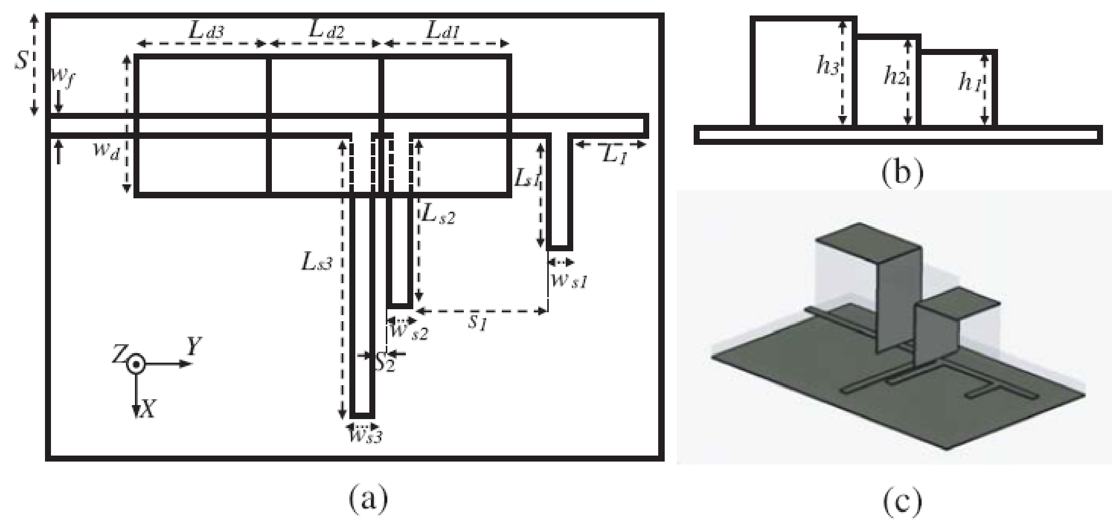

Figure 2.16: Geometry of tri-band RDRA (a) top view (b) side view (c) metalized plates [21]

Multi-band DRA using coaxial probe feed for WLAN application was simulated, fabricated and tested at center frequencies of 2.45 GHz, 5.2 GHz and 5.8 GHz [22]. Bandwidth broadening of a RDRA by merging adjacent band has generated to the TE^{y}_{111}, TE^{y}_{112} and TE^{y}_{113} modes at three frequencies of 2.92 GHz, 3.57 GHz and 4.62 GHz, respectively [6]. The dimensions of bandwidth broadening RDRA were determined using DWM.

The broadband flipped staired pyramid with RDRA and conical with CDRA using aperture coupled feed have been achieved broadside radiation patterns over frequency ranges of 7.85-12.99 GHz and 8.98 - 12.5 GHz, respectively [23]. In the past, dielectric resonator antennas for wideband applications were developed with different shapes such as flipped staired pyramid [24] and three-stepped rectangular shapes [25].

The higher order mode tri-band CP RDRA has been presented using microstrip patch feed as shown in Figure 2.17. Single coaxial cable feeds to the microstrip patch on RDRA. Microstrip patch is coupled to a double stub strip structure on the RDRA side wall [26]. In tri-band RDRA, CP is achieved and antenna gain is increased due to degenerate mode pair of $TE^x_{\delta 11}$ mode and higher order $TE^x_{\delta 23}$ mode. Ground plane area of tri-band CP RDRA was miniaturized to 40 mm $\times$ 40 mm using dielectric constant ϵ_r=10 of dielectric resonator. The volume of rectangular dielectric resonator was reduced to 25.4 mm $\times$ 14.3 mm $\times$ 26.1 mm. For ground plane area 44 mm $\times$ 44 mm, tri-band CP DRA was developed at resonance frequencies of 5.2 GHz, 6.7 GHz and 9.85 GHz [27]. The quad-band CP DRA has been investigated at 5 GHz, 6.4 GHz, 7.8 GHz and 10.3 GHz with ground plane area of 44 mm $\times$ 44 mm.

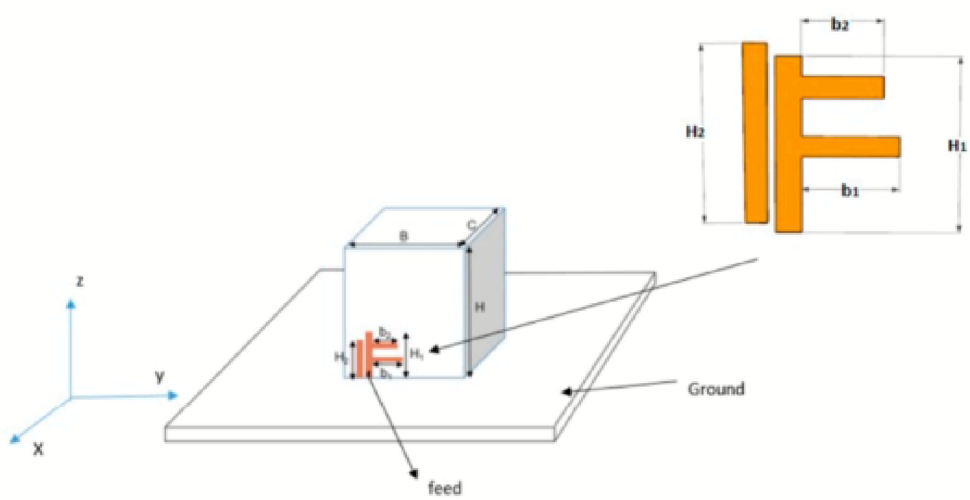

Figure 2.17: Geometry of higher order mode tri-band CP RDRA [26]

2.2.2 Dual-Band Dielectric Resonator Antennas

The dual-band CP RDRA using cross-slot-coupled feed for CNSS applications has generated broadside radiation patterns at first center frequency of 1.268 GHz with TE_{111} mode and second center frequency of 1.561 GHz with TE_{113} mode, respectively [18]. The ground plane area of dual-band RDRA was achieved 100 mm $\times$ 100 mm using dielectric constant ϵ_r=20.5 for dielectric resonator and dielectric constant ϵ_r= 2.55 for dielectric substrate. Figures 2.18 (a) and 2.18 (b) show 3-D view and top view of dual-band RDRA, respectively. The electric field distribution of TE_{111} and TE_{113} modes are shown in Figure 2.19 (a) and 2.19 (b), respectively.

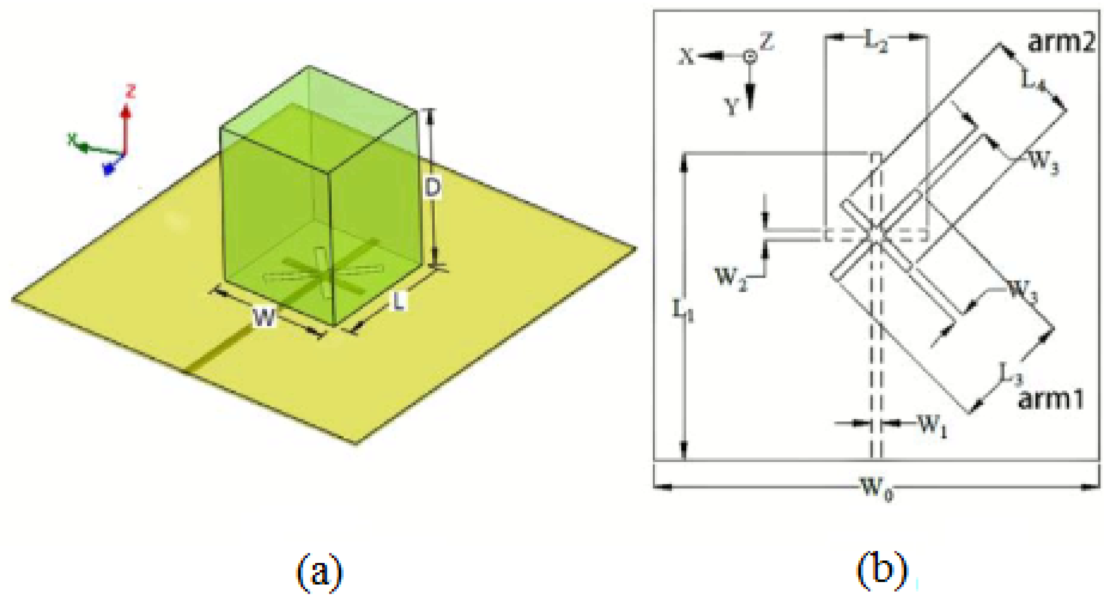

Figure 2.18: (a) 3-D view (b) top view of dual-band RDRA [18]

Fang *et al* reported dual-band CP RDRA which generates quasi-TE_{111} mode at 1.58 GHz and quasi-TE_{113} mode at 2.44 GHz, respectively [28]. Ground plane area of dual-band RDRA was reduced to 160 mm $\times$ 160 mm using dielectric constant ϵ_r=9.8 for dielectric resonator and dielectric constant ϵ_r= 2.94 for dielectric substrate. Figure 2.20 shows 3-D geometry of dual-band RDRA with two opposite corners truncation of RDR which gives circular polarization. The electric field distribution of quasi-TE_{111} and quasi-TE_{113} modes are shown in Figure 2.21 (a) and Figure 2.21 (b), respectively.

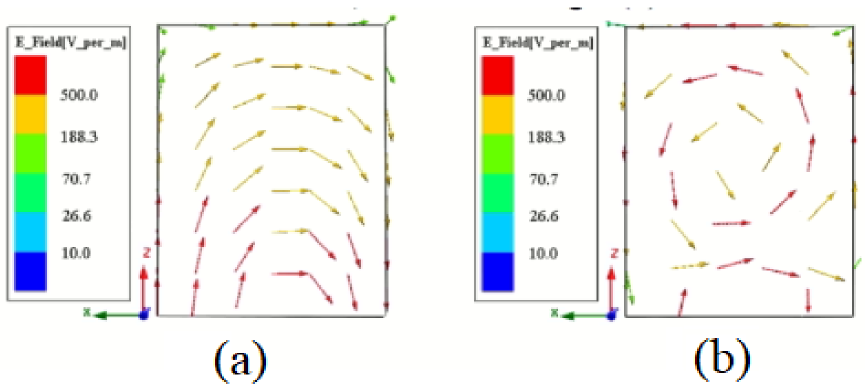

Figure 2.19: Electric field distribution of (a) TE_{111} mode (b) TE_{113} mode of dual-band RDRA [18]

Using wide dual-band CP stacked RDRA, broadside radiation patterns are achieved for lower band of 1.77–2.00 GHz using fundamental quasi-TE_{111} mode of RDRA and higher band of 2.38–2.96 GHz using higer order quasi-TE_{113} and quasi-TE_{115} modes [29]. Figure 2.22 gives structure of wide dual-band CP stacked RDRA. CP DRAs were obtained over wider bandwidth using multi-point feed compared to single point feed.

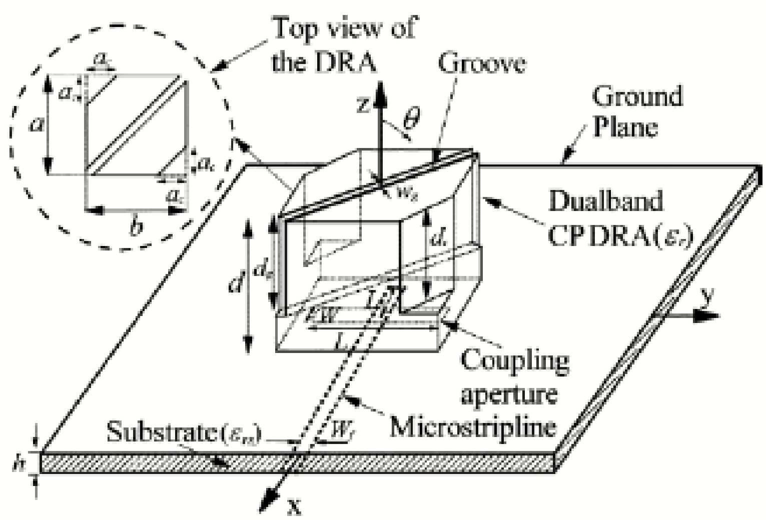

Figure 2.20: 3-D geometry of dual-band RDRA [28]

The dimensions of dual-band RDRA was determined using dual mode design formula with Covariance Matrix Adaptation Evolutionary Strategy (CMA-ES) method [28, 30]. New single and dual modes design formulas of RDRAs were derived by Fang

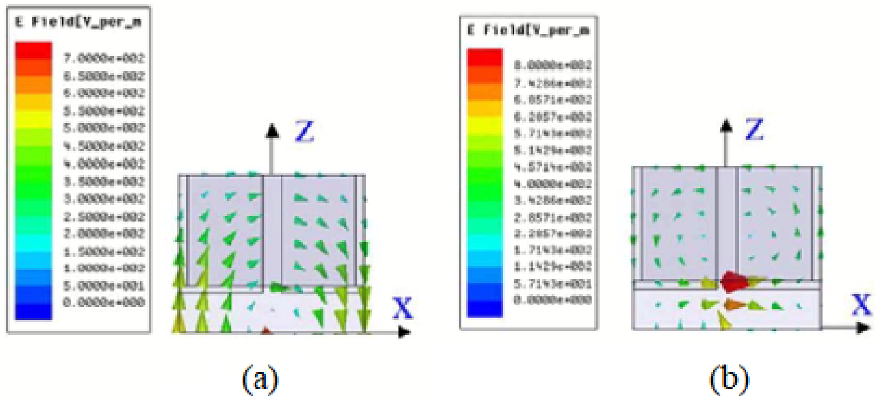

Figure 2.21: Electric field distribution of (a) quasi-TE_{111} mode (b) quasi-TE_{113} mode of dual-band RDRA [28]

et al using CMA-ES optimization method [31]. CMA-ES method is more accurate as compared to Least Squares (LS) method. In [7], dual mode design formula of RDRA gives better accuracy than DWM. The dimensions of dual-band RDRA are calculated using DWM [32].

In the past, circular polarization of dual-band DRAs have been produced using different techniques such as cross-slot-couple feed [18], two opposite corners truncated on DRA at 45° with groove on top face of the DRA[28], feed of asymmetrical cross-slot [29], zonal slot and cross-slot feed [33], two corners truncated on DRA at 45° [23] and cross slot feed with unequal slot arms [34].

A wide dual-band CP stacked RDRA was designed with ground plane area of 100 mm × 100 mm using dielectric constant ϵ_r=9.8 of dielectric resonator and dielectric constant ϵ_r=4.4 of dielectric substrate [29]. Structure of wide dual-band RDRA is shown in Figure 2.22. Dual-band zonal-slot hybrid DRA was investigated at 2.4 GHz and 5.2 GHz using conducting cavity [33]. The top and front views of dual-band zonal-slot hybrid DRA are shown in Figure 2.23 (a) and Figure 2.23 (b), respectively. The dual-band RDRA produces fundamental TE^{y}_{111} mode at first center frequency of 3.48 GHz and higher order TE^{y}_{113} mode at second center frequency of 5.28 GHz [32].

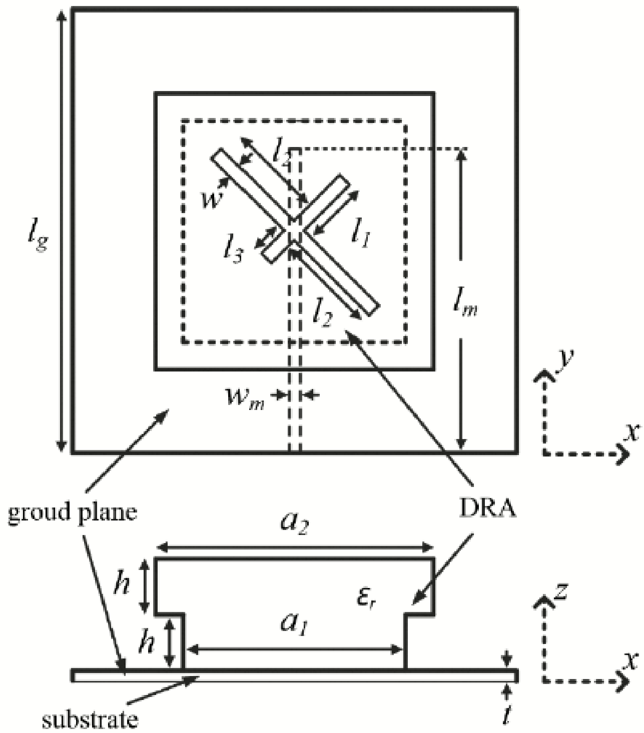

Figure 2.22: Structure of wide dual-band CP stacked RDRA [29]

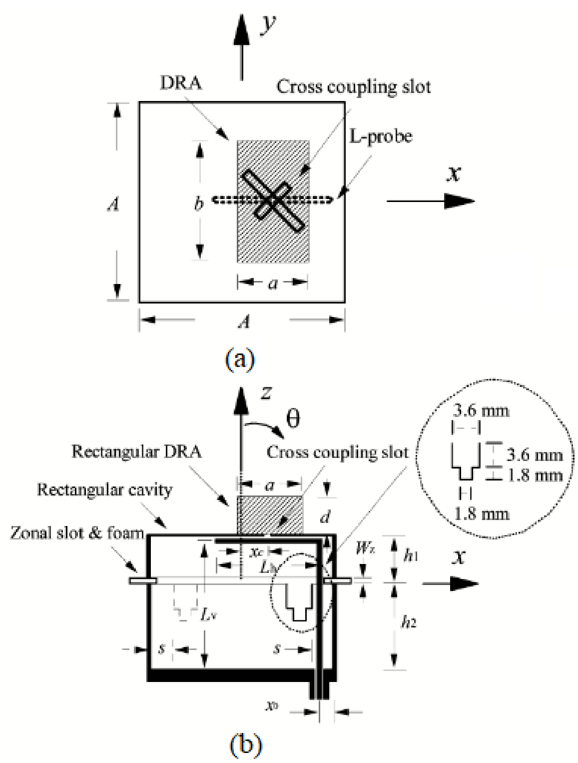

Figure 2.23: (a) Top view and (b) front view of dual-band zonal-slot hybrid DRA [33]

The ground plane areas of dual-band DRAs achieved 100 mm × 100 mm at resonance frequencies of 1.268 GHz and 1.561 GHz [18], 40 mm × 40 mm for frequency ranges of 3.4-3.58 GHz and 5.1-5.9 GHz [35], 50 mm × 50 mm at center frequencies of 5.96 GHz and 11.95 GHz [37] and 134 mm × 89 mm in frequency ranges of 2.12–2.45 GHz and 2.64–3.98 GHz [38], respectively. A wide dual-band CP RDRA with larger aspect ratio was designed using dielectric constant ϵ_r=10 of dielectric resonator and dielectric constant ϵ_r=2.33 of dielectric substrate [34]. 3-D geometry of wide dual-band CP RDRA is shown in Figure 2.24.

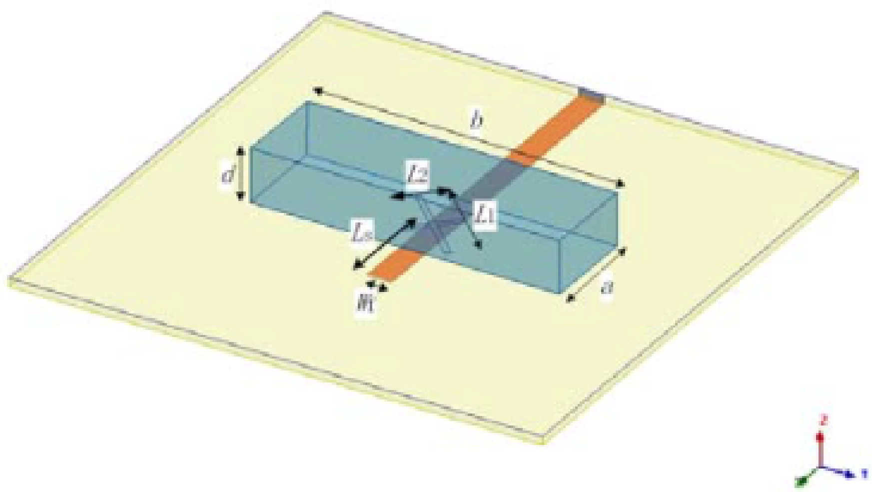

Figure 2.24: 3-D geometry of wide dual-band CP RDRA [34]

A dual-band CP aperture coupled RDRA for wireless applications was designed over two frequency bands 3.4-3.58 GHz and 5.1-5.9 GHz with ground plane area 40 mm × 40 mm [35]. The top view and 3-D geometry of dual-band RDRA are shown in Figure 2.25 (a) and 2.25 (b), respectively. Inverted sigmoid shaped multi-band CP DRA reported using dielectric constant ϵ_r=12.8 of dielectric resonator and dielectric constant ϵ_r=4.4 of dielectric substrate [36]. Figures 2.26 (a), 2.26 (b), 2.26 (c) show configuration of multi-band CP DRA, feeding patch applied at DR surface and photograph of fabricated antenna, respectively. Reconfigurable dual-/tri-band CP DRA has been investigated using dielectric constant ϵ_r=10 of dielectric resonator and dielectric constant ϵ_r=3.5 of dielectric substrate [37]. Top and side views and photographs of dual-/tri-band DRA are shown in Figures 2.27 (a), 2.27 (b) and 2.27 (c), respectively.

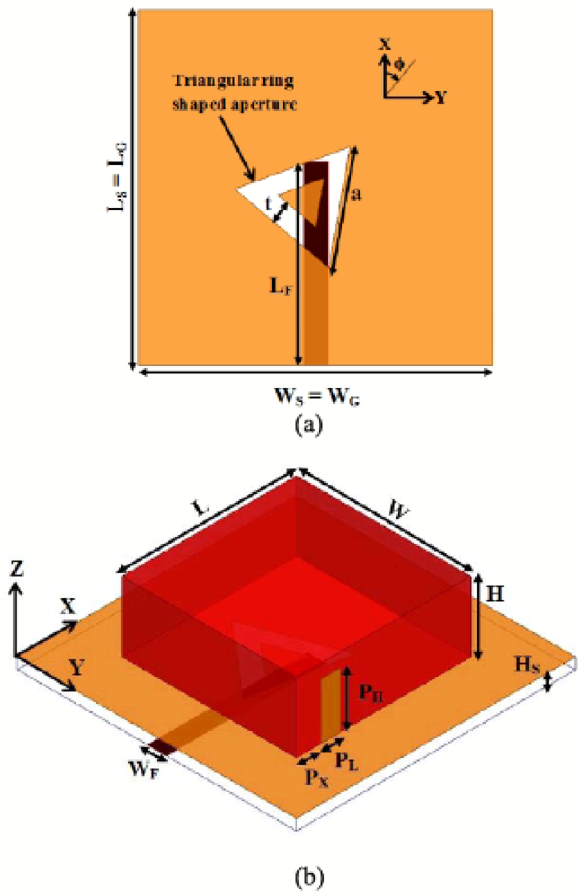

Figure 2.25: (a) Top view (b) 3-D geometry of dual-band CP RDRA [35]

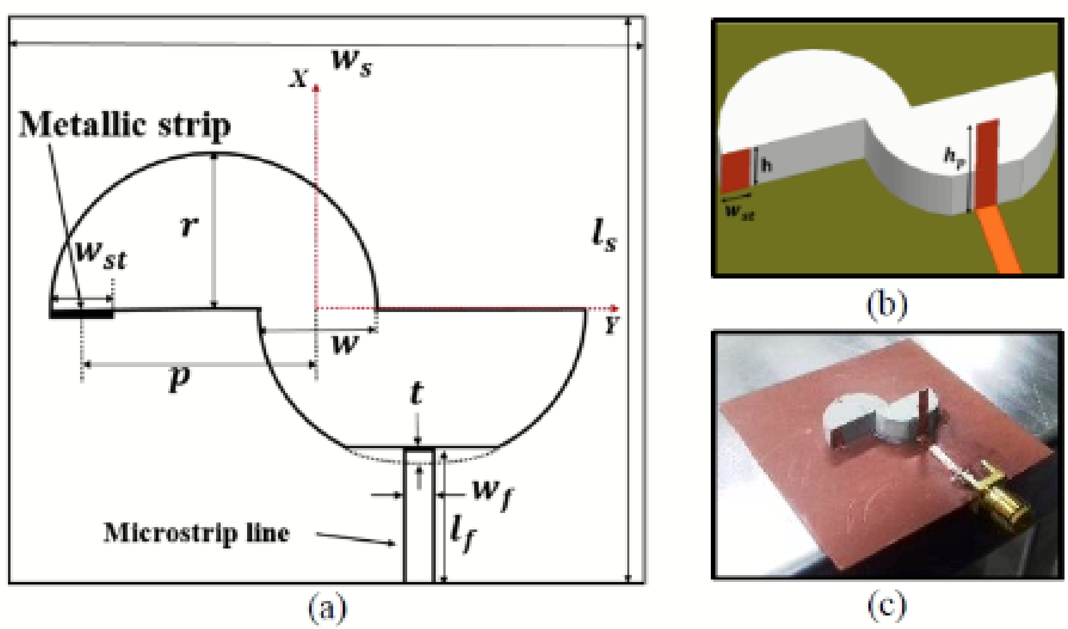

Figure 2.26: (a) Configuration of multi-band CP DRA (b) feeding patch applied at DR surface (c) photograph of fabricated antenna [36]

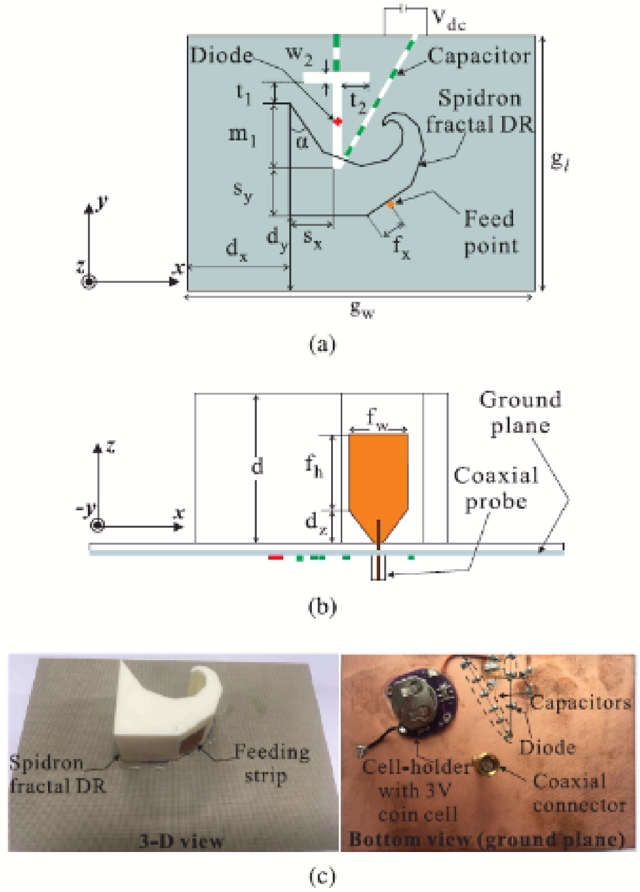

Figure 2.27: (a) Top view (b) side view (c) photograph of fabricated reconfigurable dual-/tri-band CP DRA [37]

For space applications (GNSS, Telemetry and Telecommand), a multi-permittivity 3-D printed ceramic dual-band CP DRA was designed at upper L-band (1.559 - 1.61 GHz) and S-band (2.025 - 2.29 GHz) [38]. The footprint area of 3-D printed ceramic DRA is 100 mm × 100 mm and it is embedded in cubsat or nanosatellite. The compact dual-band CP CDRA is excited using a pair of arc-shaped strips connecting coaxial probes [39]. The dual-band singly fed CP DRA was designed using elliptical shape dielectric resonator [40]. The circular polarized radiation of dual-band RDRA was obtained by circular patch over meta-surface [41]. The dual-band CP DRA is proposed using an asymmetric Y-shaped geometry of dielectric resonator [42].

2.2.3 Single- and Wide-Band Dielectric Resonator Antennas

In the past, single- and wide-band CP DRAs were developed using different dielectric resonator shapes such as rectangular [43, 44], hollow rectangular [45], cylindrical [46, 47] and hollow cylindrical [48]. The top and side views of CP DRA with wide-band feed network are shown in Figures 2.28 (a) and 2.28 (b), respectively. Figure 2.29 gives top and side views of low-profile CP higher order RDRA.

The circular polarization of DRAs are generated using wide-band branch-line coupler [43], wide-band rat-race and slot feed [46], quadrature coupler [45, 47], embedded vertical feed network [48], vertical feeding strips [49], corner chopped [50], diagonal probe feed [50] and parasitic patch [51]. The front and top views of CP hollow RDRA with an underlaid quadrature coupler are represented in Figures 2.30 (a) and 2.30 (b), respectively. Also, the electric fields of hollow RDRA is given in Figure 2.31. The 3-D view of CP hollow CDRA and layout of feed network are shown in Figures 2.32 (a) and 2.32 (b), respectively. Dimensions of single-band RDRA are determined using single mode (TE^y_{111}) formula using CMA-ES optimization method [31]. Single mode (TE^y_{111}) design formula of RDRA has received more accuracy than DWM [7]. Figure 2.33 (a) shows corner chopped CP RDRA. Diagonal probe fed CP RDRA is shown in Figure 2.33 (b).

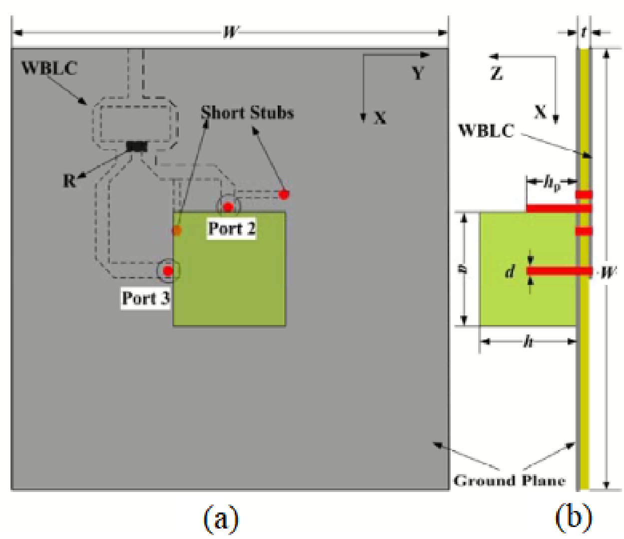

Figure 2.28: (a) Top view (b) side view of CP DRA with wide-band feed network [43]

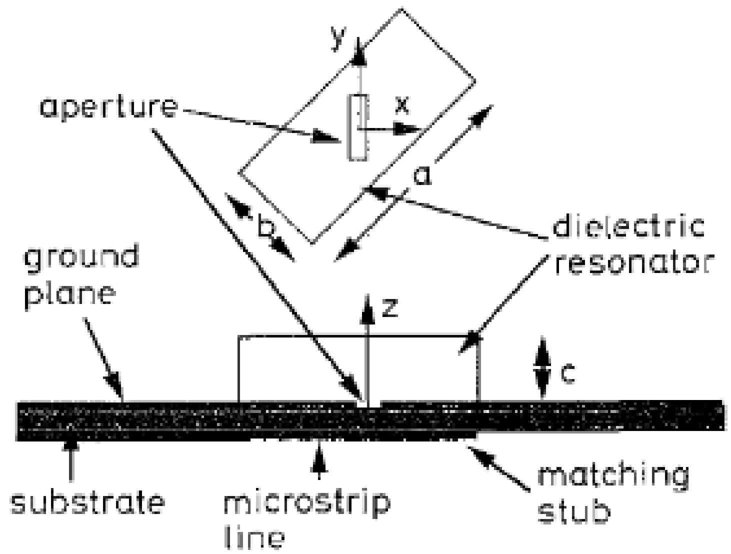

Figure 2.29: Top and side views of low-profile CP higher order RDRA [44]

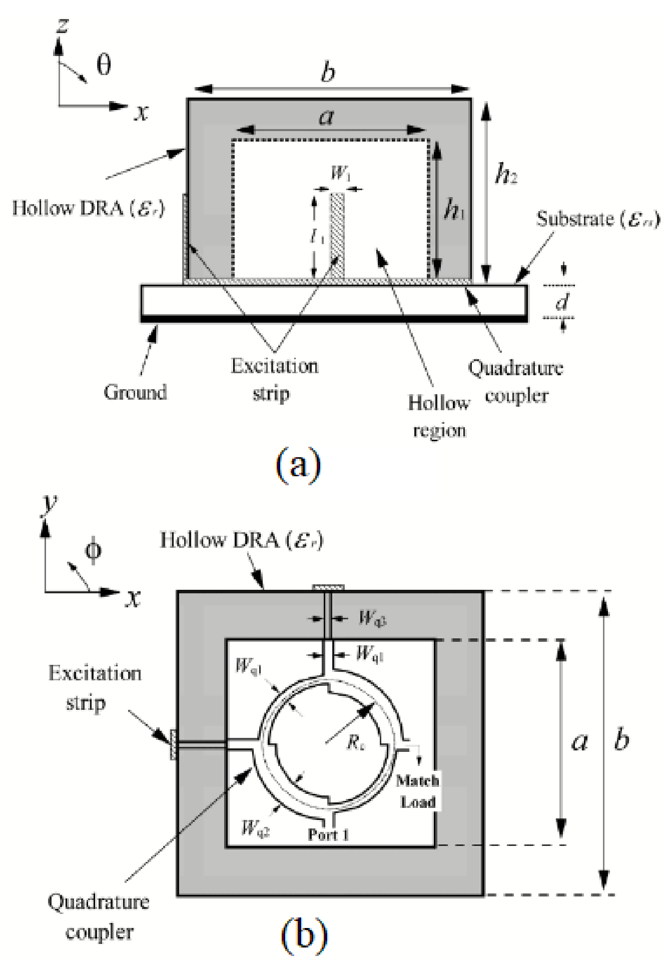

Figure 2.30: (a) Front view (b) top view of CP hollow RDRA with an underlaid quadrature coupler [45]

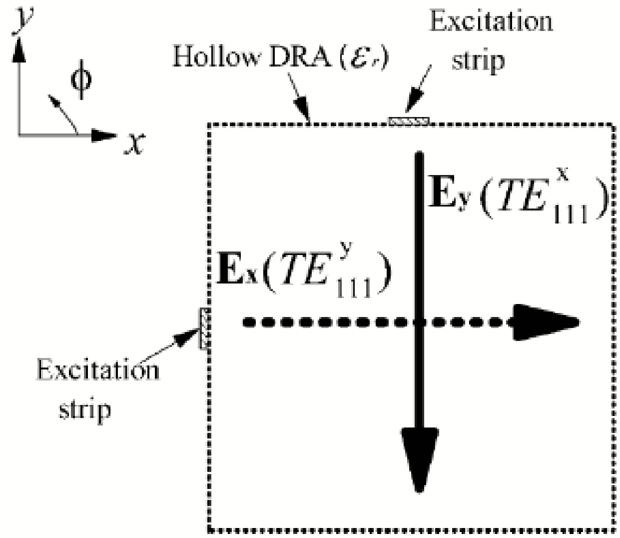

Figure 2.31: Electric fields of CP hollow RDRA [45]

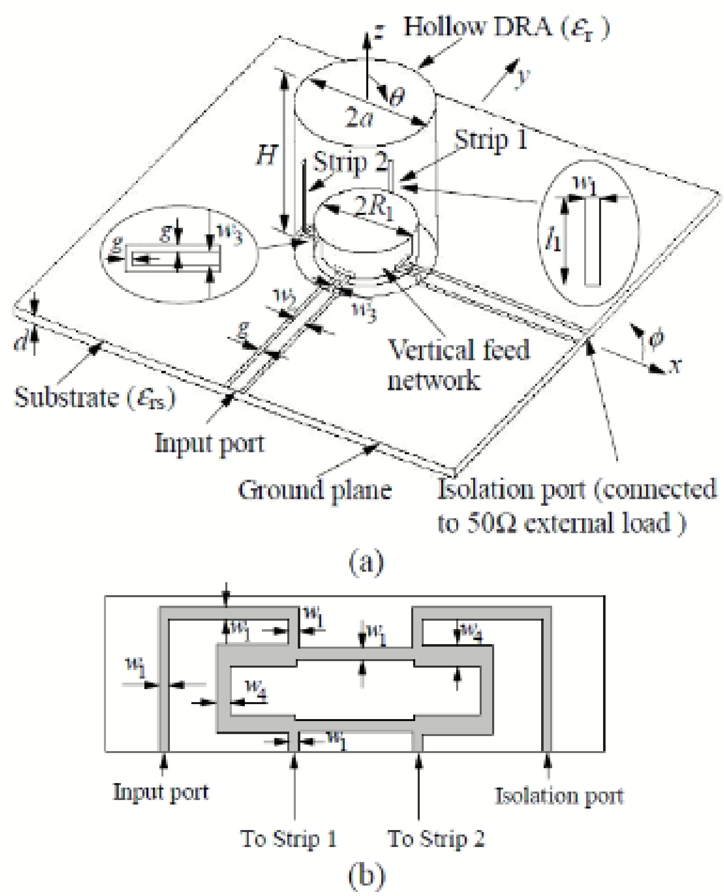

Figure 2.32: (a) 3-D view of CP hollow CDRA with embedded vertical feed network (b) layout of excitation [48]

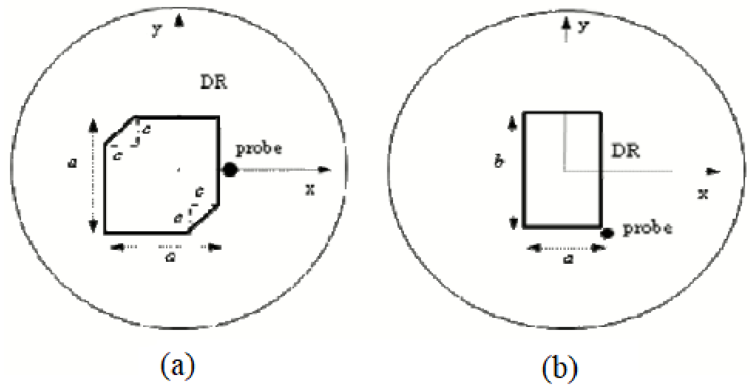

Figure 2.33: (a) Top view of structure-1 and (b) top view of structure-2 of modified CP RDRA [50]

Hen *et al* designed CP RDRA using Wide-band Branch Line Coupler (WBLC) with broadside radiation patterns at 6.5 GHz [43]. The ground plane footprint area of CP RDRA is 42 mm $\times$ 42 mm. The design equations for dual-band DRA were used to design the wide-band DRA as both the resonance frequencies of f_1 and f_2 are very closed [7]. The DWM and curve fitting technique are used to determine the dimensions of RDRAs [2, 7]. Figure 2.34 shows wide-band 4-port CP DRA. For Global Navigation Satellite System (GNSS) applications, DRAs were investigated using cylindrical shape with ground plane diameter of 90 mm [52], rectangular shape [53] and cylindrical shape ground plane diameter of 300 mm [54].

A wide-band CP DRA using sequentially rotated feed network has been investigated in frequency range of 4.2 - 8.0 GHz with broadside radiation patterns and ground plane area of 53.8 mm $\times$ 53.8 mm [55]. The top and side views of wide-band RDRA are shown in Figures 2.35 (a) and 2.35 (b), respectively.

A compact CP hybrid DRA over GNSS frequency band with broadside radiation patterns was designed by Caillet *et al* with ground plane area of 100 mm $\times$ 100 mm [56]. The miniaturization and bandwidth enhancement with two segmented high-aspect ratio RDRAs have been presented using microstrip feed [57]. Annular DRA for GNSS applications was developed in frequency range of 1.15 to 1.62 GHz [58]. Dual sense wide-band CP DRA was presented for GNSS and satellite communications with ground plane diameter of 90 mm [59].

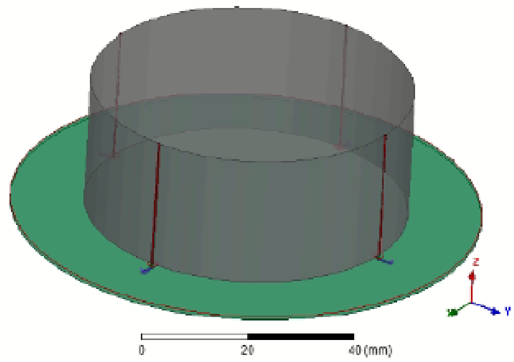

Figure 2.34: wide-band 4-port CP DRA [52]

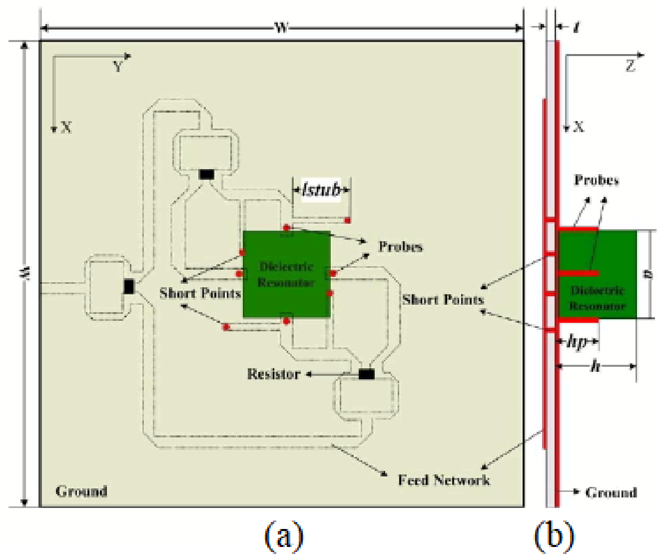

Figure 2.35: (a) Top view and (b) side view of wide-band CP RDRA with sequentially rotated feed network [55]

2.2.4 Analysis of Dielectric Resonator Antennas using Method of Moments

In analysis of the DRA, the conducting ground plane is assumed to be infinite [60, 61]. Many researchers have analyzed the effect of finite ground plane for linearly polarized RDRAs using MoM [61, 62]. The configuration of DRA is shown in Figure 2.36. Baghaee *et al* have investigated rigorous analysis of linearly polarized probe fed RDRA with effect of finite ground plane using MoM [63]. Figures 2.37 (a) and 2.37 (b) show 3-D geometry and side view of probe-fed RDRA, respectively. The numerical analysis of linearly polarized probe fed RDRA with finite ground plane is carried out using MoM [64].

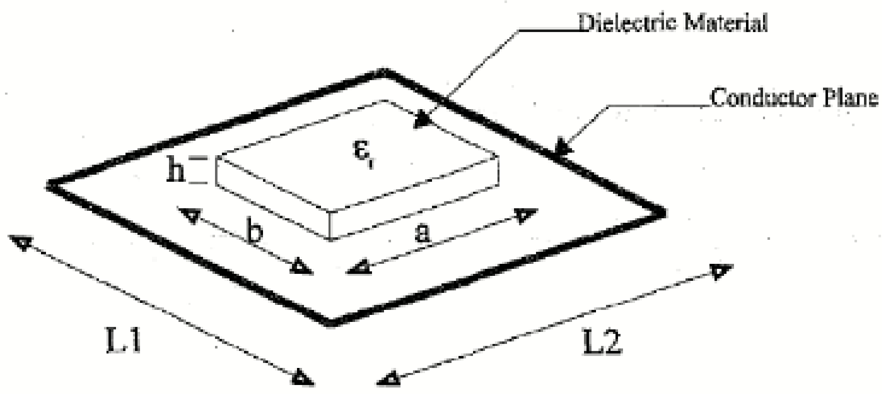

Figure 2.36: Geometry of DRA [61, 62]

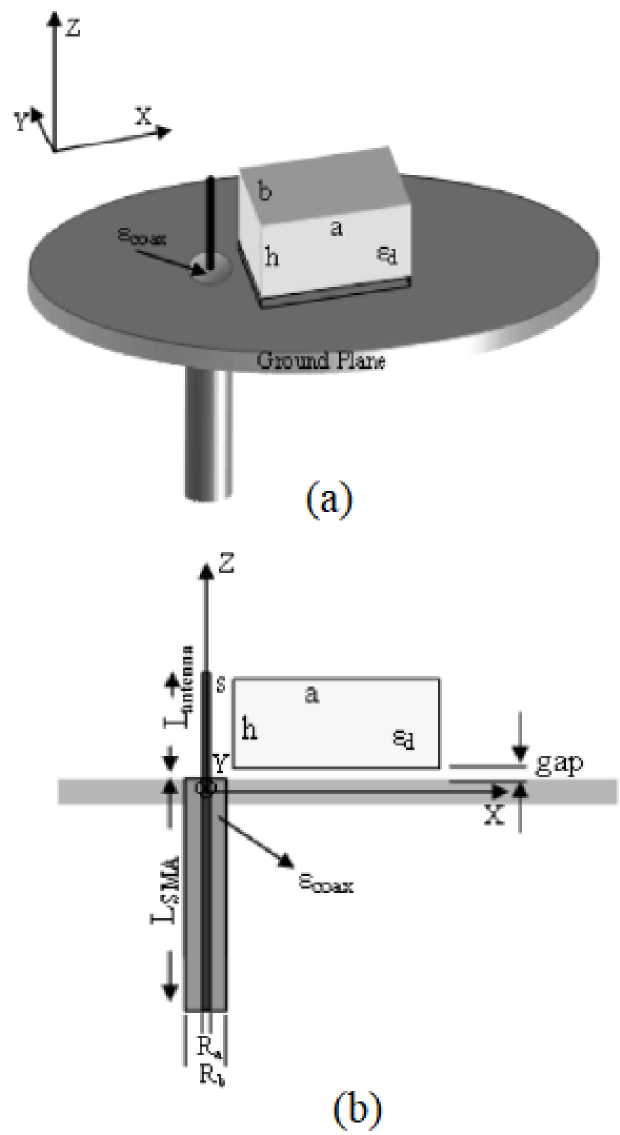

Figure 2.37: (a) 3-D Geometry (b) side view of probe-fed RDRA on finite ground plane [63]

A linearly polarized RDRA excited through slot on finite ground plane has been numerically investigated by MoM and FDTD methods for verification purpose [65]. The analysis of RDRAs using method of moment were presented with different feed schemes such as apearture coupling [66] and probe feed [67]. The effects of finite ground plane and air gaps on radiation characteristics of RDRA was analyzed using MoM by Baghaee et al [68]. The input impedance of DRA is calculated using MoM [69]. The mutual impedance of two HDRAs (excited using coaxial probes) has been determined numerically using MoM [70].

2.3 Research Gap and Design Challenges of Tri-, Dual- and Single-Band Dielectric Resonator Antennas

The compact DRAs are required in many applications where physical space is limited and larger ground plane cannot be accommodated. The effect of placing a DRA on relatively small ground plane can be quite significant, since much of the analysis has assumed that the ground plane was infinite. The small size of the ground plane is affected on lowering the maximum gain and a change in its input impedance.

The existing design techniques tri-, dual- and single-band DRAs reported in the literature have various limitations such as the volume of the dielectric resonator, ground plane area of DRA, volume of DRA not sufficient for small space applications, realization of circular polarization over single-, multi-band using feed network with high ground plane area, unavailability of single DR geometry with multi-mode for multi-band applications and multi-band design using hybrid DRA over lower frequency.

A small number of antennas have been investigated to cover the whole GNSS frequency band (1.150- 1.610 GHz) with high performance but drawback is that these are not miniaturized sufficiently to be placed on small platforms.

Tri-, dual- and single-band DRAs have many challenges such as ground plane miniaturization, circular polarization generation over multi-band and single-band, design of RDR shape, volume miniaturization of RDR at lower resonance frequencies, miniaturization of DRAs at lower resonant frequencies, return loss and gain of DRAs and broadside radiation patterns at three resonance frequencies.

There are challenges in simultaneously achieving design specifications of DRAs such as return loss, polarization, radiation patterns, RHCP gain at different zenith angle and axial ratio over tri-, dual- and single-bands.

References

[1] S.Keyrouz and D. Caratelli, "Dielectric resonator antennas: Basic concepts, design guidelines, recent developments at millimeter-wave frequencies," *International Journal of Antennas and Propagation*, vol. 2016, article id. 9, pp. 1-20, Sept. 2016.

[2] A. Petosa, "Dielectric Resonator Antenna Handbook," *Artech House*, Norwood, MA, USA, 2007.

[3] K. M. Luk and K. W. Leung, "Dielectric Resonator Antennas," *Research Studies Press LTD*, Baldock, England, 2003.

[4] T. Chang and J. Kiang, "Dual-band split dielectric resonator antenna," *IEEE Transactions on Antennas and Propagation*, vol. 55, no.11, Nov. 2004.

[5] R. Kumar Mongia and A. Ittipiboon, "Theoretical and experimental investigations on rectangular dielectric resonator antennas," *IEEE Transactions on Antennas and Propagation*, vol. 45, no. 9, pp. 1348-1356, Sept. 1997.

[6] T. Chang and J. Kiang, "Bandwidth broadening of dielectric resonator antenna by merging adjacent bands," *IEEE Transactions on Antennas and Propagation*, vol. 57, no. 10, pp. 3316-3320, Oct. 2009.

[7] X. S. Fang and K. W. Leung, “Designs of single-, dual-, wide-band rectangular dielectric resonator antennas,” *IEEE Trans. Antennas Propag.*, vol. 59, no. 6, pp. 2409–2414, Jun. 2011.

[8] U. Ullah, M. F. Ain and Z. A. Ahmad, "A review of wideband circularly polarized dielectric resonator antennas," *China Communications*, vol. 14, no. 6, pp. 65-79, 2017.

[9] W. C. Harrington, "Field computation by moment methods," *Wiley-IEEE Press*, 1993.

[10] W. C. Gibson, "The method of moments in electromagnetics," *Chapman & Hall/CRC*, Newyork, 2008.

[11] A. Altaf and M. Seo, "Triple-band dual-sense circularly polarized hybrid dielectric resonator antenna," *sensors*, Vol. 18, no. 11:3899, pp. 1-14, Nov. 2018.

[12] H. N. Bich, H. C. Ba and C. D. Ngoc, "All GPS bands dielectric resonator antenna with circular polarization for GPS application," *The 2012 International Conference on Advanced Technologies for Communications*, Hanoi, 2012, pp. 65-68.

[13] C. Cheng, F. Zhang, Y. Yao, and F. Zhang, "Triband omnidirectional circularly polarized dielectric resonator antenna with top-loaded alford loop," *International Journal of Antennas and Propagation*, Vol. 2014, no. 797930, pp. 1-7, 2014.

[14] A. Sharma, G. Das, S. Gupta and R. K. Gangwar, "Quad-Band Quad-Sense Circularly Polarized Dielectric Resonator Antenna for GPS/CNSS/WLAN/WiMAX Applications," *IEEE Antennas and Wireless Propagation Letters*, vol. 19, no. 3, pp. 403-407, March 2020.

[15] A. Sharma and R. K. Gangwar, "Compact triband cylindrical dielectric resonator antenna with circular slots for wireless application," *Journal of Electromagnetic Waves and Applications*, pp. 1-10, 2015.

[16] R. Chair, A. A. Kishk, K. F. Lee and C. E. Smith, "Broadband aperture coupled flipped staired pyramid and conical dielectric resonator antennas," *IEEE Antennas and Propagation Society Symposium, 2004, Monterey*, CA, USA, 2004, pp. 1375-1378, vol.2.

[17] K. Pliakostathis and D. Mirshekar-Syahkal, "Stepped dielectric resonator antennas for wideband applications," *IEEE Antennas and Propagation Society Symposium*, 2004, Monterey, CA, USA, 2004, pp. 1367-1370, vol.2.

[18] X. Wang, L. Sun, X. Lu, S. Liang and W. Lu, "Single-feed dual-band circularly polarized dielectric resonator antenna for CNSS applications," *IEEE Transactions on Antennas and Propagation*, vol. 65, no. 8, pp. 4283-4287, Aug. 2017.

[19] R. K. Chaudhary, K. V. Srivastava and A. Biswas, "A novel triple-band cylindrical dielectric resonator antenna using varying permittivity in ϕ-direction," *Proceedings of the 2012 IEEE International Symposium on Antennas and Propagation*, Chicago, IL, 2012, pp. 1-2. .

[20] M. Younssi, A. Jaoujal, N. Aknin and A. E. Moussaoul, "Tri-band cylindrical dielectric resonator antenna excited by a coaxial probe," *European Journal of Scientific Research*, vol.82, no.3, pp. 423-428, 2012.

[21] M. Bemani, S. Nikmehr and H. Younesiraad, "A novel small triple band rectangular dielectric resonator antenna for WLAN and WiMAX application," *Journal of Electromagnetic Waves and Applications*, vol. 25, pp. 1688-1698, 2011.

[22] N. M. Nor, M. H. Jamaluddin, J. Nasir, S. F. Roslan, H. Mohamad and N. Ramli, "Multiband dielectric resonator antenna for WLAN Application," *2014 IEEE Asia-Pacific Conference on Applied Electromagnetics (APACE)*, Johor Bahru, 2014, pp. 253-256.

[23] R. Chair, A. A. Kishk, K. F. Lee and C. E. Smith, "Broadband aperture coupled flipped staired pyramid and conical dielectric resonator antennas," *IEEE Antennas and Propagation Society Symposium, 2004, Monterey*, CA, USA, 2004, pp. 1375-1378, vol.2.

[24] R. Chair, A.A.Kishk, K.F.Lee and C.E.Smith, " Wideband flipped staired pyramid dielectric resonator antennas," *Electronics Letters*, vol. 40, no. 10, pp. 1-2, 2004.

[25] K. Pliakostathis and D. Mirshekar-Syahkal, "Stepped dielectric resonator antennas for wideband applications," *IEEE Antennas and Propagation Society Symposium*, 2004, Monterey, CA, USA, 2004, pp. 1367-1370, vol.2.

[26] M.F. Zambak, M. N. M. Yasin, I. Adam, J. Iqbal and M.N. Osman, "Higher order mode tripal-band circularly polarized rectangular dielectric resonator antenna," *Applied Science*, vol. 11, pp. 3493-3505, 2021.

[27] N.K. Darimireddy, R.R. Reddy and A.M. Prasad, "Tri-band and quad-band dual L-slot coupled circularly polarized dielectric resonator antenna," *International Journal of RF and Microwave Computer Aided Engineering*, pp. 1-13, 2018.

[28] X. Fang, K. W. Leung and E. H. Lim, "Singly-fed dual-band circularly polarized dielectric resonator antenna," *IEEE Antennas and Wireless Propagation Letters*, vol. 13, pp. 995-998, 2014.

[29] M. Zou and J. Pan, "Wide dual-Band circularly polarized stacked rectangular dielectric resonator antenna," *IEEE Antennas and Wireless Propagation Letters*, vol. 15, pp. 1140-1143, 2016.

[30] H. S. Ngan, X. S. Fang and K. W. Leung, "Design of dual-band circularly polarized dielectric resonator antenna using a higher-order mode," *2012 IEEE-APS Topical Conference on Antennas and Propagation in Wireless Communications (APWC)*, Cape Town, 2012, pp. 424-427.

[31] X. S. Fang, C. K. Chow, K. W. Leung and E. H. Lim, "New single-/dual-mode design formulas of the rectangular dielectric resonator antenna using covariance matrix adaptation evolutionary strategy," *IEEE Antennas and Wireless Propagation Letters*, vol. 10, pp. 734-737, 2011.

[32] X. S. Fang and K. W. Leung, "Dualband design of the rectangular dielectric resonator antenna," *2011 IEEE International Symposium on Antennas and Propagation (APSURSI)*, Spokane, WA, 2011, pp. 1670-1673.

[33] Y. Ding, K. W. Leung and K. M. Luk, "Compact circularly polarized dualband zonal-slot/DRA hybrid antenna without external ground plane," *IEEE Transactions on Antennas and Propagation*, vol. 59, no. 6, pp. 2404-2409, June 2011.

[34] M. Zhang, B. Li and X. Lv, "Cross-slot-coupled wide dual-band circularly po-

larized rectangular dielectric resonator antenna," *IEEE Antennas and Wireless Propagation Letters*, vol. 13, pp. 532-535, 2014.

[35] A. Gupta and R. K. Gangwar, "Dual-band circularly polarized aperture coupled rectangular dielectric resonator antenna for wireless applications," *IEEE Access*, vol. 6, pp. 11388-11396, 2018.

[36] G. Varshney, S. Gotra, V. S. Pandey and R. S. Yaduvanshi, "Inverted-sigmoid shaped multiband dielectric resonator antenna with dual-band circular polarization," *IEEE Transactions on Antennas and Propagation*, vol. 66, no. 4, pp. 2067-2072, April 2018.

[37] A. Altaf, J. Jung, Y. Yang, K. Lee and K. C. Hwang, "Reconfigurable dual-/triple-band circularly polarized dielectric resonator antenna," *IEEE Antennas and Wireless Propagation Letters*, vol. 19, no. 3, pp. 443-447, March 2020.

[38] Q. Lamotte, G. Mazingue, J. Bharker, M. Romier and N. Capet, "Multi-permittivity 3-D printed ceramic dual-band circularly polarized dielectric resonator antenna," *2021 15th European Conference on Antennas and Propagation (EuCAP)*, 2021, pp. 1-5.

[39] C. Tong, H. Tang, W. Qin, W. Yang, X. Zhang and J. Chen, "Differentially inserted-fed compact dual-band circularly polarized dielectric resonator antenna," *IEEE Antennas and Wireless Propagation Letters*, vol. 18, no. 12, pp. 2498-2502, Dec. 2019.

[40] H. Al-Lawati, Z. Nadir and S. Khamas, "Dual-band singly fed circularly polarized elliptical dielectric resonator antenna," *2019 IEEE Asia-Pacific Microwave Conference (APMC)*, 2019, pp. 551-553.

[41] G. Zhao, J. R. Wang, X. Shi and M. S. Tong, "A dual-band dielectric resonator antenna over a metasurface with circular polarization," *2020 IEEE International Symposium on Antennas and Propagation and North American Radio Science Meeting*, 2020, pp. 665-666.

[42] A. Amir and M. Seo, "Dual-band circularly polarized dielectric resonator antenna for WLAN and WiMAX applications" *Sensors*, no. 4, pp. 1137-1148, 2020.

[43] R. Han, S. Zhong and J. Liu, "Design of circularly-polarized dielectric resonator antenna with wideband feed network," *Proceedings of 2014 3rd Asia-Pacific Conference on Antennas and Propagation*, Harbin, 2014, pp. 48-50.

[44] K. P. Esselle, "Circularly polarised higher-order rectangular dielectric-resonator antenna," *Electronics Letters*, vol. 32, no. 3, pp. 150-151, 1 Feb. 1996.

[45] E. H. Lim, K. W. Leung and X. S. Fang, "The compact circularly-polarized hollow rectangular dielectric resonator antenna with an underlaid quadrature coupler," *IEEE Transactions on Antennas and Propagation*, vol. 59, no. 1, pp. 288-293, Jan. 2011.

[46] G. Massie, M. Caillet, M. Clenet and Y. M. M. Antar, "A new wideband circularly polarized hybrid dielectric resonator antenna," *IEEE Antennas and Wireless Propagation Letters*, vol. 9, pp. 347-350, 2010.

[47] X. S. Fang, K. W. Leung and R. S. Chen, "Design of wideband circularly polarized cylindrical dielectric resonator antennas," *2010 International Conference on Electromagnetics in Advanced Applications*, Sydney, NSW, 2010, pp. 224-227.

[48] W. W. Li and K. W. Leung, "Compact circularly polarized hollow dielectric resonator antenna with embedded vertical feed network," *2013 IEEE Antennas and Propagation Society International Symposium (APSURSI)*, Orlando, FL, 2013, pp. 1234-1235.

[49] M. T. Lee, K. M. Luk, E. K. N. Yung and K. W. Leung, "Circularly polarised dielectric resonator antenna with a microstrip feed," *1999 Asia Pacific Microwave Conference (APMC'99)*, Singapore, 1999, pp. 722-723 vol.3.

[50] S. A. Malekabadi, M. H. Neshati and J.Rashed-Mohassel, “Modified rectangular dielectric resonator antenna for circular polarization,” *Proceedings of iWAT2008*, Chiba, Japan, pp.538- 541, 2008.

[51] H. Raggad, M. Latrach, A. Gharsallah, T. Razban, “Circularly polarization rectangular dielectric resonator antenna for UHF RFID applications,” *2013 IEEE-APS Topical Conference on Antennas and Propagation in Wireless Communications (APWC)*, 9-13 September 2013, Torino, Italy, pp.1469 – 1472.

[52] S. Jović, M. Clénet and Y. M. M. Antar, "A compact wideband 4-port circularly polarized dielectric resonator antenna," *2017 11th European Conference on Antennas and Propagation (EUCAP)*, Paris, 2017, pp. 1957-1959.

[53] M. Clénet, M. Caillet and Y. M. M. Antar, "Wideband circularly polarized antenna elements for GPS/GNSS applications developed at DRDC Ottawa," *2010 14th International Symposium on Antenna Technology and Applied Electromagnetics & the American Electromagnetics Conference*, Ottawa, ON, 2010, pp. 1-4.

[54] S. Caizzone, M.S. Circiu, W. Elmarissi and C. Enneking,"All-GNSS-Band DRA Antenna for High-Precision Applications", *12th European Conference on Antennas and Propagation (EuCAP 2018)*, 2018, pp. 1-4.

[55] R. Han, S. Zhong and J. Liu, "Wideband circularly-polarized dielectric resonator antenna with sequentially rotated feed," *2014 IEEE Antennas and Propagation Society International Symposium (APSURSI)*, Memphis, TN, 2014, pp. 1976-1977.

[56] M. Clenet, M. Caillet and Y. M. M. Antar, “Miniaturized wideband circularly polarized hybride dielectric resonator antenna,” *Technical Memorandum*, Defence R&D, Ottawa, Canada, 2012, pp.1-48.

[57] A. Rashidian and D. M. Klymyshyn, "On the Two Segmented and High Aspect Ratio Rectangular Dielectric Resonator Antennas for Bandwidth Enhancement and Miniaturization," *IEEE Transactions on Antennas and Propagation*, vol. 57, no. 9, pp. 2775-2780, Sept. 2009.

[58] S. Jovic, M. Clénet and Y.M.M. Antar, "Multi-frequency GNSS dielectric resonator antenna with in-band filtering," *12th European Conference on Antennas and Propagation (EuCAP 2018)*, 2018, pp. 1-4.

[59] S. Jović, M. Clénet and Y. A. M.M., "Novel Wideband Antenna for GNSS and Satellite Communications," *2020 14th European Conference on Antennas and Propagation (EuCAP)*, 2020, pp. 1-5.

[60] R. S. Yaduvanshi and H. Parthasarathy, "Rectangular Dielectric Resonator Antennas Theory and Design," *Springer*, India, 2016.

[61] Y. W. Poon and W. Y. Tam, "A rigorous analysis of a dielectric resonator antenna on a finite ground plane," *IEEE Antennas and Propagation Society International Symposium. 1996 Digest*, Baltimore, MD, USA, 1996, pp. 1938-1941 vol.3.

[62] W. Y. Tam and W. Y. Poon, "Analysis of rectangular dielectric resonator antenna on a finite size ground plane," *Proceedings of 1997 Asia-Pacific Microwave Conference*, Hong Kong, 1997, pp. 1169-1171 vol.3.

[63] R. M. Baghaee, M. H. Neshati and J. R. Mohassel, "Rigorous analysis of rectangular dielectric resonator antenna with a finite ground plane," *IEEE Transactions on Antennas and Propagation*, vol. 56, no. 9, pp. 2801-2809, Sept. 2008.

[64] R. M. Baghaee, M. H. Neshati, D. Lashkari, M. Koochakzadeh and J. R. Mohassel, "Analysis of probe-fed rectangular dielectric resonator antennas on a finite ground plane using method of moment," *11th International Symposium on Antenna Technology and Applied Electromagnetics [ANTEM 2005]*, St. Malo, 2005, pp. 1-3.

[65] J. Shin, A. A. Kishk and A. W. Glisson, "Analysis of rectangular dielectric resonator antennas excited through a slot over a finite ground plane," *IEEE Antennas and Propagation Society International Symposium. Transmitting Waves of Progress to the Next Millennium. 2000 Digest. Held in conjunction with: USNC/URSI National Radio Science Meeting*, C, Salt Lake City, UT, 2000, pp. 2076-2079 vol.4.

[66] Yuehe Ge and K. P. Esselle, "The analysis of a rectangular dielectric resonator antenna using the method of moments," *IEEE Antennas and Propagation Soci-*

ety International Symposium. Transmitting Waves of Progress to the Next Millennium. 2000 Digest. Held in conjunction with: USNC/URSI National Radio Science Meeting, C, Salt Lake City, UT, 2000, pp. 1454-1457 vol.3.

[67] R. M. Baghaee, M. H. Neshati and J. R. Mohassel, "Moment method analysis of probe-fed rectangular dielectric resonator antennas with a rigorous source modeling and finite ground plane," *2005 Asia-Pacific Microwave Conference Proceedings*, Suzhou, 2005, pp. 1-4.

[68] R. M. Baghaee, M. H. Neshati and J. R. Mohassel, "The effects of air gap and finite ground plane on radiation characteristics of probe-fed rectangular dielectric resonator antennas using method of moment," *2006 IEEE Radio and Wireless Symposium*, San Diego, CA, 2006, pp. 411-414.

[69] G. P. Junker, A. A. Kishk and A. W. Glisson, "Input impedance of dielectric resonator antennas excited by a coaxial probe," *IEEE Transactions on Antennas and Propagation*, vol. 42, no. 7, pp. 960-966, July 1994.

[70] K. M. Luk, W. K. Leung and K. W. Leung, "Mutual impedance of hemispherical dielectric resonator antennas," *IEEE Transactions on Antennas and Propagation*, vol. 42, no. 12, pp. 1652-1654, Dec. 1994.

Chapter 3

Circularly Polarized Tri-Band Staired Rectangular Dielectric Resonator Antenna

3.1 Compact Circularly Polarized Tri-Band Staired Rectangular Dielectric Resonator Antenna (Two Port)

3.1.1 Introduction

A compact tri-band Circularly Polarized (CP) staired Rectangular Dielectric Resonator Antenna (RDRA) is designed, analyzed, fabricated and tested at L5, L1 and S-bands using novel design feed networks of single- and dual-section Wilkinson Power Divider (WPD) with wide-band 90° phase shifter [1]. These bands are used for Indian Regional Navigation Satellite System (IRNSS) and GPS Aided Geo Augmented Navigation (GAGAN) systems being designed by Indian Space Research Organisation (ISRO, Department of Space, Government of India). In tri-band CP DRA, area of ground plane was reduced to 40 mm × 40 mm (0.16 λ_0 × 0.16 λ_0 at lower center frequency of f_1 = 1.176 GHz) using high dielectric constant (ϵ_r = 38.67) of ceramic DR material and high dielectric constant (ϵ_r = 10.2) of dielectric substrate (Rogers RO3210) [1]. The volume of staired RDR is reduced to 27 mm × 27 mm × 35.3 mm using high dielectric constant (ϵ_r = 38.67) of ceramic DR material.

For L5 and L1-bands, tri-band DRA has generated Right Hand Circular Polarization (RHCP) using novel design feed network of dual-section WPD with wideband 90° phase shifter [1]. Single-section WPD with wideband 90° phase shifter produced RHCP in tri-band DRA at S-band. The TE^y_{111}, TE^y_{113} and TE^y_{112} modes of tri-band DRA are achieved at three center frequencies of 1.176 GHz, 1.575 GHz and 2.49 GHz, respectively. Simple geometry of staired RDR generates multi-modes with broadside radiation patterns. S-parameters, RHCP-LHCP radiation patterns, RHCP gain and axial ratio are simulated and measured for tri-band DRA. Design specifications of tri-band DRA at L5, L1 and S-bands are shown in Table 1.1 [1].

3.1.2 Design Steps of Tri-Band Rectangular Dielectric Resonator Antenna

- Choose dielectric constant ϵ_r of DR, dielectric constant ϵ_r of dielectric substrate, aspect ratios and resonance frequencies.
- Find design dimensions of staired RDR.
- Determine design dimensions of feed networks.
- Design of feed networks using reference [2].
- Verification of the S-parameters of feed networks.
- Design of staired RDRA using reference [2].
- Verification of the modes of staired RDRA.
- Verification of RHCP polarization of staired RDRA.
- Compare the simulated results with design specification of tri-band DRA.
- Fabrication of tri-band RDRA.
- Testing of tri-band RDRA.

3.1.3 Structure and Feed Networks

3.1.3.1 Structure and Mathematical Formulation

The geometry of tri-band staired RDRA with finite ground plane is shown in Figure 3.1 (a). Figure 3.1 (b) represents the feed networks such as single- and dual-sections WPD with wideband 90° phase shifter which is printed on bottom face of dielectric substrate. Figure 3.1 (c) represents the geometry dimensions of tri-band RDRA [1]. Initially, staired RDRA is considered the excitation free to determine it's geometry parameters. The 3-D geometries of tri-band RDRA are shown in Figure 3.1 (d) [1]. The staired RDRA consists of Lower Rectangular Dielectric Resonator (LRDR) and Upper Rectangular Dielectric Resonator (URDR). For LRDR, W_l, L_l, H_l and ϵ_r represents the width, length, height and dielectric constant of dielectric resonator material, respectively. For URDR, W_u, L_u and H_u are the width, length and height, respectively.

Assumed aspect ratios of $\frac{W_l}{L_l}$, $\frac{H_l}{L_l}$ and have knowledge of ϵ_r, geometry parameters of LRDR calculates at first center frequency f_1 using DWM with CMA-ES [3].

$$f_1 = \frac{c}{L_l\sqrt{\epsilon_r}} F_1(\frac{H_l}{L_l}, \frac{W_l}{L_l}) \tag{3.1}$$

Achieving $k_1 L_l$ changes the equation (3.1) as:

$$k_1 L_l = 2\pi F_1(\frac{H_l}{L_l}, \frac{W_l}{L_l}) \tag{3.2}$$

where, k_1=$2\pi f_1\sqrt{\epsilon_r}$/c, c is velocity of light and F_1 is exponentially functions. Equation (3.2) can be used to determine the value of L_l.

Similar to first center frequency of f_1, second center frequency of f_2 can be written as [3]:

$$f_2 = \frac{c}{L_l\sqrt{\epsilon_r}} F_2(\frac{H_l}{L_l}, \frac{W_l}{L_l}) \tag{3.3}$$

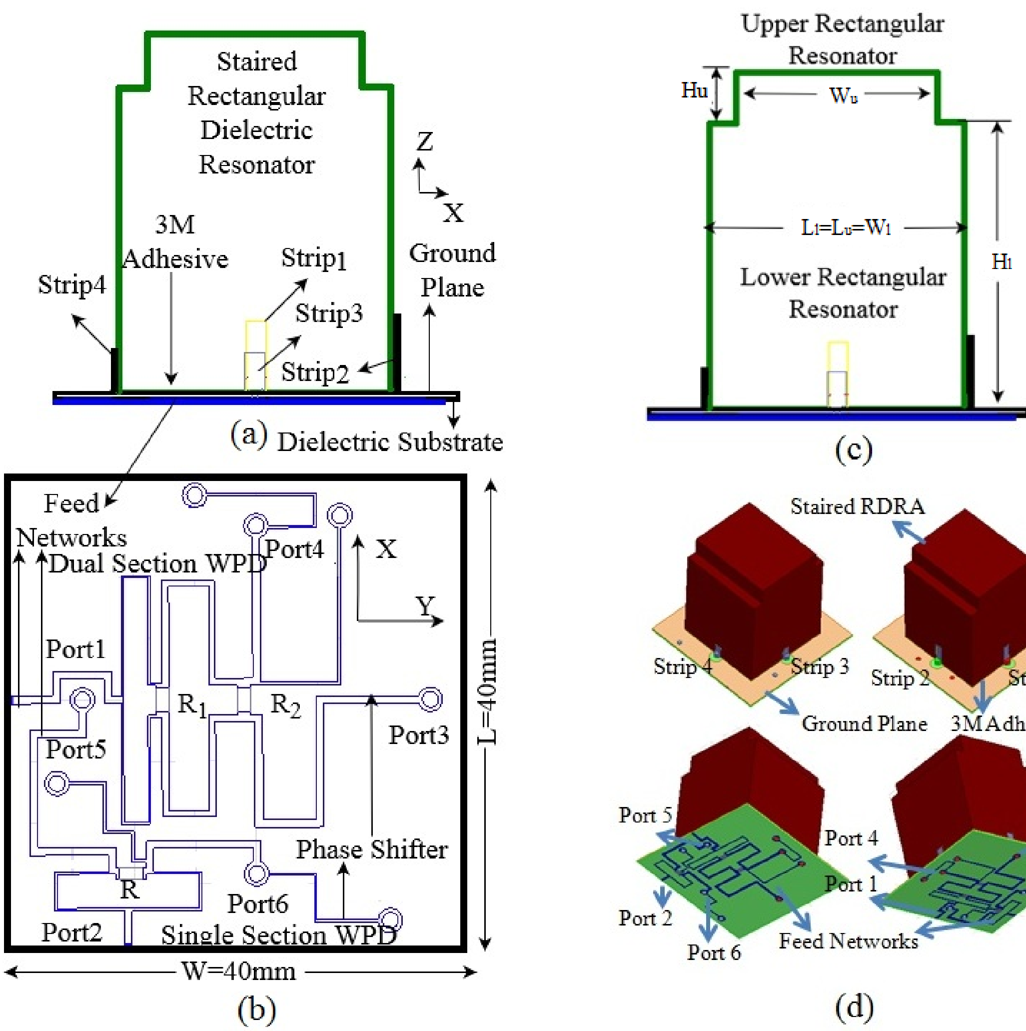

Figure 3.1: Geometry of compact tri-band RDRA with finite ground plane
(a) front view
(b) feed networks of single- and dual-sections WPD with wideband 90° phase shifter
(c) geometry dimensions representation of tri-band RDRA
(d) 3-D geometries of tri-band RDRAs [1]

Dividing equation (3.3) by equation (3.1), we get

$$\frac{f_2}{f_1} = \frac{F_2(\frac{H_l}{L_l}, \frac{W_l}{L_l})}{F_1(\frac{H_l}{L_l}, \frac{W_l}{L_l})} = F_3(\frac{H_l}{L_l}, \frac{W_l}{L_l}) \tag{3.4}$$

where F_3=F_2/F_1, value of $\frac{H_l}{L_l}$ is obtained as [3]:

$$\frac{H_l}{L_l} = F_4(\frac{W_l}{L_l}, \frac{f_2}{f_1}) \tag{3.5}$$

where, z=$\frac{H_l}{L_l}$, x=$\frac{W_l}{L_l}$, y=$\frac{f_2}{f_1}$ and F_4 is achieved from extensive data sets obtained using DWM. F_4 can be expressed as following function [3]:

$$z = F_4(x, y) \approx P(x)Q(y) \tag{3.6}$$

where,

$$P(x) = R_P e^{-xS_P} + T_P \tag{3.7}$$

$$Q(x) = R_Q e^{-xS_Q} + T_Q \tag{3.8}$$

The CMA-ES method uses to determined various parameters in 2×3 matrix **N** [3]

$$\mathbf{N} = \begin{bmatrix} R_P & S_P & T_P \\ R_Q & S_Q & T_Q \end{bmatrix} \in R^{2\times 3} \tag{3.9}$$

$$z = F_4(x, y|\mathbf{N}) \tag{3.10}$$

From matrix **N**, an optimal parameter matrix $\mathbf{N}_\circ$ can be achieved using minimizing the maximum absolute error as follow [3]:

$$E(\mathbf{N}) = \max_{i=1,2,..,|\Omega|} |z_i - F_4(x_i, y_i|\mathbf{N})| \tag{3.11}$$

where, Ω is represented as number of sample points and x_i,y_i,z_i are the sample values. This optimization process is independently repeated 100 times for global optimal solution. The final optimal parameter matrix achieved is given as below [3]:

$$\mathbf{N}_\circ = \begin{bmatrix} -0.4167 & 0.6258 & 1.5137 \\ 10.4051 & 1.7887 & 0.1221 \end{bmatrix} \tag{3.12}$$

With the knowledge of L_l, H_l of LRDR is determined from equation (3.5). W_l of LRDR is calculated from assumed value of aspect ratio $\frac{W_l}{L_l}$.

For determination of H_u, W_u and L_u of URDR, third center frequency f_3 relates to assumed aspect ratios of $\frac{H_u}{L_u}$ and $\frac{W_u}{L_u}$ as expressed below [3]:

$$f_3 = \frac{c}{L_u\sqrt{\epsilon_r}} F_5(\frac{H_u}{L_u}, \frac{W_u}{L_u}) \tag{3.13}$$

Similar to equation (3.3), achieving $k_2 L_u$ changes the equation (3.13) as:

$$k_2 L_u = 2\pi F_5(\frac{H_u}{L_u}, \frac{W_u}{L_u}) \tag{3.14}$$

where, p=$\frac{H_u}{L_u}$, q=$\frac{W_u}{L_u}$, r=$k_2 L_u$ and F_5 are exponentially decaying functions. F_5 is achieved from extensive data sets obtain using DWM. F_5 can be expressed as following function [3]:

$$r = k_2 L_u = F_5(p, q) \approx W(p) e^{-\alpha(p) q + S(p)} + H(p) \tag{3.15}$$

where,

$$W(p) = A_W e^{-pB_W} + C_W \tag{3.16}$$

$$\alpha(p) = A_\alpha e^{-pB_\alpha} + C_\alpha \tag{3.17}$$

$$S(p) = A_S e^{-pB_S} + C_S \tag{3.18}$$

$$H(p) = A_H e^{-pB_H} + C_H \tag{3.19}$$

The CMA-ES method is used to determine various parameters in 4×3 matrix **M** as follows [3]:

$$\mathbf{M} = \begin{bmatrix} A_W & B_W & C_W \\ A_\alpha & B_\alpha & C_\alpha \\ A_S & B_S & C_S \\ A_H & B_H & C_H \end{bmatrix} \in R^{4\times 3} \tag{3.20}$$

$$r = F_5(p, q|\mathbf{M}) \tag{3.21}$$

From matrix $\mathbf{M}$, an optimal parameter matrix $\mathbf{M}_\circ$ can be achieved using minimizing the maximum absolute error as follow [3]:

$$E(\mathbf{M}) = \max_{i=1,2,..,|\Omega|} |r_i - F_5(p_i, q_i|\mathbf{M})| \tag{3.22}$$

where, $\mathbf{\Omega}$ is number of sample points and p_i,q_i,r_i are sample values. The optimization process is independently repeated 100 times for global optimal solution. Finally, an optimal parameter matrix is achieved as given below [3]:

$$\mathbf{M} = \begin{bmatrix} A_W & B_W & C_W \\ A_\alpha & B_\alpha & C_\alpha \\ A_S & B_S & C_S \\ A_H & B_H & C_H \end{bmatrix} = \begin{bmatrix} 180.1639 & 14.4967 & 1.0077 \\ -2.7871 & 2.8633 & 1.5811 \\ -5.1943 & 3.8173 & 0.7584 \\ 6.5618 & 3.5343 & 3.3658 \end{bmatrix} \tag{3.23}$$

L_u can be determined from equation (3.14). Knowing L_u, H_u and W_u can be determined from assumed aspect ratios of $\frac{H_u}{L_u}$ and $\frac{W_u}{L_u}$. Suppose $\frac{H_l}{L_l}$ = 1.12, $\frac{W_l}{L_l}$ = 1.0, $\frac{H_u}{L_u}$ = 0.22, $\frac{W_u}{L_u}$ = 0.77, ϵ_r = 38.67, f_1=1.176 GHz, f_2=1.575 GHz and f_3=2.49 GHz, the geometry parameters of staired RDRA are determined as L_l = 27 mm, W_l = 27 mm, H_l = 30 mm, L_u = 27 mm, W_u = 21 mm and H_u = 5.3 mm. where, k_2=$2\pi f_3\sqrt{\epsilon_r}$/c. In proposed triband RDRA, LRDR is resonated at L5 and L1-bands. URDR of triband RDRA resonates at S-band. The combination of LRDR and URDR produces three resonance over desired L5, L1 and S-bands.

3.1.3.2 Feed Networks

The WPD has useful properties such as lossless network when output ports are matched and good isolation between output port-2 and port-3 [4, 5]. For L5- and L1-band, RHCP of tri-band DRA is produced using novel design of dual-section WPD with wide-band 90° phase shifter [1]. RHCP of tri-band DRA at S-band is achieved using single-section WPD with wide-band 90° phase shifter. The configuration of dual-section WPD with wide-band 90° phase shifter is shown in Figure 3.2 (a). Figure 3.2 (b) shows configuration of single-section WPD with wide-band 90° phase shifter [1].

In dual-section WPD, Z_1 and Z_2 are characteristic impedances of microstrip transmission lines. l_1 and l_2 are length of microstrip transmission lines. R_1 and R_2 represents two resistors. The relation between characteristic impedances of transmission lines and physical lengths of transmission lines was produced using even mode analysis [5]. Absorption resistors are determined through characteristic impedances and physical lengths of microstrip lines using odd-mode analysis [5].

Characteristic impedances Z_1 and Z_2 can be expressed using even mode analysis as [5]

$$Z_1 = \frac{Z_0}{a}\sqrt{\frac{(1+a^2)\sqrt{1+8a^2b^2} - 1 + 4a^4 - a^2(1+4b^2)}{1+2a^2-b^2}} \tag{3.24}$$

$$Z_2 = \frac{1+\sqrt{1+8a^2b^2}}{4ab}Z_1 \tag{3.25}$$

Using odd mode analysis, resistors R_1 and R_2 can be represented as [5]:

$$R_1 = \frac{2Z_1Z_2}{Z_0\sqrt{V}} \tag{3.26}$$

$$R_2 = 2\frac{Z_0Z_1Z_2 + \frac{b}{a}Z_2^3 + Z_2Z_0^2\sqrt{V}}{Z_1Z_0(\frac{Z_2^2}{Z_0^2} - 1) + Z_2Z_0(\frac{b}{a}\frac{Z_2^2}{Z_0^2} + \frac{1}{ab})} \tag{3.27}$$

where, a=tan $\beta_1 l_1$, b=tan $\beta_2 l_2$ and

$$V = (Z_1^2/Z_0^2) + ((b^2-1)/ab)(Z_1Z_2/Z_0^2) - (1/a^2)(Z_2^2/Z_0^2) \tag{3.28}$$

The propagation constants β_1 and β_2 applies to resonance frequencies f_1 and f_2, respectively. In phase shifter, characteristic impedance Z_3 is expressed as [6]:

$$Z_3 = 1.52Z_0 \tag{3.29}$$

The characteristic impedances Z_4 and Z_5 are equal to Z_0 as given in [5].

In dual section WPD with wide-band 90° phase shifter, Z_1, Z_2, Z_3 and Z_4 are characteristic impedances of quarter wavelength transmission lines and Z_5 is charac-

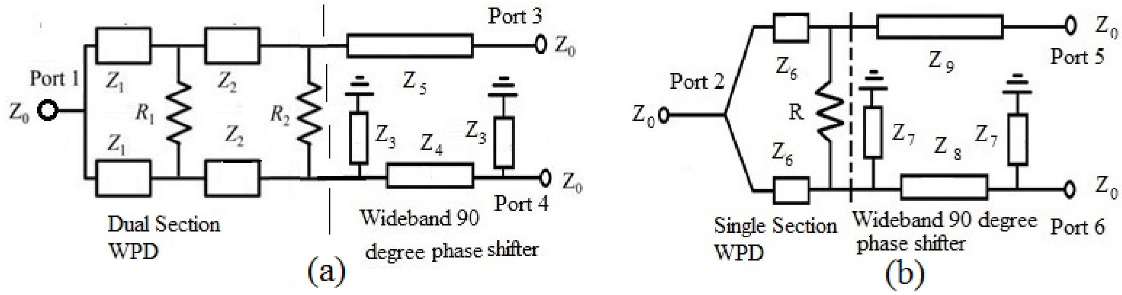

Figure 3.2: Feed networks of triband staired RDRA (a) configuration of dual section WPD with wideband 90° phase shifter (b) configuration of single-section WPD with wideband 90° phase shifter [1, 5, 6, 7]

teristic impedance of half wavelength transmission line [1]. The values of resistances are R_1=110 Ω and R_2=150 Ω. Z_1, Z_2 and Z_3 are obtained using equations (3.24) to (3.29).

In single-section WPD, characteristic impedance Z_6 and resistance R can be expressed as [6]:

$$Z_6 = \sqrt{2Z_0^2} \tag{3.30}$$

$$R = 2Z_0 \tag{3.31}$$

In phase shifter, characteristic impedance Z_7 is written as [6]:

$$Z_7 = 1.52Z_0 \tag{3.32}$$

The characteristic impedances Z_8 and Z_9 are equal to Z_0 as given in [6].

In single-section WPD with wide-band 90° phase shifter, Z_6, Z_7 and Z_8 are characteristic impedances of quarter wavelength transmission lines and Z_9 is characteristic impedance of half wavelength transmission line [1]. The value of absorption resistance is R=100 Ω. Z_6 and Z_7 are obtained using equations (3.30) and (3.32). Table 3.1 gives optimized design dimensions of dual and single-sections WPD with phase shifter.

Table 3.1: Optimized design dimensions of dual-section WPD with wide-band 90° phase shifter at 1.176 GHz, 1.575 GHz and single section WPD with wide-band 90° phase shifter at 2.49 GHz

Characteristic impedance (Ω)	**Length (mm)**	**Width (mm)**
Z_1=70.7	22.07	0.25
Z_2=55.0	22.38	0.50
Z_3=76.0	19.80	0.20
Z_4=50.0	15.00	0.70
Z_5=50.0	32.80	0.70
Z_6=70.7	14.00	0.20
Z_7=76.0	12.00	0.20
Z_8=50.0	12.90	0.60
Z_9=50.0	25.00	0.60

Dual-section WPD at L1- and L5-bands are developed for half-power division by Z_1, Z_2, R_1 and R_2 at port 3 and port 4 [1]. In dual-section WPD, 90° phase shift is received by Z_4 and Z_5. The resistances R_1 and R_2 are obtained from equations (3.26) and (3.27), respectively. In single section WPD, half power division at port 5 and port 6 is obtained by Z_6 and R for S-band [1]. 90° phase shift is obtained by Z_8 and Z_9 in single section WPD. The resistance R is obtained from equation (3.31). In single- and dual-sections WPD, two short stubs necessaries for smooth phase change over wide-band and impedance matching [1].

Design of dual-section WPD with wideband 90° phase shifter is verified using reference [2]. S_{11}, S_{31}, S_{41} and S_{34} of dual-section WPD with phase shifter at L5- and L1-bands are represented in Figure 3.3 (a). Figure 3.3 (b) shows the phase shift of dual-section WPD with phase shifter at L5 and L1-bands. The return loss ($|S_{11}|$) at port-1 of dual-section WPD with phase shifter is achieved to be better than 17 dB over L5 and L1-bands. The isolation ($|S_{34}|$) of dual-section WPD with phase shifter is found to be better than 20 dB over L5- and L1-bands. $|S_{31}|$ and $|S_{41}|$ are found to be better than 3.97 dB over L5 and L1-bands.

Design of single-section WPD with wideband 90° phase shifter is verified using reference [2]. S_{22}, S_{52}, S_{62} and S_{56} of single-section WPD with phase shifter at

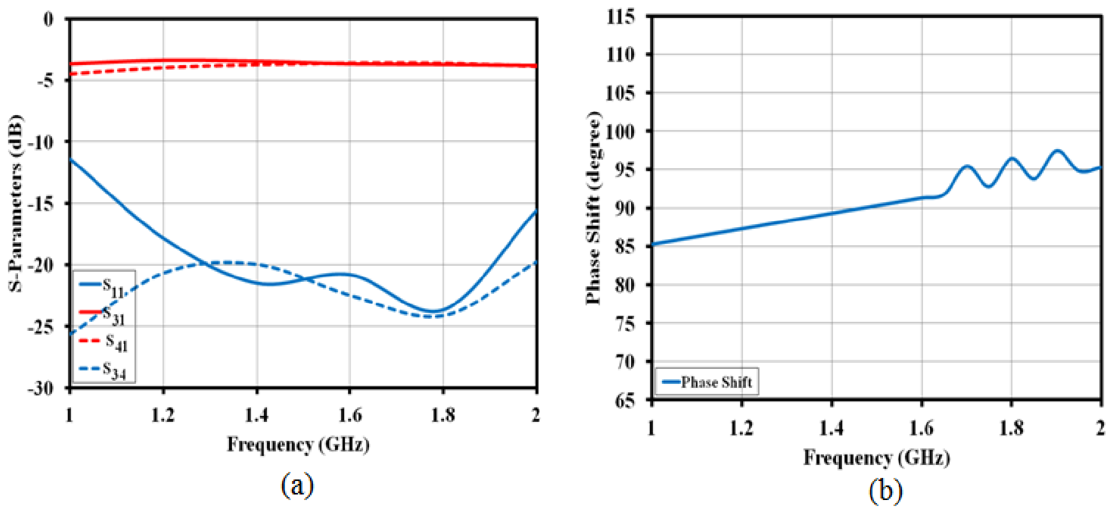

Figure 3.3: (a) S_{11}, S_{31}, S_{41} and S_{34} (b) phase shift of dual-section WPD with wide-band 90° phase shifter at L5- and L1-band [1]

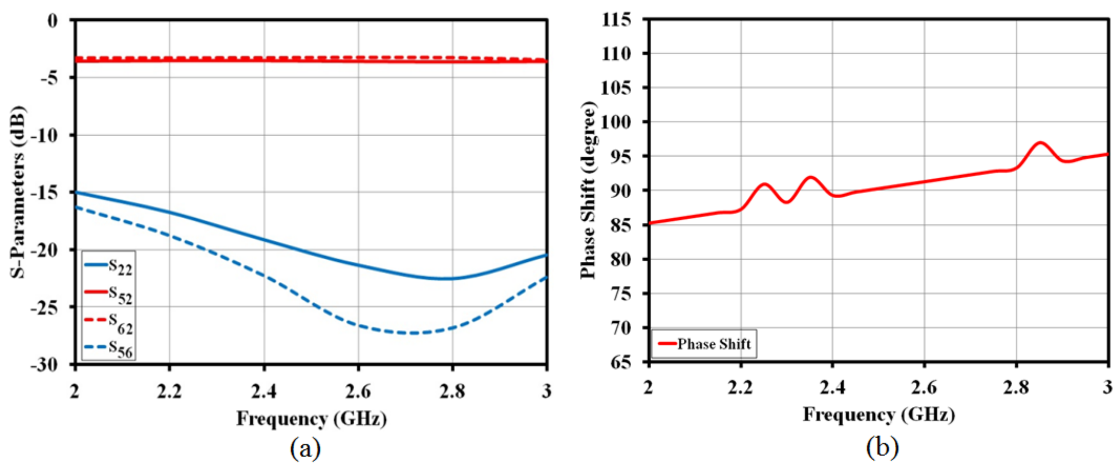

Figure 3.4: (a) S_{22}, S_{52}, S_{62} and S_{56} (b) phase shift of single section WPD with wide-band 90° phase shifter at S-band [1]

S-band are shown in Figure 3.4 (a). Figure 3.4 (b) shows the phase shift of single-section WPD with phase shifter at S-band. Non-linearity (wiggles) in the simulated phase shift data are achieved due to high impedances of stubs in phase shifters. The return loss ($|S_{22}|$) at port-2 of single-section WPD with phase shifter is obtained to be better than 20 dB over S-band. The isolation ($|S_{56}|$) of single-section WPD with phase shifter is achieved to be better than 23 dB over S-band. $|S_{52}|$ and $|S_{62}|$ of single-section WPD with phase shifter are found to be better than 3.6 dB over S-band.

3.1.4 Electric Field Distribution

Figures 3.5 (a), (b) and (c) show the electric field distribution of TE^y_{111} mode at 1.176 GHz, TE^y_{113} mode at 1.575 GHz and TE^y_{112} mode at 2.49 GHz of triband DRA, respectively. TE^y_{111}, TE^y_{113} and TE^y_{112} modes are detected as $0.5\lambda_0$, $1.5\lambda_0$ and λ_0 on z-direction. Electric field **E** vectors at 1.176 GHz, 1.575 GHz and 2.49 GHz rotate in anticlockwise direction as phase changes from 0° to 90° as shown in Figures 3.6 (a) to (f). The anticlockwise rotation of electric fields shows RHCP. All electric field distributions of tri-band DRA are simulated using reference [2].

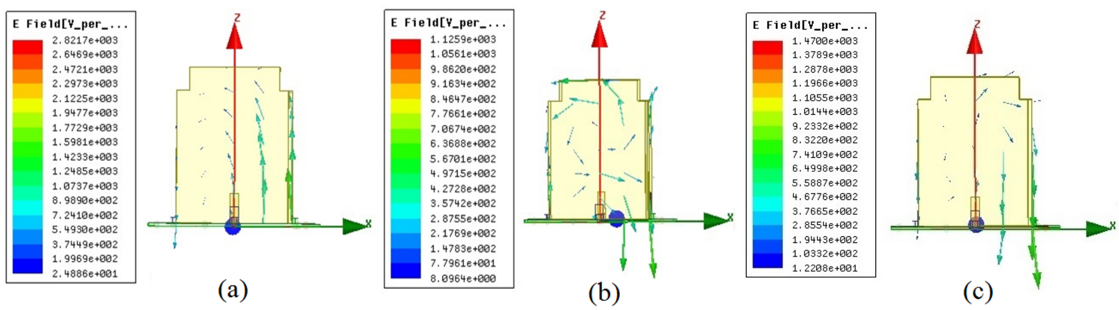

Figure 3.5: Electric field distribution of tri-band RDRA
(a) TE^y_{111} mode at 1.176 GHz
(b) TE^y_{113} mode at 1.575 GHz
(c) TE^y_{112} mode at 2.49 GHz [1]

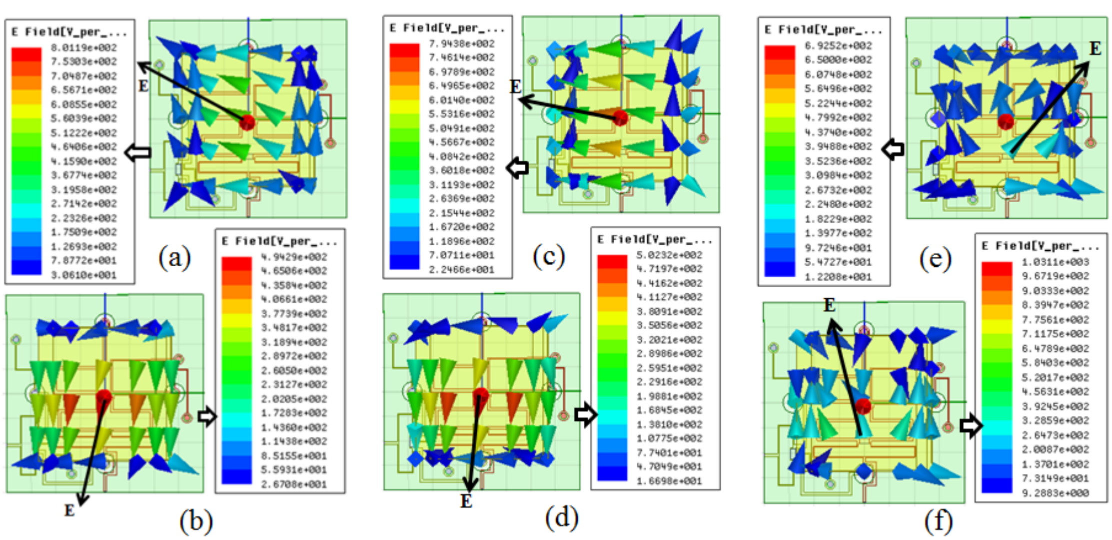

Figure 3.6: Electric field distribution of tri-band RDRA (a) 1.176 GHz with respect to 0° (b) 1.176 GHz with respect to 90° (c) 1.575 GHz with respect to 0° (d) 1.575 GHz with respect to 90° (e) 2.49 GHz with respect to 0° (f) 2.49 GHz with respect to 90° [1]

3.1.5 Fabrication and Testing

Tri-band RDRA consists of staired RDR, dielectric substrate, single- and dual-sections WPD with wide-band 90° phase shifter, ground plane, strips and 3M adhesive. The feed networks of tri-band RDRA are located on bottom side of dielectric substrate as shown in Figure 3.7 (a). Top side of dielectric substrate is represented as ground plane. The staired RDR and ground plane are connected using 3M adhesive with size of 27 mm × 27 mm × 0.05 mm as shown in Figure 3.7 (b) [1]. The side view photograph of fabricated tri-band RDRA is given in Figure 3.7 (c).

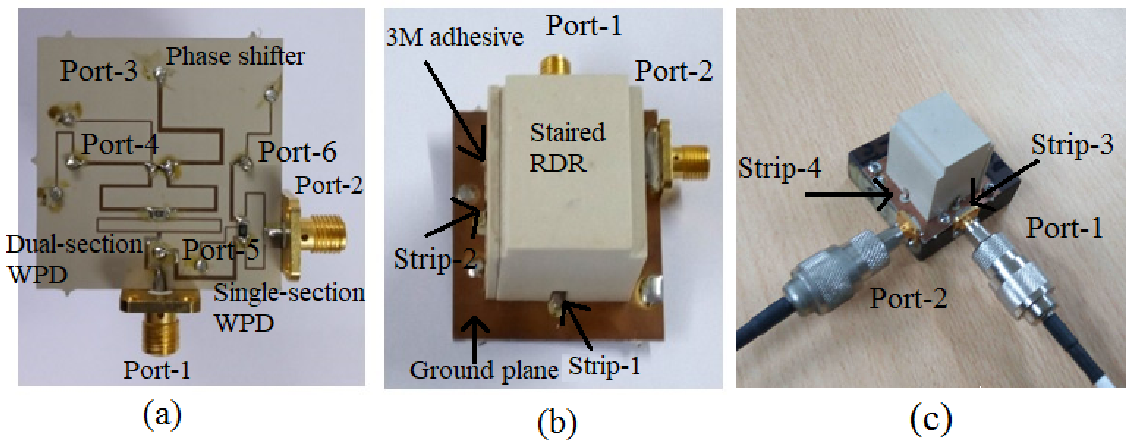

Figure 3.7: Photograph of fabricated triband RDRA (a) bottom view (b) top view (c) side view [1]

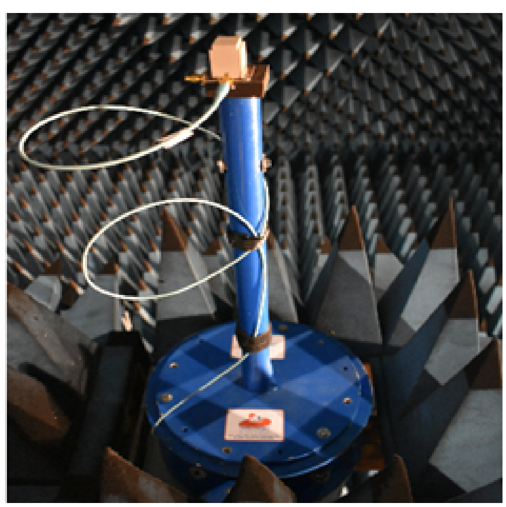

Figure 3.8: Photograph of fabricated triband RDRA with bakelite support, mounting fixture and fixure pipe in anechoic chamber [1]

The strips are attached to sidewalls of staired RDR using 3M adhesive. Port 1 and port 2 acts as input ports of triband DRA. As shown in Figure 3.7, strips 1, 2, 3 and 4 are soldered to ports 3, 4, 5 and 6, respectively. The isolation between ground plane and strips is obtained by removing four 2 mm radius patches of copper in the ground plane. The ground plane area of triband RDRA is 40 mm × 40 mm. Lengths of vertical feeding strips 1, 2, 3 and 4 are 8.135 mm, 8.135 mm, 5.135 mm and 5.135 mm, respectively. The widths of all feeding strips are 2 mm. Thickness of dielectric substrate is 0.635 mm.

The simulated and measured parameters of tri-band RDRA are S_{11}, S_{22}, S_{12}, S_{21}, RHCP-LHCP radiation patterns, RHCP gain and axial ratio. S_{11}, S_{22}, S_{12} and S_{21} are measured using E5071B Vector Network Analyzer (VNA). Figure 3.8 shows photograph of fabricated tri-band RDRA with bakelite support, mounting fixture and fixure pipe in anechoic chamber. In an anechoic chamber, the measurements of tri-band RDRA are taken using an automated system (Appendix A.1). Measurement of radiation patterns are discussed in Appendix A.2. The gain transfer method (Appendix A.3) was used to measure the gain of tri-band RDRA. The rotating source method (Appendix A.4) was employed to measure the axial ratio of tri-band RDRA.

3.2 Miniaturized Circularly Polarized Tri-Band Staired Rectangular Dielectric Resonator Antenna (Single Port)

3.2.1 Introduction

For IRNSS and GAGAN applications, miniaturized tri-band CP staired RDRA was designed, analyzed, fabricated and tested for L5, L1 and S-bands [8]. Tri-band RDRA produces RHCP using a novel tri-section WPD with wideband 90° phase shifter as feed network. A single input port is used for L5, L1 and S-bands. The ground plane footprint area of tri-band RDRA is miniaturized to 40 mm × 40 mm using high dielectric constant (ϵ_r= 51.92) of DR material and high dielectric constant ($\epsilon_r = 10.2$) of dielectric substrate (Rogers RO3210) [8]. The volume of staired RDR is reduced to 23.2 mm × 23.2 mm × 28.25 mm because of high dielectric constant of DR material. The TE^y_{111}, TE^y_{113} and TE^y_{112} modes in tri-band RDRA produces broadside radiation patterns at 1.176 GHz, 1.575 GHz and 2.49 GHz, respectively. The return loss, RHCP-LHCP field patterns, RHCP gain and axial ratio are simulated and measured for tri-band RDRA [8].

3.2.2 Configuration and Feed Network

The dimensions of staired RDR are obtained using equations (3.1) to (3.23) with assumed aspect ratios of RDRs. Assume $\frac{H_l}{L_l} = 1.13$, $\frac{W_l}{L_l} = 1.0$, $\frac{H_u}{L_u} = 0.13$, $\frac{W_u}{L_u} = 1.38$, $\epsilon_r = 51.92$, f_1=1.176 GHz, f_2=1.575 GHz and f_3=2.49 GHz, as design dimensions of staired RDR, which gives $L_l = 23.2$ mm, $W_l = 23.2$ mm, $H_l = 26.1$ mm, $L_u =$ 16.9 mm, $W_u = 23.2$ mm and $H_u = 2.15$ mm [8]. The front view of tri-band RDRA is shown in Figure 3.9 (a). Figure 3.9 (b) represents the bottom view of tri-band RDRA. 3-D views of tri-band RDRA is shown in Figure 3.9 (c).

For L5, L1 and S-bands, RHCP of tri-band RDRA is produced by tri-section WPD with wideband 90° phase shifter. Figure 3.9 (d) represents schematic diagram of tri-section WPD with wideband 90° phase shifter. In tri-section WPD, three transmission sections of characteristic impedances Z_1, Z_2 and Z_3 have lengths l_1, l_2 and l_3 [9, 10], respectively. The electrical lengths θ_1= $\beta_1 l_1$, θ_2= $\beta_1 l_2$ and θ_3= $\beta_1 l_3$ at first frequency f_1 are less than or equal to $\pi/2$ [9]. β_1 is equal to $(\frac{2\pi f_1}{c\sqrt{\epsilon_s}})$. Z_1, Z_2, Z_3, θ_1, θ_2 and θ_3 are obtained by even mode analysis of tri-section WPD. u_1= $\frac{f_2}{f_1}$ and u_2= $\frac{f_3}{f_1}$ where, $1 < u_1 < u_2 < 3$ [9, 10].

The characteristic impedance Z_1 and electric length θ_1 are given by equations (3.33) to (3.38) as follows [9]:

$$Z_1 = [3.595u_1^2 - 11.686u_1 + 59.52]e^{u_2 p} \tag{3.33}$$

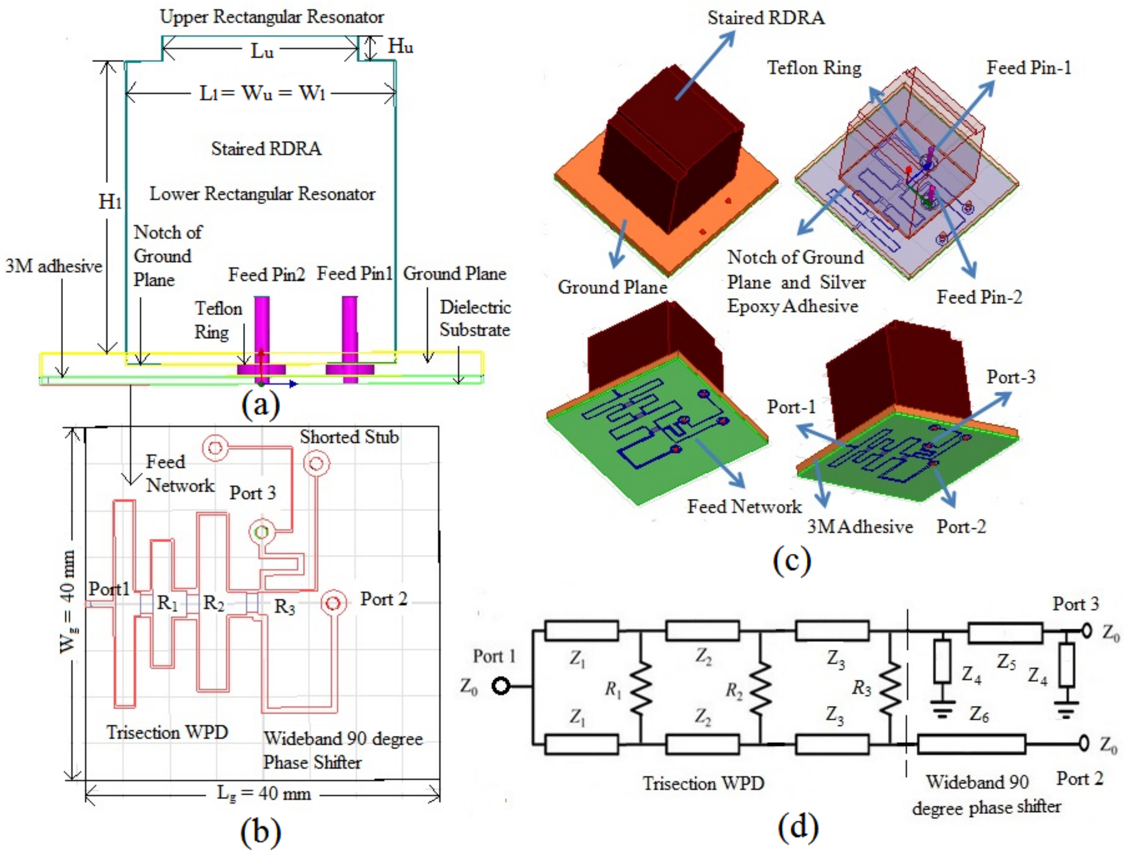

Figure 3.9: Configuration of miniaturized tri-band CP RDRA
(a) front view
(b) bottom view
(c) 3-D views of tri-band RDRA
(d) Feed network of miniaturized triband CP RDRA [6, 7, 8]

$$\theta_1 = \frac{\pi}{180}[u_2 q + rs] \tag{3.34}$$

where,

$$p = \frac{1.361 - e^{-0.451u_1}}{10.015 + e^{1.09u_1}} \tag{3.35}$$

$$q = 0.616u_1 + 3.822(u_1 - 3.714)^2 \tag{3.36}$$

$$r = 0.821u_1 + 3.113(u_1 - 3.208)^2 \tag{3.37}$$

$$s = u_2 - 1.994u_1 - 0.555(u_1 - 2.363)^2 \tag{3.38}$$

Z_2, θ_2, Z_3 and θ_3 are given by (3.39) to (3.42) [9].

$$Z_2 = \sqrt{2}Z_0 \tag{3.39}$$

$$\theta_2 = -\arctan\left(\frac{\cot\theta_1 + b\tan\theta_1}{2a}\right) \tag{3.40}$$

$$Z_3 = \frac{Z_2^2}{Z_1} \tag{3.41}$$

$$\theta_3 = \theta_2 \tag{3.42}$$

The parameters a and b are shown in equations (3.43) and (3.44), respectively as follows [9]:

$$a = \sqrt{2}\left(\frac{2Z_0}{Z_1} - \frac{Z_1}{2Z_0}\right) \tag{3.43}$$

$$b = 2\left(\frac{2Z_0}{Z_1}\right)^2 - \left(\frac{Z_1}{2Z_0}\right)^2 \tag{3.44}$$

R_1, R_2 and R_3 are obtained using odd-mode analysis of tri-section WPD [9]. R_1, R_2 and R_3 can be found by numerically solving equation (6) in reference [9] for frequencies f_1, f_2 and f_3 with known parameters (Z_1, Z_2, Z_3, θ_1, θ_2 and θ_3) obtained from equations (3.33) to (3.44). The values of R_1, R_2 and R_3 are 110Ω, 150Ω, 176Ω, respectively.

Z_4 is equal to 1.52Z_0 [6]. Z_5 and Z_6 are equal to Z_0 as given in [6]. Z_4 is characteristic impedance of half wavelength transmission line. Z_5 and Z_6 are characteristic impedances of quarter wavelength transmission lines. The electrical lengths are $\theta_4 = \beta_1 l_4$, $\theta_5 = \beta_1 l_5$ and $\theta_6 = \beta_1 l_6$. θ_4, θ_5 and θ_6 are 180°, 90° and 90°, respectively. The optimized design dimensions of tri-section WPD with wide-band 90° phase shifter at 1.176 GHz, 1.575 GHz and 2.49 GHz are given in Table 3.2.

Table 3.2: Optimized design dimensions of tri-section WPD with wide-band 90° phase shifter at 1.176 GHz, 1.575 GHz and 2.49 GHz

Characteristic impedance (Ω)	**Length (mm)**	**Width (mm)**
Z_1=88.09	l_1=23.27	0.13
Z_2=70.70	l_2=16.15	0.25
Z_3=56.75	l_3=23.88	0.45
Z_4=76.00	l_4=16.40	0.20
Z_5=50.00	l_5=19.80	0.60
Z_6=50.00	l_6=30.10	0.60

Tri-section WPD with wide-band 90° phase shifter is analyzed using reference [2]. The S-parameters of tri-section WPD with wide-band 90° phase shifter are shown in Figure 3.10 (a). $|S_{11}|$, $|S_{21}|$, $|S_{31}|$ and $|S_{23}|$ are found to be better than 16 dB, 3.99 dB, 4.5 dB and 17 dB over L5, L1, and S-bands, respectively [8]. The phase shift of tri-section WPD with wide-band 90° phase shifter is shown in Figure 3.10 (b). Tri-section WPD with wide-band 90° phase shifter achieved the phase shift of 90° over all band.

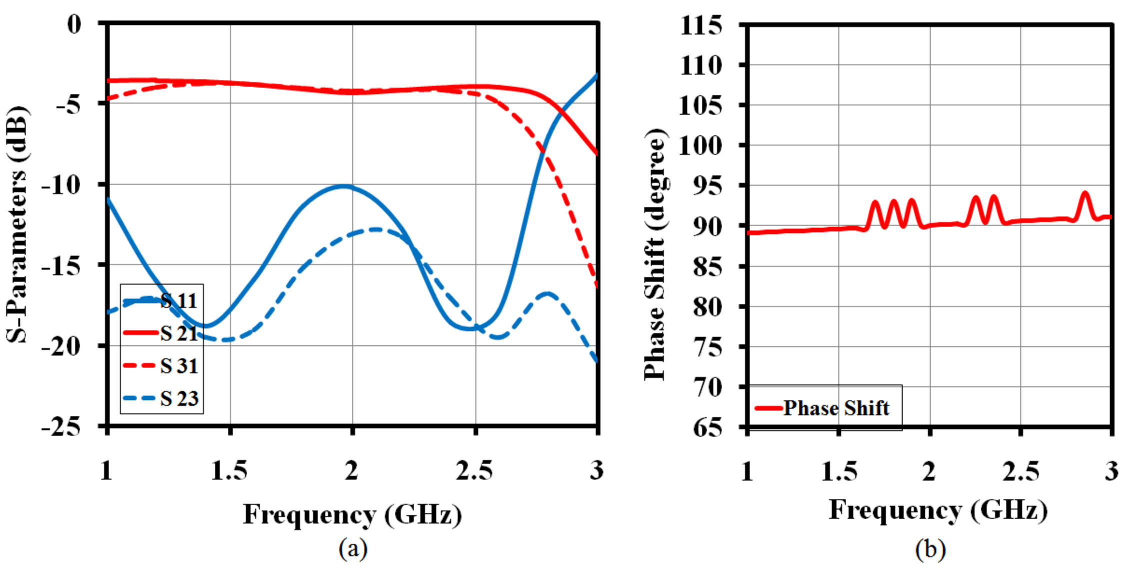

Figure 3.10: (a) S_{11}, S_{21}, S_{31} and S_{23} (b) phase shift of tri-section WPD with wide-band 90° phase shifter [8]

TE^y_{111} at 1.176 GHz, TE^y_{113} at 1.575 GHz and TE^y_{112} at 2.49 GHz modes of tri-band RDRA are shown in Figure 3.11 (a), (b) and (c), respectively. The TE^y_{111}, TE^y_{113} and TE^y_{112} modes are observed $0.5\lambda_0$ at 1.176 GHz, $1.5\lambda_0$ at 1.575 GHz and

λ_0 at 2.49 GHz, respectively. Figures 3.12 (a) to (f) show simulated **E** vectors rotate in anticlockwise direction as phase change from 0° to 90° at 1.176 GHz, 1.575 GHz and 2.49 GHz. This produced RHCP.

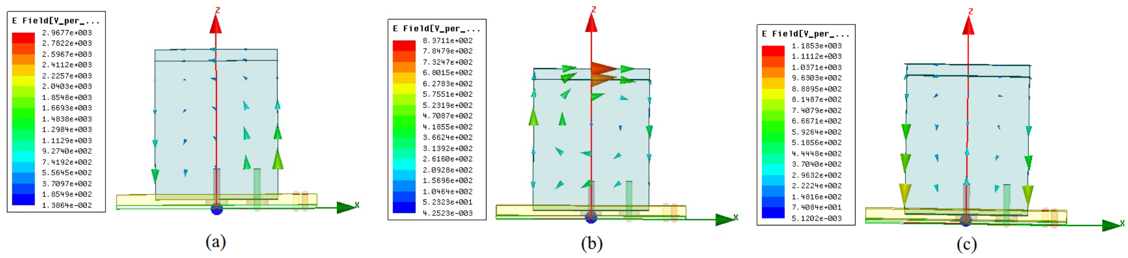

Figure 3.11: Electric field distribution of tri-band RDRA (a) TE^y_{111} mode at 1.176 GHz (b) TE^y_{113} mode at 1.575 GHz (c) TE^y_{112} mode at 2.49 GHz [8]

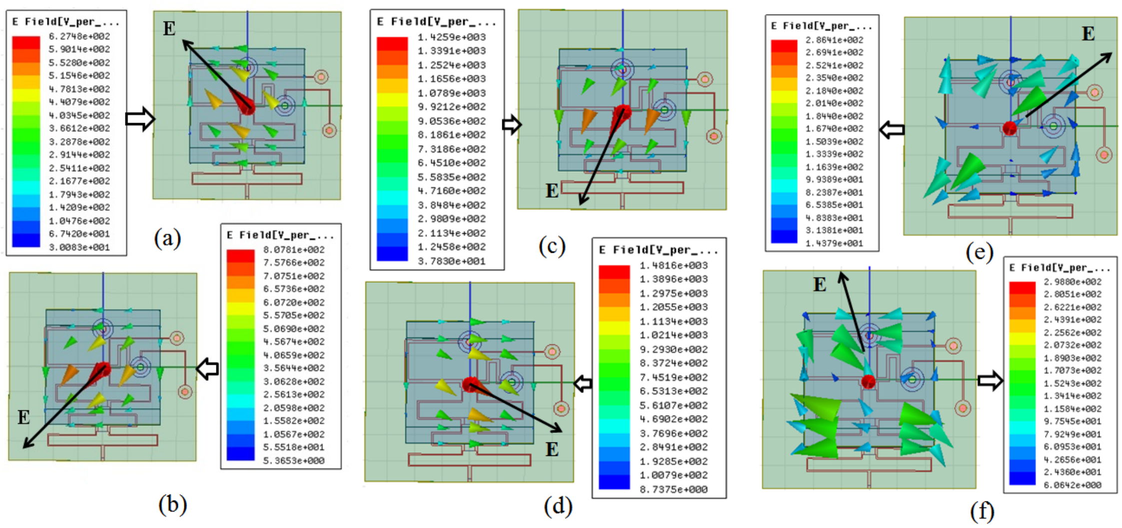

Figure 3.12: Electric field distribution of tri-band RDRA (a) 1.176 GHz with respect to 0° (b) 1.176 GHz with respect to 90° (c) 1.575 GHz with respect to 0° (d) 1.575 GHz with respect to 90° (e) 2.49 GHz with respect to 0° (f) 2.49 GHz with respect to 90° [8]

3-D and bottom views of fabricated tri-band RDRA are given in Figures 3.13 (a) and 3.13 (b), respectively. Tri-band RDRA in the anechoic chamber is shown in Figure 3.14. Tri-band RDRA contains staired RDR, tri-section WPD with wide-band 90° phase shifter, dielectric substrate, copper metal sheet (ground plane), feed pins 1 and 2, teflon rings, 3M adhesive and silver epoxy adhesive as shown in Figure 3.9 (a) and (b). Tri-section WPD with wide-band 90° phase shifter is placed on bottom face of dielectric substrate as shown in Figure 3.13 (b). Copper is fully removed on top side of dielectric substrate. Metal sheet is used as the ground plane in this antenna. Copper metal sheet is protecting the dielectric substrate from bending and it can also handle the weight of RDR. Port 1 is input port of antenna. Output port 2 and port 3 of feed network are connected to the feed pin 1 and 2, respectively.

Top face of dielectric substrate is attached to the bottom face of the copper metal sheet using 3M adhesive with size of 40 mm × 40 mm × 0.05 mm. Air gap between copper metal sheet and dielectric substrate is removed using 3M adhesive. Groove with volume (23.2 mm × 23.2 mm × 1 mm) is created on top side of copper metal sheet. Copper metal sheet with groove is attached to the staired RDR using silver epoxy adhesive with size of 23.2 mm × 23.2 mm × 0.06 mm . Teflon rings are used for isolating the ground plane and feed pins 1 and 2 [8]. Volume ($L_g \times W_g \times H_g$) of ground plane is 40 mm × 40 mm × 2mm. Heights of feed pin-1 and 2 are 7.5 mm. Diameter of all pins are 1.3 mm. Locations of feed pin-1 and pin-2 are (0, 7.65, 0) and (7.65, 0, 0), respectively. Thickness of dielectric substrate is 0.635 mm.

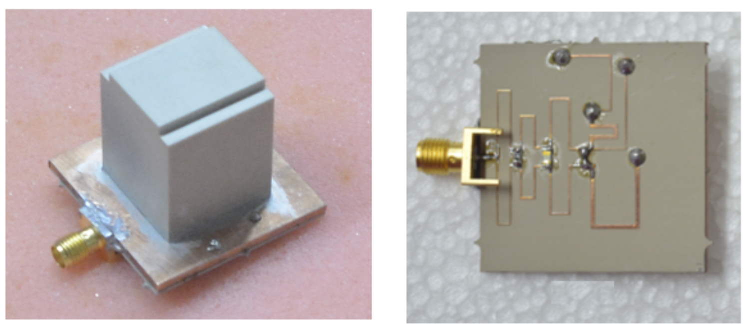

(a) (b)

Figure 3.13: (a) 3-D view and (b) bottom view of fabricated tri-band RDRA [8]

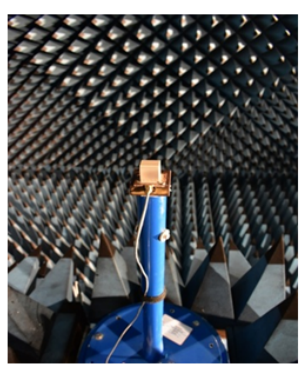

Figure 3.14: Fabricated tri-band RDRA in anechoic chamber [8]

3.3 Simulated and Measured Results

3.3.1 Tri-Band Staired Rectangular Dielectric Resonator Antenna (Two Port)

The simulated return loss at port-1 is found to be better than 13 dB for L5-band and 20 dB for L1-band as given in Figure 3.15. The measured return loss at port-1 is achieved better than 13.7 dB for L5-band and 10 dB for L1-band as shown in Figure 3.15. The simulated and measured return loss at port-2 are better than 15 dB over S-band as given in Figure 3.16. Figure 3.17 and 3.18 show simulated and measured $|S_{12}|$ and $|S_{21}|$ which are better than 13 dB for L5-band, 13 dB for L1-band and 15 dB for S-band, respectively.

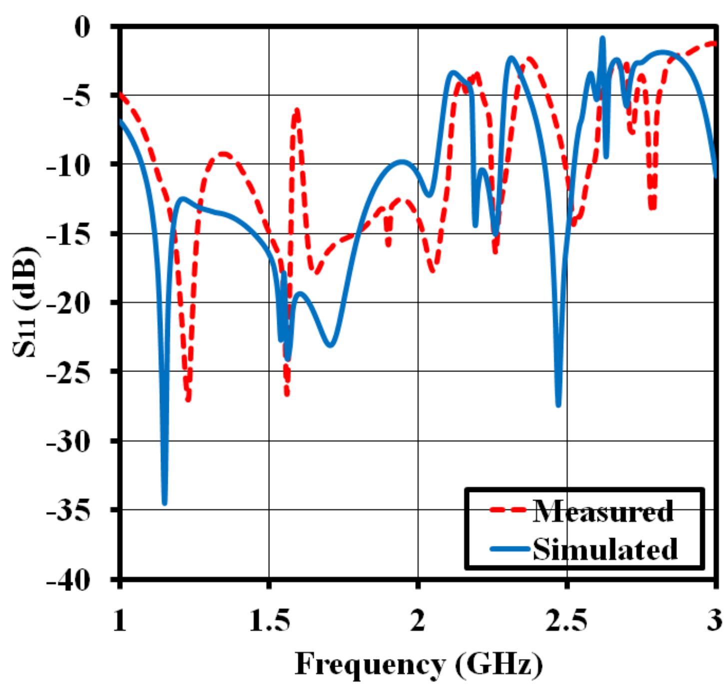

Figure 3.15: Simulated and measured S_{11} of tri-band RDRA (two port) [1]

The dielectric resonator material (dielectric constant of $\epsilon_r = 38.67$) was obtained from TCI Ceramics (Division of National Magnetics Group, Bethlehem, PA, USA). The dielectric constant of this material was measured as $\epsilon_r = 37.59$ at 5 GHz using Rectangular Dielectric Waveguide (RDWG) method [11, 12]. Simulated value of tri-band RDRA was obtained by prescribed dielectric constant $\epsilon_r = 38.67$ provided by

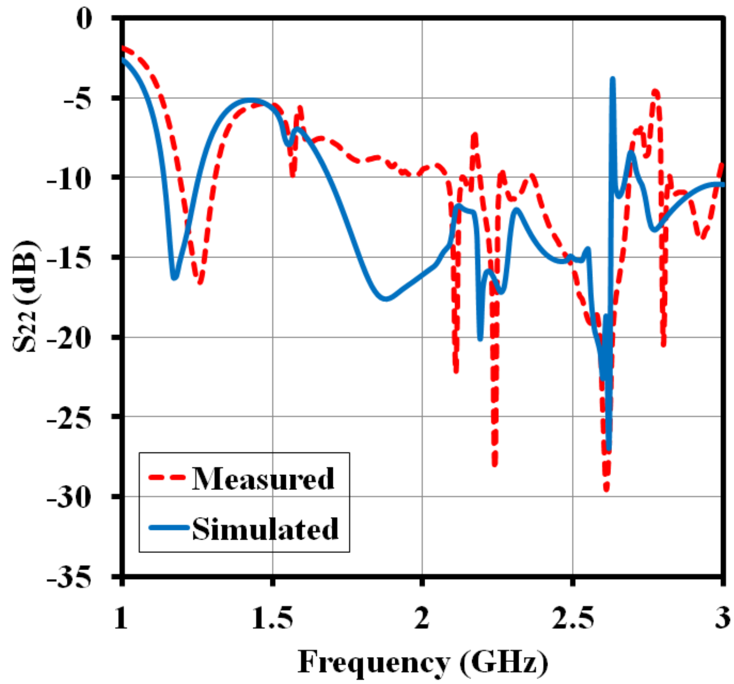

Figure 3.16: Simulated and measured S_{22} of tri-band RDRA (two port) [1]

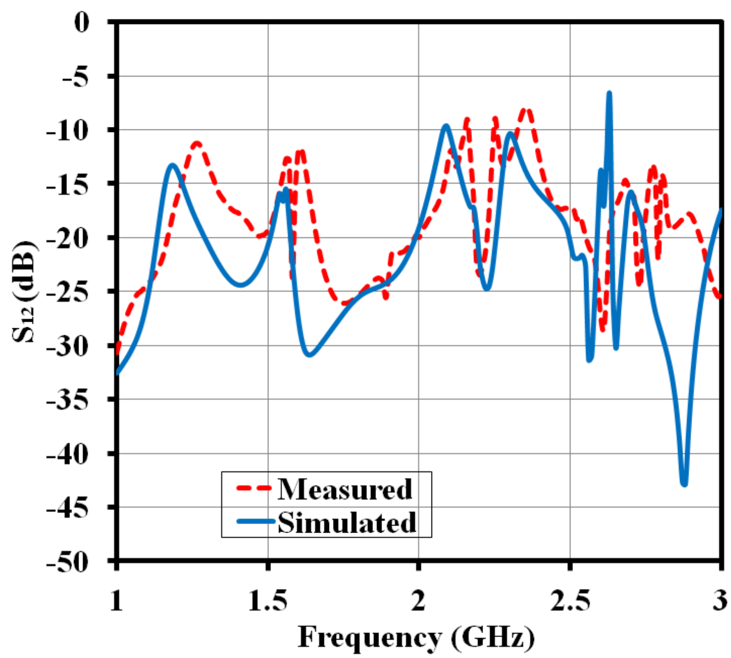

Figure 3.17: Simulated and measured S_{12} of tri-band RDRA (two port) [1]

the manufacturer of DR material. Simulated and measured return loss and isolation are matched except shift in center frequencies. This shift in center frequencies is due to difference between prescribed dielectric constant ($\epsilon_r = 38.67$) provided by the manufacturer and measured dielectric constant ($\epsilon_r = 37.59$) of DR material.

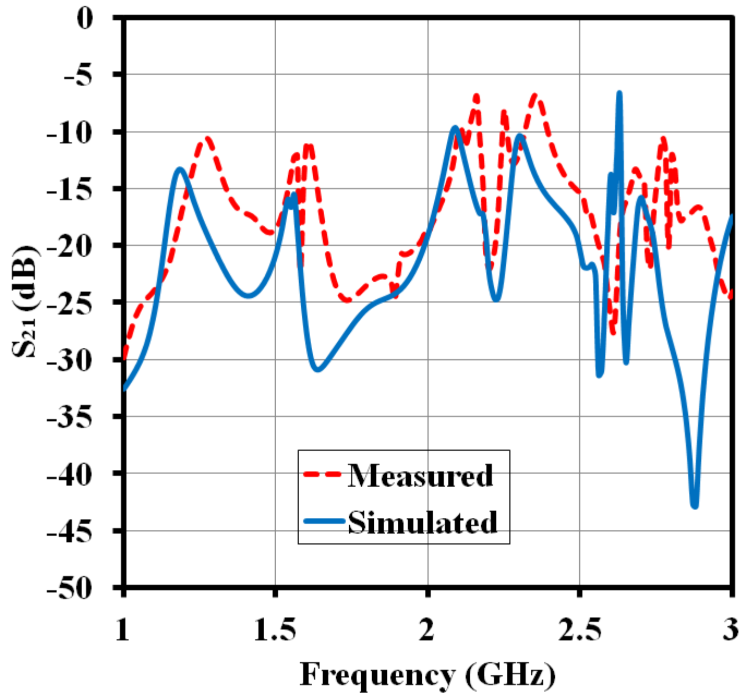

Figure 3.18: Simulated and measured S_{21} of tri-band RDRA (two port) [1]

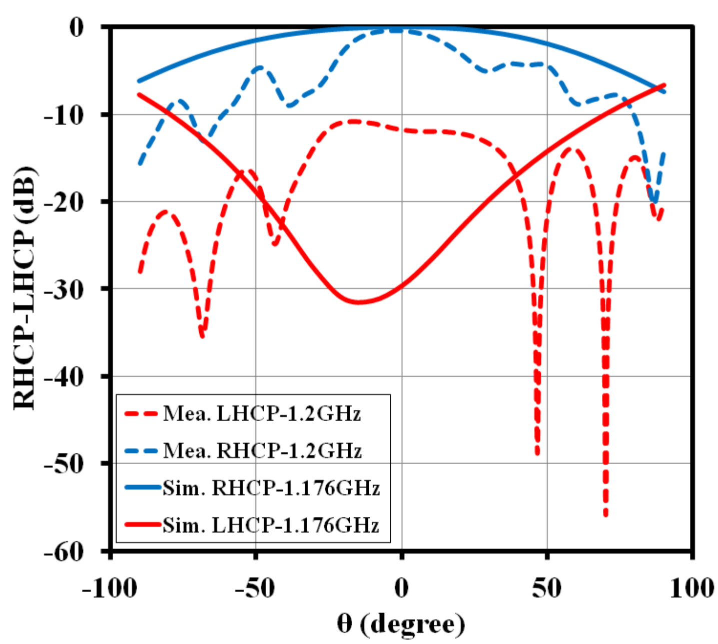

Figure 3.19: Simulated and measured RHCP-LHCP radiation patterns of tri-band RDRA at L5-band for ϕ=0° [1]

The simulated and measured RHCP-LHCP radiation patterns at ϕ=0° for L5, L1, and S-bands are given in Figures 3.19, 3.20 and 3.21, respectively. For ϕ=45°, Figures 3.22, 3.23 and 3.24 represents simulated and measured RHCP-LHCP radiation

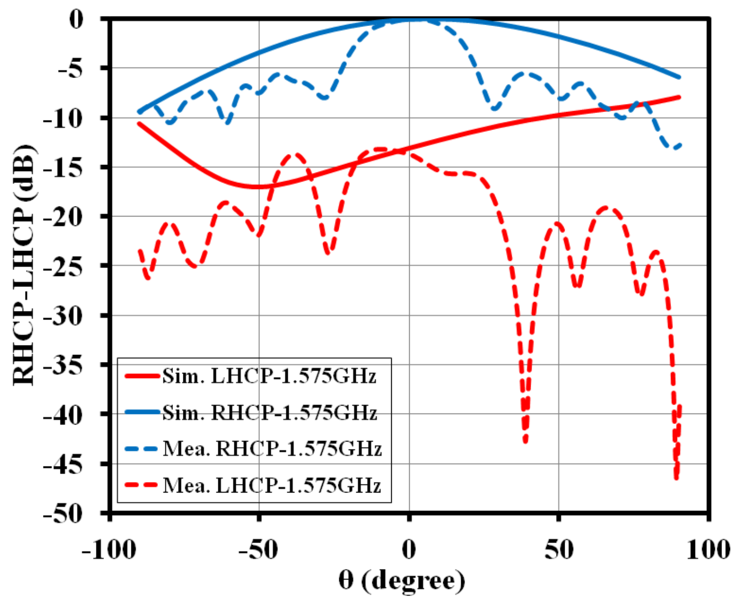

Figure 3.20: Simulated and measured RHCP-LHCP radiation patterns of tri-band RDRA at L1-band for ϕ=0° [1]

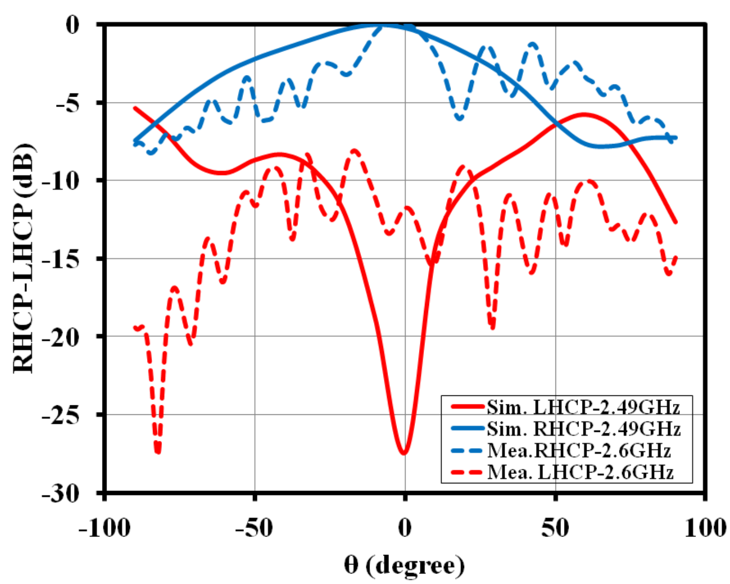

Figure 3.21: Simulated and measured RHCP-LHCP radiation patterns of tri-band RDRA at S-band for ϕ=0° [1]

patterns for L5, L1, and S-bands, respectively. The simulated and measured RHCP-LHCP radiation patterns at ϕ=90° for L5, L1, and S-bands are shown in Figures 3.25, 3.26 and 3.27, respectively.

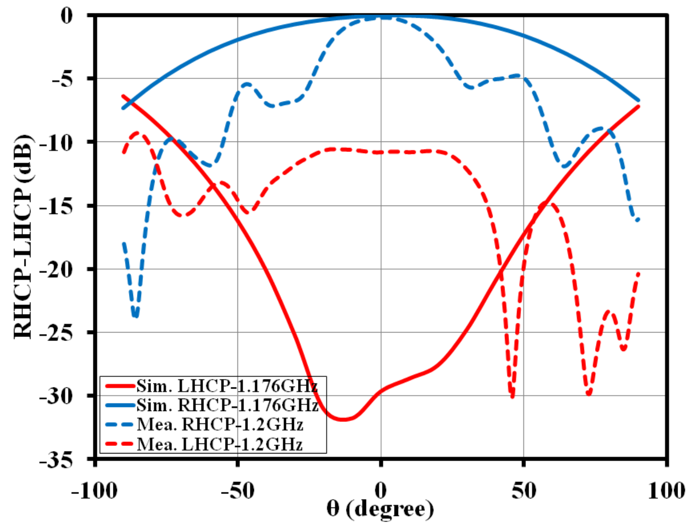

Figure 3.22: Simulated and measured RHCP-LHCP radiation patterns of triband RDRA at L5-band for ϕ=45° [1]

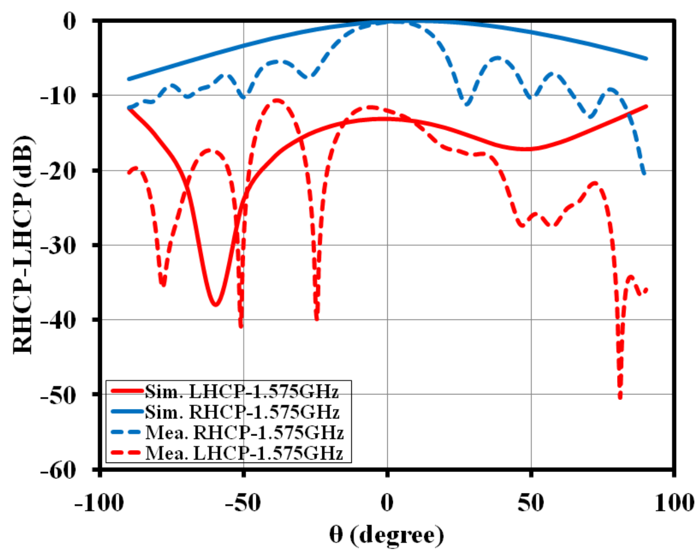

Figure 3.23: Simulated and measured RHCP-LHCP radiation patterns of tri-band RDRA at L1-band for ϕ=45° [1]

In Figures 3.19 to 3.27 and Table 3.4, L5, L1 and S-bands are shifted because of the difference between prescribed dielectric constant $\epsilon_r = 38.67$ and measured dielectric constant $\epsilon_r = 37.59$. RHCP-LHCP radiation patterns of tri-band RDRA achieved to be broadside directions over L5, L1 and S-bands. The reduction of Half Power Beam Width (HPBW) and multiple ripples in measured RHCP-LHCP radiation patterns are observed because of bakelite support, fixture pipe and mounting fixture in an anechoic chamber (Figure 3.8).

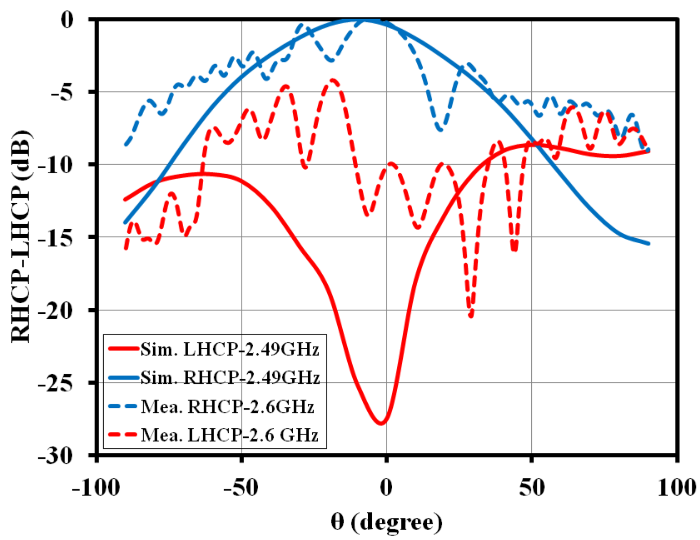

Figure 3.24: Simulated and measured RHCP-LHCP radiation patterns of tri-band RDRA at S-band for ϕ=45° [1]

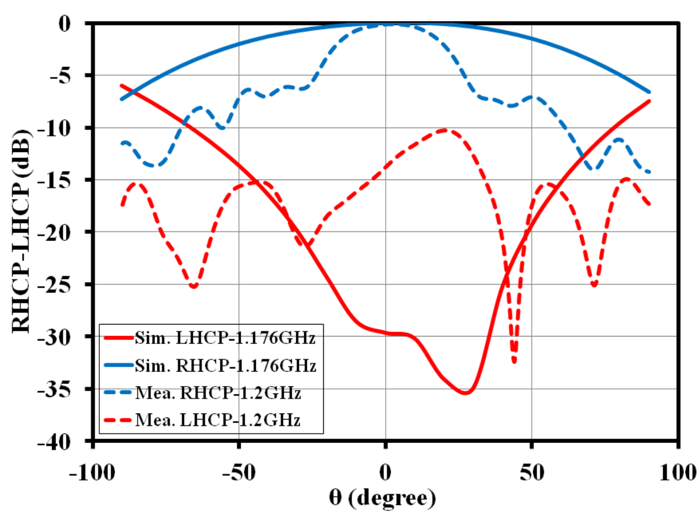

Figure 3.25: Simulated and measured RHCP-LHCP radiation patterns of tri-band RDRA at L5-band for ϕ=90° [1]

The simulated RHCP gain and axial ratio of tri-band RDRA are represented in Table 3.3. RHCP gain is the peak gain of the center frequencies of L5, L1 and S-bands. Axial ratio at $\theta = 0°$ to $\pm 60°$ is lower than 3 dB over L5, L1 and S-bands. For L5, L1 and S-bands, simulated and measured parameters (gain, axial ratio) of tri-band RDRA are shown in Table 3.4. In tri-band RDRA, simulated and measured parameters (gain, axial ratio) are mismatched due to errors introduced by bakelite support, mounting fixture and fixture pipe in anechoic chamber (Figure 3.8).

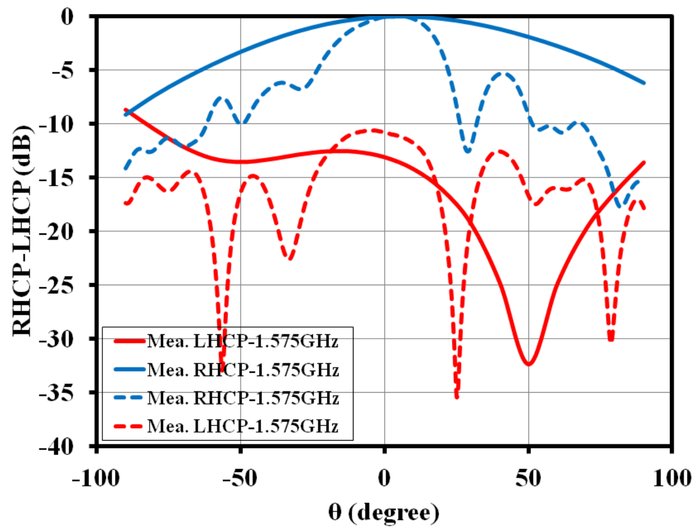

Figure 3.26: Simulated and measured RHCP-LHCP radiation patterns of tri-band RDRA at L1-band for ϕ=90° [1]

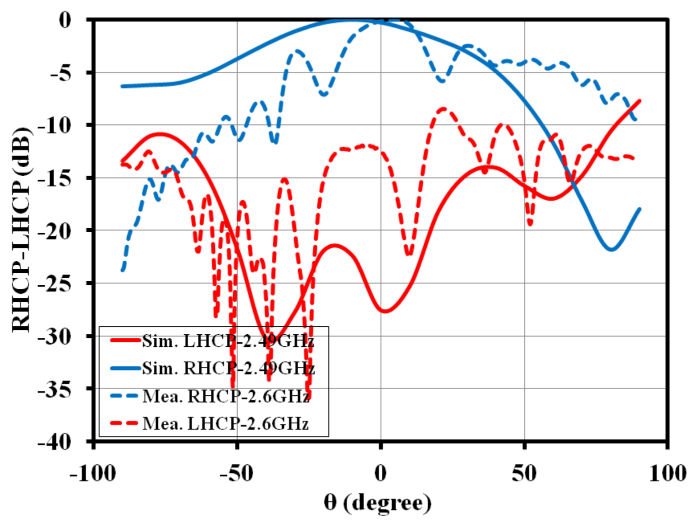

Figure 3.27: Simulated and measured RHCP-LHCP radiation patterns of tri-band RDRA at S-band for ϕ=90° [1]

Table 3.3: Simulated RHCP gain and axial ratio of tri-band RDRA [1]

Design Parameters	**L5-Band**	**L1-Band**	**S-Band**
RHCP Gain at $\theta = 0°$	2.0 dB	1.9 dB	2.0 dB
RHCP Gain at $\theta = \pm 60°$	-1.8 dB	-1.5 dB	-1.6 dB
RHCP Gain at $\theta = \pm 70°$	-2.7 dB	-2.7 dB	-2.7 dB
RHCP Gain at $\theta = \pm 80°$	-4.1 dB	-3.9 dB	-3.9 dB
Axial Ratio at $\theta = 0°$ to $\pm 60°$	$<$ 3.0 dB	$<$ 3.0 dB	$<$ 3.0 dB

Table 3.4: Simulated and measured gain and axial ratio of tri-band RDRA [1]

Frequency (GHz)	Simulated Gain (dB)	Measured Gain (dB)	Simulated AR (dB)	Measured AR (dB)
1.164	1.00	0.61	2.25	6.29
1.176	2.00	2.75	1.60	4.18
1.118	1.00	4.14	2.80	2.35
1.200	0.60	4.50	3.50	1.20
1.565	0.90	2.01	2.85	7.02
1.575	1.90	2.91	2.00	5.08
1.585	0.89	2.59	2.80	0.91
2.600	1.00	2.00	2.20	2.40

3.3.2 Tri-Band Staired Rectangular Dielectric Resonator Antenna (Single Port)

The simulated and measured return loss of tri-band RDRA are shown in Figure 3.28. Simulated $|S_{11}|$ is found to be better than 12 dB over L5-, L1- and S-bands. The measured $|S_{11}|$ of tri-band RDRA is shifted to higher frequency as shown in Figure 3.28.

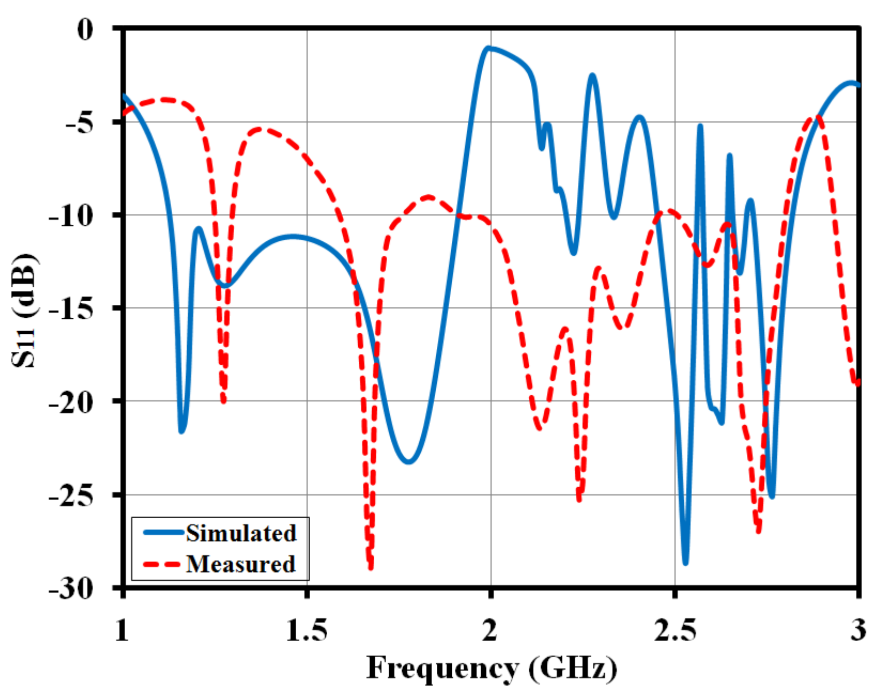

Figure 3.28: Simulated and measured S_{11} of tri-band RDRA (single port) [8]

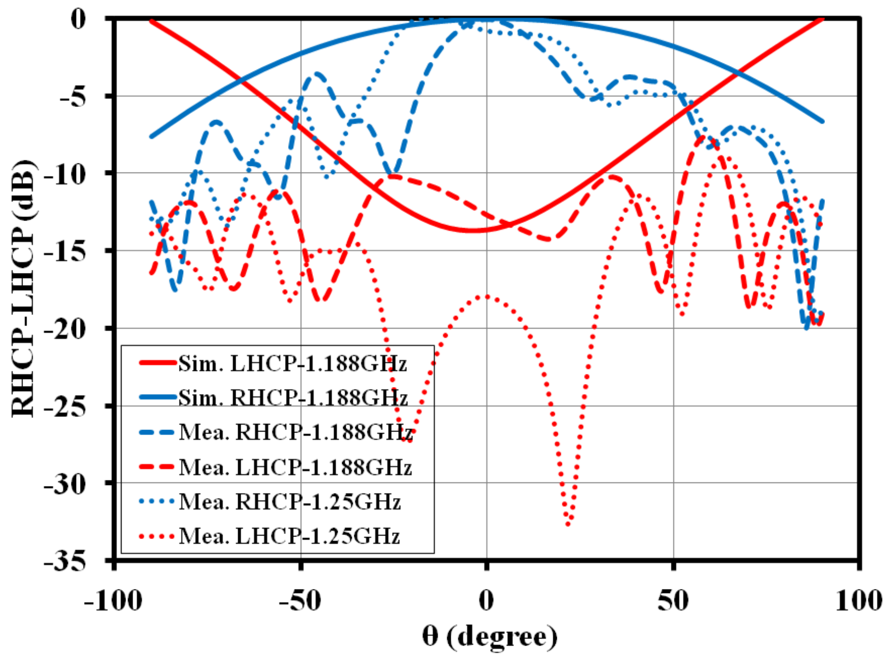

Figure 3.29: Simulated and measured RHCP-LHCP radiation patterns at L5-band for ϕ=0° of tri-band RDRA (single port) [8]

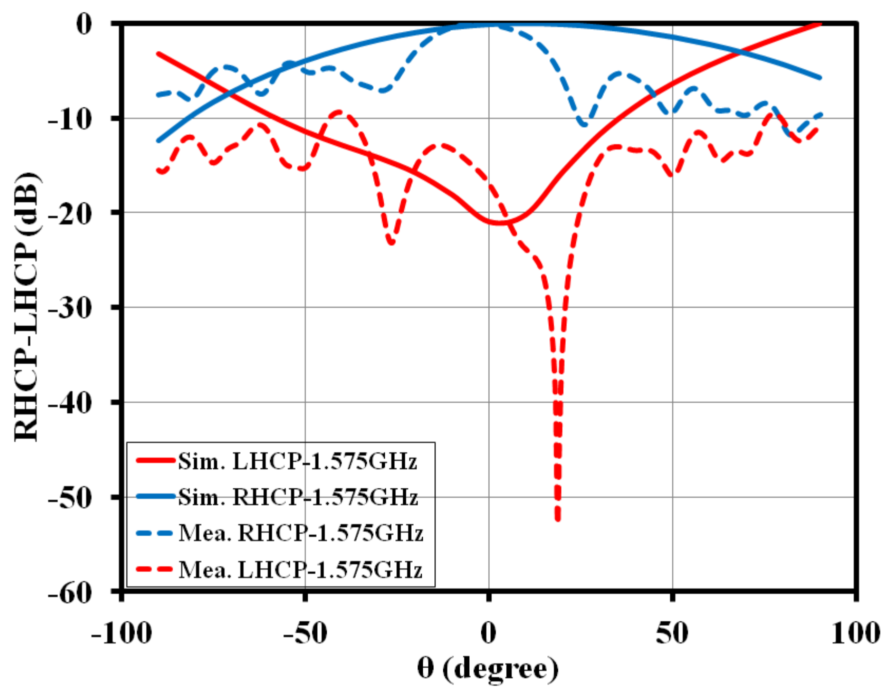

Figure 3.30: Simulated and measured RHCP-LHCP radiation patterns at L1-band for ϕ=0° of tri-band RDRA (single port) [8]

The dielectric resonator material (dielectric constant of $\epsilon_r = 51.92$) was obtained from TCI Ceramics (Division of National Magnetics Group, Bethlehem, PA, USA).

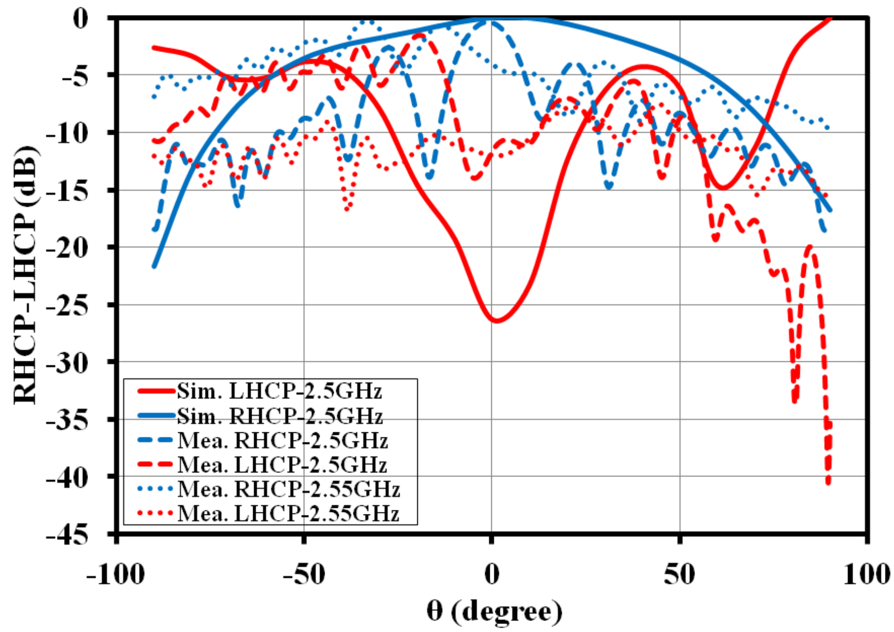

Figure 3.31: Simulated and measured RHCP-LHCP radiation patterns at S-band for ϕ=0° of tri-band RDRA (single port) [8]

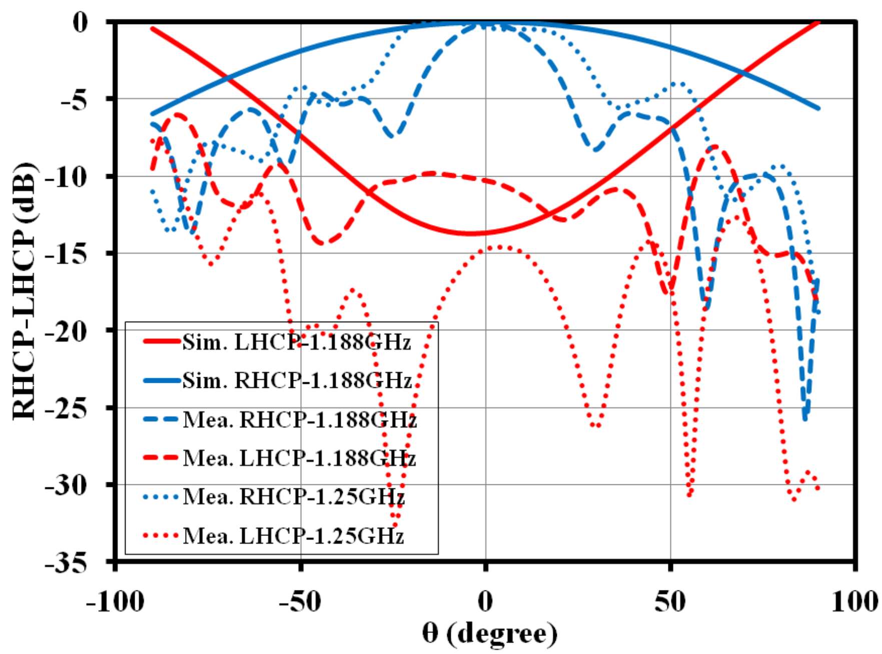

Figure 3.32: Simulated and measured RHCP-LHCP radiation patterns at L5-band for ϕ=45° of tri-band RDRA (single port) [8]

The dielectric constant of this material was measured as $\epsilon_r = 47.35$ at 5 GHz using RDWG method [11, 12]. Simulated value of tri-band RDRA was obtained by prescribed dielectric constant $\epsilon_r = 51.92$ provided by the manufacturer of DR material.

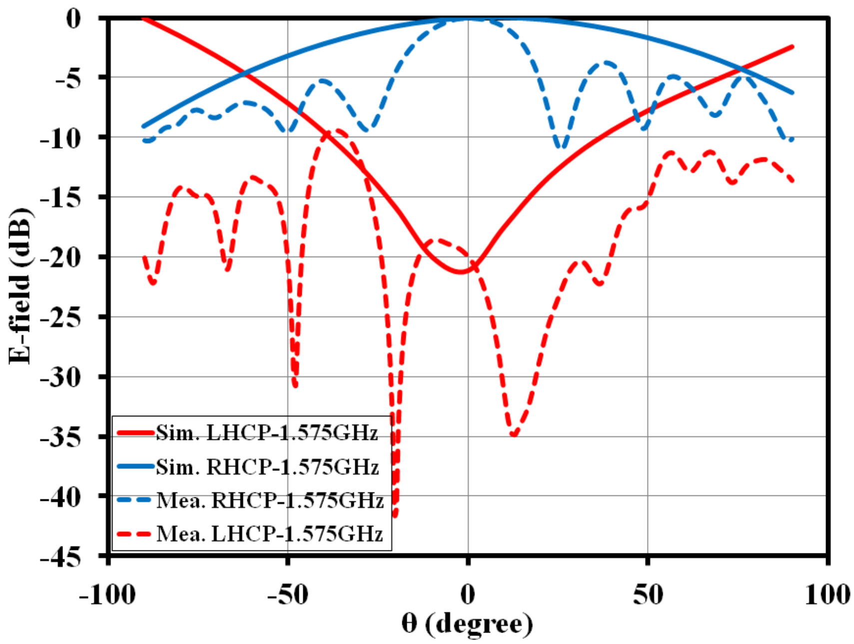

Figure 3.33: Simulated and measured RHCP-LHCP radiation patterns at L1-band for ϕ=45° of tri-band RDRA (single port) [8]

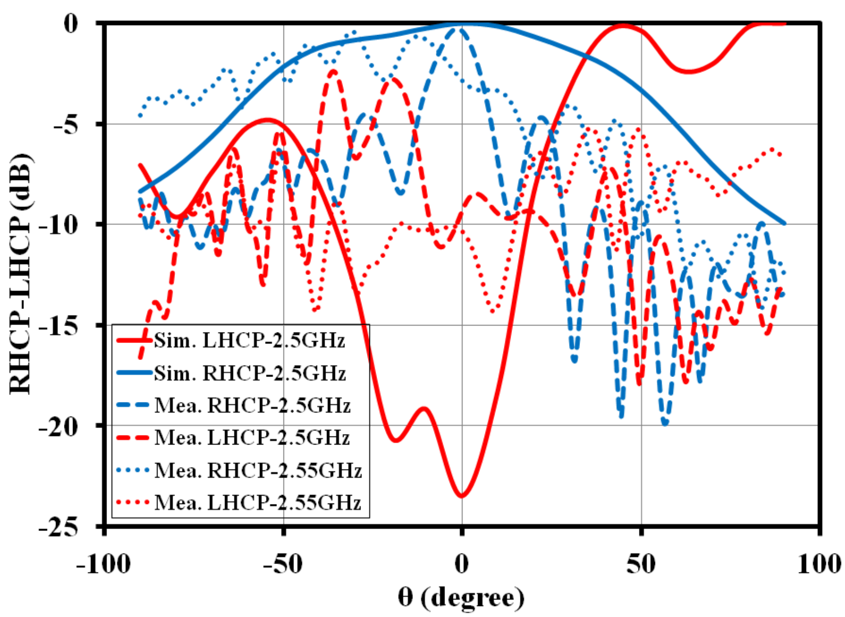

Figure 3.34: Simulated and measured RHCP-LHCP radiation patterns at S-band for ϕ=45° of tri-band RDRA (single port) [8]

The simulated and measured return loss are matched except shift in center frequencies. This shift in center frequencies is due to difference between prescribed dielectric constant ($\epsilon_r = 51.92$) provided by the manufacturer and measured dielectric constant ($\epsilon_r = 47.35$) of DR material.

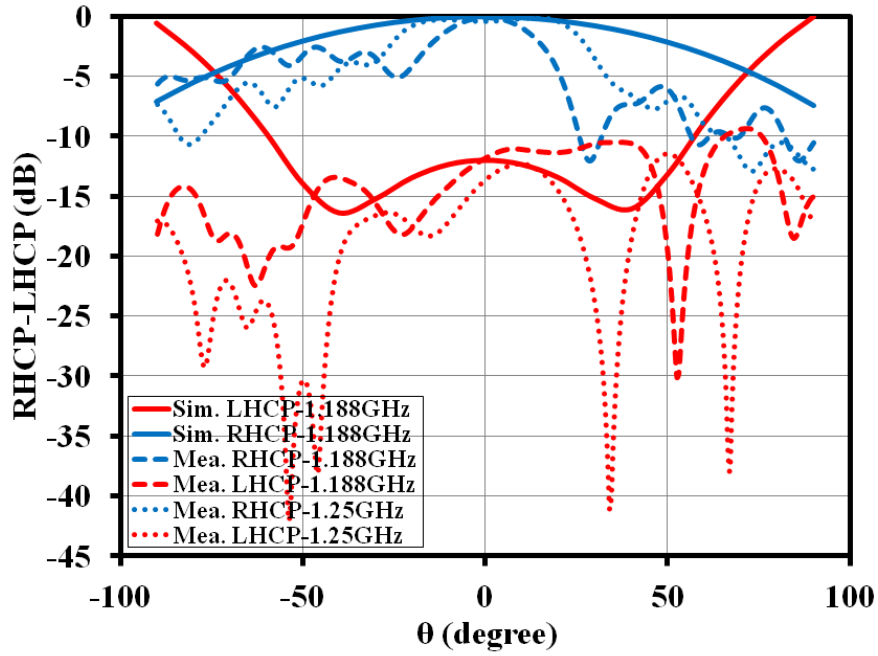

Figure 3.35: Simulated and measured RHCP-LHCP radiation patterns at L5-band for ϕ=90° of tri-band RDRA (single port) [8]

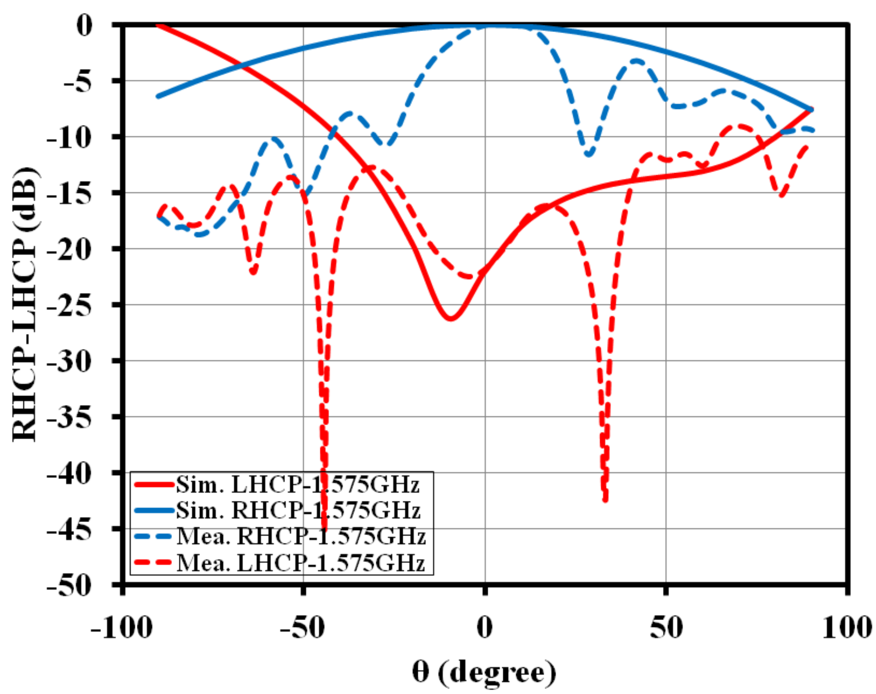

Figure 3.36: Simulated and measured RHCP-LHCP radiation patterns at L1-band for ϕ=90° of tri-band RDRA (single port) [8]

Simulated and measured RHCP-LHCP radiation patterns at ϕ=0° for L5, L1, and S-bands are given in Figures 3.29, 3.30 and 3.31, respectively. For ϕ=45°, Figures

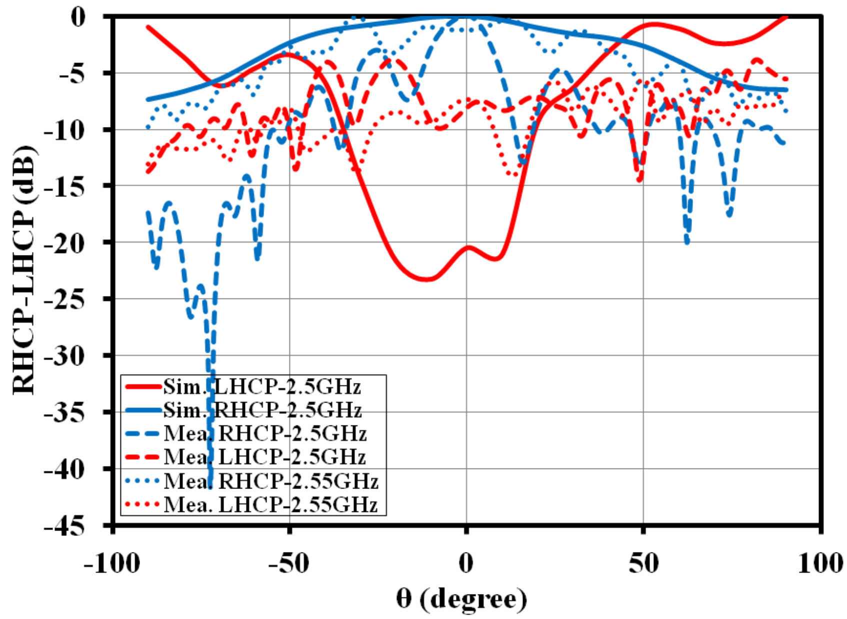

Figure 3.37: Simulated and measured RHCP-LHCP radiation patterns at S-band for ϕ=90° of tri-band RDRA (single port) [8]

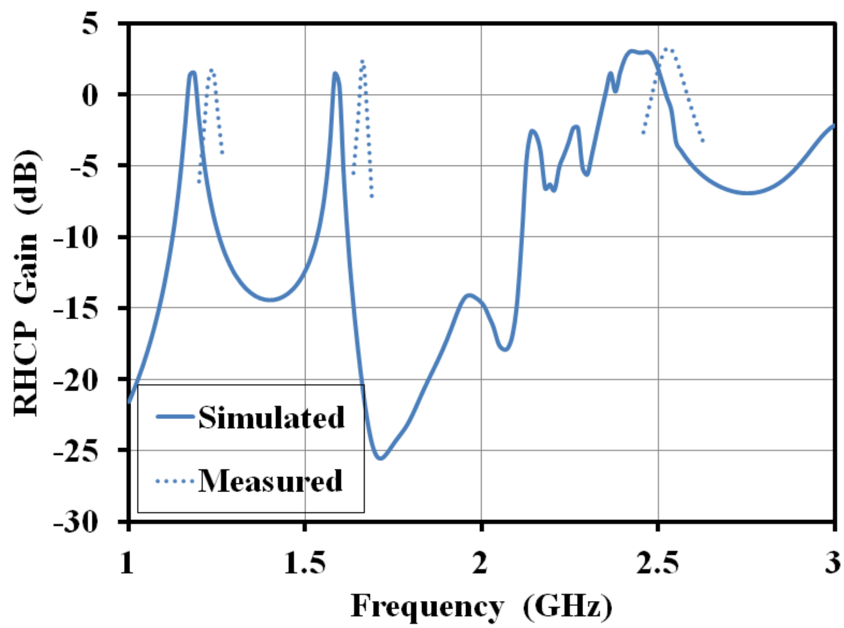

Figure 3.38: Simulated and measured RHCP gain of tri-band RDRA (single port)

3.32, 3.33 and 3.34 represents simulated and measured RHCP-LHCP radiation patterns for L5, L1, and S-bands, respectively. Simulated and measured RHCP-LHCP radiation patterns at ϕ=90° for L5, L1, and S-bands are shown in Figures 3.35, 3.36 and 3.37, respectively. In Figure 3.38, simulated and measured RHCP gain are shown. Simulated and measured axial ratio are given in Figure 3.39.

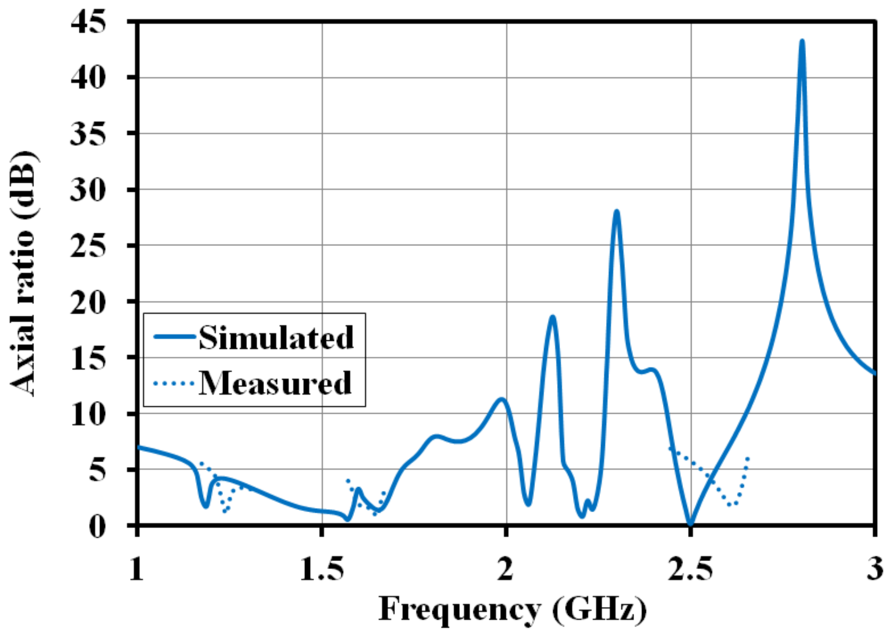

Figure 3.39: Simulated and measured axial ratio of tri-band RDRA (single port)

In Figures 3.28 to 3.39, L5, L1 and S-bands are shifted because of difference between prescribed dielectric constant $\epsilon_r = 51.92$ and measured dielectric constant $\epsilon_r = 47.35$. RHCP-LHCP radiation patterns of tri-band RDRA was achieved in broadside directions over L5, L1 and S-bands. Reduction of HPBW and multiple ripples in measured RHCP-LHCP radiation patterns are observed because of bakelite support, fixture pipe and mounting fixture in an anechoic chamber (Figure 3.14). In tri-band RDRA, simulated and measured parameters (gain and axial ratio) are mismatched due to errors introduced by bakelite support, mounting fixture and fixture pipe in anechoic chamber (Figure 3.14). Simulated return loss, RHCP gain and axial ratio of tri-band RDRA are shown in Table 3.5.

Table 3.5: Simulated return loss, RHCP gain and axial ratio of tri-band RDRA [7]

Design Parameters	**L5-Band**	**L1-Band**	**S-Band**
Return Loss (RL)	>10.0 dB	>10.0 dB	>10.0 dB
RHCP Gain at $\theta = 0°$	1.3 dB	1.1 dB	1.1 dB
RHCP Gain at $\theta = \pm 60°$	-1.5 dB	-3.0 dB	-4.4 dB
RHCP Gain at $\theta = \pm 70°$	-2.7 dB	-4.4 dB	-7.1 dB
RHCP Gain at $\theta = \pm 80°$	-4.0 dB	-6.0 dB	-10.7 dB
Axial Ratio (AR) at $\theta = 0°$ to $\pm 50^0$	$<$ 3.0 dB	$<$ 3.0 dB	$<$ 3.0 dB

3.4 Conclusions and Discussion of Results

Table 3.6 shows comparison of tri-band RDRA (two port) and tri-band RDRA (single port) with published research work. Ground plane areas of tri-band RDRA (two port) and tri-band RDRA (single port) are much lower than published research work. Radiated areas of tri-band RDRA (two port) and tri-band RDRA (single port) are much lower than published research work. Compact tri-band RDRA (two port) and tri-band RDRA (single port) are designed, analyzed, fabricated and tested for IRNSS and GAGAN applications. Simulated return loss, radiation patterns, RHCP gain, axial ratio of tri-band RDRA (two port) and tri-band RDRA (single port) are as per required specifications. Measured return loss, radiation patterns, gain, and axial ratio of tri-band RDRA (two port) and tri-band RDRA (single port) are found to be in close agreement with simulated results considering inaccuracy in the knowledge of dielectric constant of DR material and errors due to mounting fixture in an anechoic chamber.

Table 3.6: Comparison of tri-band RDRA (two port) and tri-band RDRA (single port) with published research work

Reference	**[13]**	**[14]**	**[15]**	**Our work (two port)**	**Our work (one port)**
Antenna type	Hybrid DRA	Hybrid DRA	DRA	DRA	DRA
Shape of DR	Hexagonal DR	Cylindrical DR	Cylindrical cone DR	**Staired RDR**	**Staired RDR**
Feed	Microstrip line	Axial probe	Hybrid ring	**Dual section WPD, WPD with phase shifter**	**Tri-section WPD with phase shifter**
ϵ_r **of DR**	9.9	9.8	9.8	**38.67**	**51.92**
ϵ_r **of substrate**	3.5	-	4.4	**10.2**	**10.2**
Mode	TM_{11}, TE_{111}, quasi-TM_{21}, quasi-TE_{111}	-	$HEM_{11\delta}$	TE^y_{111}, TE^y_{113}, TE^y_{112}	TE^y_{111}, TE^y_{113}, TE^y_{112}
Polarization	LHCP, RHCP	RHCP, LHCP	RHCP	RHCP	RHCP
Radiation pattern	Broadside	Omni-directional	Broadside	Broadside	Broadside
f_1 **(GHz)** f_2 **(GHz)** f_3 **(GHz)**	1.865 2.670 3.645	1.937 2.45 3.51	1.176 1.227 1.575	1.176 1.575 2.49	1.176 1.575 2.49
Ground plane area (λ_0^2) **at** f_1	0.2200	0.1020	0.0841	**0.0256**	**0.0256**
Radiator area (λ_0^2) **of DRA**	0.0480	0.0900	0.0441	**0.0112**	**0.0083**
Height (λ_0) **of DRA**	0.150	0.145	0.200	**0.140**	**0.110**
RL at f_1 **RL at** f_2 **RL at** f_3 **(RL in dB)**	17 20 18	29 28 16	18 25 13	15 20 16	20 15 24
Gain at f_1 **Gain at** f_2 **Gain at** f_3 **(Gain in dB)**	5.0 5.3 2.4	1.2 1.6 -1.5	-1.8 -0.8 2.6	2.75 2.91 2.0	1.3 1.1 1.1
AR at f_1 **AR at** f_2 **AR at** f_3 **(AR in dB)**	1.0 0.7 1.1	1.5 0.2 1.8	1.8 1.8 1.7	1.6 2.0 2.1	2.3 0.9 0.9

References

[1] P. Chaudhary, D. K. Ghodgaonkar, S. Gupta, R. Jyoti and M. B. Mahajan, "Compact circularly polarized triband staired rectangular dielectric resonator antenna using single and dual sections WPD with phase shifter for navigational satellite applications," *Microwave and Optical Technology Letters*, vol. 62, no.5, pp. 2047-2058, May 2020.

[2] Ansys High Frequency Structure Simulator (HFSS) is a 3-D Electromagnetic (EM) simulation software for designing and simulating high-frequency electronic products such as antennas, antenna arrays, Radio Frequency (RF) or microwave components, high-speed interconnects, filters, connectors, Integrated Circuit (IC) packages and printed circuit boards. https://www.ansys.com/en-in/products/electronics/ansys-hfss

[3] X. S. Fang, C. K. Chow, K. W. Leung and E. H. Lim, "New single-/dual-mode design formulas of the rectangular dielectric resonator antenna using covariance matrix adaptation evolutionary strategy," *IEEE Antennas and Wireless Propagation Letters*, vol. 10, pp. 734-737, 2011.

[4] D. M. Pozar, "Microwave Engineering," *John Wiley & Sons, Inc*, USA, 2011.

[5] X. Wang, Z. Ma and M. Ohira, "Theory and Experiment of Two-Section Two-Resistor Wilkinson Power Divider With Two Arbitrary Frequency Bands," *IEEE Transactions on Microwave Theory and Techniques*, vol. 66, no. 3, pp. 1291-1300, March 2018.

[6] R. Han, S. Zhong and J. Liu, "Design of circularly-polarized dielectric resonator antenna with wideband feed network," *Proceedings of 2014 3rd Asia-Pacific Conference on Antennas and Propagation*, Harbin, 2014, pp. 48-50.

[7] S.Y.Eom and H.K.Park, "New switched-network phase shifter with broadband characteristics," *Microwave and Optical Technology Letters*, vol. 38, no. 4, pp. 255-257, August 2003.

[8] P. Chaudhary, D. K. Ghodgaonkar, S. Gupta, R. Jyoti and M. B. Mahajan, "Minaturized tri-band circularly polarized staired rectangular dielectric resonator antenna for navigational satellite applications," will be submitted to *International Journal of Microwave and Optical Technology*, 2021.

[9] M. Chongcheawchamnan, S. Patisang, M. Krairiksh and I. D. Robertson, "Tri-band Wilkinson power divider using a three-section transmission-line transformer," *IEEE Microwave and Wireless Components Letters*, Vol. 16, No. 8, pp. 452-454, 2006.

[10] M. Chongcheawchamnan, S. Patisang, S. Srisathit, R. Phromloungsri and S. Bunnjaweht, "Analysis and design of a three-section transmission line transformer," *IEEE Transactions on Microwave Theory and Techniques*, Vol. 53, No. 7, pp. 2458-2462, July 2005.

[11] R. Vashisth, D. Ghodgaonkar and S. Gupta,"Design and Fabrication of Broadband Microwave Absorber using FSS embedded in CISR sheets," *2018 IEEE MTT-S International Microwave and RF Conference (IMaRC)*, Kolkata, India, Dec 2018, pp. 1-4.

[12] Z. Abbas, R.D. Pollard and R.W. Kelsall, "Complex permittivity measurements at Ka-band using rectangular dielectric waveguide," *IEEE Transactions on Instrumentation and Measurement*, Vol.50, no. 5, pp. 1334-1342, October 2001.

[13] A. Altaf and M. Seo, "Triple-band dual-sense circularly polarized hybrid dielectric resonator antenna," *sensors*, Vol. 18, no. 11:3899, pp. 1-14, Nov. 2018.

[14] C. Cheng, F. Zhang, Y. Yao, and F. Zhang, "Triband omnidirectional circularly polarized dielectric resonator antenna with top-loaded alford loop," *International Journal of Antennas and Propagation*, Vol. 2014, no. 797930, pp. 1-7, 2014.

[15] H. N. Bich, H. C. Ba and C. D. Ngoc, "All GPS bands dielectric resonator antenna with circular polarization for GPS application," *The 2012 International Conference on Advanced Technologies for Communications*, Hanoi, 2012, pp. 65-68.

Chapter 4

Compact Circularly Polarized Dual-Band Rectangular Dielectric Resonator Antenna

4.1 Introduction

A compact dual-band (L5 and L1-bands) Circularly Polarized (CP) Rectangular Dielectric Resonator Antenna (RDRA) is designed, analyzed, fabricated and tested [1]. Right Hand Circular Polarization (RHCP) of dual-band CP RDRA was generated using novel design feed network of dual-section WPD with wide-band 90° phase shifter for L5 and L1-bands. Miniaturized ground plane area 40 mm × 40 mm of dual-band RDRA is achieved using high dielectric constant (ϵ_r= 51.92) of Dielectric Resonator (DR) material and high dielectric constant (ϵ_r = 10.2) of dielectric substrate (Rogers RO3210). The TE^y_{111} and TE^y_{113} modes of dual-band DRA are produced at 1.176 GHz and 1.575 GHz, respectively [1].

Single geometry Rectangular DR (RDR) generates dual-mode which gives broadside radiation patterns over L5 and L1-bands. Volume of RDR was reduced to 24.2 mm × 24.2 mm × 26.2 mm using high dielectric constant (ϵ_r= 51.92) of DR material [1]. Compact dual-band RDRA consists of RDR, dual-section WPD with wide-band 90° phase shifter, dielectric substrate, copper metal sheet ground plane, 3M adhesive, silver epoxy adhesive and feeding probes [1]. Design specifications of dual-band RDRA at L5 and L1-bands are given in Table 1.1. Simulated and measured parameters of dual-band RDRA are $|S_{11}|$, RHCP-LHCP radiation patterns, RHCP gain and axial ratio [1]. The design steps of dual-band RDRA are similar to section 3.1.2.

4.2 Geometry and Excitation of Dual-Band Rectangular Dielectric Resonator Antenna

4.2.1 Geometry of Dual-Band Rectangular Dielectric Resonator Antenna

Front view and bottom view of dual-band CP RDRA are depicted in Figures 4.1 and 4.2, respectively [1]. Figure 4.3 presents the 3-D views of dual-band CP RDRA. The optimized dimensions of RDR are obtained width W=24.2 mm, length L=24.2 mm and height H=26.2 mm using dual-mode design of equations (3.1) to (3.12) using DWM with CMA-ES by assuming $\frac{H}{L}$ = 1.08, $\frac{W}{L}$ = 1.0, ϵ_r= 51.92, f_1=1.176 GHz and f_2=1.575 GHz [2].

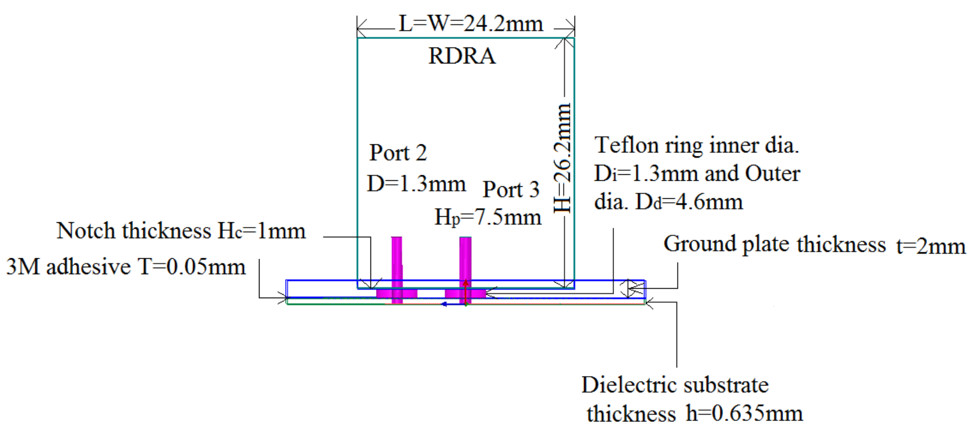

Figure 4.1: Front view of dual-band RDRA [1]

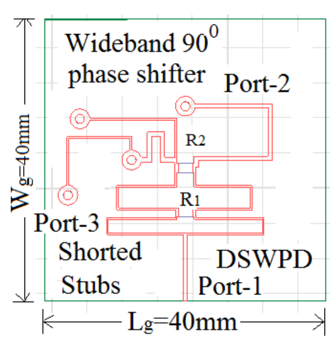

Figure 4.2: Bottom view of dual-band RDRA [1]

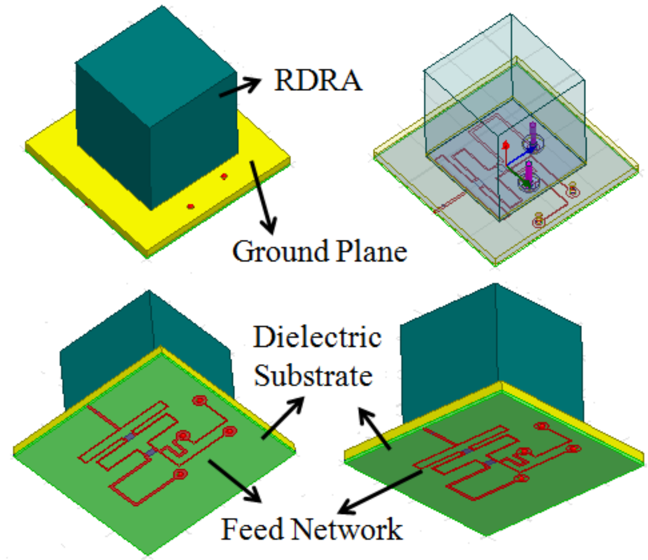

Figure 4.3: 3-D geometry views of dual-band RDRA [1]

4.2.2 Dual-Section Wilkinson Power Divider with Phase Shifter

Dual-section WPD with wide-band 90° phase shifter is represented as feed network in Figure 4.4 [1]. Characteristic impedances Z_1, Z_2, Z_3, Z_4, Z_5 and resistances R_1, R_2 are calculated using equations (3.24) to (3.31) [3, 4, 5]. Z_1, Z_2, Z_3, Z_4 are characteristic impedances of quarter wavelength transmission lines [3, 4]. Z_5 is characteristic impedance of half wavelength transmission line [4]. The values of absorption resistances are R_1=110 Ω and R_2=150 Ω [1]. Half-power division of dual-section WPD in L5 and L1-bands is achieved by Z_1, Z_2, R_1 and R_2 at port-2 and port-3. In dual-section WPD, 90° phase shift is obtained by Z_4 and Z_5. Two short stubs Z_3 are required for smooth phase change over wide-band and impedance matching. The optimized design dimensions of dual-section WPD with wide-band 90° phase shifter are shown in Table 4.1 at 1.176 GHz and 1.575 GHz.

Port-1 is input port of dual-section WPD with wide-band 90° phase shifter. Port-2 and port-3 are output ports of dual-section WPD with wide-band 90° phase shifter. The design of dual-section WPD with wide-band 90° phase shifter is verified using reference [6]. Figure 4.5 (a) depicts S-parameters of dual-section WPD with wide-band 90° phase shifter for L5 and L1-bands. Phase shift of dual-section WPD with wide-band 90° phase shifter for L5 and L1-bands is indicated in Figure 4.5 (b). $|S_{11}|$ is found to be better than 15 dB over L5 and L1-bands. $|S_{21}|$ is achieved to be better than 4 dB over L5 and L1-bands. $|S_{31}|$ is determined to be better than 4.5 dB over L5 and L1-bands. $|S_{23}|$ is obtained to be better than 20 dB over L5 and L1-bands.

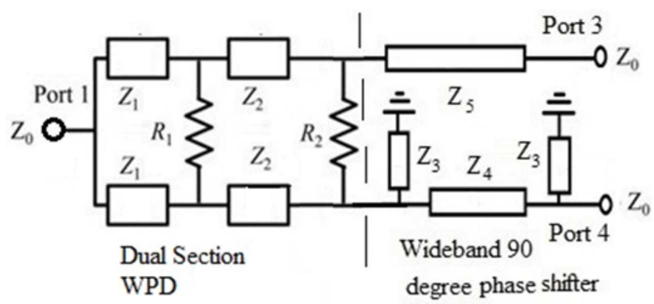

Figure 4.4: Dual-section WPD with wide-band 90° phase shifter [1]

Table 4.1: Optimized design dimensions of dual-section WPD with wide-band 90° phase shifter at 1.176 GHz and 1.575 GHz [1]

Characteristic impedance (Ω)	Length (mm)	Width (mm)
Z_1=70.70	23.00	0.25
Z_2=55.00	22.38	0.50
Z_3=76.00	20.00	0.20
Z_4=50.00	15.00	0.50
Z_5=50.00	32.80	0.70

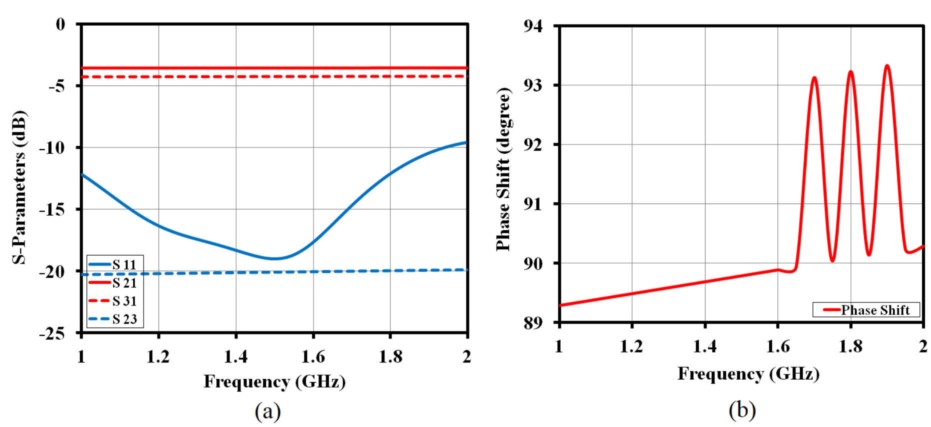

Figure 4.5: Results of feed network (a) S-parameters of dual section WPD with 90^0 phase shifter (b) phase shift of dual section WPD with 90^0 phase shifter

4.3 Electric Field Distribution

Figures 4.6 (a) depicts TE^{y}_{111} mode at 1.176 GHz in dual- band RDRA. TE^{y}_{113} mode at 1.575 GHz of dual-band RDRA is shown in Figure 4.6 (b). The TE^{y}_{111} and TE^{y}_{113} modes are recognized as $0.5\lambda_0$ and $1.5\lambda_0$ in vertical z-direction, respectively. The electric field distribution at 1.176 GHz with respect to 0° of dual-band RDRA is shown in Figure 4.7 (a).

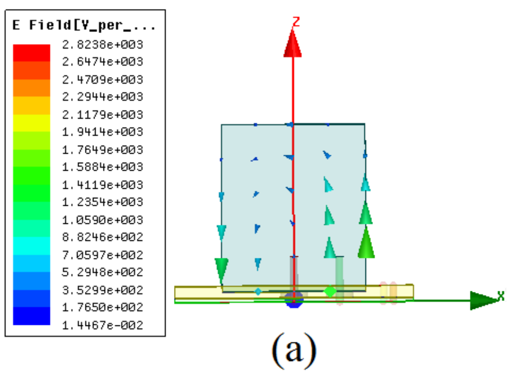

Figure 4.6: Electric field distribution of dual-band RDRA (a) TE^{y}_{111} mode at 1.176 GHz (b) TE^{y}_{113} mode at 1.575 GHz [1]

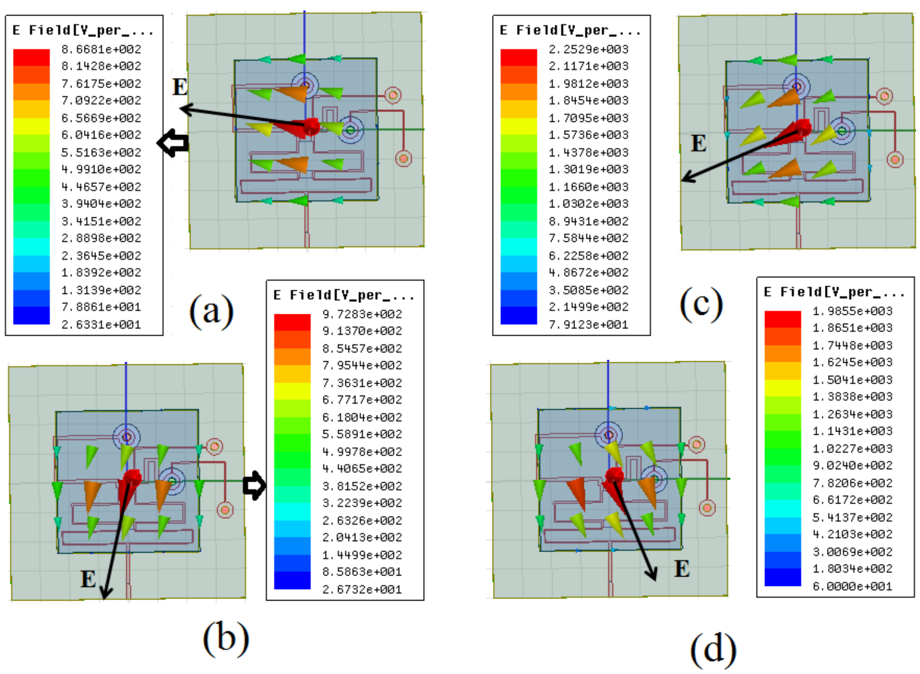

Figure 4.7: Electric field distribution of dual-band RDRA
(a) 1.176 GHz with respect to 0° (b) 1.176 GHz with respect to 90°
(c) 1.575 GHz with respect to 0° (d) 1.575 GHz with respect to 90°

In dual-band RDRA, Figure 4.7 (b) represents electric field distribution at 1.176 GHz with respect to 90°. The electric field **E** vectors at 1.176 GHz are rotated in anticlockwise direction as phase changes from 0° to 90° as shown in Figures 4.7 (a) and 4.7 (b). The electric field distribution at 1.575 GHz with respect to 0° of dual-band RDRA is given in Figure 4.7 (c). In dual-band RDRA, Figure 4.7 (d) depicts electric field distribution at 1.575 GHz with respect to 90°. Electric field **E** vectors at 1.575 GHz are rotated in anticlockwise direction as phase changes from 0° to 90° as shown in Figures 4.7 (c) and (d). The anticlockwise rotation of electric fields gives RHCP. All Electric field distributions of dual-band RDRA are verified using reference [6].

4.4 Fabrication and Testing

The dual-band RDRA consists of rectangular dielectric resonator, dielectric substrate, ground plane of copper metal plate, 3M adhesive, silver epoxy adhesive, dual-section WPD with wide-band 90° phase shifter, two feeding probes and two teflon rings. Figures 4.8 (a) and 4.8 (b) show bottom and top views of dual-band RDRA, respectively. The dual-band RDRA in the anechoic chamber is depicted in Figure 4.9. Dual-section WPD with wide-band 90° phase shifter is placed on bottom face of dielectric substrate as shown in Figure 4.8 (a). Copper is fully removed on top side of dielectric substrate. Metal sheet is used as the ground plane in this antenna. Copper metal sheet is protecting the dielectric substrate from bending and it can also handle the weight of RDR.

Top face of dielectric substrate is attached to the bottom face of the copper metal sheet using 3M adhesive with size of 40 mm × 40 mm × 0.05 mm. Air gap between copper metal sheet and dielectric substrate is removed using 3M adhesive. Groove with volume (24.2 mm × 24.2 mm × 1 mm) is created on top side of copper metal sheet. Copper metal sheet with groove is attached to the RDR using silver epoxy adhesive with size of 24.2 mm × 24.2 mm × 0.06 mm [1]. Port-1 represents input port of dual-band RDRA. Port-2 and port-3 are connected to the feeding probes 1 and 2, respectively. Volume ($L_g \times W_g \times H_g$) of ground plane is 40 mm × 40 mm × 2mm. Heights of feed pin-1 and 2 are 7.5 mm. Diameter of all pins are 1.3 mm. Locations of feed pin-1 and pin-2 are (0, 7.65, 0) and (7.65, 0, 0), respectively. Thickness of dielectric substrate is 0.635 mm.

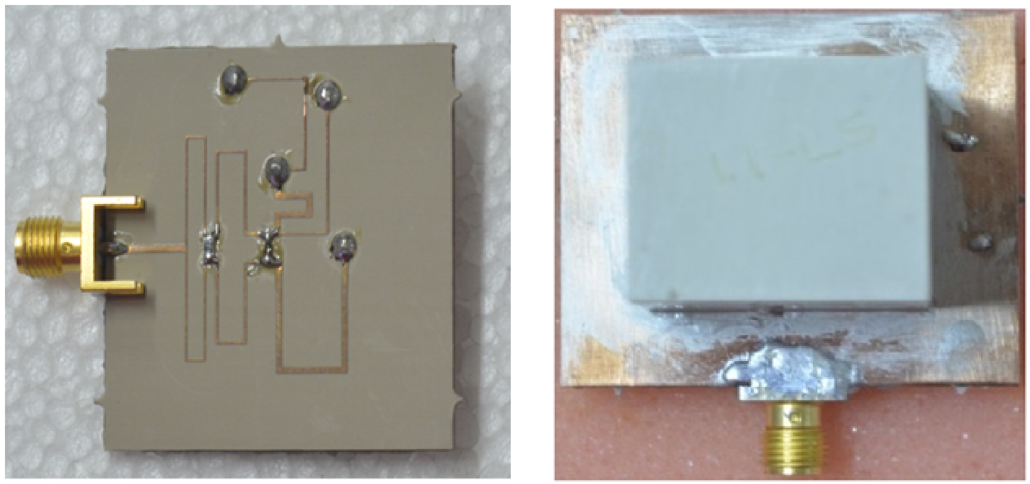

(a) (b)

Figure 4.8: Fabricated dual-band RDRA (a) bottom view (b) top view

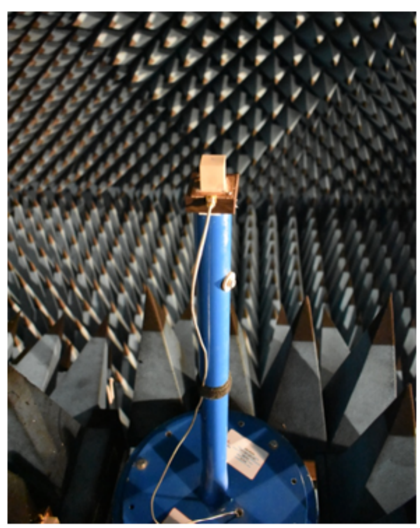

Figure 4.9: Testing of fabricated dual-band RDRA in the anechoic chamber

4.5 Simulated and Measured Results

The simulated and measured return loss of dual-band RDRA are shown in Figure 4.10. These are found to be better 10 dB over L5 and L1-bands. The dielectric resonator material ($\epsilon_r = 51.92$) was obtained from TCI Ceramics (Division of National Magnetics Group, Bethlehem, PA, USA). The dielectric constant of this material was measured as $\epsilon_r = 47.35$ at 5 GHz using RDWG method [7, 8]. The simulated and measured return loss of dual-band RDRA are matched except a slight shift in resonance frequencies. This shift in center frequencies is due to difference between prescribed dielectric constant (ϵ_r= 51.92) provided by the manufacturer and measured dielectric constant (ϵ_r= 47.35) of DR material.

The simulated and measured RHCP-LHCP radiation patterns at ϕ=0° are given in Figures 4.11 over L5 and L1-bands. For ϕ=45°, simulated and measured RHCP-LHCP radiation patterns are shown in Figure 4.12. In dual-band RDRA, Figure 4.13 clearly shows simulated and measured RHCP-LHCP radiation patterns at ϕ=90° for L5 and L1-bands. RHCP-LHCP radiation patterns are obtained broadside over L5 and L1-bands. The reduction of HPBW and multiple ripple in measured RHCP-LHCP radiation patterns are observed due to bakelite support, fixture pipe and mounting fixture in the anechoic chamber (Figure 4.9).

Figure 4.14 shows simulated and measured RHCP gain of dual-band RDRA for L5 and L1-bands. Simulated and measured axial ratio of dual-band RDRA are given in Figure 4.15. Simulated RHCP gain and axial ratio of dual-band RDRA for L5 and L1-bands are shown in Table 4.2 [6]. Measured RHCP-LHCP radiation patterns, RHCP gain and axial ratio are mismatched because of error introduced by bakelite support, fixture pipe and mounting fixture in the anechoic chamber (Figure 4.9).

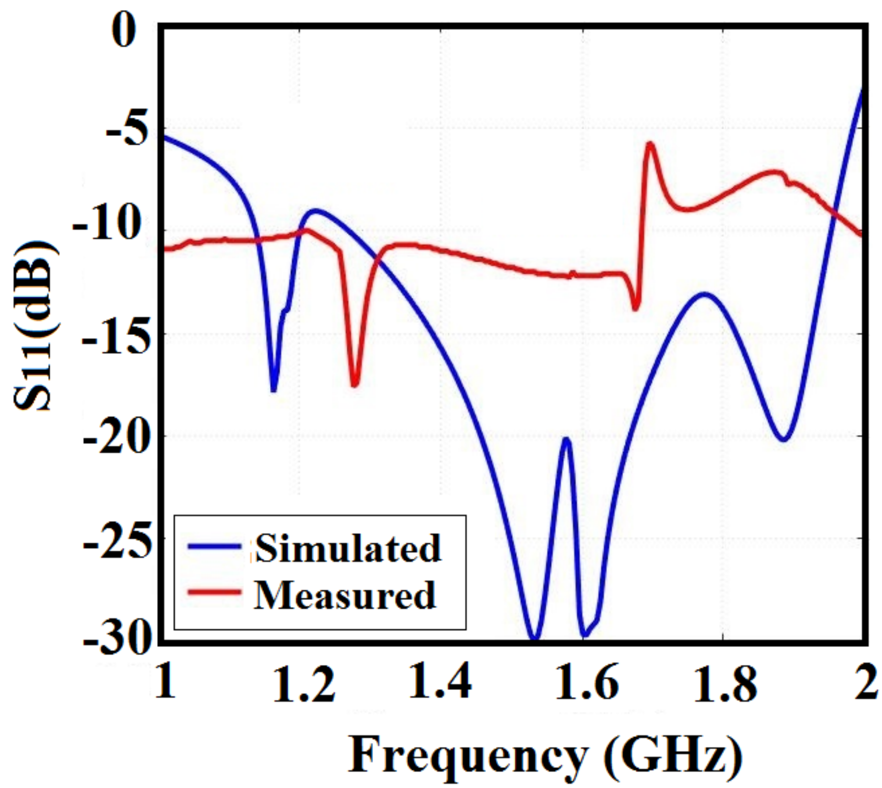

Figure 4.10: Simulated and measured return loss of dual-band CP RDRA for L5 and L1-bands [1]

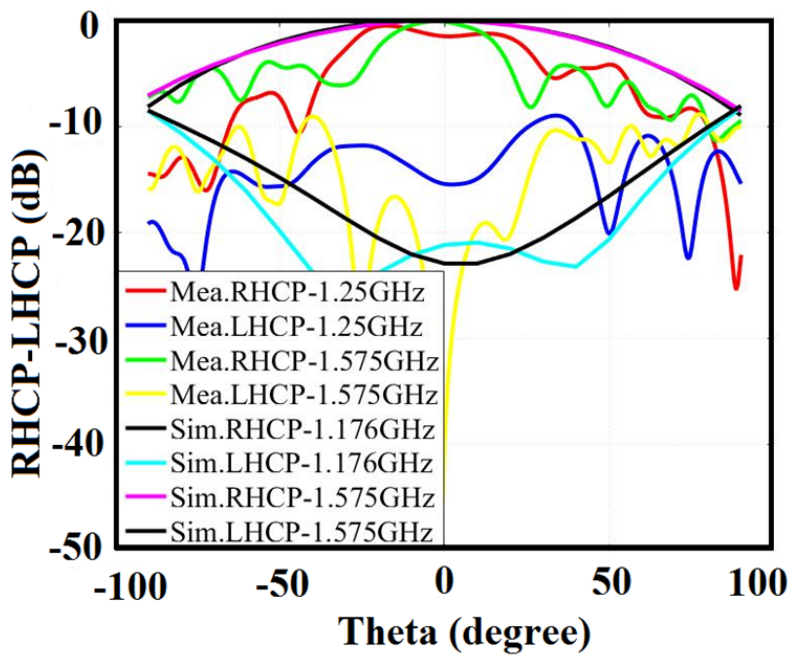

Figure 4.11: Simulated and measured RHCP-LHCP radiation patterns at L5 and L1-band of dual-band DRA for ϕ=0° [1]

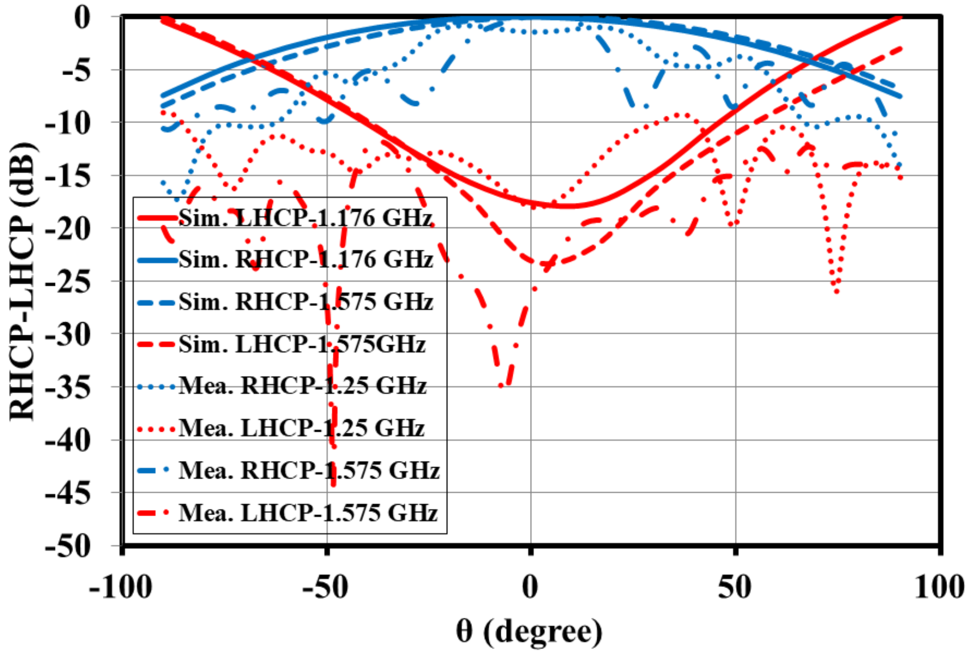

Figure 4.12: Simulated and measured RHCP-LHCP radiation patterns at L5 and L1-band of dual-band DRA for ϕ=45°

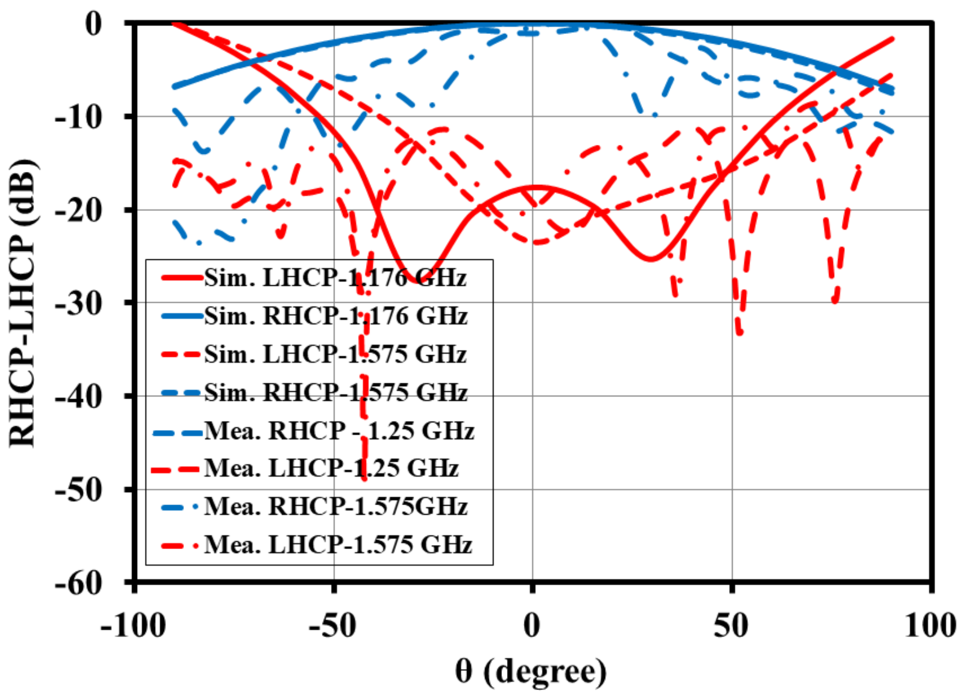

Figure 4.13: Simulated and measured RHCP-LHCP radiation patterns at L5 and L1-band of dual-band DRA for ϕ=90°

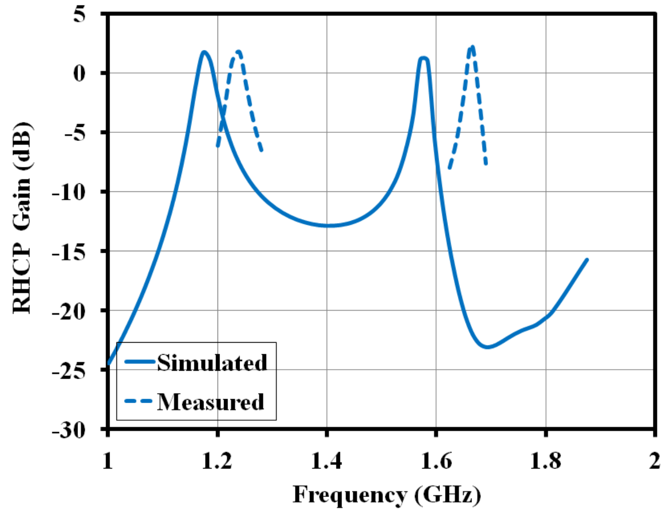

Figure 4.14: Simulated and measured RHCP gain at L5 and L1-bands of dual-band RDRA

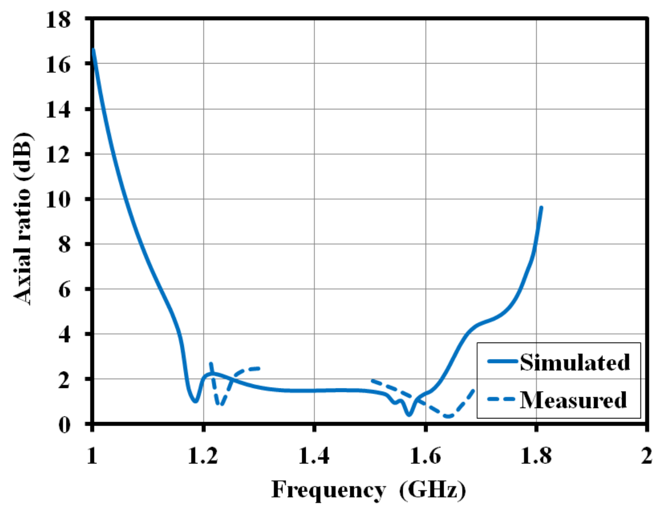

Figure 4.15: Simulated and measured axial ratio at L5 and L1-bands of dual-band RDRA

Table 4.2: Simulated RHCP gain and axial ratio of dual-band RDRA [6]

Parameters	**L5-Band**	**L1-Band**
RHCP Gain at $\theta = 0^0$	1.5 dB	1.5 dB
RHCP Gain at $\theta = \pm 60^0$	-1.3 dB	-0.9 dB
RHCP Gain at $\theta = \pm 70^0$	-2.6 dB	-2.2 dB
RHCP Gain at $\theta = \pm 80^0$	-4.12 dB	-3.7 dB
Axial Ratio at $\theta = 0^0 to \pm 55^0$	$<$ 3dB	$<$ 3 dB

4.6 Conclusion and Discussion of Results

Table 4.3 shows comparison of dual-band RDRA with published research work. The ground plane and radiated areas of dual-band RDRA are miniaturized using high dielectric constant (ϵ_r= 51.92) of DR material and high dielectric constant (ϵ_r = 10.2) of dielectric substrate (Rogers RO3210). Both Ground plane and radiated areas of dual-band RDRA are much lower than published research work. Compact dual-band RDRA is designed, analyzed, fabricated and tested. The simulated and measured results of dual-band RDRA are in closed agreement except a small shift in center frequencies. This is due to difference between prescribed dielectric constant (ϵ_r= 51.92) provided by the manufacturer and measured dielectric constant (ϵ_r= 47.35) of DR material.

Table 4.3: Comparison of dual-band RDRA with published research work

Reference	[9]	[10]	[11]	**Our work**
Antenna type	DRA	DRA	DRA	DRA
Shape of DR	RDR	RDR	Stacked RDR	RDR
Feed	Cross-slot	Apearture coupled	Cross-slot	**DSWPD with PS**
ϵ_r **of DR**	20.5	9.8	9.8	**51.92**
ϵ_r **of substrate**	2.55	2.94	4.4	**10.2**
Mode	TE^y_{111}, TE^y_{113}	TE^y_{111}, TE^y_{113}	Quasi-TE^y_{111}, TE_{113}, TE_{115}	TE^y_{111}, TE^y_{113}
Polarization	RHCP	LHCP	LHCP	RHCP
Radiation pattern	Broadside	Broadside	Broadside	Broadside
Resonance frequencies f_1 **(GHz)** f_2 **(GHz)**	1.268 1.561	1.58 2.40	1.83 2.60	1.176 1.575
Ground plane area (λ_0^2) **at** f_1	0.1790	0.7098	0.3717	**0.0256**
Radiator area (λ_0^2) **of DRA**	0.0160	0.0410	0.0595	**0.0090**
Height (λ_0) **of DRA**	0.299	0.2122	0.2439	**0.1027**
RL (dB) at f_1 **RL (dB) at** f_2	14 13	13 14	13 15	11 12
Gain (dB) at f_1 **Gain (dB) at** f_2	6.0 6.5	6.0 8.5	6.0 7.0	1.5 1.5
AR (dB) at f_1 **AR (dB) at** f_2	1.0 1.5	0.2 0.1	0.1 0.2	1.5 0.1

References

[1] P. Chaudhary, D. K. Ghodgaonkar, S. Gupta and A. Shukla, "Dual band circularly polarized dielectric resonator antenna using DSWPD with phase shifter for IRNSS," *IEEE International RF and Microwave Conference (RFM-2018)*, Penang, Malaysia, 17–19 December 2018, pp.246-249.

[2] X. S. Fang, C. K. Chow, K. W. Leung and E. H. Lim, "New single-/dual-mode design formulas of the rectangular dielectric resonator antenna using covariance matrix adaptation evolutionary strategy," *IEEE Antennas and Wireless Propagation Letters*, vol. 10, pp. 734-737, 2011.

[3] X. Wang, Z. Ma and M. Ohira, "Theory and Experiment of Two-Section Two-Resistor Wilkinson Power Divider With Two Arbitrary Frequency Bands," *IEEE Transactions on Microwave Theory and Techniques*, vol. 66, no. 3, pp. 1291-1300, March 2018.

[4] R. Han, S. Zhong and J. Liu, "Design of circularly-polarized dielectric resonator antenna with wideband feed network," *Proceedings of 2014 3rd Asia-Pacific Conference on Antennas and Propagation*, Harbin, 2014, pp. 48-50.

[5] S.Y.Eom and H.K.Park, "New switched-network phase shifter with broadband characteristics," *Microwave and Optical Technology Letters*, vol. 38, no. 4, pp. 255-257, August 2003.

[6] Ansys High Frequency Structure Simulator (HFSS) is a 3-D Electromagnetic (EM) simulation software for designing and simulating high-frequency electronic products such as antennas, antenna arrays, Radio Frequency (RF) or microwave components, high-speed interconnects, filters, connectors, Integrated

Circuit (IC) packages and printed circuit boards. https://www.ansys.com/en-in/products/electronics/ansys-hfss

[7] R. Vashisth, D. Ghodgaonkar and S. Gupta,"Design and Fabrication of Broadband Microwave Absorber using FSS embedded in CISR sheets," *2018 IEEE MTT-S International Microwave and RF Conference (IMaRC)*, Kolkata, India, Dec 2018, pp. 1-4.

[8] Z. Abbas, R.D. Pollard and R.W. Kelsall, "Complex permittivity measurements at Ka-band using rectangular dielectric waveguide," *IEEE Transactions on Instrumentation and Measurement*, Vol.50, no. 5, pp. 1334-1342, October 2001.

[9] X. Wang, L. Sun, X. Lu, S. Liang and W. Lu, "Single-feed dual-band circularly polarized dielectric resonator antenna for CNSS applications," *IEEE Transactions on Antennas and Propagation*, vol. 65, no. 8, pp. 4283-4287, Aug. 2017.

[10] X. Fang, K. W. Leung and E. H. Lim, "Singly-fed dual-band circularly polarized dielectric resonator antenna," *IEEE Antennas and Wireless Propagation Letters*, vol. 13, pp. 995-998, 2014.

[11] M. Zou and J. Pan, "Wide dual-Band circularly polarized stacked rectangular dielectric resonator antenna," *IEEE Antennas and Wireless Propagation Letters*, vol. 15, pp. 1140-1143, 2016.

Chapter 5

Compact Circularly Polarized Single-Band Rectangular Dielectric Resonator Antennas

5.1 Single-Band Rectangular Dielectric Resonator Antenna at S-Band

5.1.1 Introduction

A compact single-band Circularly Polarized (CP) Rectangular Dielectric Resonator Antenna (RDRA) using Wilkinson Power Divider (WPD) with wide-band 90^0 phase shifter is designed, analysed, fabricated and tested for S-band [1]. Finite ground plane area of S-band CP RDRA is reduced to 25 mm × 25 mm using high dielectric constant (ϵ_r=20.4) of Dielectric Resonator (DR) and high dielectric constant (ϵ_r=10.2) of dielectric substrate (Rogers R03210). Volume of Rectangular Dielectric Resonator (RDR) was miniaturized to 18.2 mm × 18.2 mm × 13.0 mm because of high dielectric constant (ϵ_r=20.4) of DR material. The mode of single-band RDRA is TE^y_{111} [1]. The radiation patterns of single-band RDRA was broadside. WPD with wide-band 90^0 phase shifter generates RHCP in single-band RDRA.

The single-band RDRA consists of RDR, dielectric substrate, ground plane, WPD with 90^0 phase shifter, 3M adhesive and two feeding probes [1]. 3M adhesive is used for remove air gap between RDR and ground plane. The design specifications of single band DRA at S-band are given in Table 1.1. The design steps of single-band RDRA are similar to section 3.1.2. Simulated and measured parameters of single-band RDRA are $|S_{11}|$, RHCP-LHCP radiation patterns, RHCP gain and axial ratio.

5.1.2 Structure and Feed Network

5.1.2.1 Structure

The front view, bottom view and 3-D geometries of single-band RDRA are shown in Figures 5.1, 5.2 and 5.3, respectively. Initially, RDR is considered as excitation free. L, W and H are length, width and height of RDR, respectively. Assuming aspect ratios $\frac{H}{L} = 0.74$, $\frac{W}{L} = 1.0$, ϵ_r=20.4 and resonant frequency f_0 of 2.49 GHz, optimized dimensions of RDR are determined using DWM with CMA-ES method (equations (3.13) to (3.23)) [2]. L, W and H of RDR are 18.2 mm, 18.2 mm and 13.0 mm, respectively. single-band RDRA is designed and analyzed at resonant frequency of 2.49 GHz [1].

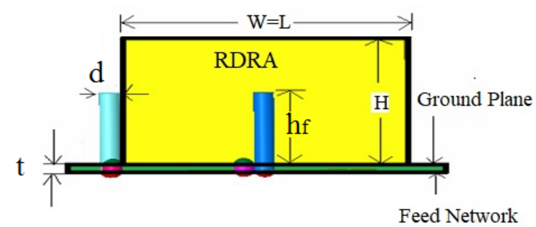

Figure 5.1: Front view of single-band RDRA [1]

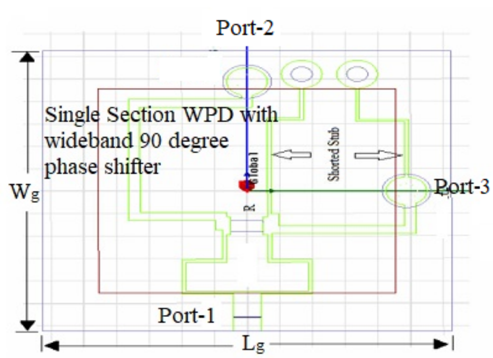

Figure 5.2: Bottom view of single-band RDRA [1]

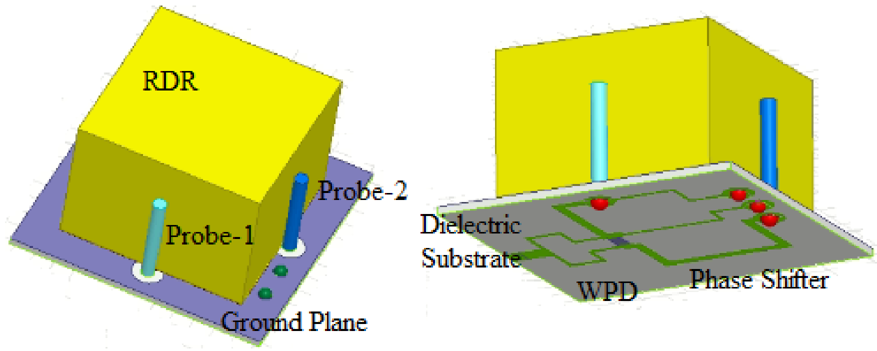

Figure 5.3: 3-D geometry views of single-band RDRA

5.1.2.2 Feed Network

The feed network consists of WPD and wide-band 90° phase shifter. Figure 5.4 shows the schematic of WPD with wide-band 90° phase shifter. The characteristic impedance Z_1 and resistance R are obtained using equation (3.30) and (3.31), respectively [3]. The characteristic impedance Z_2 is calculated using equation (3.32) [3]. The characteristic impedances Z_3 and Z_4 are equal to Z_0 [3]. Z_1, Z_2 and Z_3 are characteristic impedances of quarter wavelength transmission lines. Z_4 is the characteristic impedance of half wavelength transmission line. The value of resistance R is equal to 100Ω. Table 5.1 shows optimized design dimensions of WPD with wide-band 90° phase shifter at 2.49 GHz.

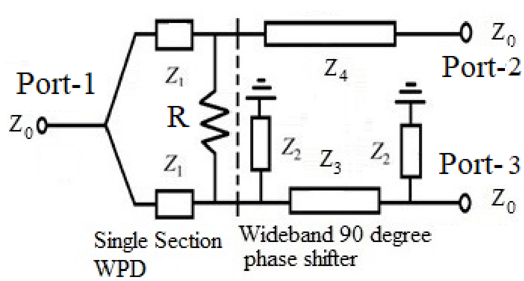

Figure 5.4: Feed network of WPD with wide-band 90° phase shifter [1, 3, 4]

The design of single-band RDRA is verified using reference [5]. The S-parameters of WPD with wide-band 90° phase shifter are depicted in Figure 5.5 (a). $|S_{11}|$, $|S_{21}|$, $|S_{31}|$, $|S_{23}|$ are found to be better than 16 dB, 4 dB, 3.9 dB and 27 dB, respectively over S-band. Figure 5.5 (b) represents phase shift of WPD with wide-band 90° phase shifter.

Table 5.1: Optimized design dimensions of WPD with wide-band 90° phase shifter at 2.49 GHz

Characteristic impedance (Ω)	Length (mm)	Width (mm)
Z_1=70.70	12.00	0.25
Z_2=76.00	12.70	0.20
Z_3=50.00	12.95	0.70
Z_4=50.00	25.00	0.70

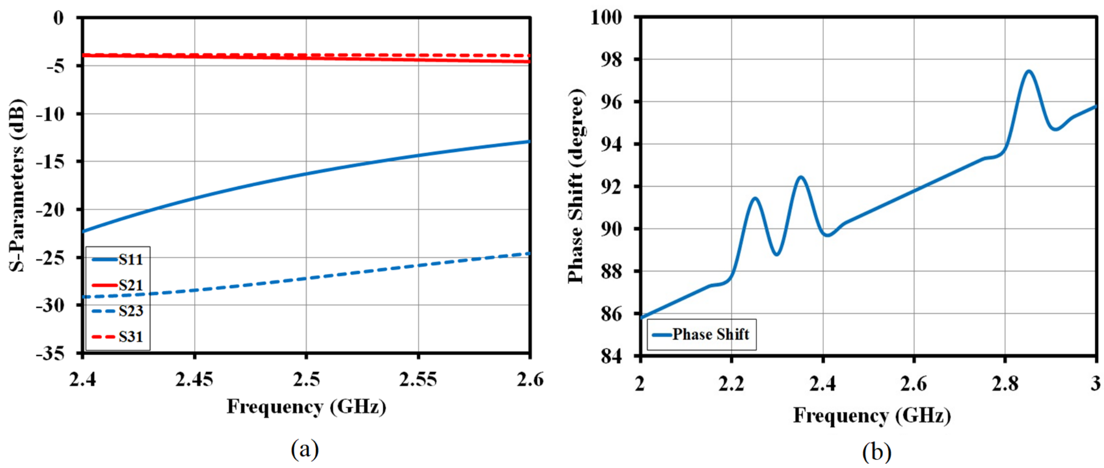

Figure 5.5: (a) S-parameters (S_{11}, S_{21}, S_{31}, S_{23})
(b) phase shift of WPD with wideband 90° phase shifter

5.1.3 Electric Field Distribution

The electric field distribution of TE^y_{111} mode at 2.49 GHz is shown in Figure 5.6. In z-direction, TE^y_{111} mode is analyzed as $0.5\lambda_0$ at 2.49 GHz [1]. The electric field distribution at 2.49 GHz with respect to 0^0 is shown in Figure 5.7 (a). In single-band RDRA, Figure 5.7 (b) shows electric field distribution at 2.49 GHz with respect to 90^0. The electric field vector **E** revolves in anticlockwise direction as phase change from 0^0 to 90^0 generates RHCP as given in Figures 5.7 (a) and 5.7 (b), respectively.

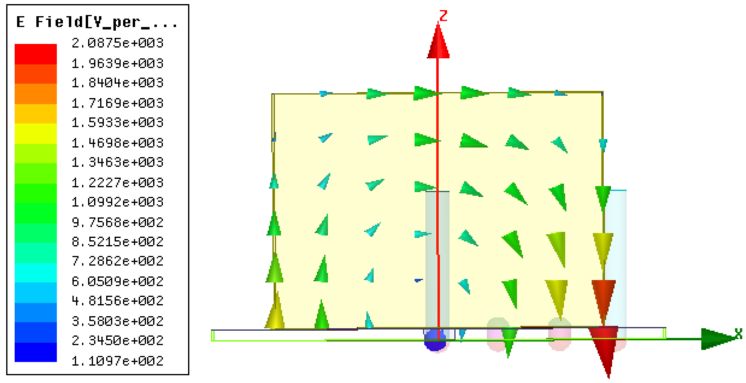

Figure 5.6: Electric field distribution of TE^{y}_{111} mode at 2.49 GHz

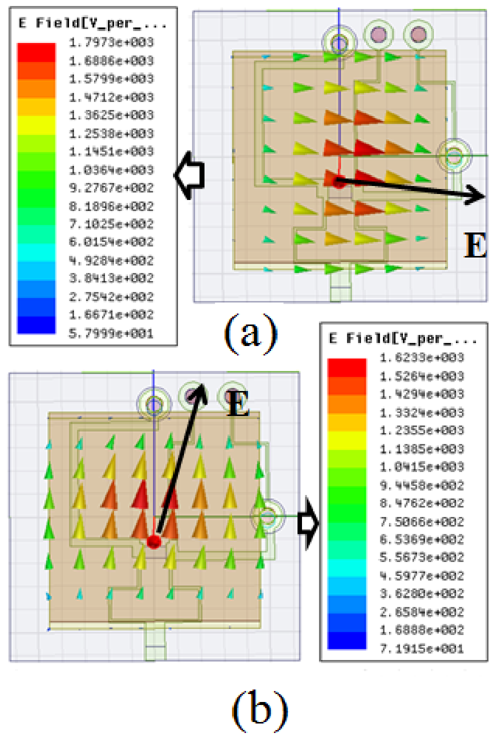

Figure 5.7: (a) Electric field distribution at 2.49 GHz with respect to 0^0, and (b) electric field distribution at 2.49 GHz with respect to 90^0

5.1.4 Fabrication and Testing

The single-band RDRA consists of rectangular dielectric resonator, WPD with wideband 90° phase shifter, dielectric substrate, ground plane, two vertical feed probes and 3M adhesive. WPD with wide-band 90° phase shifter is located on bottom face of dielectric substrate (Figure 5.2). The top part of dielectric substrate is represented as ground plane (Figure 5.1). The ground plane is connected to the

RDR using 3M adhesive with size of 18.2 mm $\times$ 18.2 mm $\times$ 0.05 mm. Port-1 is represented as input port of single-band RDRA [1].

Two vertical feed probes are attached to the port-2 and port-3 using soldering, respectively. Two side walls of RDR are excited through two vertical feed probes. Feeding probes and ground plane are isolated by removing 4 mm diameter copper metal from ground plane.The area ($L_g \times W_g$) of ground plane is 25 mm $\times$ 25 mm. The height and the diameter of both the feed pin-1 and 2 are 8.11 mm and 1.3 mm, respectively. The locations of feed pin-1 and pin-2 are (0, 9.75, 0) and (9.75, 0, 0), respectively.The thickness of dielectric substrate is 0.635 mm. In Figure 5.8, photographs of single-band RDRA parts are shown. Figure 5.9 presents photograph of fabricated single-band RDRA for test and measurement in the anechoic chamber.

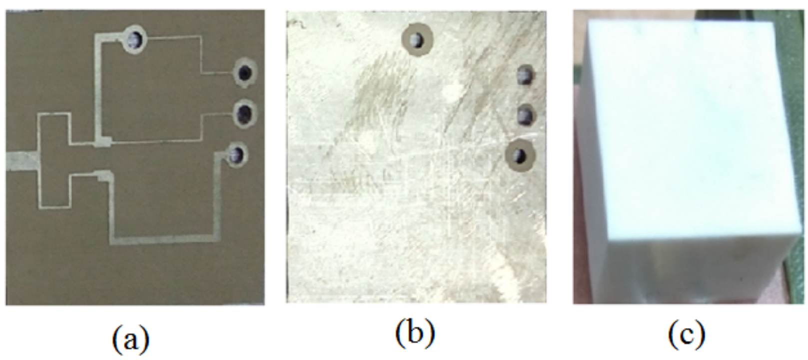

Figure 5.8: Photographs of single-band RDRA parts (a) bottom view of dielectric substrate (b) top view of dielectric substrate (c) rectangular dielectric resonator [1]

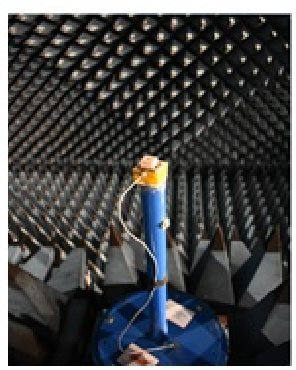

Figure 5.9: Photograph of fabricated single-band RDRA for test and measurement in the anechoic chamber

5.2 Single-Band Rectangular Dielectric Resonator Antenna at L1-Band

5.2.1 Introduction

A compact single band CP RDRA using WPD with wide-band 90^0 phase shifter is designed, analyzed, fabricated and tested for L1-band. Finite ground plane footprint area of single-band RDRA is miniaturized to 28 mm × 28 mm using high dielectric constant (ϵ_r= 51.92) of dielectric resonators and high dielectric constant (ϵ_r= 10.2) of dielectric substrate (Rogers R03210) [6]. The volume of RDR is reduced to 18 mm × 18 mm × 25 mm for L1-band using high dielectric constant (ϵ_r= 51.92) of dielectric resonator. The mode of single-band RDRA is TE^y_{111}. The radiation patterns of single-band RDRA are broadside. WPD with wide-band 90^0 phase shifter produces RHCP in single-band RDRA [6].

The single band RDRA consists of RDR, dielectric substrate, copper ground plane metal sheet, WPD with wide-band 90^0 phase shifter, 3M adhesive and two feeding probes [6]. The design specifications of single-band RDRA at L1-band are given in Table 1.1. The design steps of single-band RDRA are similar to section 3.1.2. The simulated and measured parameters of single-band RDRA are $|S_{11}|$, RHCP-LHCP radiation patterns, RHCP gain and axial ratio.

5.2.2 Configuration and Excitation of Single-Band Rectangular Dielectric Resonator Antenna

5.2.2.1 Configuration

The front view, bottom view and 3-D geometries of single-band RDRA are shown in Figures 5.10, 5.11 and 5.12, respectively. Initially, RDR is considered as excitation free. L, W and H are length, width and height of RDR, respectively. Assuming aspect ratios $\frac{H}{L}$ = 1.139, $\frac{W}{L}$ = 1.0, ϵ_r=51.92 and resonant frequency of 1.575 GHz, optimized dimensions of RDR are obtained using equations (3.13) to (3.23) (DWM with CMA-ES method) [2]. L, W and H of RDR are 18.0 mm, 18.0 mm and 25.0 mm, respectively [6].

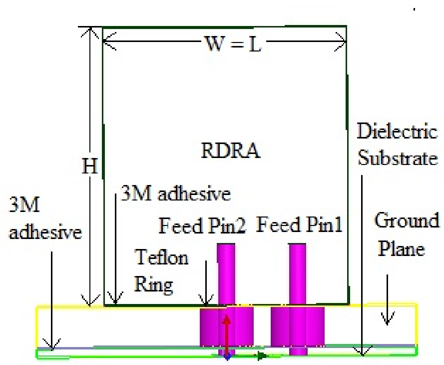

Figure 5.10: Front view of single-band RDRA [6]

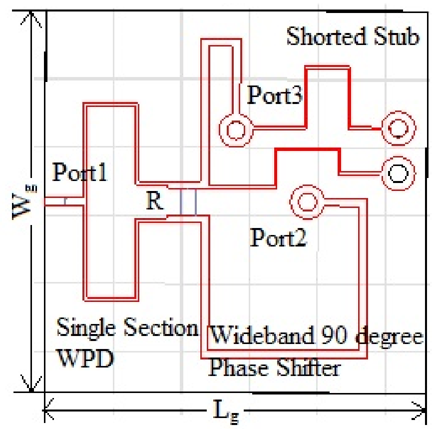

Figure 5.11: Bottom view of single-band RDRA [6]

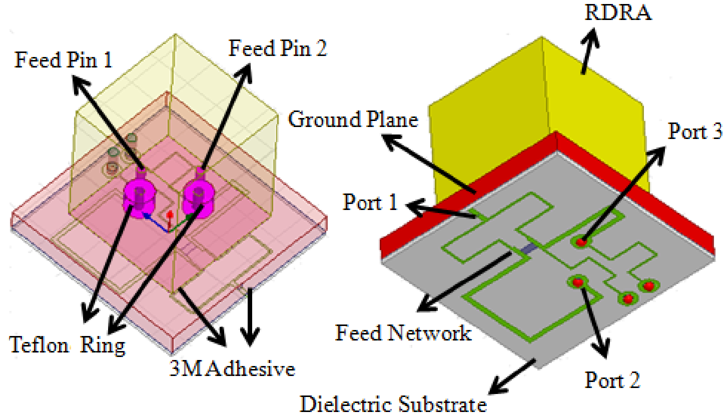

Figure 5.12: 3-D geometries of single-band RDRA [6]

5.2.2.2 Excitation

The feed network consists of WPD and wide-band 90° phase shifter. Figure 5.13 shows the schematic of WPD with wide-band 90° phase shifter. The characteristic impedance Z_1 and resistance R are obtained using equation (3.30) and (3.31), respectively [3]. The characteristic impedance Z_2 is calculated using equation (3.32) [3]. The characteristic impedances Z_3 and Z_4 are equal to Z_0 [3]. Z_1, Z_2 and Z_3 are characteristic impedances of quarter wavelength transmission lines. Z_4 is the characteristic impedance of half wavelength transmission line. The value of resistance R is equal to 100 **Ω**. Table 5.2 shows optimized design dimensions of WPD with wide-band 90° phase shifter at 1.575 GHz.

The design of single-band RDRA is verified using reference [5]. The S-parameters of WPD with wide-band 90° phase shifter are depicted in Figure 5.14 (a). $|S_{11}|$, $|S_{21}|$, $|S_{31}|$, $|S_{23}|$ are found to be better than 15 dB, 4 dB, 4 dB and 20 dB, respectively over L1-band. Figure 5.14 (b) represents phase shift of WPD with wide-band 90° phase shifter.

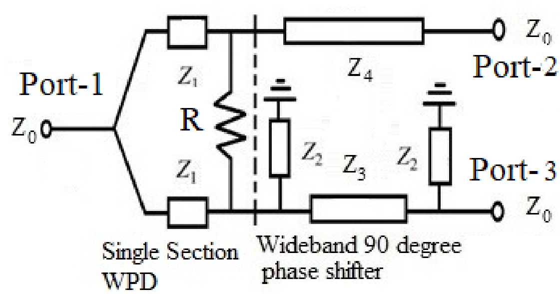

Figure 5.13: Feed network of WPD with wide-band 90° phase shifter [1, 3, 4]

Table 5.2: Optimized design dimensions of WPD with wide-band 90° phase shifter at 1.575 GHz

Characteristic impedance (Ω)	Length (mm)	Width (mm)
Z_1=70.70	21.18	0.25
Z_2=76.00	19.80	0.20
Z_3=50.00	18.00	0.70
Z_4=50.00	36.90	0.70

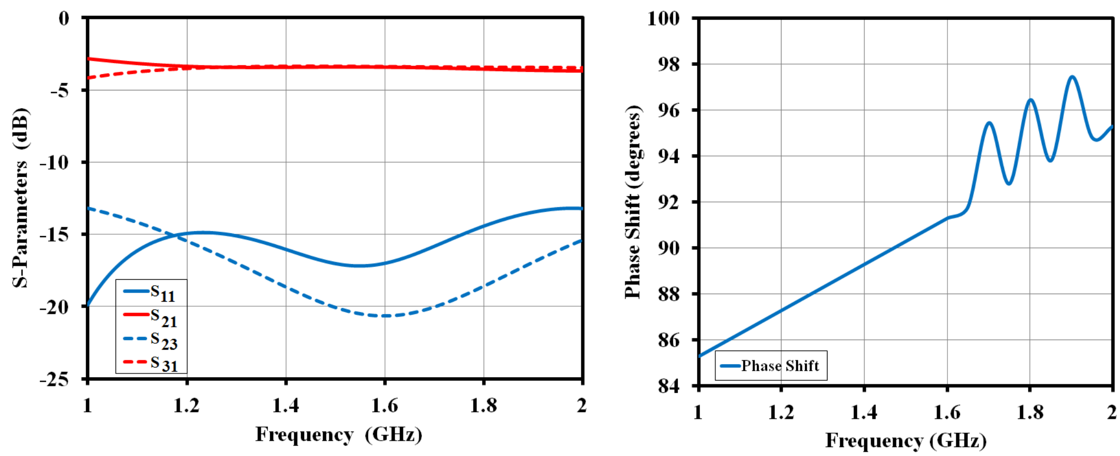

(a) (b)

Figure 5.14: (a) S-parameters (S_{11}, S_{21}, S_{31}, S_{23})
(b) phase shift of WPD with wideband 90° phase shifter

5.2.3 Electric Field Distribution

The electric field distribution of TE^{y}_{111} mode at 1.575 GHz is shown in Figure 5.15. In z-direction, TE^{y}_{111} mode is analyzed as $0.5\lambda_0$ at 1.575 GHz [6]. The electric field distribution at 1.575 GHz with respect to 0^0 is shown in Figure 5.16 (a). In single-band RDRA, Figure 5.16 (b) shows electric field distribution at 1.575 GHz with respect to 90^0. The electric field vector **E** revolves in anticlockwise direction as phase change from 0^0 to 90^0 generates RHCP as given in Figure 5.16 (a) and 5.16 (b), respectively.

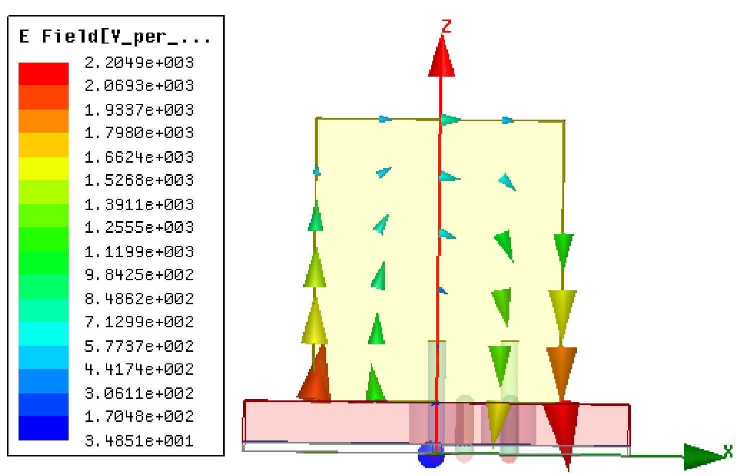

Figure 5.15: Electric field distribution of TE^{y}_{111} mode at 1.575 GHz [6]

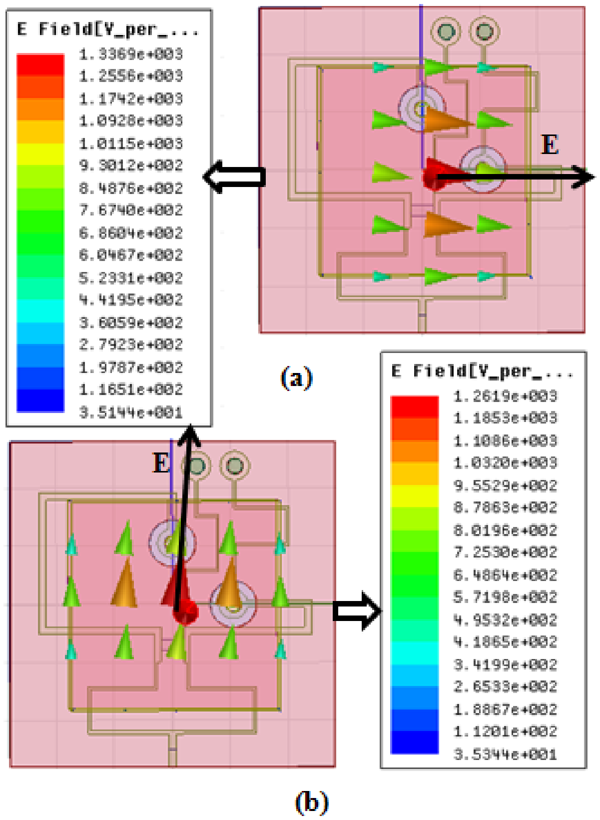

Figure 5.16: (a) Electric field distribution at 1.575 GHz with respect to 0^0, and (b) electric field distribution at 1.575 GHz with respect to 90^0 [6]

5.2.4 Fabrication and Testing

Single-band RDRA consists of rectangular dielectric resonator, WPD with wide-band 90° phase shifter, dielectric substrate, copper metal sheet (ground plane), two vertical feed probes and 3M adhesive [6]. WPD with wide-band 90° phase shifter is located on bottom face of dielectric substrate. Copper is fully removed from the top side of dielectric substrate. A copper metal sheet, used as the ground plane in this antenna, not only protect the dielectric substrate from bending but can also handle the weight of RDR. The top face of the dielectric substrate is attached to the bottom face of the copper metal sheet using 3M adhesive with size of 28 mm × 28mm × 0.05 mm. The air gap between the copper metal sheet and dielectric substrate is removed using 3M adhesive [6].

The top face of copper metal sheet is connected to the RDR using 3M adhesive [1]. The air gap between RDR and copper metal sheet is removed by 3M adhesive with size of 18 mm × 18 mm × 0.05 mm. Port-1 is represented as input port of single-band RDRA. Two vertical feed probes are attached to the port-2 and port-3 using soldering. The RDR is excited through two vertical feed probes [6].

The feeding probes and copper metal sheet are isolated by teflon rings. The 4 mm diameter copper is removed from metal sheet. The volume ($L_g \times W_g \times H_g$) of ground plane is 28 mm × 28 mm × 3mm. The height and diameter of both the feed pin-1 and 2 are 8.2 mm and 1.3 mm, respectively. The locations of feed pin-1 and pin-2 are (0, 5.25, 0) and (5.25, 0, 0), respectively. The thickness of dielectric substrate is 0.635 mm. Figure 5.17 show bottom view and 3-D geometries of fabricated single-band RDRA. The photograph of fabricated single-band RDRA for test and measurement is shown in Figure 5.18 [6].

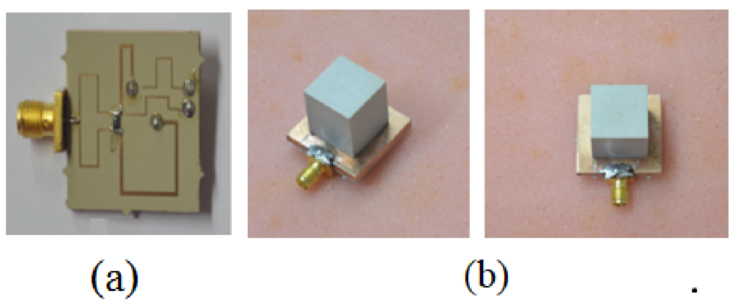

Figure 5.17: Photograph of (a) bottom view (b) 3-D geometries views of fabricated single-band RDRA [6]

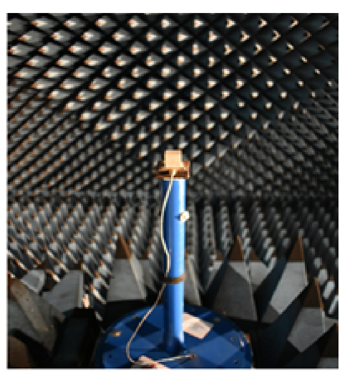

Figure 5.18: Photograph of fabricated single-band RDRA for test and measurement in the anechoic chamber

5.3 Single-Band Rectangular Dielectric Resonator Antenna at L5-Band

5.3.1 Introduction

A compact single band CP RDRA using WPD with wide-band 90^0 phase shifter is designed, analyzed, fabricated and tested for L5-band. The finite ground plane footprint area of single-band RDRA is miniaturized to 40 mm $\times$ 40 mm for L5-band using high dielectric constant (ϵ_r= 51.92) of dielectric resonator and high dielectric constant (ϵ_r= 10.2) of dielectric substrate (Rogers R03210) [6]. The volume of RDR is reduced to 23.1 mm $\times$ 23.1 mm $\times$ 28.0 mm for L5-band. The mode of single-band RDRA is TE^y_{111}. The radiation patterns of single-band RDRA are broadside. WPD with wide-band 90^0 phase shifter produces RHCP [6].

The single-band RDRA consists of RDR, dielectric substrate, copper metal sheet (ground plane), WPD with wide-band 90^0 phase shifter, 3M adhesive, silver epoxy adhesive and two feeding probes [6]. The design specifications of single-band RDRA at L5-band are given in Table 1.1. Simulated and measured parameters of single-band RDRA are $|S_{11}|$, RHCP-LHCP radiation patterns, RHCP gain and axial ratio.

5.3.2 Geometry and Feed Network of Single-Band RDRA

5.3.2.1 Geometry

The front view, bottom view and 3-D geometries of single-band RDRA are shown in Figures 5.19, 5.20 and 5.21, respectively. Initially, RDR is considered as excitation free. L, W and H are length, width and height of RDR, respectively. Assuming aspect ratios $\frac{H}{L}$ = 1.21, $\frac{W}{L}$ = 1.0, ϵ_r=51.92 and resonant frequency of 1.176 GHz, optimized dimensions of RDR are obtained using equations (3.13) to (3.23) (DWM with CMA-ES method) [2]. L, W and H of RDR are 23.1 mm, 23.1 mm and 28.0 mm, respectively [6].

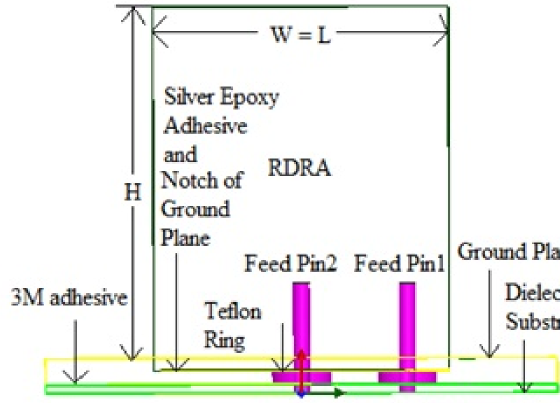

Figure 5.19: Front view of single-band RDRA [6]

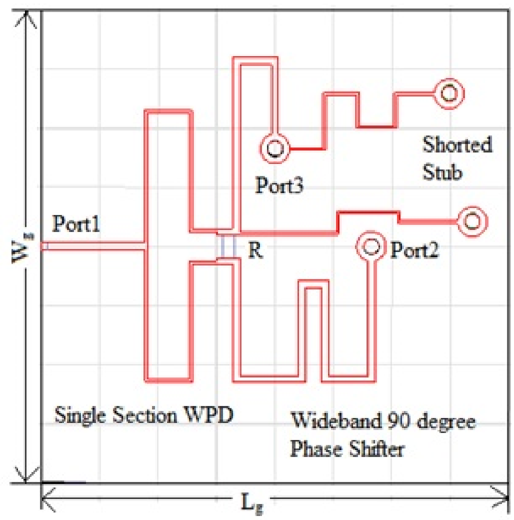

Figure 5.20: Bottom view of single-band RDRA [6]

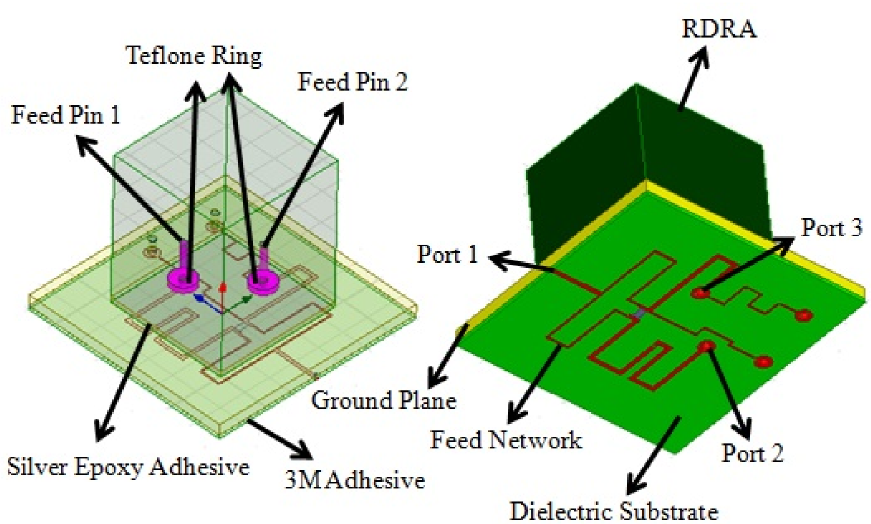

Figure 5.21: 3-D geometries of single-band RDRA [6]

5.3.2.2 Feed Network

The feed network consists of WPD and wide-band 90° phase shifter. Figure 5.22 shows the schematic of WPD with 90° phase shifter. The characteristic impedance Z_1 and resistance R are obtained using equation (3.30) and (3.31), respectively [3]. The characteristic impedance Z_2 is calculated using equation (3.32) [3]. The characteristic impedances Z_3 and Z_4 are equal to Z_0 [3]. Z_1, Z_2 and Z_3 are characteristic impedances of quarter wavelength transmission lines. Z_4 is the characteristic impedance of half wavelength transmission line. The value of resistance R is equal to 100 **Ω**. Table 5.3 shows optimized design dimensions of WPD with wide-band 90° phase shifter at 1.176 GHz.

The design of single-band RDRA is verified using reference [5]. The S-parameters of WPD with wide-band 90° phase shifter are depicted in Figure 5.23 (a). $|S_{11}|$, $|S_{21}|$, $|S_{31}|$, $|S_{23}|$ are found to be better than 15 dB, 4 dB, 4 dB and 20 dB, respectively over L5-band. Figure 5.23 (b) represents phase shift of WPD with wide-band 90° phase shifter.

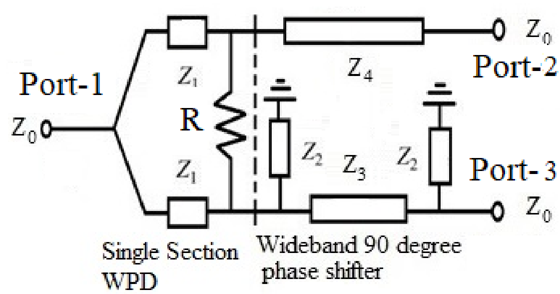

Figure 5.22: Feed network of WPD with wide-band 90° phase shifter [1, 3, 4]

Table 5.3: Optimized design dimensions of WPD with wide-band 90° phase shifter at 1.176 GHz

Characteristic impedance (Ω)	Length (mm)	Width (mm)
Z_1=70.70	27.68	0.25
Z_2=76.00	25.35	0.20
Z_3=50.00	28.10	0.70
Z_4=50.00	47.80	0.70

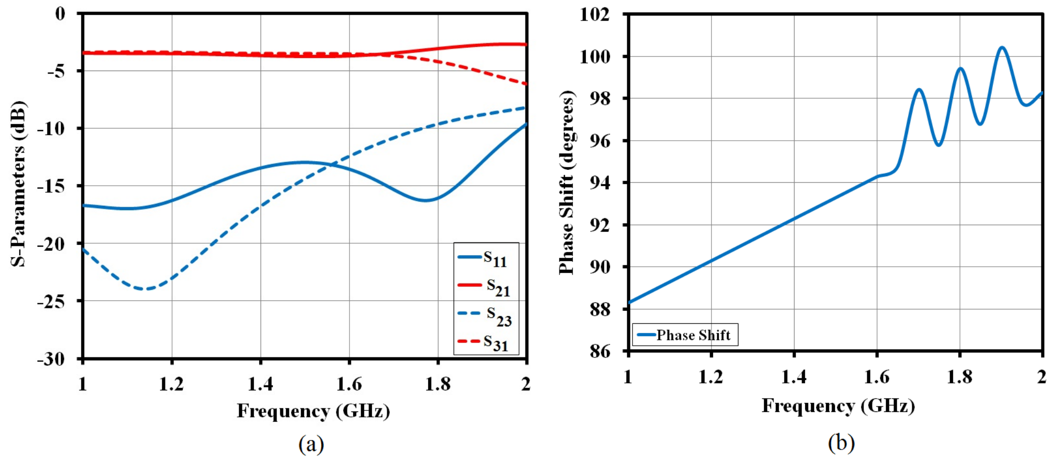

Figure 5.23: (a) S-parameters (S_{11}, S_{21}, S_{31}, S_{23})
(b) the phase shift of WPD with wideband 90° phase shifter

5.3.3 Electric Field Distribution

The electric field distribution of TE^y_{111} mode at 1.176 GHz is shown in Figure 5.24. In z-direction, TE^y_{111} mode is analyzed as $0.5\lambda_0$ at 1.176 GHz [6]. The electric field distribution at 1.176 GHz with respect to 0^0 is shown in Figure 5.25 (a). In single-band RDRA, Figure 5.25 (b) shows electric field distribution at 1.176 GHz with respect to 90^0. The electric field vector **E** revolves in anticlockwise direction as phase change from 0^0 to 90^0 generates RHCP as given in Figure 5.25 (a) and 5.25 (b), respectively.

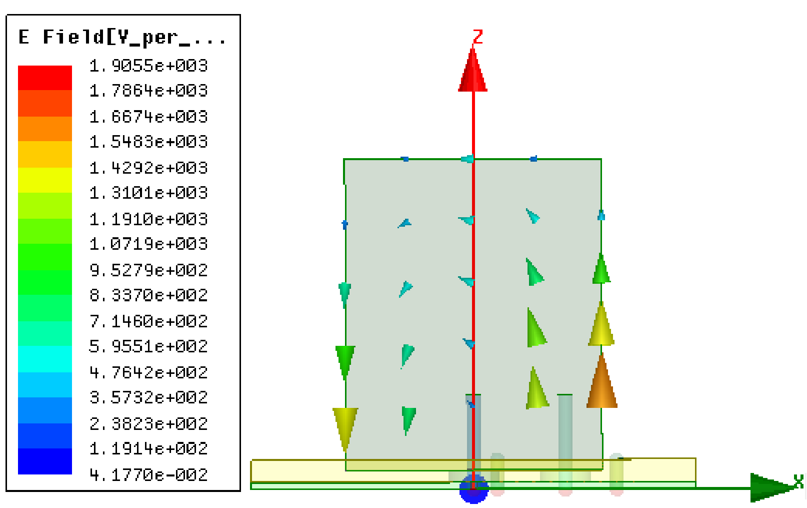

Figure 5.24: Electric field distribution of TE^y_{111} mode at 1.176 GHz [6]

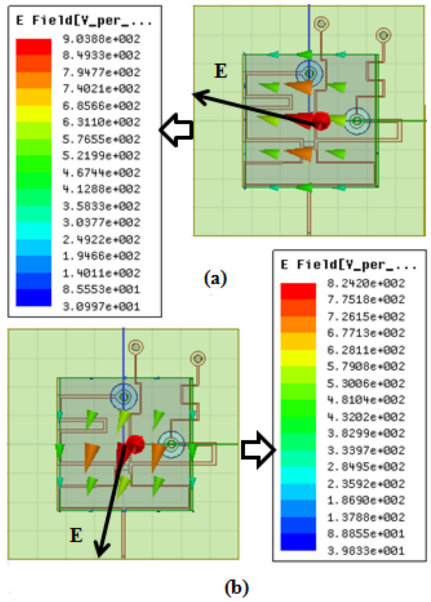

Figure 5.25: (a) Electric field distribution at 1.176 GHz with respect to 0^0, and (b) electric field distribution at 1.176 GHz with respect to 90^0 [6]

5.3.4 Fabrication and Testing

The single-band RDRA consists of rectangular dielectric resonator, WPD with 90° phase shifter, dielectric substrate, copper metal sheet (ground plane), two vertical feed probes, silver epoxy adhesive and 3M adhesive [6]. WPD with wide-band 90° phase shifter is located on bottom face of dielectric substrate. Copper is fully removed from the top side of dielectric substrate. A copper metal sheet, used as the ground plane in this antenna, not only protect the dielectric substrate from bending but can also handle the weight of RDR.

The top face of dielectric substrate is attached to the bottom face of the copper metal sheet using 3M adhesive with size of 40 mm × 40 mm × 0.05 mm. The air gap between copper metal sheet and dielectric substrate is removed using 3M adhesive. A groove with volume (23.15 mm × 23.15 mm × 1 mm) is created on top side of the copper metal sheet. The copper metal sheet with groove is attached to the RDR using silver epoxy adhesive with size of 23.15 mm × 23.15 mm × 0.06 mm. Air gap between RDR and copper metal sheet is removed using silver epoxy adhesive. Port-1 is represented as input port of single-band RDRA. Two vertical feed probes are attached to the port-2 and port-3 using soldering.

The RDR is excited through two vertical feed probes [6]. The feeding probes and copper metal sheet are isolated by teflon rings. The 4 mm diameter copper is removed from metal sheet. Volume ($L_g \times W_g \times H_g$) of ground plane is 40 mm $\times$ 40 mm $\times$ 2 mm. The height and diameter of both feed pin-1 and 2 are 8.5 mm and 1.3 mm, respectively. The locations of feed pin-1 and pin-2 are (0, 8.25, 0) and (8.25, 0, 0), respectively. The thickness of dielectric substrate is 0.635 mm. In Figure 5.26, photographs of single-band RDRA parts are shown. Figure 5.27 shows the photograph of fabricated single-band RDRA for test and measurement in the anechoic chamber [6].

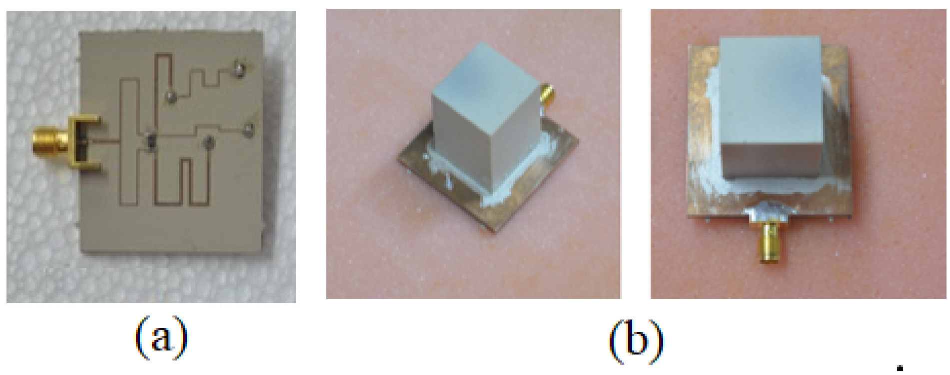

Figure 5.26: Photograph of (a) bottom view (b) 3-D geometries views of fabricated single-band RDRA [6]

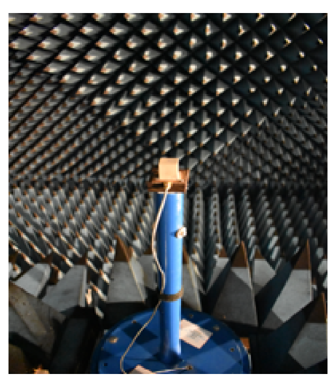

Figure 5.27: Photograph of fabricated single-band RDRA for test and measurement in the anechoic chamber

5.4 Simulated and Measured Results

5.4.1 Single-Band Rectangular Dielectric Resonator Antenna at S-Band

The simulated and measured return loss are found to be better than 15 dB over S-band as shown in Figure 5.28. The simulated and measured RHCP-LHCP radiation patterns at ϕ=0° are given in Figure 5.29 over S-band. For ϕ=45°, simulated and measured RHCP-LHCP radiation patterns are shown in Figure 5.30 over S-band. In single-band RDRA, Figure 5.31 shows simulated and measured RHCP-LHCP radiation patterns at ϕ=90° over S-band. RHCP-LHCP radiation patterns are obtained broadside over S-band. Figure 5.32 shows simulated and measured RHCP gain of single-band RDRA for S-band. The simulated and measured axial ratio of single-band RDRA for S-band is depicted in Figure 5.33.

The simulated RHCP gain and axial ratio are given in Table 5.4. Measured RHCP-LHCP radiation patterns, RHCP gain and AR are closed to simulated parameters except shift in resonant frequency due to 3M adhesive, air gap between feeding probes and RDR walls, fixture pipe and mounting fixture. The reduction of HPBW and multiple ripples are observed in measured radiation patterns due to mounting fixture and fixture pipe in the anechoic chamber.

Table 5.4: Simulated RHCP gain and axial ratio of single-band RDRA for S-band

Parameters	**S-Band**
RHCP Gain at $\theta = 0^0$	2.90 dB
RHCP Gain at $\theta = \pm 60^0$	-0.46 dB
RHCP Gain at $\theta = \pm 70^0$	-1.77 dB
RHCP Gain at $\theta = \pm 80^0$	-3.40 dB
Axial Ratio at $\theta = 0^0$ to $\pm 60^0$	< 3 dB

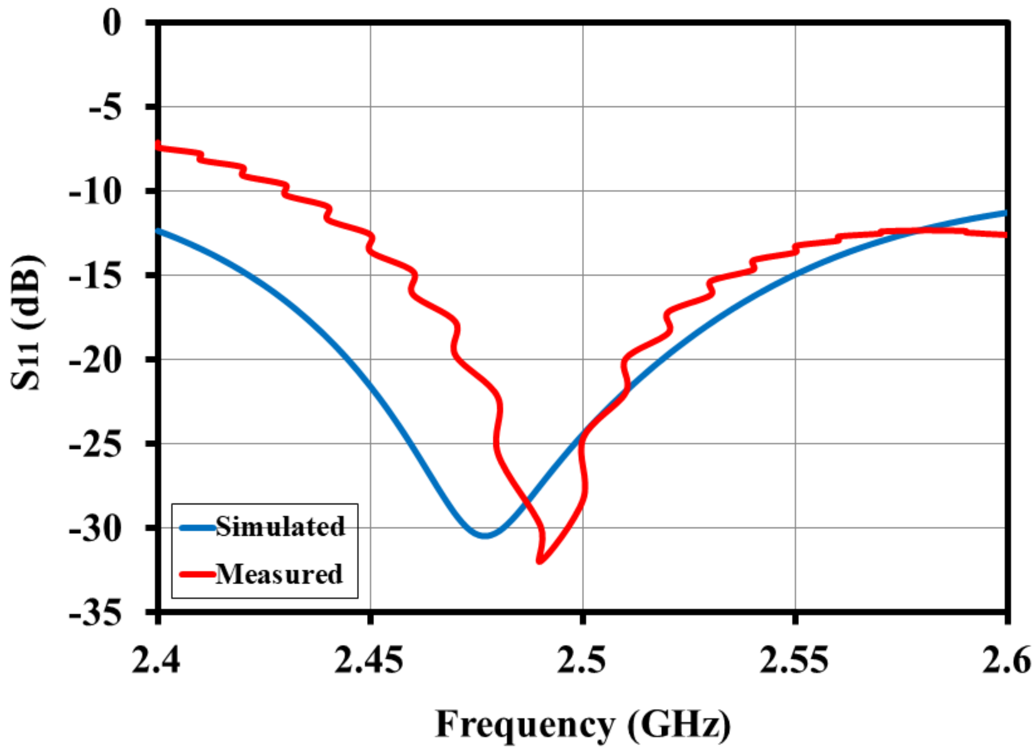

Figure 5.28: Simulated and measured S_{11} of single-band RDRA

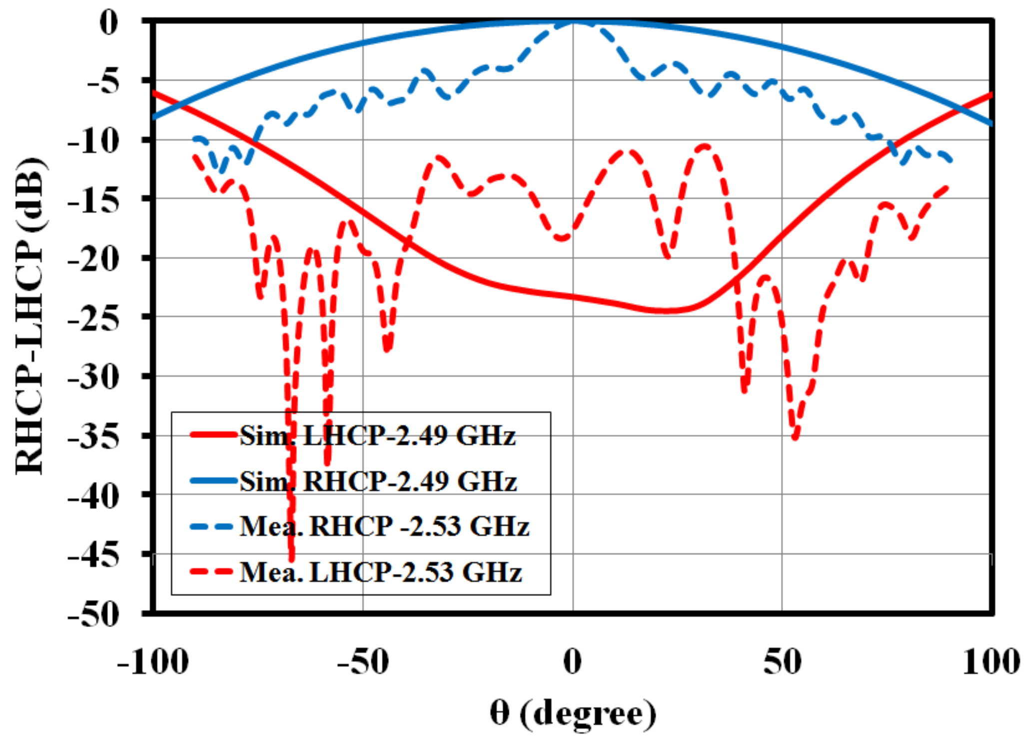

Figure 5.29: Simulated and measured RHCP-LHCP far field radiation patterns for S-band at ϕ=0°

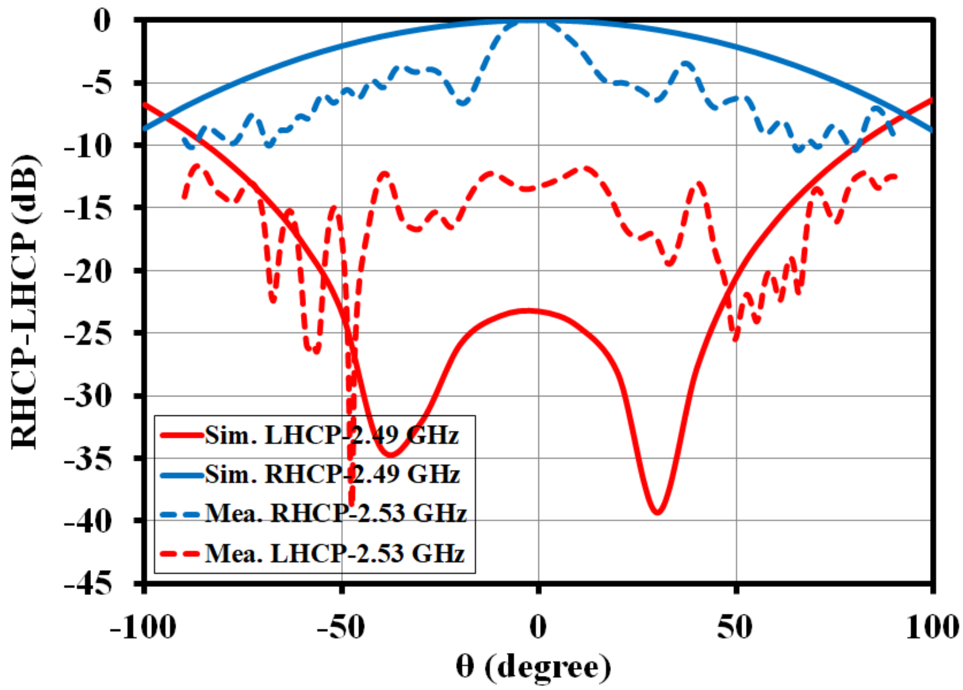

Figure 5.30: Simulated and measured RHCP-LHCP far field radiation patterns for S-band at ϕ=45°

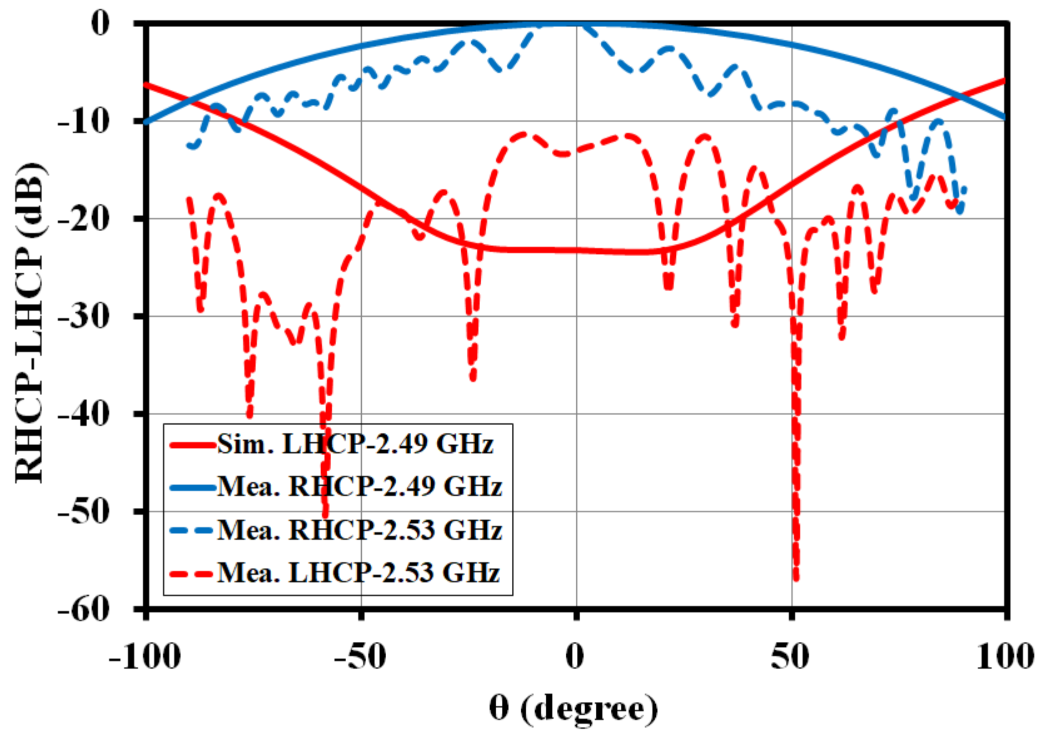

Figure 5.31: Simulated and measured RHCP-LHCP far field radiation patterns for S-band at ϕ=90°

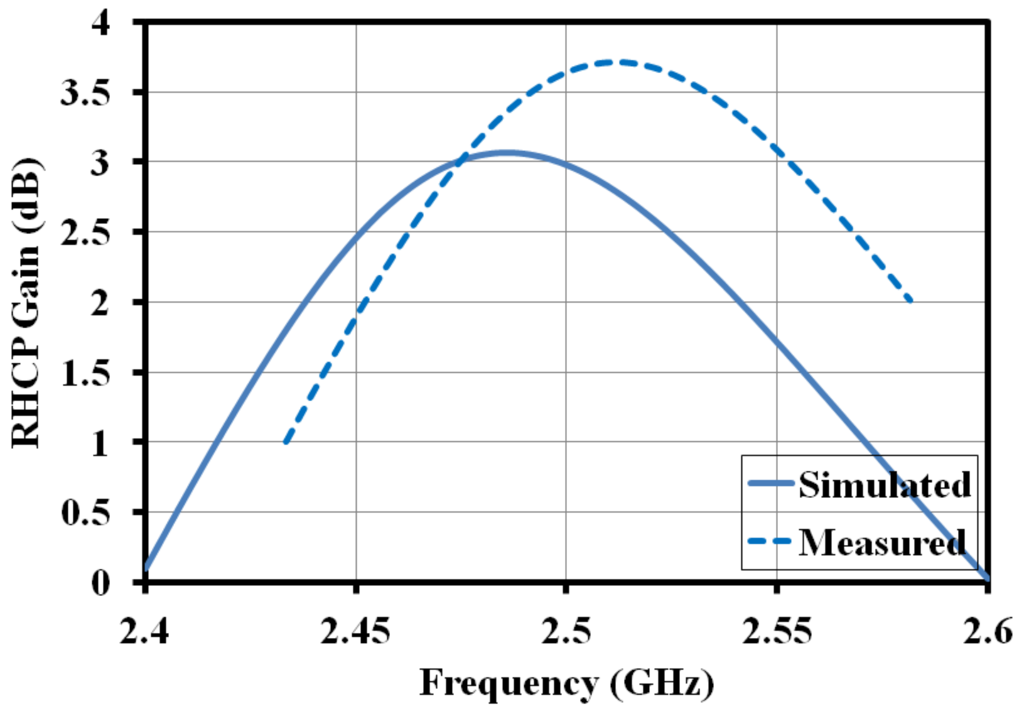

Figure 5.32: Simulated and measured RHCP gain of single-band RDRA

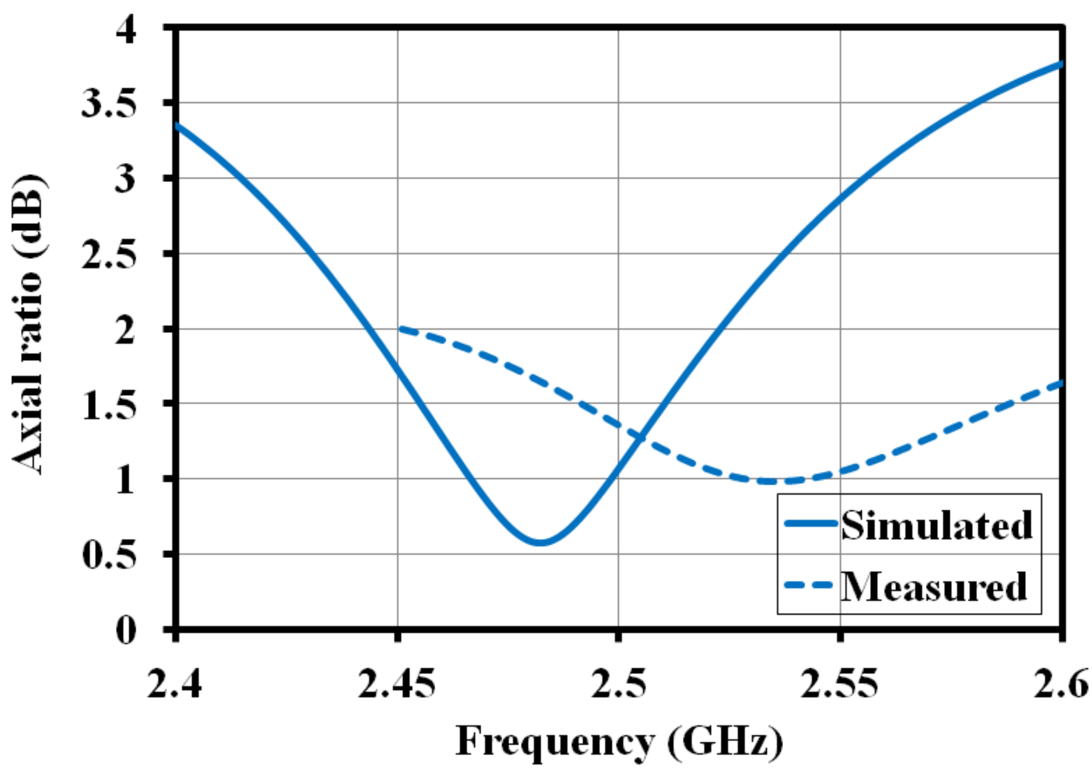

Figure 5.33: Simulated and measured axial ratio of single-band RDRA

5.4.2 Single-Band Rectangular Dielectric Resonator Antenna at L1-Band

The simulated and measured return loss are found to be better than 14 dB over L1-band as shown in Figure 5.34 [6]. The dielectric resonator material (ϵ_r = 51.92) was obtained from TCI Ceramics (Division of National Magnetics Group, Bethlehem, PA, USA). The dielectric constant of this material was measured as ϵ_r = 47.35 at 5 GHz using RDWG method [7, 8]. The simulated and measured return loss of single-band RDRA are matched except a slight shift in resonance frequencies. This shift in center frequencies is due to difference between prescribed dielectric constant (ϵ_r= 51.92) provided by the manufacturer and measured dielectric constant (ϵ_r= 47.35) of DR material.

The simulated and measured RHCP-LHCP radiation patterns at ϕ=0° are given in Figure 5.35 over L1-band. For ϕ=45°, simulated and measured RHCP-LHCP radiation patterns are shown in Figure 5.36 over L1-band. In single-band RDRA, Figure 5.37 shows simulated and measured RHCP-LHCP radiation patterns at ϕ=90° over L1-band. RHCP-LHCP radiation patterns are obtained broadside over L1-band. Figure 5.38 shows simulated and measured RHCP gain of single-band RDRA for L1-band. The simulated and measured axial ratio of single-band RDRA for L1-band are shown in Figure 5.39. The reduction of HPBW and multiple ripples in measured RHCP-LHCP radiation patterns are observed due to bakelite support, fixture pipe and mounting fixture in the anechoic chamber (Figure 5.18). The simulated RHCP gain and axial ratio of single-band RDRA for L1-band are shown in Table 5.5 [6]. The measured RHCP-LHCP radiation patterns, RHCP gain and axial ratio are mismatched because of error introduced by bakelite support, fixture pipe and mounting fixture in the anechoic chamber (Figure 5.18).

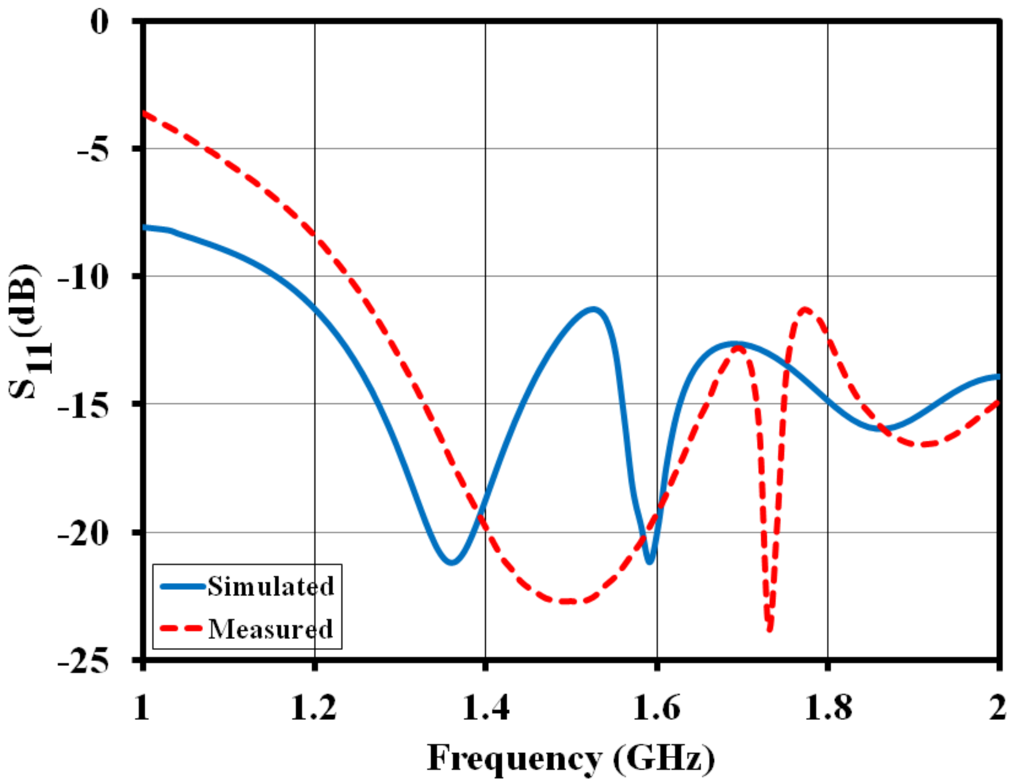

Figure 5.34: Simulated and measured S_{11} of single-band RDRA [6]

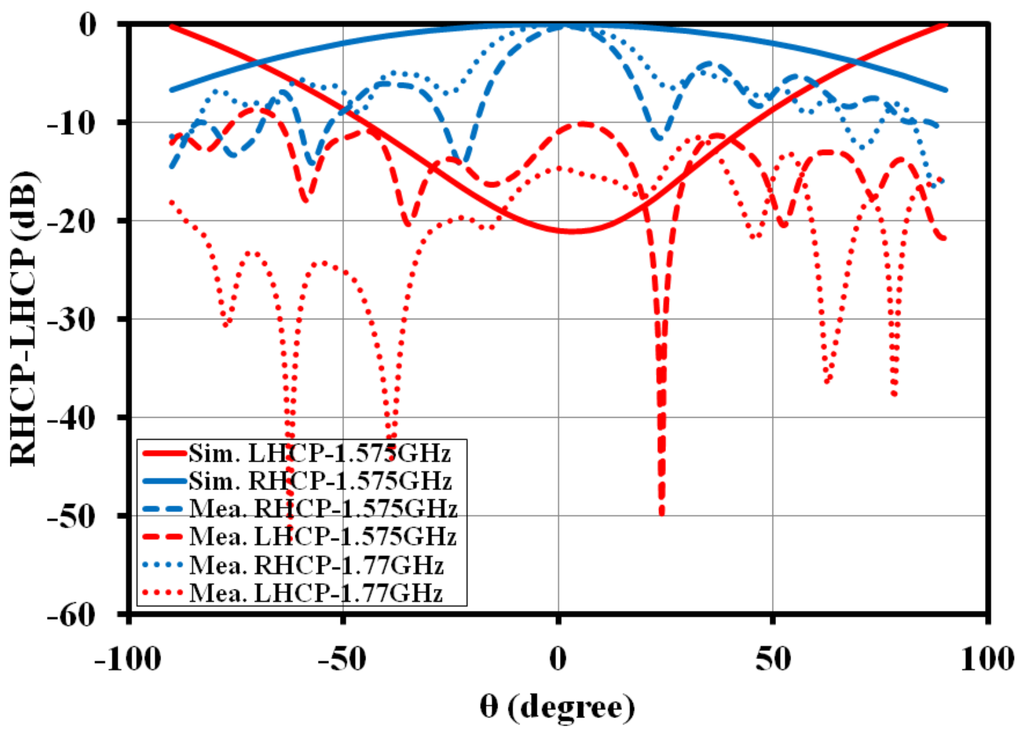

Figure 5.35: Simulated and measured RHCP-LHCP far field radiation patterns for L1-band at ϕ=0° [6]

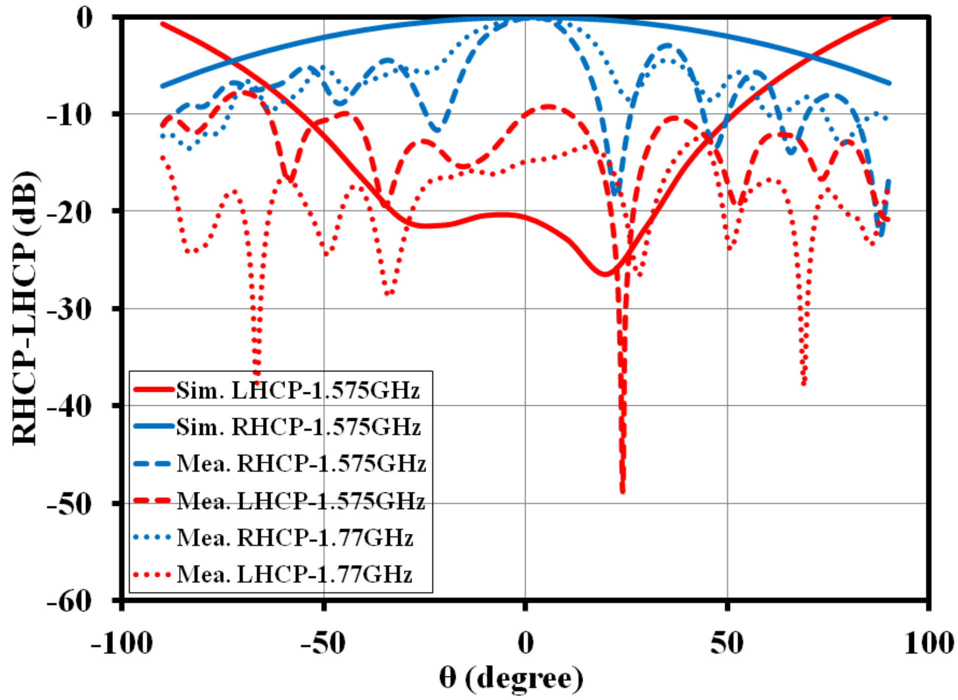

Figure 5.36: Simulated and measured RHCP-LHCP far field radiation patterns for L1-band at ϕ=45° [6]

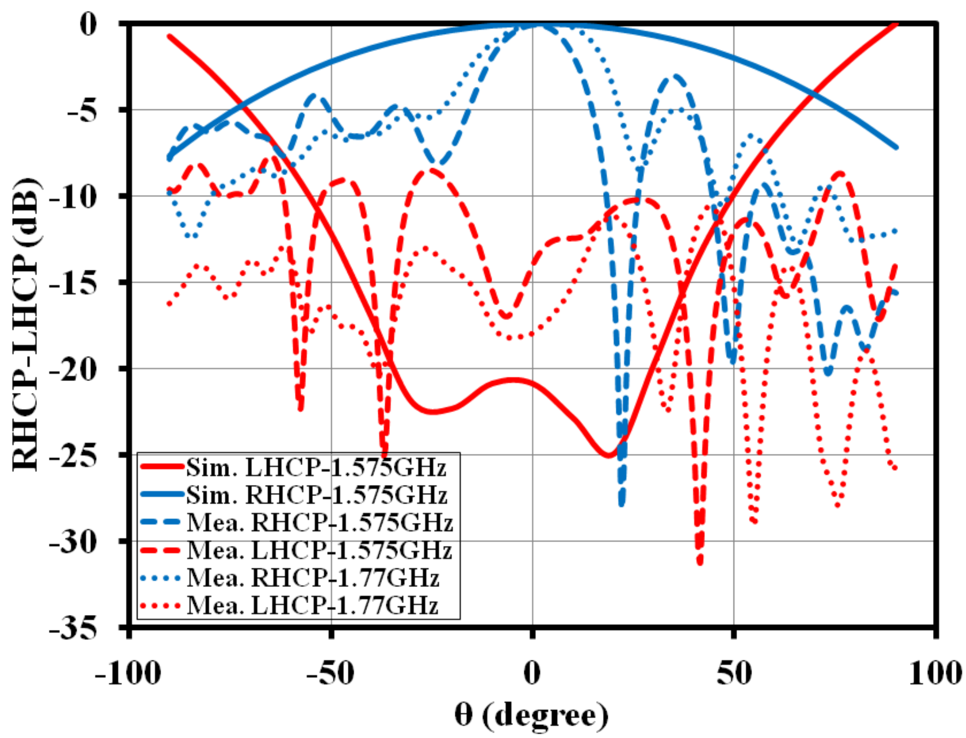

Figure 5.37: Simulated and measured RHCP-LHCP far field radiation patterns for L1-band at ϕ=90° [6]

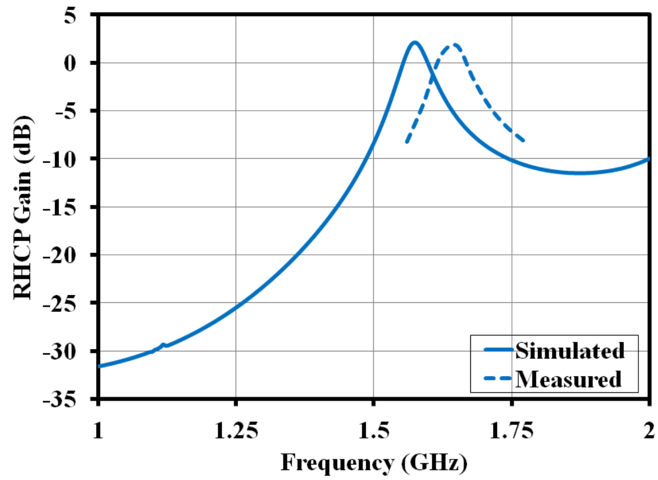

Figure 5.38: Simulated and measured RHCP gain of single-band RDRA [6]

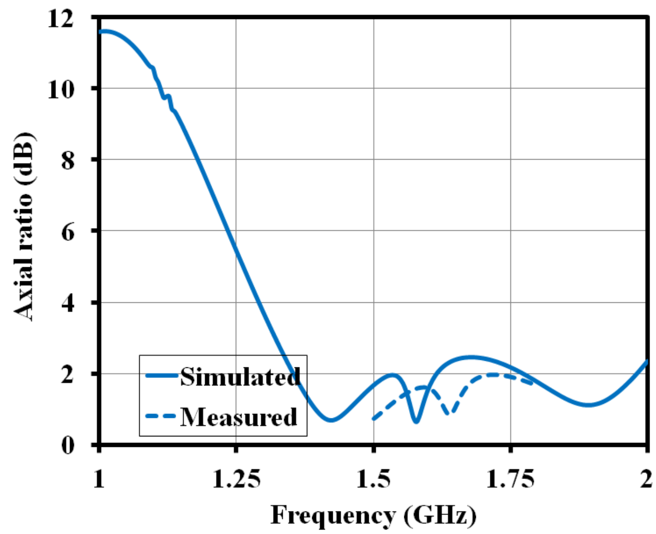

Figure 5.39: Simulated and measured axial ratio of single-band RDRA [6]

Table 5.5: Simulated RHCP gain and axial ratio of single-band RDRA for L1-band [6]

Parameters	**L1-Band**
RHCP Gain at $\theta = 0^0$	2.05 dB
RHCP Gain at $\theta = \pm 60^0$	-1.00 dB
RHCP Gain at $\theta = \pm 70^0$	-3.00 dB
RHCP Gain at $\theta = \pm 80^0$	-3.98 dB
Axial Ratio at $\theta = 0^0$ to $\pm 50^0$	< 3 dB

5.4.3 Single-Band Rectangular Dielectric Resonator Antenna at L5-Band

The simulated and measured return loss are found to be better than 14 dB over L5-band as shown in Figure 5.40 [6]. The dielectric resonator material ($\epsilon_r = 51.92$) was obtained from TCI Ceramics (Division of National Magnetics Group, Bethlehem, PA, USA). The dielectric constant of this material was measured as $\epsilon_r = 47.35$ at 5 GHz using RDWG method [7, 8]. The simulated and measured return loss of single-band RDRA are matched except a slight shift in resonance frequencies. This shift in center frequencies is due to difference between prescribed dielectric constant (ϵ_r= 51.92) provided by the manufacturer and measured dielectric constant (ϵ_r= 47.35) of DR material.

The simulated and measured RHCP-LHCP radiation patterns at ϕ=0° are given in Figure 5.41 over L5-band. For ϕ=45°, simulated and measured RHCP-LHCP radiation patterns are shown in Figure 5.42 over L5-band. In single-band RDRA, Figure 5.43 shows simulated and measured RHCP-LHCP radiation patterns at ϕ=90° over L5-band. RHCP-LHCP radiation patterns are obtained broadside over L5-band. Figure 5.44 shows simulated and measured RHCP gain of single-band RDRA for L5-band.

The simulated and measured axial ratio of single-band RDRA for L5-band are depicted in Figure 5.45. The reduction of HPBW and multiple ripples in measured RHCP-LHCP radiation patterns are observed due to bakelite support, fixture pipe and mounting fixture in the anechoic chamber (Figure 5.27). The simulated RHCP gain and axial ratio of single-band RDRA for L5-band are shown in Table 5.6 [6]. The measured RHCP-LHCP radiation patterns, RHCP gain and axial ratio are mismatched because of error introduced by bakelite support, fixture pipe and mounting fixture in the anechoic chamber (Figure 5.27).

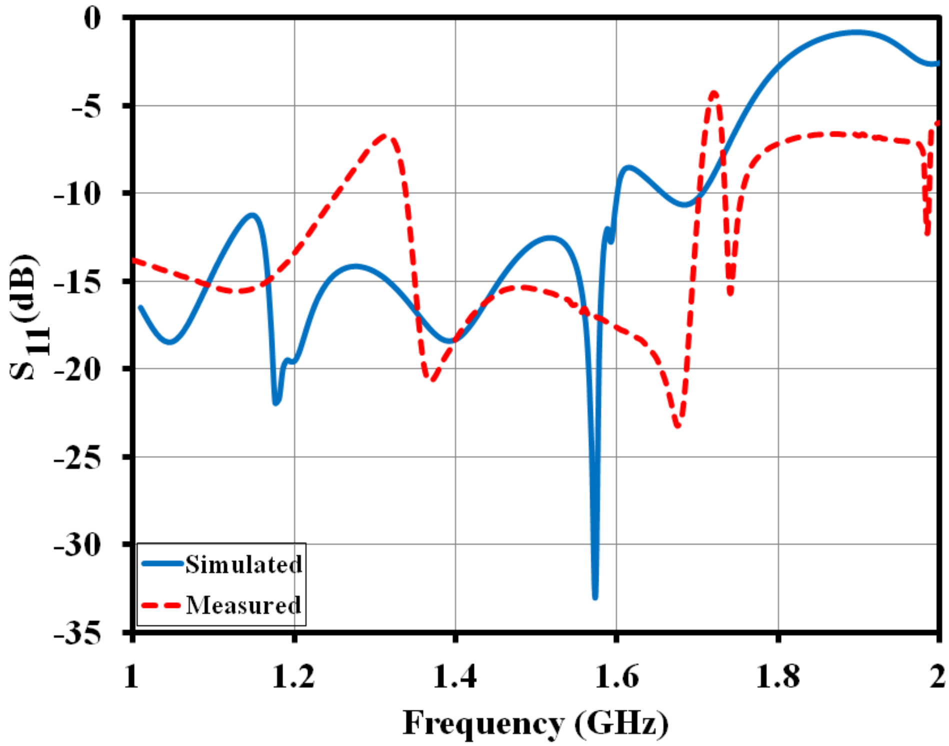

Figure 5.40: Simulated and measured S_{11} of single-band RDRA [6]

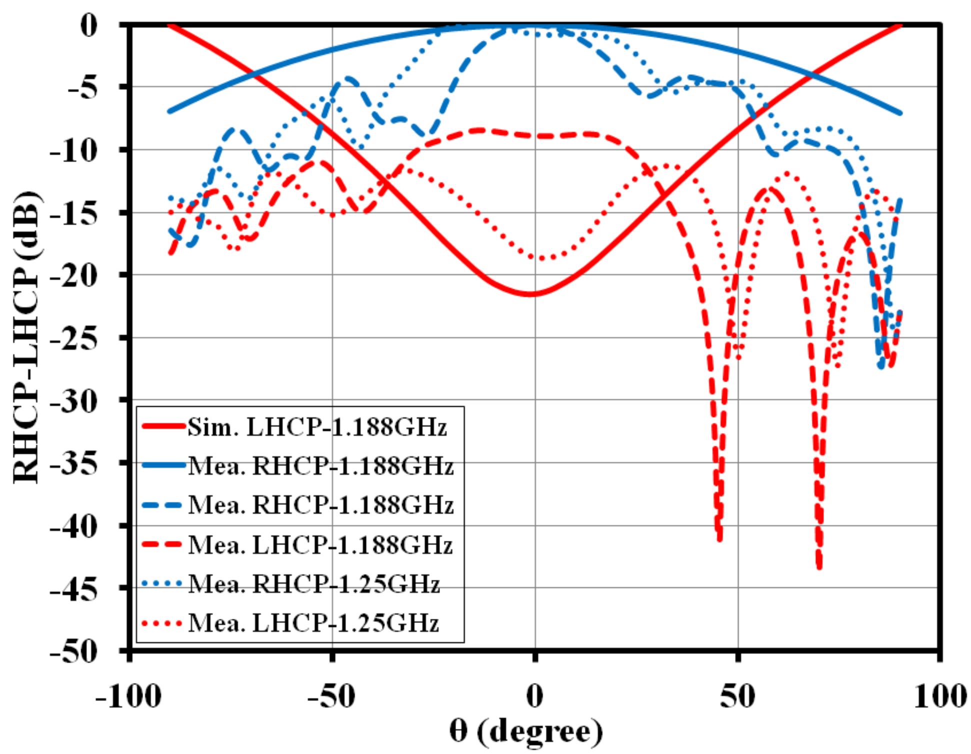

Figure 5.41: Simulated and measured RHCP-LHCP far field radiation patterns for L5-band at ϕ=0° [6]

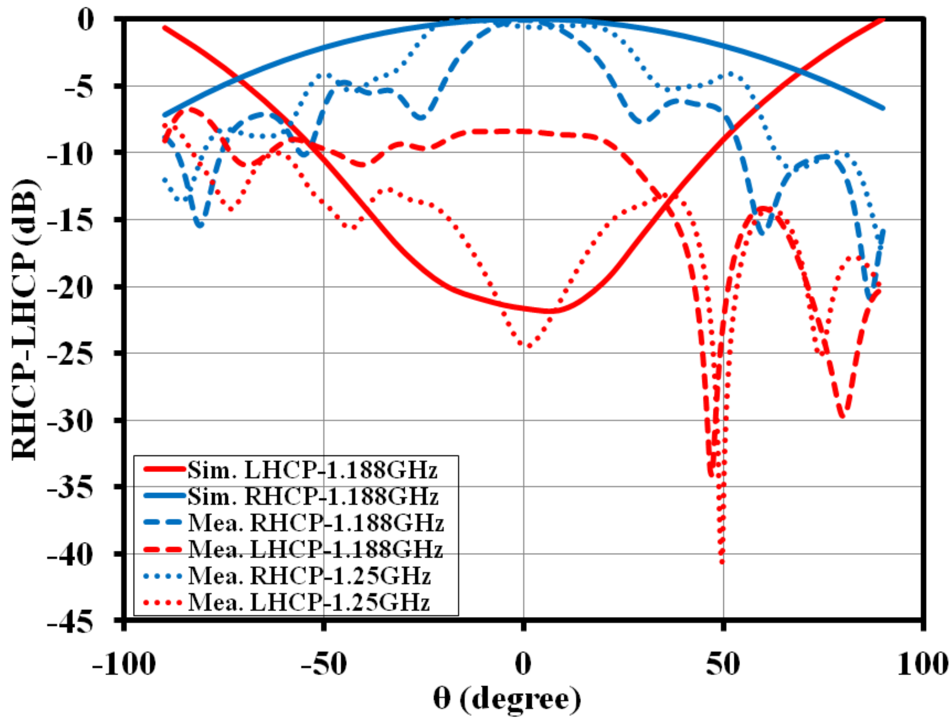

Figure 5.42: Simulated and measured RHCP-LHCP far field radiation patterns for L5-band at ϕ=45° [6]

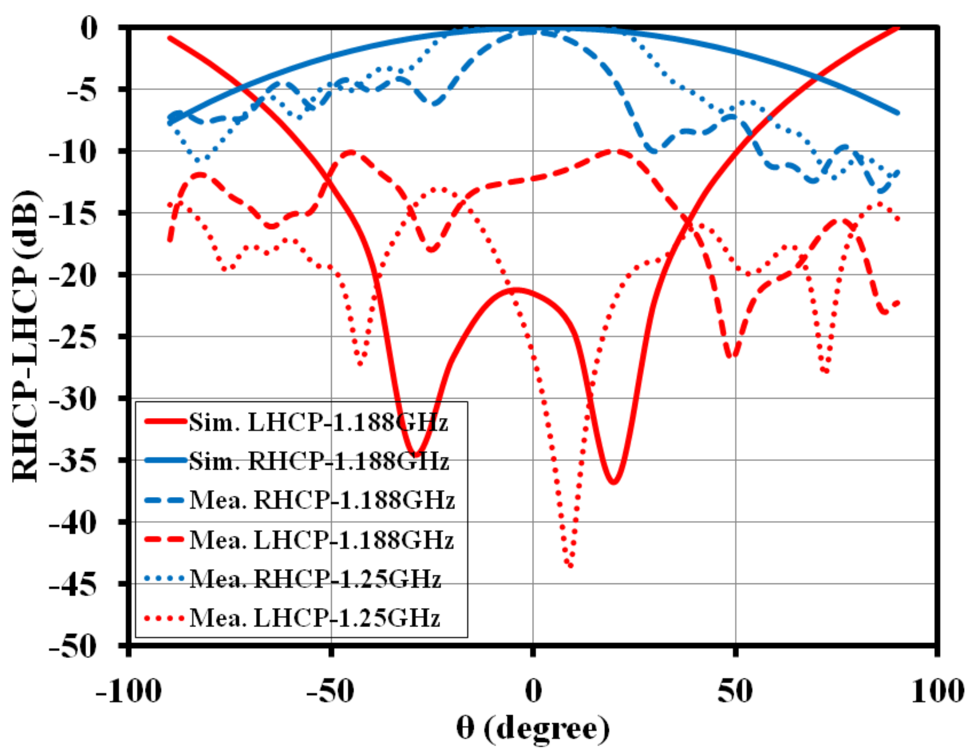

Figure 5.43: Simulated and measured RHCP-LHCP far field radiation patterns for L5-band at ϕ=90° [6]

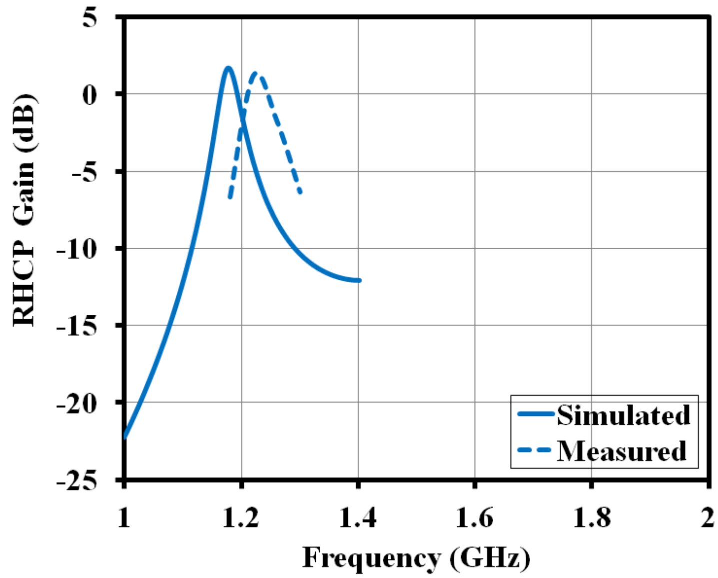

Figure 5.44: Simulated and measured RHCP gain of single-band RDRA [6]

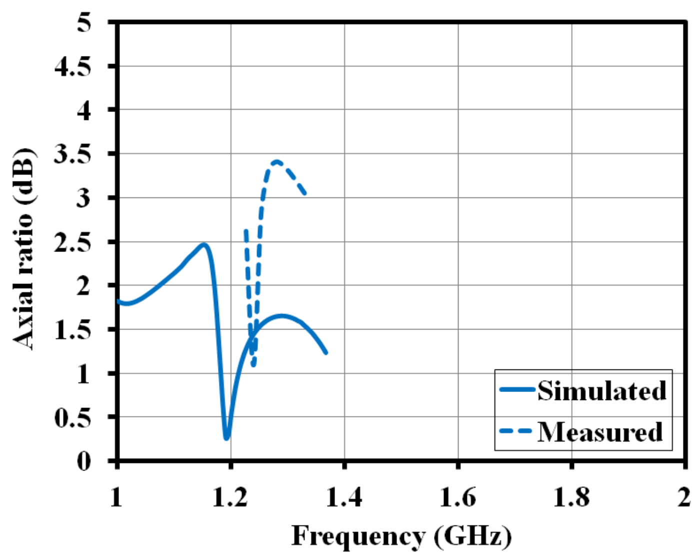

Figure 5.45: Simulated and measured axial ratio of single-band RDRA [6]

Table 5.6: Simulated RHCP gain and axial ratio of single band RDRA for L5-band

Parameters	L5-Band
RHCP Gain at $\theta = 0^0$	1.6 dB
RHCP Gain at $\theta = \pm 60^0$	-1.0 dB
RHCP Gain at $\theta = \pm 70^0$	-2.5 dB
RHCP Gain at $\theta = \pm 80^0$	-3.35 dB
Axial Ratio at $\theta = 0^0$ to $\pm 50^0$	$<$ 3 dB

5.5 Conclusions and Discussion of Results

Table 5.7 shows comparison of single-band RDRAs with published research work. The ground plane and radiated areas of single-band RDRAs are miniaturized using high dielectric constant (ϵ_r= 20.4 and 51.92) of DR material and high dielectric constant (ϵ_r = 10.2) of dielectric substrate (Rogers RO3210). Both the ground plane and the radiated areas of single-band RDRAs are much lower than published research work. The compact single-band RDRAs are designed, analyzed, fabricated and tested for S, L1 and L5-bands. The simulated and measured results of single-band RDRAs are in closed agreement except a small shift in center frequencies. This is due to difference between prescribed dielectric constant (ϵ_r= 51.92) provided by the manufacturer and measured dielectric constant (ϵ_r= 47.35) of DR material.

Table 5.7: Comparison of single-band RDRAs with published research work

Reference	**[9]**	**[10]**	**[11]**	**L1-band**	**L5-band**	**S-band**
Antenna type	DRA	DRA	DRA	DRA	DRA	DRA
Shape of DR	CDR	RDR	Hollow RDR	RDR	RDR	RDR
Feed	Four port strips	Aperture	Quadrature coupler	WPD with PS	WPD with PS	WPD with PS
ϵ_r **of DR**	9.9	30	10	**51.92**	**51.92**	**20.4**
ϵ_r **of substrate**	-	4.4	6.15	**10.2**	**10.2**	**10.2**
Mode	- TE_{111}, quasi-TM_{21}, quasi-TE_{111}	-	TE_{111}	TE^y_{111}	TE^y_{111}	TE^y_{111}
Polarization	RHCP	CP	LHCP	RHCP	RHCP	RHCP
Radiation pattern	Broadside	Broadside	Broadside	Broadside	Broadside	Broadside
Resonance frequencies f_1 **(GHz)**	1.275	0.866	2.4	1.575	1.176	2.490
Ground plane area (λ_0^2) **at** f_1	0.113	0.120	0.922	**0.022**	**0.0246**	**0.0433**
Radiator area (λ_0^2) **of DRA**	0.054	0.0121	0.0645	**0.0090**	**0.00821**	**0.0225**
Height (λ_0) **of DRA**	0.102	0.0867	0.0269	0.132	0.101	0.108
RL (dB)	10	20	12	20	15	25
Gain (dB)	4.5	3.75	6.0	2.05	1.6	2.9
AR (dB)	0.1	1.0	0.2	1.0	1.7	1.0

References

[1] Pankaj Chaudhary, D. K. Ghodgaonkar, Sanjeev Gupta and G. D. Makwana, "Design of compact circularly polarized rectangular dielectric resonator antenna with WBLC for navigational satellite applications," *2017 IEEE International Conference on Antenna Innovations and Modern Technologies for Ground, Aircraft and Satellite Application (iAIM)*, pp.1-5, 24 – 26 November 2017, Bangalore, India.

[2] X. S. Fang, C. K. Chow, K. W. Leung and E. H. Lim, "New single-/dual-mode design formulas of the rectangular dielectric resonator antenna using covariance matrix adaptation evolutionary strategy," *IEEE Antennas and Wireless Propagation Letters*, vol. 10, pp. 734-737, 2011.

[3] R. Han, S. Zhong and J. Liu, "Design of circularly-polarized dielectric resonator antenna with wideband feed network," *Proceedings of 2014 3rd Asia-Pacific Conference on Antennas and Propagation*, Harbin, 2014, pp. 48-50.

[4] S.Y.Eom and H.K.Park, "New switched-network phase shifter with broadband characteristics," *Microwave and Optical Technology Letters*, vol. 38, no. 4, pp. 255-257, August 2003.

[5] Ansys High Frequency Structure Simulator (HFSS) is a 3-D Electromagnetic (EM) simulation software for designing and simulating high-frequency electronic products such as antennas, antenna arrays, Radio Frequency (RF) or microwave components, high-speed interconnects, filters, connectors, Integrated Circuit (IC) packages and printed circuit boards. https://www.ansys.com/en-in/products/electronics/ansys-hfss

[6] P. Chaudhary, D. K. Ghodgaonkar, S. Gupta, R. Jyoti and M. B. Mahajan, "Miniaturized L1 and L5-bands circularly polarized rectangular dielectric resonator antennas for navigation satellite applications," will be submitted in *Indian Conference on Antenna and Propagation*, 2021.

[7] R. Vashisth, D. Ghodgaonkar and S. Gupta,"Design and Fabrication of Broadband Microwave Absorber using FSS embedded in CISR sheets," *2018 IEEE MTT-S International Microwave and RF Conference (IMaRC)*, Kolkata, India, Dec 2018, pp. 1-4.

[8] Z. Abbas, R.D. Pollard and R.W. Kelsall, "Complex permittivity measurements at Ka-band using rectangular dielectric waveguide," *IEEE Transactions on Instrumentation and Measurement*, Vol.50, no. 5, pp. 1334-1342, October 2001.

[9] S. Jović, M. Clénet and Y. M. M. Antar, "A compact wideband 4-port circularly polarized dielectric resonator antenna," *2017 11th European Conference on Antennas and Propagation (EUCAP)*, Paris, 2017, pp. 1957-1959.

[10] H. Raggad, M. Latrach, A. Gharsallah, T. Razban, “Circularly polarization rectangular dielectric resonator antenna for UHF RFID applications,” *2013 IEEE-APS Topical Conference on Antennas and Propagation in Wireless Communications (APWC)*, 9-13 September 2013, Torino, Italy, pp.1469 – 1472.

[11] E. H. Lim, K. W. Leung and X. S. Fang, "The compact circularly-polarized hollow rectangular dielectric resonator antenna with an underlaid quadrature coupler," *IEEE Transactions on Antennas and Propagation*, vol. 59, no. 1, pp. 288-293, Jan. 2011.

Chapter 6

Design and Analysis of Effect of Finite Ground Plane on Circularly Polarized Single and Dual-Band Rectangular Dielectric Resonator Antennas

6.1 Design and Analysis of Finite Ground Plane Circularly Polarized Single-Band Rectangular Dielectric Resonator Antennas

6.1.1 Introduction

In analysis of DRA, the conducting ground plane is assumed to be infinite [1, 2]. Circularly Polarized (CP) single-band Rectangular Dielectric Resonator Antennas (RDRAs) are analyzed for finite ground plane using reference [3]. The finite ground plane area of CP single-band RDRAs for L5 and L1-bands were reduced to 25 mm × 25 mm using high dielectric constant (ϵ_r= 100) of dielectric resonators and high dielectric constant (ϵ_r= 10.2) of dielectric substrates (Rogers R03210) [4]. The volume of Rectangular Dielectric Resonators (RDRs) for L5 and L1-bands are 16.9 mm × 16.9 mm × 65 mm and 12.8 mm × 12.8 mm × 28 mm, respectively. The Right Hand Circular Polarization (RHCP) of RDRAs for L5 and L1-bands are generated using Wilkinson Power Dividers (WPDs) with wide-band 90° phase shifters [4]. The single-band RDRAs for L5 and L1-bands consists of RDR, dielectric substrate, WPD with 90° phase shifter, ground plane and two vertical feeding probes.

Port-1 is the input port of RDRAs for L5 and L1-bands. Port-2 and port-3 of WPD with wide-band 90° phase shifter are connected to two vertical feeding probes [4]. The design specifications for single-band RDRAs are given in Table 1.1. The simulated parameters of RDRAs for L5 and L1-bands are return loss, RHCP-LHCP radiation patterns, RHCP gain and axial ratio.

6.1.2 Design and Analysis

The geometries of RDRAs for L5 and L1-bands are shown in Figure 6.1 (a) and 6.1 (b), respectively. By assuming aspect ratios $\frac{H}{L}$=3.84, $\frac{W}{L}$=1.0 and ϵ_r=100, L, W and H for L5-band RDR are 16.9 mm, 16.9 mm and 65.0 mm respectively, as obtained using equations (1) to (4) from reference [5]. For L1-band RDR, L, W and H are 12.8 mm, 12.8 mm and 28.0 mm respectively, obtained using equation (1) to (4) from reference [5] by assuming aspect ratios $\frac{H}{L}$=2.18, $\frac{W}{L}$=1.0 and ϵ_r=100. The ground plane areas ($W_g \times L_g$) of L5 and L1-bands RDRAs are 25 mm × 25 mm [4].

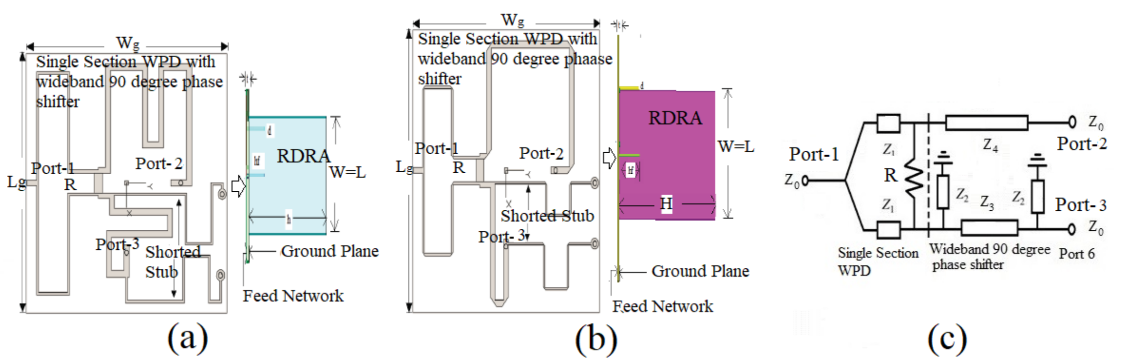

Figure 6.1: Geometries of single-band RDRAs (a) L5-band RDRA (b) L1-band RDRA and (c) schematic of feed network [4]

The schematic of WPD with wide-band 90° phase shifter is shown in Figure 6.1 (c) [4]. The feed networks for L5 and L1-bands are printed on bottom face of the dielectric substrates. The ground planes are placed on top faces of the dielectric substrates which are connected to the RDRs for both L5 and L1-bands. The height and diameter of vertical feeding probes for L5-band are 5.5 mm and 0.5 mm, respectively. For L1-band, the height and diameter of vertical feeding probes are 6.52 mm and 0.5 mm, respectively.

The characteristic impedance Z_1 and resistance R are obtained using equation (3.30) and (3.31), respectively [4]. The characteristic impedance Z_2 is calculated using equation (3.32) [4]. The characteristic impedances Z_3 and Z_4 are equal to Z_0 [4]. Z_1, Z_2 and Z_3 are characteristic impedances of quarter wavelength transmission lines. Z_4 is the characteristic impedance of half wavelength transmission line. The value of resistance R is equal to 100 Ω.

The characteristic impedances Z_1, Z_2, Z_3 and Z_4 for L5 and L1-bands are 70.7 Ω, 76 Ω, 50 Ω and 50 Ω, respectively. l_1, l_2, l_3 and l_4 which are lengths of microstrip lines for L5-band are 27.68 mm, 25.35 mm, 28.5 mm and 49.8 mm, respectively. l_1, l_2, l_3 and l_4 which are lengths of microstrip lines for L1-band are 21.18 mm, 19.3 mm, 19.4 mm and 36.9 mm, respectively. w_1, w_2, w_3 and w_4 which are widths of microstrip lines for L5 and L1-bands are 0.25 mm, 0.2 mm, 0.6 mm and 0.6 mm, respectively [4].

6.2 Analysis of Dual and Single-Band Rectangular Dielectric Resonator Antennas using Method of Moments

In analysis of DRA, the conducting ground plane is assumed to be infinite [1, 2]. For dual (L5 and L1) and single (L5)-bands CP RDRAs, Method of Moments (MoM) is used to analyze the effect of finite ground plane. The geometry of CP dual and single-band RDRAs is shown in Figure 6.2. The phase difference between port-1 and port-2 is 90^0 which generates RHCP. The effect of different radii of circular ground plane on dual and single-bands RDRAs are analyzed using MoM and reference [3]. The formulation of dual and single-band CP RDRAs using MoM is given in Appendix B. For different radii of finite ground plane, return loss, isolation, RHCP gain, radiation patterns and axial ratio are analyzed using MoM and reference [3].

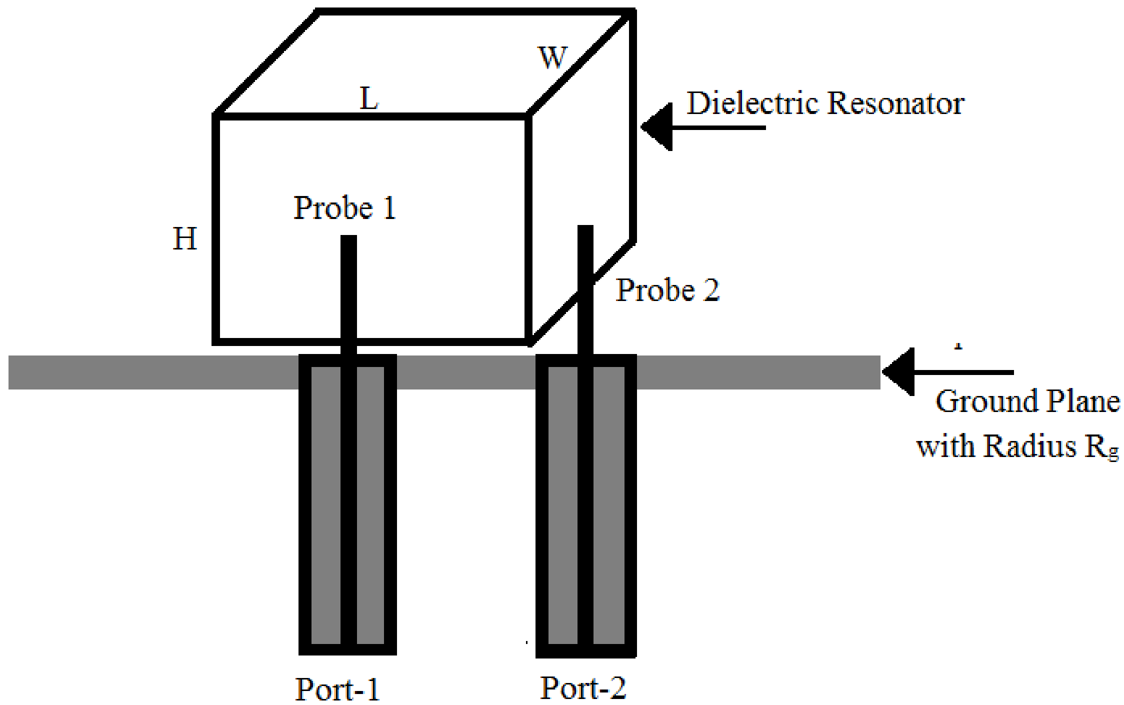

Figure 6.2: Geometry of CP dual and single-band RDRAs

6.3 Simulated Results

6.3.1 Finite Ground Plane Circularly Polarized Single-Band Rectangular Dielectric Resonator Antennas

Figure 6.3 (a) shows S_{11} of L5-band RDRA. S_{11} of L1-band RDRA is given in Figure 6.3 (b). The return loss of RDRAs are found to be better than 17 dB over L5 and L1-bands. The broadside radiation patterns for both L5 and L1-bands are shown in Figures 6.4 (a) and 6.4 (b), respectively. Figures 6.4 (a) and 6.4 (b) indicates simulated RHCP-LHCP radiation patterns at ϕ=0°, ϕ=45° and ϕ=90° for L5 and L1-bands RDRAs, respectively [4]. The simulated parameters of single and dual-band RDRAs for L5 and L1-bands are given in Table 6.1 [4].

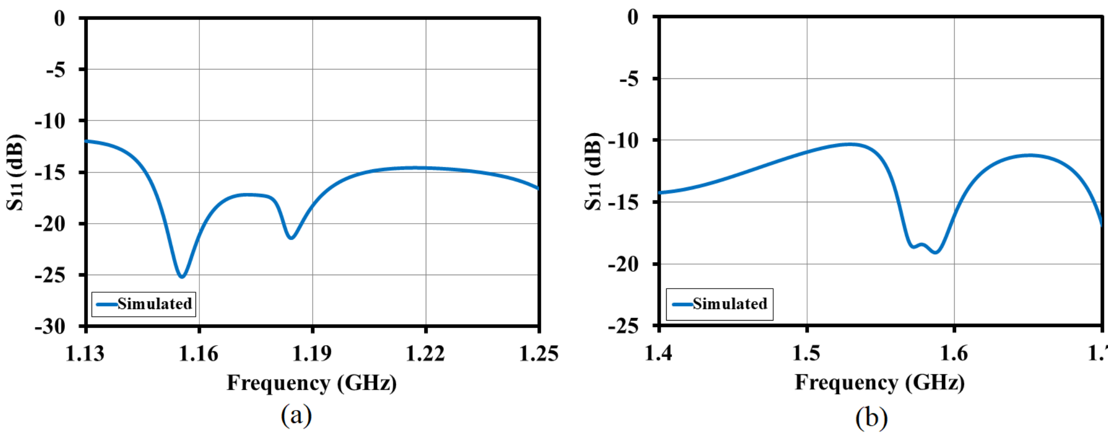

Figure 6.3: Simulated S_{11} of (a) L5-band RDRA and (b) L1-band RDRA [4]

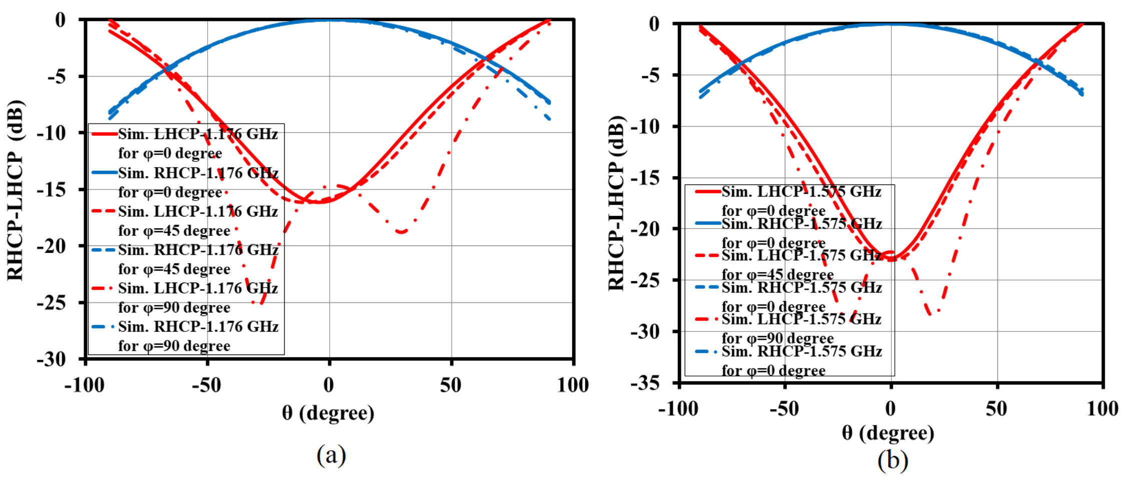

Figure 6.4: Simulated RHCP-LHCP far field radiation patterns of (a) L5-band RDRA and (b) L1-band RDRA [4]

Table 6.1: Simulated parameters of single-band CP RDRA for L1 and L5-bands [4]

Parameters	**L5-Band**	**L1-Band**
Return loss	Better than 17 dB	Better than 17 dB
Radiation pattern	Broadside	Broadside
Polarization	RHCP	RHCP
RHCP Gain at $\theta = 0^0$	3.5 dB	2.0 dB
RHCP Gain at $\theta = \pm 60^0$	-1.55 dB	-2.1 dB
RHCP Gain at $\theta = \pm 70^0$	-3.0 dB	-3.32 dB
RHCP Gain at $\theta = \pm 80^0$	-4.75 dB	-4.83dB
Axial Ratio at $\theta = 0^0$ to $\pm 50^0$	< 3 dB	< 3 dB

6.3.2 Dual and Single-Band Rectangular Dielectric Resonator Antennas using Method of Moments

Figure 6.5 (a) shows comparison S_{11} of dual-band RDRAs in L5 and L1-bands using reference [3] and MoM. S_{12} of dual-band RDRA is obtained using reference [3] and MoM as shown in Figure 6.5 (b). S_{22} and S_{21} of dual-band RDRA are given in Figures 6.6 (a) and 6.6 (b), respectively. Figures 6.7 (a) and 6.7 (b) present gain and axial ratio of dual-band RDRA, respectively. The normalized radiation patterns at 1.176 GHz using reference [3] and MoM are shown in Figures 6.8 (a) and 6.8 (b), respectively. The normalized radiation patterns at 1.575 GHz using reference [3] and MoM are given in Figures 6.9 (a) and 6.9 (b), respectively. The broadside radiation patterns are achieved in dual-band RDRA.

S_{11}, S_{12}, S_{22} and S_{21} of single-band RDRA for L5-band are viewed in Figures 6.10 (a), 6.10 (b), 6.11 (a) and 6.11 (b), respectively. For single-band RDRA using reference [3] and MoM, gain, axial ratio, normalized radiation patterns at 1.176 GHz are demonstrated in Figures 6.12 (a), 6.12 (b), 6.13 (a) and 6.13 (b), respectively. The broadside radiation patterns are obtained at 1.176 GHz in single-band RDRA. Table 6.2 shows return loss and gain of dual and single-band RDRAs at L5-band for different radii of circular ground planes. The return loss and gain of dual-band RDRA at L1-band are given in Table 6.3 for different radii of ground planes.

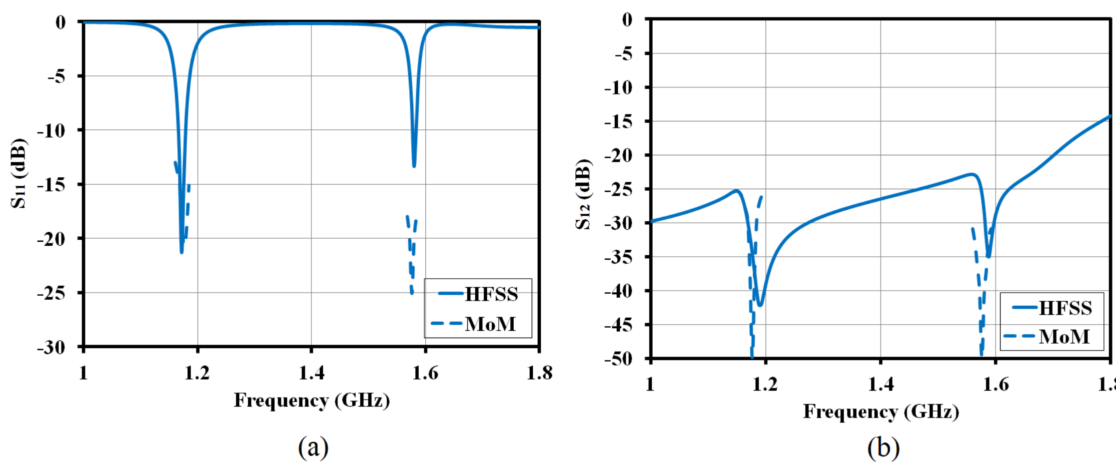

Figure 6.5: (a) S_{11} and (b) S_{12} of dual-band RDRA using reference [3] and MoM

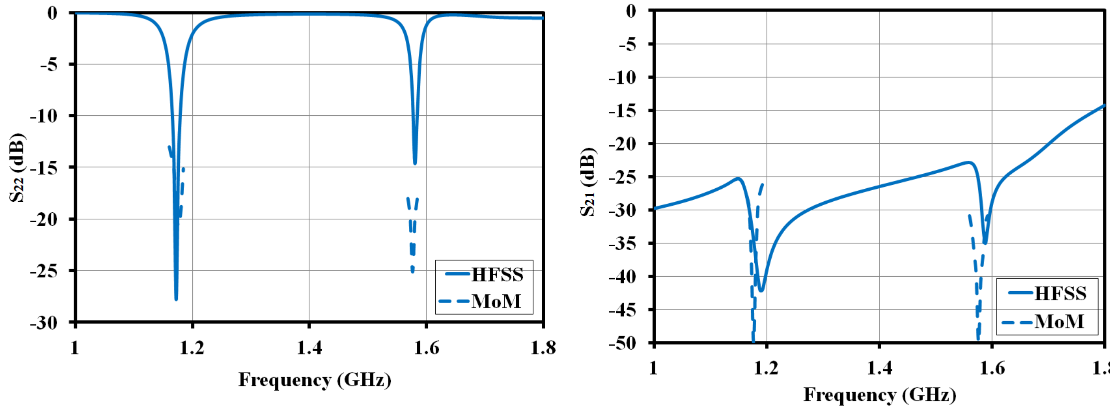

(a) (b)

Figure 6.6: (a) S_{22} and (b) S_{21} of dual-band RDRA using reference [3] and MoM

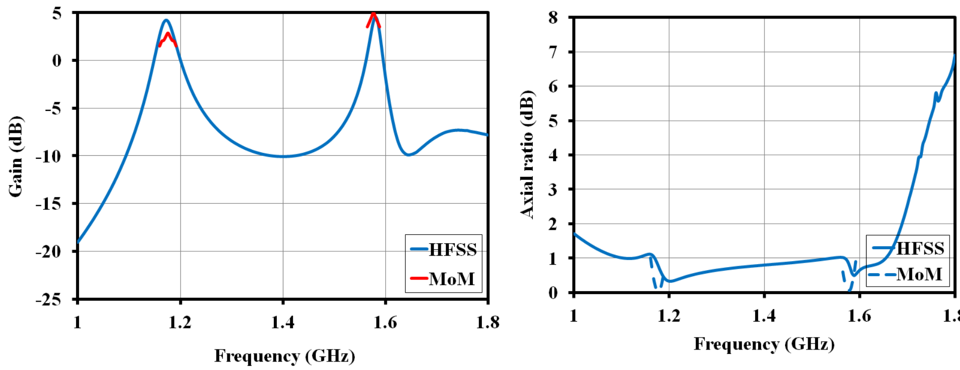

(a) (b)

Figure 6.7: (a) Gain and (b) axial ratio of dual-band RDRA using reference [3] and MoM

The return loss at port-1 and port-2 of dual- and single-band RDRAs using reference [3] are found to be better than 10 dB over L5 and L1-bands. Using MoM, the return loss at port-1 and port-2 of dual- and single-band RDRAs are obtained to be better than 20.72 dB over L5 and L1-bands. $|S_{21}|$ and $|S_{12}|$ of dual- and single-band RDRA using reference [3] are found to be better than 30 dB over L5 and L1-bands. Using MoM, $|S_{21}|$ and $|S_{12}|$ of dual- and single-band RDRAs are found to be better than 40 dB over L5 and L1-bands.

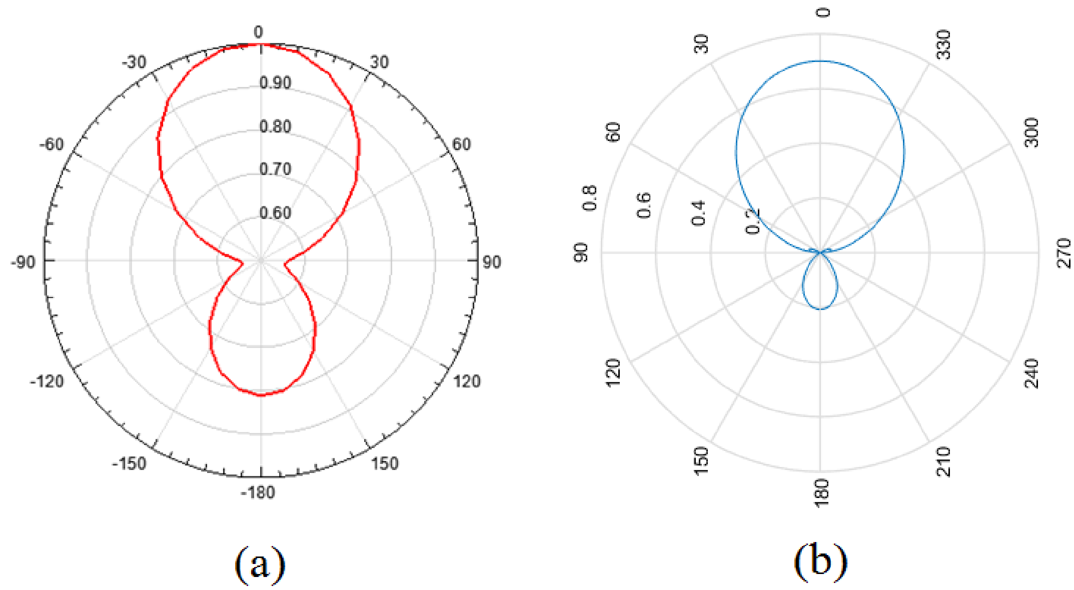

Figure 6.8: (a) Normalized electric field radiation patterns at 1.176 GHz of dual-band RDRA using reference [3] (b) Normalized electric field radiation patterns at 1.176 GHz of dual-band RDRA using MoM

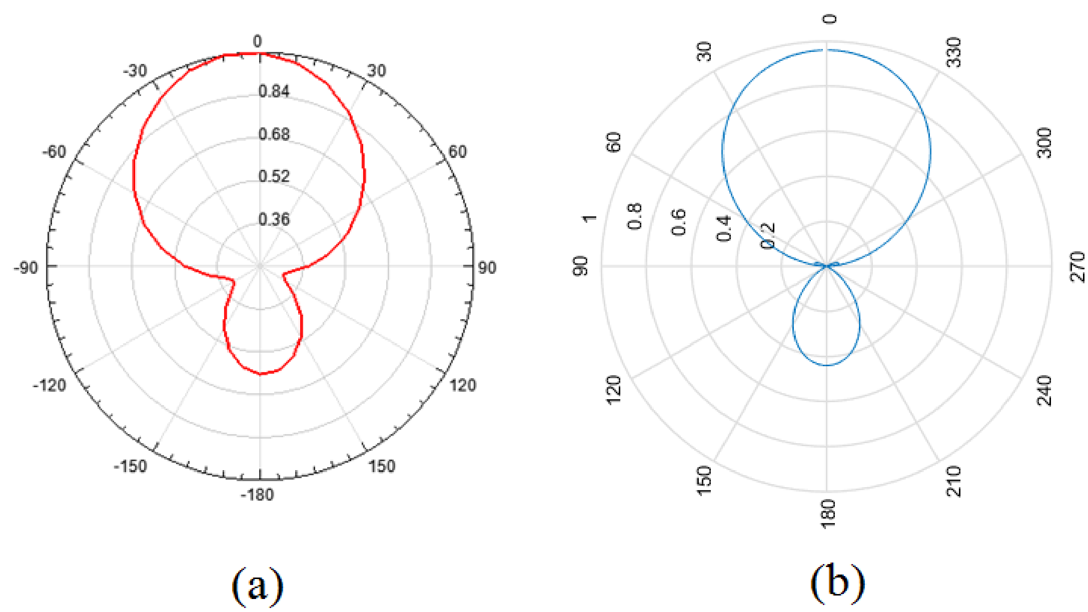

Figure 6.9: (a) Normalized electric field radiation patterns at 1.575 GHz of dual-band RDRA using refernce [3] (b) Normalized electric field radiation patterns at 1.575 GHz of dual-band RDRA using MoM

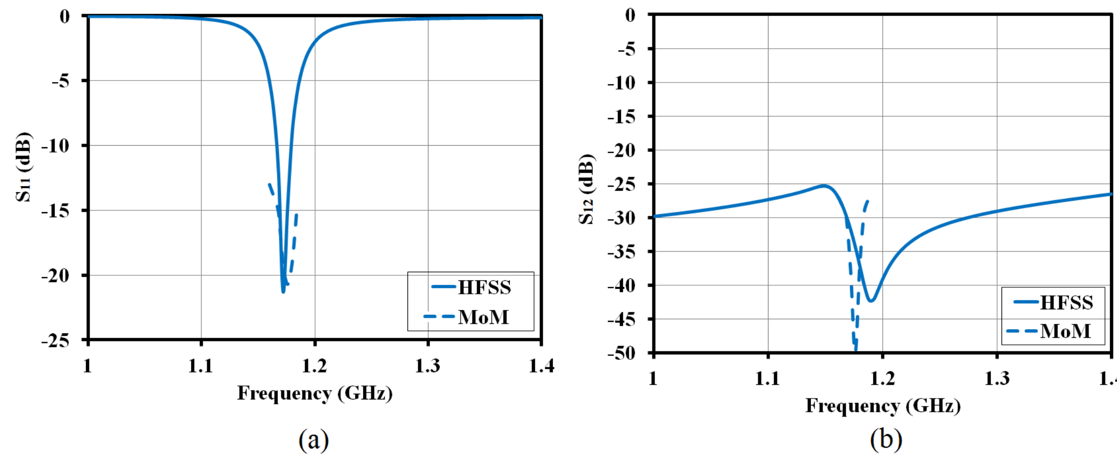

Figure 6.10: (a) S_{11} and (b) S_{12} of single-band RDRA using reference [3] and MoM

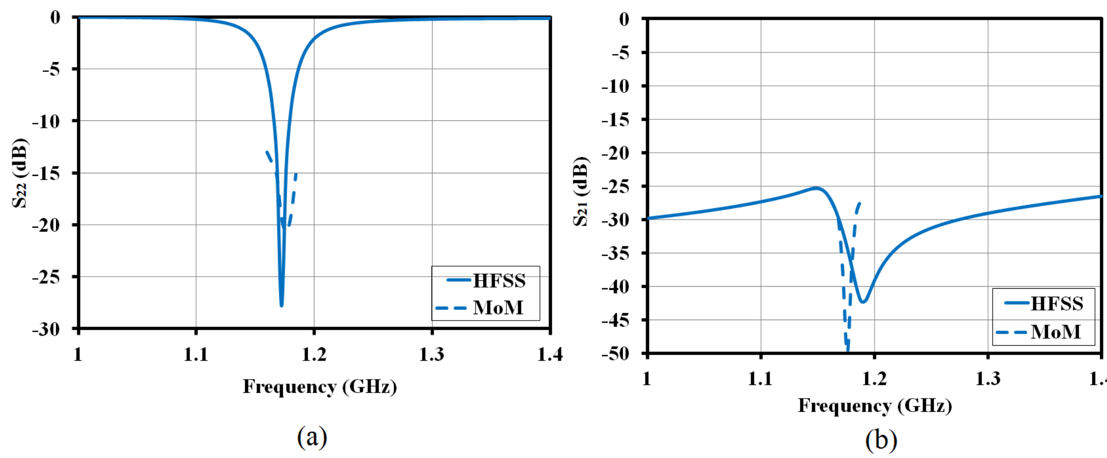

Figure 6.11: (a) S_{22} and (b) S_{21} of single-band RDRA using reference [3] and MoM

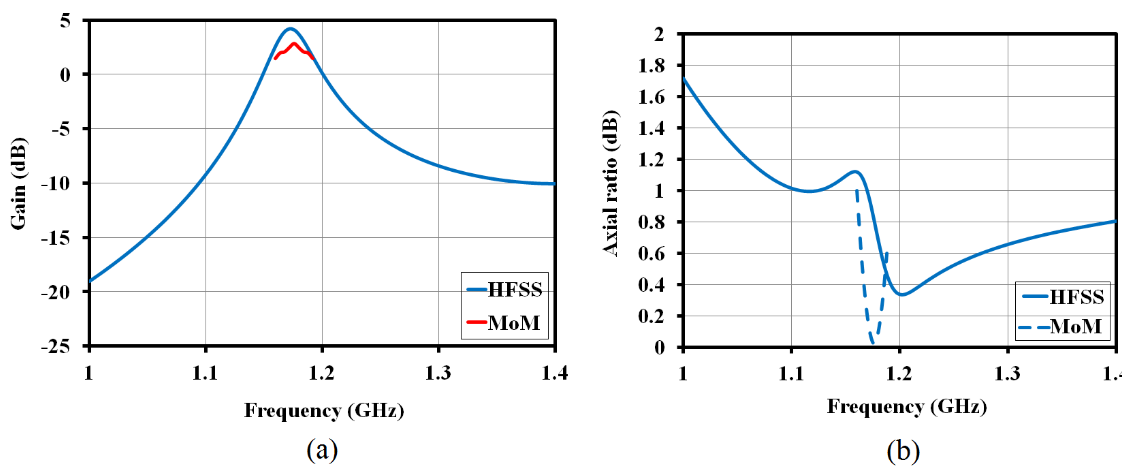

Figure 6.12: (a) Gain and (b) axial ratio of single-band RDRA using reference [3] and MoM

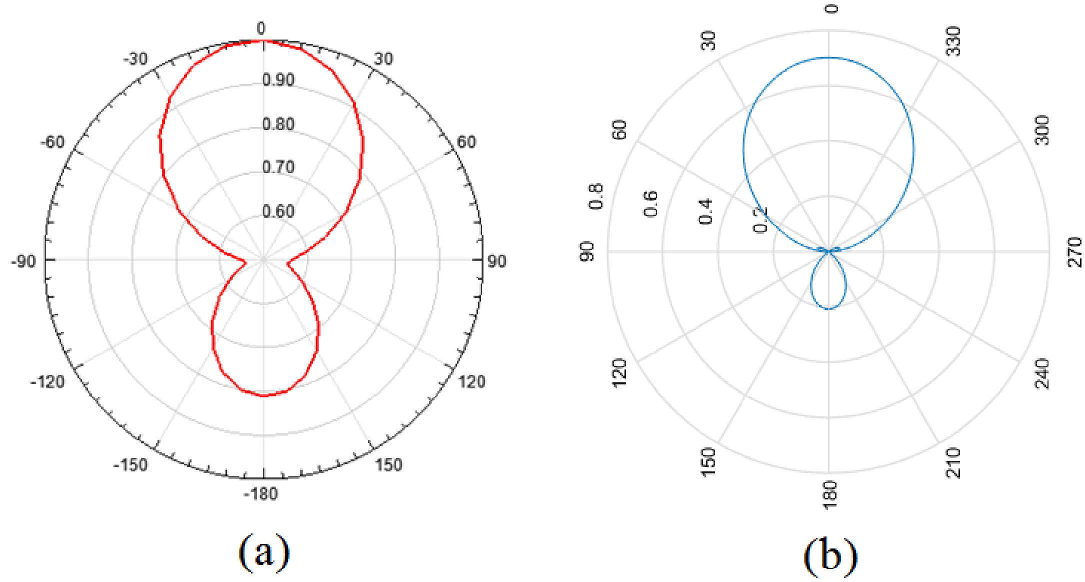

Figure 6.13: (a) Normalized electric field radiation patterns at 1.176 GHz of single-band RDRA using reference [3] (b) Normalized electric field radiation patterns at 1.176 GHz of single-band RDRA using MoM

Table 6.2: Effect of different radii of finite ground plane in dual- and single-band RDRAs for L5-band

R_g (mm)	RL (HFSS)	RL (MoM)	Gain (HFSS)	Gain (MoM)
40	> 21.26 dB	> 20.72 dB	4.27 dB	2.86 dB
35	> 26.28 dB	> 30.77 dB	4.00 dB	1.02 dB
30	> 16.71 dB	> 27.20 dB	3.49 dB	-1.14 dB

Table 6.3: Effect of different radii of finite ground plane in dual-band RDRA for L1-band

R_g (mm)	RL (HFSS)	RL (MoM)	Gain (HFSS)	Gain (MoM)
40	> 13.31 dB	> 25.01 dB	4.76 dB	6.84 dB
35	> 17.16 dB	> 42.22 dB	4.58 dB	5.12 dB
30	> 21.14 dB	> 21.92 dB	4.21 dB	3.06 dB

6.4 Conclusions and Discussion of Results

In section 6.1, single-band RDRAs are analyzed using reference [3]. The ground plane and radiated areas of single-band RDRAs are miniaturized using high dielectric constant (ϵ_r= 100) of dielectric resonator material and high dielectric constant (ϵ_r =

10.2) of dielectric substrate (Rogers RO3210). In section 6.1.1, the simulated results of single-band RDRAs are matched with design specifications.

In section 6.2, dual- and single-band RDRAs are analyzed using reference [3] and MoM. The radiated areas of dual- and single-band RDRAs are reduced using high dielectric constant (ϵ_r= 51.92) of dielectric resonator material. In Tables 6.2 and 6.3, the effect of different radii circular ground planes of dual- and single-band RDRAs are observed for L5 and L1-bands. The gain of dual- and single-band RDRAs using reference [3] and MoM are found to be better than 2.86 dB over L5 and L1-bands. Using reference [3] and MoM, axial ratio of dual- and single-band RDRAs are obtained to be lower than 0.5 dB over L5 and L1-bands. The gain of dual- and single-band RDRAs are increased due to increasing radius of finite ground plane.

References

[1] Y. W. Poon and W. Y. Tam, "A rigorous analysis of a dielectric resonator antenna on a finite ground plane," *IEEE Antennas and Propagation Society International Symposium. 1996 Digest*, Baltimore, MD, USA, 1996, pp. 1938-1941 vol.3.

[2] W. Y. Tam and W. Y. Poon, "Analysis of rectangular dielectric resonator antenna on a finite size ground plane," *Proceedings of 1997 Asia-Pacific Microwave Conference*, Hong Kong, 1997, pp. 1169-1171 vol.3.

[3] Ansys High Frequency Structure Simulator (HFSS) is a 3-D Electromagnetic (EM) simulation software for designing and simulating high-frequency electronic products such as antennas, antenna arrays, Radio Frequency (RF) or microwave components, high-speed interconnects, filters, connectors, Integrated Circuit (IC) packages and printed circuit boards. https://www.ansys.com/en-in/products/electronics/ansys-hfss

[4] P. Chaudhary, D. K. Ghodgaonkar, S. Gupta and G. D. Makwana, "Design of compact circularly polarized rectangular dielectric resonator antenna with finite ground planes for navigational satellite applications," *10th International Conference of Antenna Test and Measurement Society (ATMS-2017)*, Hyderabad, India, 7 - 8 February 2017, pp. 221-225.

[5] A. Rashidian and D. M. Klymyshyn, "On the Two Segmented and High Aspect Ratio Rectangular Dielectric Resonator Antennas for Bandwidth Enhancement and Miniaturization," *IEEE Transactions on Antennas and Propagation*, vol. 57, no. 9, pp. 2775-2780, Sept. 2009.

Chapter 7

Conclusions and Future Work

7.1 Conclusions

Compact Circularly Polarized (CP) tri-, dual- and single-band Rectangular Dielectric Resonator Antennas (RDRAs) are designed, analyzed, fabricated and tested at L5, L1 and S-bands for navigation satellite applications. The Right Hand Circularly Polarized (RHCP) electromagnetic waves are generated using feed networks of tri-, dual- and single-sections Wilkinson Power Dividers (WPDs) with wide-band 90° phase shifters for tri-, dual- and single-band RDRAs, respectively. The feed networks of tri-, dual- and single-sections WPDs with wide-band 90° phase shifters are analyzed using reference [1].

The TE^y_{111}, TE^y_{113} and TE^y_{112} modes of tri-, dual- and single-band RDRAs are generated at center frequencies of 1.176 GHz, 1.575 GHz and 2.49 GHz, respectively. The broadside radiation patterns with multi-modes are produced by in simple geometries of staired RDRs for tri-band and RDR for dual-band. The simple structure of RDRs generates single modes with broadside radiation patterns at center frequencies of 1.176 GHz, 1.575 GHz and 2.49 GHz for L5, L1 and S-bands RDRAs, respectively.

The ground plane footprint areas of tri-, dual- and single (L5)-band RDRAs are miniaturized to 40 mm × 40 mm by using high dielectric constant (ϵ_r = 38.67 and 51.92) of Dielectric Resonator (DR) materials and high dielectric constant (ϵ_r = 10.2) of the dielectric substrates. Single-band RDRA for L1-band, ground plane footprint area is reduced to 28 mm × 28 mm by using high dielectric constant (ϵ_r

= 51.92) of DR material and high dielectric constant (ϵ_r = 10.2) of the dielectric substrate. The ground plane foot print area of 25 mm $\times$ 25 mm is achieved by using high dielectric constant (ϵ_r = 20.4) of DR material and high dielectric constant (ϵ_r = 10.2) of dielectric substrate for single-band RDRA for S-band.

The volumes of staired RDR (two port), staired RDR (single port) and RDR (dual-band) are miniaturized to 27 mm $\times$ 27 mm $\times$ 35.3 mm, 23.2 mm $\times$ 23.2 mm $\times$ 28.25 mm and 24.2 mm $\times$ 24.2 mm $\times$ 26.2 mm by using high dielectric constant (ϵ_r = 38.67 and 51.92) of DR materials, respectively. The volumes of RDRs for L5, L1 and S-bands are reduced to 23.1 mm $\times$ 23.1 mm $\times$ 28.0 mm, 18.0 mm $\times$ 18.0 mm $\times$ 25.0 mm and 18.2 mm $\times$ 18.2 mm $\times$ 13.0 mm by using high dielectric constant (ϵ_r = 51.92 and 20.4) of DR materials, respectively.

The measured return loss, RHCP-LHCP radiation patterns, RHCP gains and axial ratios of tri-, dual- and single-band RDRAs were found to be in close agreement with simulated results except shift in resonance frequencies due to inaccuracy in the measured and specified values of the dielectric constant of RDRs material and errors due to mounting fixture in the anechoic chamber.

The finite ground plane areas of 25 mm $\times$ 25 mm were obtained by using DR material of ϵ_r = 100 and high dielectric constant (ϵ_r = 10.2) of dielectric substrates for L5 and L1-bands CP RDRAs. The return loss, radiation patterns, RHCP gains and axial ratios are reported for L5 and L1-bands RDRAs. The effect of different radii of circular ground plane on CP single (L5) and dual (L5 and L1)-bands RDRAs are analyzed by Method of Moments (MoM) and reference [1] using high dielectric constant (ϵ_r = 51.92) of DR materials. The return loss, isolations, radiation patterns, gains and axial ratios of single- and dual-band RDRAs are compared using MoM and reference [1]. The effect of different radii of circular ground plane on single- and dual-band RDRAs are analyzed for return loss and gains. The gains of dual- and single-bands RDRAs increase with increasing radii of finite circular ground plane.

7.2 Proposed Future Work

This work can be further extended by designing and analyzing a compact wide-band linearly polarized DRA at UHF band with unidirectional radiation pattern and gain requirements better than 0 dB over entire band. The design can be improved further to ensure smooth gain variation with the frequency. This antenna can be analyzed using numerical methods such as MoM and Finite Difference Time Domain (FDTD).

Compact wide-band CP DRA can be designed for Global Navigation Satellite System (GNSS) and Radio-Frequency Identification (RFID) applications [2, 3].

Dual linear polarization DRA array can be designed for 5G and other millimeter wave (mm wave) frequency application [4, 5].

References

[1] Ansys High Frequency Structure Simulator (HFSS) is a 3-D Electromagnetic (EM) simulation software for designing and simulating high-frequency electronic products such as antennas, antenna arrays, Radio Frequency (RF) or microwave components, high-speed interconnects, filters, connectors, Integrated Circuit (IC) packages and printed circuit boards. https://www.ansys.com/en-in/products/electronics/ansys-hfss

[2] S. Jovic, M. Clenet and Y. M. M. Antar, " Novel wideband antenna for GNSS and satellite communication," *2020 14th European Conference on Antennas and Propagation (EuCAP)* , Copenhagen, Denmark, 2020, pp. 1-5.

[3] H. Raggad, M. Latrach, A. Gharsallah, T. Razban, "Circularly polarization rectangular dielectric resonator antenna for UHF RFID applications," *2013 IEEE-APS Topical Conference on Antennas and Propagation in Wireless Communications (APWC)*, 9-13 September 2013, Torino, Italy, pp.1469 – 1472.

[4] G. Federico, D. Caratelli, G. Theis and A. B. Smolders, "A Review of antenna array technologies for point-to-point and point-to-multipoint wireless communications at millimeter-wave frequencies," *International Journal of Antennas and Propagation*, vol. 2021, pp. 1-18, April 2021.

[5] M. Niayesh and A. Kouki, "LTCC-Integrated Dielectric Resonant Antenna Array for 5G Applications," *Sensors 2021*, vol.21, pp. 1-18, 2021

Appendix A

Measurement of Rectangular Dielectric Resonator Antennas

A.1 Measurement System

The measurement system, as shown in Figure A.1, is used for the measurement of the radiation patterns, gain and axial ratio of Circularly Polarized (CP) Rectangular Dielectric Resonator Antennas (RDRAs). This system operates over a wide range of frequencies and it is divided into five categories as given below [1, 2].

1. Source antenna and transmitting system
2. Test antenna and receiving system
3. Positioning system
4. Recording system
5. Data processing system

The source antenna is a large CP horn antenna. The transmitting system must be chosen so that it has frequency control, frequency stability, spectral purity, power level and modulation. The antennas to be tested are CP tri-, dual- and single-band RDRAs. The receiver system can be as simple as bolometer detector, followed by an amplifier and a recorder. The positioning system has the capability to rotate in various planes to achieve the desired plane cuts. There are primarily two types of recorders- linear (rectangular) plot and polar plot [1]. Recording data is then passed through the data processing system.

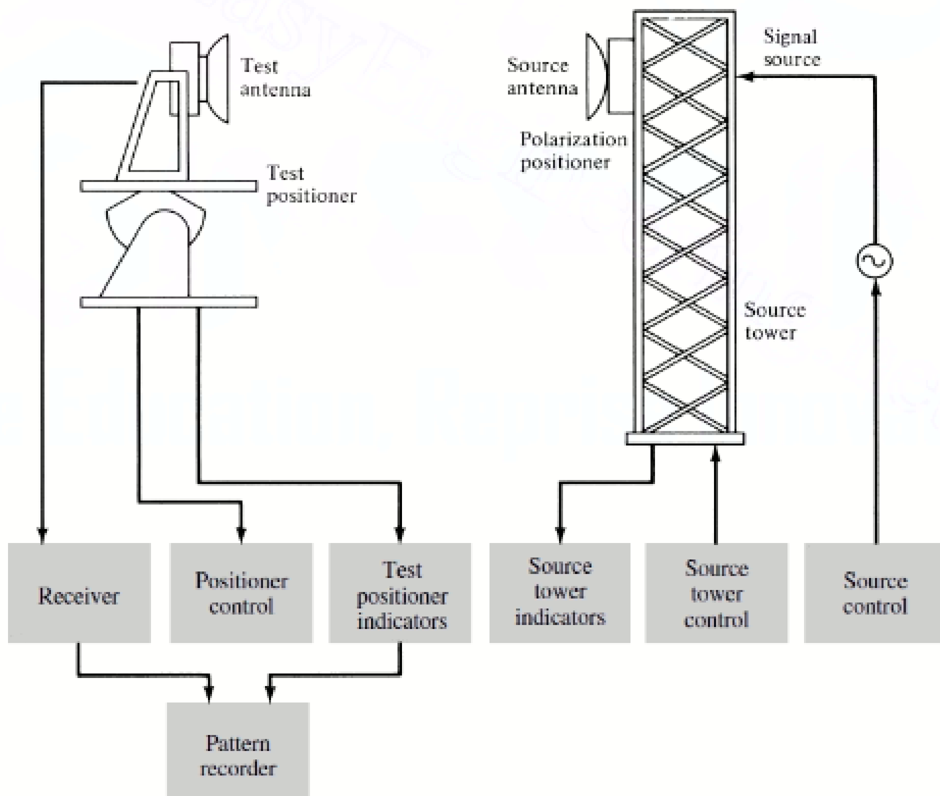

Figure A.1: Measurement system for CP RDRAs in the anechoic chamber [1]

A.2 Measurement of Radiation Patterns

In radiation patterns (amplitude and phase) measurement, two coordinates (θ, ϕ) are required for position identification. The radiation pattern of an antenna is defined as a representation of the radiation characteristics of the radiator as a function of θ and ϕ for a constant radial distance and frequency [1, 2]. Pattern cut refers as a two-dimensional radiation patterns. It is achieved by fixing one of angles (θ or ϕ) while varying the other. Pattern cuts are obtained by fixing ϕ=0^0, 45^0 and 90^0 and varying θ from -90^0 to -90^0.

A.3 Gain Transfer Method

The gain transfer method is used to measure the gain of the antenna. This method utilizes a gain standard (known gain) to determine absolute gains. Initially, the relative gain measurements are performed which are compared with the known gain of the CP standard antenna. Two sets of measurements are required in this procedure [1].

In first set, test CP antenna is used as the receiving antenna. The received power (P_T) into matched load is recorded. In second set, the test CP antenna is replaced by CP standard gain antenna. The received power P_S in to a matched load is recorded. The geometrical arrangement is maintained intact (only replacing the receiving antennas) in first and second sets. The input power is maintained the same. For free-space or reflection ranges, gain of the antenna under test can be expressed as [1]:

$$(G_T)_{dB} = (G_S)_{dB} + 10\log_{10}\left(\frac{P_T}{P_S}\right) \tag{A.1}$$

where G_S is gain of standard gain antennas.

A.4 Rotating Source Method

The axial ratio (and not the sense of polarization or the tilt angle) can be found as function of direction by using the rotating-source method. The method consists of continuously rotating source antenna as the direction of observation of the test antenna is changed [2].

This method has suitable for testing nearly circularly polarized antennas. The rotating source antenna causes the tilt angle τ_W of the incident field to rotate at the same rate. The rate of rotation τ_W shall be very much greater than that of θ or ϕ cuts are made and recorded [2].

References

[1] C. A. Balanis, "Antenna Theory: Analysis and Design," *John Wiley & Sons*, New York,USA, 1989.

[2] "IEEE Standard Test Procedures for Antennas," *ANSI/IEEE Std 149-1979*, vol., no., pp. 1-135, 1979.

Appendix B

Formulation of Antennas using Method of Moments and Energy Conservation

B.1 Formulation of Two Port Single- and Dual-Band Circularly Polarized Rectangular Dielectric Resonator Antennas

Two port single- and dual-band RDRAs consist of RDR with dielectric constant $\epsilon_r = 51.92$, ground plane with radius R_g, probe-1 of length L_{ant1} and radius R_{a1}, core-1, clad-1, internal dielectric-1 with dielectric constant $\epsilon_{intcoax1} = 2.1$, probe-2 of length L_{ant2} and radius R_{a2}, core-2, clad-2 and internal dielectric-2 with dielectric constant $\epsilon_{intcoax2} = 2.1$. Figure B.1 represents the geometry of two port single- and dual-band RDRAs. The dimension parameters of RDR are length L, width W and height H. Parameters of RDRAs are given in Table B.1. Probe-1 is connected to the SMA feed-1 with inner radius R_{a1}, outer radius R_{b1} and length of L_{sma1}. Probe-2 is attached to the SMA feed-2 with inner radius R_{a2}, outer radius R_{b2} and length L_{sma2}. Phase difference between port-1 of feed-1 and port-2 of feed-2 is 90° for generation of RHCP.

The radiation field of an antenna is determined as follows [1]:

1. Select the cartesian coordinate system.
2. Find magnetic vector potential from unknown currents [I] which are obtained

using MoM.

3. Calculate magnetic field intensity **H** and electric field intensity **E**.
4. Determine the far fields.

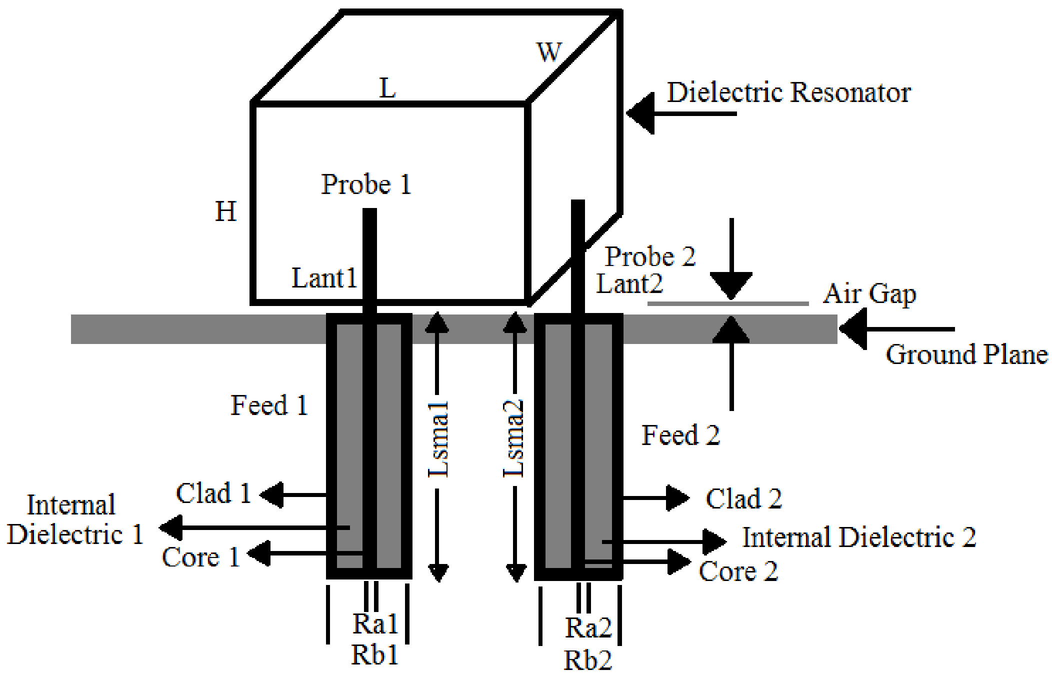

Figure B.1: Geometry of two port single- and dual-band CP RDRAs

The MoM is used to convert integral equations to linear system of equations by using boundary conditions [2, 3, 4, 5]. The formulation steps for RDRAs using MoM are given below.

- Step-1: Apply boundary conditions on single- and dual-band CP RDRAs. Basic Perfect Electric Conductor (PEC) boundary conditions will be considered for each metal parts of single- and dual-band CP RDRAs. The dielectric boundary conditions will be considered for each dielectric material parts of single- and dual-band CP RDRAs. PEC boundary condition applies on surface of probe-1 ($\hat{\rho} \times \vec{E}_{Total}$=0), core-1 ($\hat{z} \bullet \vec{E}_{Total}$=0), clad-1 ($\hat{z} \bullet \vec{E}_{Total}$=0), probe-2 ($\hat{\rho} \times \vec{E}_{Total}$=0), core-2 ($\hat{z} \bullet \vec{E}_{Total}$=0), clad-2 ($\hat{z} \bullet \vec{E}_{Total}$=0) and ground plane

Table B.1: Optimized dimensions of single- and dual-band RDRAs at L5 and L1-bands

Parameter	Dimensions
Lenght L of RDR	23.4 mm
Width W of RDR	23.4 mm
Height H of RDR	28.1 mm
Radius of ground plane R_g	40 mm
L_{ant1} and L_{ant2}	8.5 mm
L_{sma1} and L_{sma2}	15.5 mm
R_{a1} and R_{a2}	0.65 mm
R_{b1} and R_{b2}	2 mm
Dielectric constant ϵ_r of RDR	51.92
Dielectric constant ϵ_r of Teflon	2.1

($\hat{z} \times \vec{E}_{Total}$=0). where,

$$\vec{E}_{Total} = [\vec{E}_{impressed}(\vec{J}_{feed}) + \vec{E}_s(\vec{J}_{probe-1}) + \vec{E}_s(\vec{J}_{core-1}) + \vec{E}_s(\vec{J}_{clad-1})+ \vec{E}_s(\vec{J}_{intcoax-1}) + \vec{E}_s(\vec{J}_{probe-2}) + \vec{E}_s(\vec{J}_{core-2}) + \vec{E}_s(\vec{J}_{clad-2}) + \vec{E}_s(\vec{J}_{intcoax-2})+ \vec{E}_s(\vec{J}_{RDR}) + \vec{E}_s(\vec{J}_{ground})] \tag{B.1}$$

- Step-2: The geometries of two port single- and dual-band CP RDRAs are discretized in to N subsegments, each of length Δx in x-direction, each of width Δy in y-direction and each of height Δz in Z-direction. In boundary conditions, impressed and scattered electric fields of all parts of single- and dual-band CP RDRAs are function of unknown current densities. Complex antenna geometries, pulse signals chooses as basis functions to expand the unknown current densities. Unknown current densities are expanded using known N basis functions with N unknown weighting coefficients.

- Step-3: After expanded unknown current densities functions in boundary conditions are converting to system of inner products using Galarkin's test procedure. In Galarkin method, basis functions are same as testing function. We have tested both side of equations with basis functions using inner product.

- Step-4: The system of inner products gives linear system of equations.

- Step-5: The linear system of equations is converted in to the matrix form $[Z]_{N\times N}[I]_{N\times 1}$=$[V]_{N\times 1}$.

PEC boundary condition on the surface of core-1, clad-1, core-2 and clad-2:

$$\hat{z}\bullet[\vec{E}_{impressed}(\vec{J}_{feed})+\vec{E}_s(\vec{J}_{probe-1})+\vec{E}_s(\vec{J}_{core-1})+\vec{E}_s(\vec{J}_{clad-1})+\\ \vec{E}_s(\vec{J}_{intcoax-1})+\vec{E}_s(\vec{J}_{probe-2})+\vec{E}_s(\vec{J}_{core-2})+\vec{E}_s(\vec{J}_{clad-2})+\vec{E}_s(\vec{J}_{intcoax-2})+\\ \vec{E}_s(\vec{J}_{RDR})+\vec{E}_s(\vec{J}_{ground})]=0 \tag{B.2}$$

PEC boundary condition on the surface of ground plane:

$$\hat{z}\times[\vec{E}_{impressed}(\vec{J}_{feed})+\vec{E}_s(\vec{J}_{probe-1})+\vec{E}_s(\vec{J}_{core-1})+\vec{E}_s(\vec{J}_{clad-1})+\\ \vec{E}_s(\vec{J}_{intcoax-1})+\vec{E}_s(\vec{J}_{probe-2})+\vec{E}_s(\vec{J}_{core-2})+\vec{E}_s(\vec{J}_{clad-2})+\vec{E}_s(\vec{J}_{intcoax-2})+\\ \vec{E}_s(\vec{J}_{RDR})+\vec{E}_s(\vec{J}_{ground})]=0 \tag{B.3}$$

The polarization currents are presented in volume of internal dielectric-1 of feed-1, internal dielectric-2 of feed-2 and RDR. The dielectric boundary condition is applied in volume of internal dielectric-1 of feed-1 ($\vec{E}_{Total}$=$\frac{\vec{J}_{intcoax-1}}{j\omega(\epsilon_{intcoax-1}-\epsilon_0)}$), internal dielectric-2 of feed-2 ($\vec{E}_{Total}$=$\frac{\vec{J}_{intcoax-2}}{j\omega(\epsilon_{intcoax-2}-\epsilon_0)}$) and RDR ($\vec{E}_{Total}$=$\frac{\vec{J}_{RDR}}{j\omega(\epsilon_r-\epsilon_0)}$). where, ϵ_0 is free space permittivity and ω represents as angular velocity. The dielectric boundary condition is applied in volume of internal dielectric-1 of feed-1:

$$\vec{E}_{impressed}(\vec{J}_{feed})+\vec{E}_s(\vec{J}_{probe-1})+\vec{E}_s(\vec{J}_{core-1})+\vec{E}_s(\vec{J}_{clad-1})+\vec{E}_s(\vec{J}_{intcoax-1})+\\ \vec{E}_s(\vec{J}_{probe-2})+\vec{E}_s(\vec{J}_{core-2})+\vec{E}_s(\vec{J}_{clad-2})+\vec{E}_s(\vec{J}_{intcoax-2})+\vec{E}_s(\vec{J}_{RDR})+\\ \vec{E}_s(\vec{J}_{ground})=\frac{\vec{J}_{intcoax-1}}{j\omega(\epsilon_{intcoax-1}-\epsilon_0)} \tag{B.4}$$

The dielectric boundary condition is applied in volume of internal dielectric-2 of feed-2:

$$\vec{E}_{impressed}(\vec{J}_{feed}) + \vec{E}_s(\vec{J}_{probe-1}) + \vec{E}_s(\vec{J}_{core-1}) + \vec{E}_s(\vec{J}_{clad-1}) + \vec{E}_s(\vec{J}_{intcoax-1}) +$$
$$\vec{E}_s(\vec{J}_{probe-2}) + \vec{E}_s(\vec{J}_{core-2}) + \vec{E}_s(\vec{J}_{clad-2}) + \vec{E}_s(\vec{J}_{intcoax-2}) + \vec{E}_s(\vec{J}_{RDR}) +$$
$$\vec{E}_s(\vec{J}_{ground}) = \frac{\vec{J}_{intcoax-2}}{j\omega(\epsilon_{intcoax-2} - \epsilon_0)} \tag{B.5}$$

The dielectric boundary condition is applied in volume of RDR:

$$\vec{E}_{impressed}(\vec{J}_{feed}) + \vec{E}_s(\vec{J}_{probe-1}) + \vec{E}_s(\vec{J}_{core-1}) + \vec{E}_s(\vec{J}_{clad-1}) + \vec{E}_s(\vec{J}_{intcoax-1}) +$$
$$\vec{E}_s(\vec{J}_{probe-2}) + \vec{E}_s(\vec{J}_{core-2}) + \vec{E}_s(\vec{J}_{clad-2}) + \vec{E}_s(\vec{J}_{intcoax-2}) + \vec{E}_s(\vec{J}_{RDR}) +$$
$$\vec{E}_s(\vec{J}_{ground}) = \frac{\vec{J}_{RDR}}{j\omega(\epsilon_r - \epsilon_0)} \tag{B.6}$$

The electric field (in integral form) of equations (B.1) to (B.6) can be expressed as in form of magnetic vector potential $\vec{A}$ [2, 3, 4, 5]:

$$\vec{E}(\vec{J}) = -j\omega\vec{A}_i(\vec{J}) - \frac{j}{\omega\mu\epsilon_0}\nabla(\nabla\cdot\vec{A}_i(\vec{J})) \tag{B.7}$$

In the volume of dielectrics, the magnetic vector potential is given by following equation:

$$\vec{A}_{i=v}(\vec{J}) = \mu_0 \iiint\limits_v \vec{J}G_0 dv' \tag{B.8}$$

On the surface of PECs, the magnetic vector potential is given by following equation:

$$\vec{A}_{i=s}(\vec{J}) = \mu_0 \iint\limits_s \vec{J}G_0 dv' \tag{B.9}$$

where, $G_0 = \frac{exp(-jk_0|R-R'|)}{4\pi\epsilon_0|R-R'|}$. The unknown current density functions are expanded into a set of basis functions. The current densities of probe-1, core-1 and clad-1 are given by following equations:

$$\vec{J}_{probe-1} = \sum_{n=1}^{3N_{p1}} a_n J_{p1n} \tag{B.10}$$

$$\vec{J}_{core-1} = \sum_{n=1}^{3N_{c1}} b_n J_{c1n} \tag{B.11}$$

$$\vec{J}_{clad-1} = \sum_{n=1}^{3N_{cl1}} c_n J_{cl1n} \tag{B.12}$$

Probe-2, core-2 and clad-2 current densities are given by equations (B.13), (B.14) and (B.15), respectively.

$$\vec{J}_{probe-2} = \sum_{n=1}^{3N_{p2}} d_n J_{p2n} \tag{B.13}$$

$$\vec{J}_{core-2} = \sum_{n=1}^{3N_{c2}} e_n J_{c2n} \tag{B.14}$$

$$\vec{J}_{clad-2} = \sum_{n=1}^{3N_{cl2}} f_n J_{cl2n} \tag{B.15}$$

Internal dielectric-1 of feed-1, internal dielectric-2 of feed-2, RDR and ground plane current densities are given by following equations:

$$\vec{J}_{intcoax-1} = \sum_{n=1}^{3N_{i1}} g_n J_{i1n} \tag{B.16}$$

$$\vec{J}_{intcoax-2} = \sum_{n=1}^{3N_{i2}} h_n J_{i2n} \tag{B.17}$$

$$\vec{J}_{RDR} = \sum_{n=1}^{3N_{rd}} i_n J_{rdn} \tag{B.18}$$

$$\vec{J}_{ground} = \sum_{n=1}^{3N_{g}} k_n J_{gn} \tag{B.19}$$

PEC boundary conditions on the surface of core-1, clad-1, probe-1, core-2, clad-2, probe-2 and ground plane are expressed in terms of basis function and weighting coefficient:

$$\begin{aligned}
&\sum_{n=1}^{3N_{p1}} a_n\vec{E}_s(\vec{J}_{p1n}) + \sum_{n=1}^{3N_{c1}} b_n\vec{E}_s(\vec{J}_{c1n}) + \sum_{n=1}^{3N_{cl1}} c_n\vec{E}_s(\vec{J}_{cl1}) + \\
&\sum_{n=1}^{3N_{p2}} d_n\vec{E}_s(\vec{J}_{p2n}) + \sum_{n=1}^{3N_{c2}} e_n\vec{E}_s(\vec{J}_{c2}) + \sum_{n=1}^{3N_{cl2}} f_n\vec{E}_s(\vec{J}_{cl2}) + \\
&\sum_{n=1}^{3N_{i1}} g_n\vec{E}_s(\vec{J}_{i1n}) + \sum_{n=1}^{3N_{i2}} h_n\vec{E}_s(\vec{J}_{i2}) + \sum_{n=1}^{3N_{rd}} i_n\vec{E}_s(\vec{J}_{rdn}) + \\
&\sum_{n=1}^{3N_{g}} k_n\vec{E}_s(\vec{J}_{gn}) = -\vec{E}_{impressed}(\vec{J}_{feed})
\end{aligned} \tag{B.20}$$

The dielectric boundary condition on internal dielectric-1 of feed-1 is expressed in terms of basis function and weighting coefficient:

$$\begin{aligned}
&\sum_{n=1}^{3N_{p1}} a_n\vec{E}_s(\vec{J}_{p1n}) + \sum_{n=1}^{3N_{c1}} b_n\vec{E}_s(\vec{J}_{c1n}) + \sum_{n=1}^{3N_{cl1}} c_n\vec{E}_s(\vec{J}_{cl1}) + \\
&\sum_{n=1}^{3N_{p2}} d_n\vec{E}_s(\vec{J}_{p2n}) + \sum_{n=1}^{3N_{c2}} e_n\vec{E}_s(\vec{J}_{c2}) + \sum_{n=1}^{3N_{cl2}} f_n\vec{E}_s(\vec{J}_{cl2}) + \\
&\sum_{n=1}^{3N_{i1}} g_n\vec{E}_s(\vec{J}_{i1n}) + \sum_{n=1}^{3N_{i2}} h_n\vec{E}_s(\vec{J}_{i2}) + \sum_{n=1}^{3N_{rd}} i_n\vec{E}_s(\vec{J}_{rdn}) + \\
&\sum_{n=1}^{3N_{g}} k_n\vec{E}_s(\vec{J}_{gn}) - \frac{g_n\vec{J}_{i1n}}{j\omega(\epsilon_{intcoax-1} - \epsilon_0)} = -\vec{E}_{impressed}(\vec{J}_{feed})
\end{aligned} \tag{B.21}$$

Similarly, dielectric boundary conditions on internal dielectric-2 of feed-2 and RDR can be expressed similar to equation (B.21).

PEC and dielectric boundary conditions equations are tested both side with basis functions using inner products. Tested both side of PEC boundary condition equation of core-1 with basis functions using inner products as given below:

$$\sum_{n=1}^{3N_{p1}} a_n\langle\vec{J}_{c1m}, \vec{E}_s(\vec{J}_{p1n})\rangle + \sum_{n=1}^{3N_{c1}} b_n\langle\vec{J}_{c1m}, \vec{E}_s(\vec{J}_{c1n})\rangle + \sum_{n=1}^{3N_{cl1}} c_n\langle\vec{J}_{c1m}, \vec{E}_s(\vec{J}_{cl1n})\rangle +$$
$$\sum_{n=1}^{3N_{p2}} d_n\langle\vec{J}_{c1m}, \vec{E}_s(\vec{J}_{p2n})\rangle + \sum_{n=1}^{3N_{c2}} e_n\langle\vec{J}_{c1m}, \vec{E}_s(\vec{J}_{c2n})\rangle + \sum_{n=1}^{3N_{cl2}} f_n\langle\vec{J}_{c1m}, \vec{E}_s(\vec{J}_{cl2n})\rangle +$$
$$\sum_{n=1}^{3N_{i1}} g_n\langle\vec{J}_{c1m}, \vec{E}_s(\vec{J}_{i1n})\rangle + \sum_{n=1}^{3N_{i2}} h_n\langle\vec{J}_{c1m}, \vec{E}_s(\vec{J}_{i2n})\rangle + \sum_{n=1}^{3N_{rd}} i_n\langle\vec{J}_{c1m}, \vec{E}_s(\vec{J}_{rdn})\rangle +$$
$$\sum_{n=1}^{3N_g} k_n\langle\vec{J}_{c1m}, \vec{E}_s(\vec{J}_{gn})\rangle = -\langle\vec{J}_{c1m}, \vec{E}_{impressed}(\vec{J}_{feed})\rangle \tag{B.22}$$

Similarly, PEC boundary condition equations are tested both side of clad-1, probe-1, core-2, clad-2, probe-2 and ground plane with basis functions using inner products.

Tested both side of dielectric boundary condition equation of internal dielectric-1 of feed-1 with basis functions using inner products as given below:

$$\sum_{n=1}^{3N_{p1}} a_n\langle\vec{J}_{i1m}, \vec{E}_s(\vec{J}_{p1n})\rangle + \sum_{n=1}^{3N_{c1}} b_n\langle\vec{J}_{i1m}, \vec{E}_s(\vec{J}_{c1n})\rangle + \sum_{n=1}^{3N_{cl1}} c_n\langle\vec{J}_{i1m}, \vec{E}_s(\vec{J}_{cl1n})\rangle +$$
$$\sum_{n=1}^{3N_{p2}} d_n\langle\vec{J}_{i1m}, \vec{E}_s(\vec{J}_{p2n})\rangle + \sum_{n=1}^{3N_{c2}} e_n\langle\vec{J}_{i1m}, \vec{E}_s(\vec{J}_{c2n})\rangle + \sum_{n=1}^{3N_{cl2}} f_n\langle\vec{J}_{i1m}, \vec{E}_s(\vec{J}_{cl2n})\rangle +$$
$$\sum_{n=1}^{3N_{i1}} g_n\langle\vec{J}_{i1m}, \vec{E}_s(\vec{J}_{i1n}) - \frac{\vec{J}_{i1n}}{j\omega(\epsilon_{intcoax-1} - \epsilon_0)}\rangle + \sum_{n=1}^{3N_{i2}} h_n\langle\vec{J}_{i1m}, \vec{E}_s(\vec{J}_{i2n})\rangle +$$
$$\sum_{n=1}^{3N_{rd}} i_n\langle\vec{J}_{i1m}, \vec{E}_s(\vec{J}_{rdn})\rangle + \sum_{n=1}^{3N_g} k_n\langle\vec{J}_{i1m}, \vec{E}_s(\vec{J}_{gn})\rangle = -\langle\vec{J}_{i1m}, \vec{E}_{impressed}(\vec{J}_{feed})\rangle \tag{B.23}$$

Similarly, dielectric boundary condition equations are tested both side of internal dielectric-2 of feed-2 and RDR with basis functions using inner products.

In single and dual-band CP RDRAs, ten different parts contains ten boundary condition equations with basis functions using inner products and ten unknowns. Boundary condition equations of ten different parts with basis functions using inner products and ten unknowns are converted in to matrix form. where, impedance, current and voltage elements of internal dielectric-1 with probe-1 are expressed as following equations:

$$Z_{i1p1} = \langle \vec{J}_{i1m}, \vec{E}_s(\vec{J}_{p1n}) \rangle \tag{B.24}$$

$$I_{i1p1} = \sum_{n=1}^{3N_{p1}} a_n \tag{B.25}$$

$$V_{i1} = -\langle \vec{J}_{i1m}, \vec{E}_{impressed}(\vec{J}_{feed}) \rangle \tag{B.26}$$

Similarly, other boundary conditions are represented with basis functions using inner product, unknowns coefficients and feeding in form of impedance, current and voltage elements. The impedance matrix [Z] of single- and dual-band RDRAs can be written as:

$$\begin{bmatrix}
[Z_{p1p1}] & [Z_{p1c1}] & [Z_{p1cl1}] & [Z_{p1i1}] & [Z_{p1p2}] & [Z_{p1c2}] & [Z_{p1cl2}] & [Z_{p1i2}] & [Z_{p1dr}] & [Z_{p1g}] \\
[Z_{c1p1}] & [Z_{c1c1}] & [Z_{c1cl1}] & [Z_{c1i1}] & [Z_{c1p2}] & [Z_{c1c2}] & [Z_{c1cl2}] & [Z_{c1i2}] & [Z_{c1dr}] & [Z_{c1g}] \\
[Z_{cl1p1}] & [Z_{cl1c1}] & [Z_{cl1cl1}] & [Z_{cl1i1}] & [Z_{cl1p2}] & [Z_{cl1c2}] & [Z_{cl1cl2}] & [Z_{cl1i1}] & [Z_{cl1dr}] & [Z_{cl1g}] \\
[Z_{i1p1}] & [Z_{i1c1}] & [Z_{i1cl1}] & [Z_{i1i1}] & [Z_{i1p2}] & [Z_{i1c2}] & [Z_{i1cl2}] & [Z_{i1i2}] & [Z_{i1dr}] & [Z_{i1g}] \\
[Z_{p2p1}] & [Z_{p2c1}] & [Z_{p2cl1}] & [Z_{p2i1}] & [Z_{p2p2}] & [Z_{p2c2}] & [Z_{p2cl2}] & [Z_{p2i2}] & [Z_{p2dr}] & [Z_{p2g}] \\
[Z_{c2p1}] & [Z_{c2c1}] & [Z_{c2cl1}] & [Z_{c2i1}] & [Z_{c2p2}] & [Z_{c2c2}] & [Z_{c2cl2}] & [Z_{c2i2}] & [Z_{c2dr}] & [Z_{c2g}] \\
[Z_{cl2p1}] & [Z_{cl2c1}] & [Z_{cl2cl1}] & [Z_{cl2i1}] & [Z_{cl2p2}] & [Z_{cl2c2}] & [Z_{cl1cl2}] & [Z_{cl2i2}] & [Z_{cl2dr}] & [Z_{cl2g}] \\
[Z_{i2p1}] & [Z_{i2c1}] & [Z_{i2cl1}] & [Z_{i2i1}] & [Z_{i2p2}] & [Z_{i2c2}] & [Z_{i2cl1}] & [Z_{i2i2}] & [Z_{i2dr}] & [Z_{i2g}] \\
[Z_{drp1}] & [Z_{drc1}] & [Z_{drcl1}] & [Z_{dri1}] & [Z_{drp2}] & [Z_{drc2}] & [Z_{drcl2}] & [Z_{dri2}] & [Z_{drdr}] & [Z_{drg}] \\
[Z_{gp1}] & [Z_{gc1}] & [Z_{gcl1}] & [Z_{gi1}] & [Z_{gp2}] & [Z_{gc2}] & [Z_{gcl2}] & [Z_{gi2}] & [Z_{gdr}] & [Z_{gg}]
\end{bmatrix}$$

The unknown current matrix [I] is given as:

$$\begin{bmatrix} [I_{p1p1}] \\ [I_{c1p1}] \\ [I_{cl1p1}] \\ [I_{i1p1}] \\ [I_{p2p1}] \\ [I_{c2p1}] \\ [I_{cl2p1}] \\ [I_{i2p1}] \\ [I_{drp1}] \\ [I_{gp1}] \end{bmatrix} \tag{B.27}$$

The incident voltage matrix [V] is indicated as:

$$\begin{bmatrix} [V_{p1}] \\ [V_{c1}] \\ [V_{cl1}] \\ [V_{i1}] \\ [V_{p2}] \\ [V_{c2}] \\ [V_{cl2}] \\ [V_{i2}] \\ [V_{dr}] \\ [V_{g}] \end{bmatrix} \tag{B.28}$$

The total number of basis functions N is expressed as:

$$N = 3N_{p1} + 3N_{c1} + 3N_{cl1} + 3N_{i1} + 3N_{p2} + 3N_{c2} + 3N_{cl2} + 3N_{i2} + 3N_{dr} + 3N_{g} \tag{B.29}$$

The number of basis functions on probe-1, core-1, clad-1, probe-2, core-2, clad-2 and ground plane are N_{p1}, N_{c1}, N_{cl1}, N_{p2}, N_{c2}, N_{cl2} and N_g, respectively. The number of basis functions in internal dielectric-1, internal dielectric-2 and rectangular dielectric resonator are N_{i1},N_{i2} and N_{dr}, respectively.

Here, unknown currents matrix or unknown weighting coefficients [I] is determined using admittance matrix [Y] and incident voltage matrix [V]. Here, the admittance matrix [Y] is obtained from the impedance matrix [Z].

$$[I]_{N\times 1} = [Y]_{N\times N}[V]_{N\times 1} \tag{B.30}$$

The input impedance, return loss, isolation, radiation pattern, gain and axial ratio of single- and dual-band RDRAs are then obtained using the currents as compared above.

B.2 Energy Conservation

In DRA, the input power P_I expresses in terms of the accepted power P_A and the reflected power P_R:

$$P_I = P_A + P_R \tag{B.31}$$

where, $P_A = P_O + P_L$. P_O and P_L are the output power and the loss power, respectively. Thus, the input power P_I can be expressed as [6]:

$$P_I = P_O + P_L + P_R \tag{B.32}$$

In DRA, the output power P_O is equal to the radiated power P_{Ra}. The input power P_I of DRA can be given as:

$$P_I = P_{Ra} + P_L + P_R \tag{B.33}$$

The loss power of dielectric material can be calculated using below equation [7]:

$$P_{LD} = \frac{\omega}{2} \int\limits_V \epsilon_d |E|^2 dv \tag{B.34}$$

The loss power (ohmic) of metal can be determined as [7]:

$$P_{LOhmic} = \int\limits_r \frac{1}{2} |J(r)|^2 \frac{1}{R_s} dr \tag{B.35}$$

where, surface resistance $R_s = \frac{1}{\sigma \delta_s}$ and skin depth $\delta_s = \sqrt{\frac{2}{\omega \mu \sigma}}$. The loss power $P_L = P_{LD} + P_{LOhmic}$. For single- and dual-band CP RDRAs, dielectric loss power P_{LD} can be expressed as:

$$P_{LD} = P_{LDR} + P_{Li1} + P_{Li2} \tag{B.36}$$

For single and dual band CP RDRAs, metal loss power P_{LOhmic} can be represented as:

$$P_{LOhmic} = P_{Lp1} + P_{Lc1} + P_{Lcl1} + P_{Lp2} + P_{Lc2} + P_{Lcl2} + P_{Lg} \tag{B.37}$$

The loss power of each dielectric material part in equation (B.36) is calculated using equation (B.34). The loss power of each metal part in equation (B.37) is determined using equation (B.35). The energy conservation of different radius of single- and dual-band RDRA are shown in Table B.2 and B.3.

Table B.2: Energy conservation at different radius of finite ground plane in single- and dual-band CP RDRA

R_g	P_I	P_R	P_{Ra}	P_L	P_R+P_{Ra}+P_L
40 mm	31.3 mW	0.313 mW	20.4 mW	10.5 mW	31.3 mW
35 mm	31.3 mW	0.0 mW	16.0 mW	15.3 mW	31.3 mW
30 mm	31.3 mW	0.0 mW	11.9 mW	19.4 mW	31.3 mW

Table B.3: Energy conservation at different radius of finite ground plane in single- and dual-band CP RDRA (in percentage form)

R_g **(mm)**	P_I (%)	P_R (%)	P_{Ra} (%)	P_L (%)	P_R+P_{Ra}+P_L(%)
40	100	1.0	65.17	33.54	100
35	100	0.0	51.11	48.88	100
30	100	0.0	38.01	61.98	100

References

[1] M. N.O. Sadiku, "Principles of Electromagnetics," *Oxford University Press Inc*, 2009.

[2] R. M. Baghaee, M. H. Neshati and J. R. Mohassel, "Rigorous Analysis of Rectangular Dielectric Resonator Antenna With a Finite Ground Plane," *in IEEE Transactions on Antennas and Propagation*, vol. 56, no. 9, pp. 2801-2809, Sept. 2008.

[3] W. C. Harrington, "Field computation by moment methods," *Wiley-IEEE Press*, 1993.

[4] W. C. Gibson, "The method of moments in electromagnetics," *Chapman* & *Hall/CRC*, Newyork, 2008.

[5] R. M. Baghaee, M. H. Neshati, D. Lashkari, M. Koochakzadeh and J. R. Mohassel, "Analysis of probe-fed rectangular dielectric resonator antennas on a finite ground plane using method of moment," *11th International Symposium on Antenna Technology and Applied Electromagnetics [ANTEM 2005]*, St. Malo, 2005, pp. 1-3.

[6] C.H. Durney, H.Massoudi and M.F.Iskander, "Radiofrequency Radiation," USAFSAM-TRs, December 1985.

[7] R.Vaughan and J.B. Andersen, "Channels, Propagation and Antennas for Mobile Communication, "IET Electromagnetic Wave Series 50, 1989.

Appendix C

MATLAB Sample Code

C.1 Tri-Band Staired RDRA

The dimensions of staired Rectangular Dielectric Resonator (RDR) are obtained by using this code. The input parameters of staired RDR are x=$\frac{W_l}{L_l}$, y=$\frac{f_1}{f_2}$, p=$\frac{W_l}{L_l}$, q=$\frac{W_l}{L_l}$, f_3 and ϵ_r. The output parameters of staired RDR are L_l, W_l, H_l, L_u, H_u and W_u.

```
clc;
close all;
clear all;
% For lower rectangular dielectric resonator
c= 3*10^8;
x=1.0;
f1=1.176*10^9;
f2=1.575*10^9;
er=38.67;
y=f2/f1;
w = 180.1639*exp(-14.4967*x) + 1.0077;
t = -2.7871*exp(-2.8633*x)+1.5811 ;
s = -5.1943*exp(-3.8633*x)+0.7584 ;
h = 6.5618*exp(-3.5343*x)+3.3658 ;
k=2*pi*sqrt(er)*f1/c ;
```

```
j = w*exp((-t*y)+s)+h;
L_l=j/k;
s=1;
m = -0.4167*exp(-0.6258*s) + 1.5137 ;
n = 10.4051*exp(-1.7887*y) + 0.1221 ;
z = m*n;
H_l=z*L_l;
W_l= L_l*x;
% For upper rectangular dielectric resonator
p=0.22;
q=0.77;
f3=2.49*10^9;
w1 = 180.1639*exp(-14.4967*p) + 1.0077 ;
t1 = -2.7871*exp(-2.8633*p)+1.5811 ;
s1 = -5.1943*exp(-3.8633*p)+0.7584 ;
h1 = 6.5618*exp(-3.5343*p)+3.3658 ;
k_0=2*pi*sqrt(er)*f3/c ;
j1 = w1*exp((-t1*q)+s1)+h1;
L_u=j1/k_0;
H_u= p*L_u;
W_u=q*L_u;
```

C.2 Dual-Band RDRA

The dimensions of RDR are determined by using this code. The input parameters of RDR are x=$\frac{W}{L}$, y=$\frac{f_1}{f_2}$ and ϵ_r. The output parameters of RDR are L, W and H.

```
clc;
close all;
clear all;
c= 3*10^8;
x=1.0;
f1=1.176*10^9;
f2=1.575*10^9;
er=51.92;
y=f2/f1;
w = 180.1639*exp(-14.4967*x) + 1.0077;
t = -2.7871*exp(-2.8633*x)+1.5811 ;
s = -5.1943*exp(-3.8633*x)+0.7584 ;
h = 6.5618*exp(-3.5343*x)+3.3658 ;
k=2*pi*sqrt(er)*f1/c ;
j = w*exp((-t*y)+s)+h;
L=j/k;
m = -0.4167*exp(-0.6258*x) + 1.5137 ;
n = 10.4051*exp(-1.7887*y) + 0.1221 ;
z = m*n;
H=z*L;
W= L*x;
```

C.3 Single-Band RDRA

The dimensions of RDR are found by using this code. The input parameters of RDR are p=$\frac{H}{L}$, q=$\frac{W}{L}$, f_1 and ϵ_r. The output parameters of RDR are L, W and H.

```
clc;
close all;
clear all;
p=0.74;
q=1.0;
f1=2.49*10^9;
c=3*10^9;
er=20.4;
w = 180.1639*exp(-14.4967*p) + 1.0077 ;
t = -2.7871*exp(-2.8633*p)+1.5811 ;
s = -5.1943*exp(-3.8633*p)+0.7584 ;
h = 6.5618*exp(-3.5343*p)+3.3658 ;
c= 3*10^8;
k=2*pi*sqrt(er)*f1/c ;
j = w*exp((-t*q)+s)+h;
L=j/k;
H= p*L;
W=q*L;
```

List of Publications

- **Journal publications**

  1. Pankaj Chaudhary, D. K. Ghodgaonkar, Sanjeev Gupta, Rajeev Jyoti and M. B. Mahajan, "Miniaturized triband circularly polarized staired rectangular dielectric resonator antenna for navigation satellite applications". *International Journal of Microwave and Optical Technology*, vol. 17, no.1, January 2022.

  2. Pankaj Chaudhary, D. K. Ghodgaonkar, Sanjeev Gupta, Rajeev Jyoti and M. B. Mahajan, "Compact circularly polarized triband staired rectangular dielectric resonator antenna using single and dual sections WPD with phase shifter for navigational satellite applications," *Microwave and Optical Technology Letters*, vol. 62, no.5, pp. 2047-2058, May 2020.

- **Conference publications**

  1. Pankaj Chaudhary, D. K. Ghodgaonkar, Sanjeev Gupta, Rajeev Jyoti and M. B. Mahajan, "Miniaturized L1 and L5-band circularly polarized rectangular dielectric resonator antennas for navigation satellite applications," *2021 IEEE Indian Conference on Antennas and Propagation (INCAP 2021)*, 13-16 December 2021, Jaipur, India.

  2. Pankaj Chaudhary, D. K. Ghodgaonkar, Sanjeev Gupta and Abhishek Shukla, "Dual band circularly polarized dielectric resonator antenna using DSWPD with phase shifter for IRNSS," *IEEE International RF and Microwave Conference (RFM-2018)*, pp.246-249, 17–19 December 2018, Penang, Malaysia.

3. Pankaj Chaudhary, D. K. Ghodgaonkar, Sanjeev Gupta and G. D. Makwana, "Design of compact circularly polarized rectangular dielectric resonator antenna with WBLC for navigational satellite applications," *2017 IEEE International Conference on Antenna Innovations and Modern Technologies for Ground, Aircraft and Satellite Application (iAIM)*, pp.1-5, 24 – 26 November 2017, Bangalore, India.

4. Pankaj Chaudhary, D. K. Ghodgaonkar, Sanjeev Gupta and G. D. Makwana, "Design of compact circularly polarized rectangular dielectric resonator antenna with finite ground planes for navigational satellite applications," *10th International Conference of Antenna Test and Measurement Society (ATMS-2017)*, pp. 221-225, 7 - 8 February 2017, Hyderabad, India.